USE OF GOLD NANOPARTICLE EMBEDDED POLYELECTROLYTE MULTILAYER FILMS AS SERS SUBSTRATES

A THESIS SUBMITTED TO
THE GRADUATE SCHOOL OF NATURAL AND APPLIED SCIENCES
OF
MIDDLE EAST TECHNICAL UNIVERSITY

BY

SEZİN ÖZDEMİR

IN PARTIAL FULFILLMENT OF THE REQUIREMENTS
FOR
THE DEGREE OF DOCTOR OF PHILOSOPHY
IN
CHEMISTRY

SEPTEMBER 2023

Approval of the thesis:

USE OF GOLD NANOPARTICLE EMBEDDED POLYELECTROLYTE MULTILAYER FILMS AS SERS SUBSTRATES

submitted by **SEZİN ÖZDEMİR** in partial fulfillment of the requirements for the degree of **Doctor of Philosophy** in **Chemistry, Middle East Technical University** by,

Prof. Dr. Halil Kalıpçılar
Dean, Graduate School of **Natural and Applied Sciences**

Prof. Dr. Özdemir Doğan
Head of the Department, **Chemistry**

Prof. Dr. Gülay Ertaş
Supervisor, **Chemistry, METU**

Prof. Dr. İrem Erel Göktepe
Co-Supervisor, **Chemistry, METU**

Examining Committee Members:

Prof. Dr. Zeynep Çulfaz Emecen
Chemical Engineering, METU

Prof. Dr. Gülay Ertaş
Chemistry, METU

Prof. Dr. Murat Kaya
Chemical Engineering, Atılım University

Prof. Dr. Eda Ayşe Aksoy
Basic Pharmaceutical Sciences, Hacettepe University

Assist. Prof. Dr. Erol Yıldırım
Chemistry, METU

Date: 11.09.2023

I hereby declare that all information in this document has been obtained and presented in accordance with academic rules and ethical conduct. I also declare that, as required by these rules and conduct, I have fully cited and referenced all material and results that are not original to this work.

Name Last name : Sezin Özdemir

Signature :

ABSTRACT

USE OF GOLD NANOPARTICLE EMBEDDED POLYELECTROLYTE MULTILAYER FILMS AS SERS SUBSTRATES

Özdemir, Sezin
Doctor of Philosophy, Chemistry
Supervisor: Prof. Dr. Gülay Ertaş
Co-Supervisor: Prof. Dr. İrem Erel Göktepe

September 2023, 189 pages

Surface-enhanced Raman spectroscopy (SERS) is a powerful technique for enhancement in Raman scattering of molecules adsorbed on SERS active surfaces. It is commonly used in chemical, material and life sciences applications. This study examined the the potential use of nanoparticles (NPs) containing layer-by-layer (LbL) films as SERS substrates. Firstly, the effects of chemical nature of the LbL building blocks, surface morphology and the film architecture on SER signal have been investigated. Poly(allylamine hydrochloride) (PAH) was used as the polycation, whereas poly(acrylic acid) (PAA) and tannic acid (TA) were used as polyanions for the construction of LbL films. The surface of PAH and PAA films were smoother compared to PAH/TA multilayers with highly rough surface morphology. The enhancement factor (EF) of PAH/TA, best system of this part, was calculated as 10^6.

Secondly, positively-charged, branched poly ethylene imine (BPEI)-capped Au NPs were synthesized in solution. The effects of BPEI concentration and pH of NPs growth solution on the size of NPs were examined. Multilayers using BPEI-capped Au NPs and TA or polystyrene sulfonate (PSS) as polyanions increased SERS signal

approximately 3 times as compared to 1-layer NP including films. Both LbL systems (NPs/TA and NPs/PSS) provided more reproducible SER signal as compared to 1-layer NP including films.

Lastly, LbL films (PAH/TA, PAH/PAA, BPEI/TA) were used as *in situ* photoreactors for the synthesis of both Au and Ag NPs. The effects of assembly conditions on SER signals of CV molecule were investigated. In order to obtain reproducible and better SER signals among multilayer systems, PAH/TA worked well for *in situ* synthesis of Ag NPs using Xe radiation.

Keywords: Raman Spectroscopy, SERS Substrate, Layer-by-Layer Technique, Polyelectrolyte, Nanoparticle.

ÖZ

ALTIN NANOPARÇACIK GÖMÜLÜ POLİELEKTROLİT ÇOK KATMANLI FİLMLERİN YGRS ALTTAŞI OLARAK KULLANILMASI

Özdemir, Sezin
Doktora, Kimya
Tez Yöneticisi: Prof. Dr. Gülay Ertaş
Ortak Tez Yöneticisi: Prof. Dr. İrem Erel Göktepe

Eylül 2023, 189 sayfa

Yüzeyde güçlendirilmiş Raman spektroskopisi (YGRS), moleküllerin YGRS aktif yüzeylere adsorbe edildiği yüzeylerde moleküler Raman saçılma şiddetinin arttırmasında güçlü bir tekniktir. Kimyasal, malzeme ve yaşam bilimleri uygulamalarında yaygın olarak kullanılmaktadır. Bu çalışma, nanoparçacık (NP) içeren katman katman (LbL) polimer filmlerin YGRS alttaşları olarak potansiyel kullanımını incelemiştir. İlk olarak, LbL film yapıtaşlarının kimyasal doğası, yüzey morfolojisi ve film mimarisinin YGR sinyali üzerindeki etkileri araştırılmıştır. Poli(allilamin hidroklorür) (PAH), polikatyon olarak kullanılırken, poli(akrilik asit) (PAA) ve tanik asit (TA), çok katmanlı filmlerinin yapısının oluşturulmasında polianyon olarak kullanılmıştır. PAH ve PAA filmlerinin yüzeylerinin PAH/TA çok-katmanlı filmlerine göre daha pürüzsüz olduğu gözlenmiştir. Bu bölümün en iyi sistemi olan PAH/TA'nın zenginleştirme faktörü (EF) 10^6 olarak hesaplanmıştır.

İkinci olarak, pozitif yüklü, dallı polietilen imin (BPEI) ile kaplı Au NP'ler çözelti içerisinde sentezlenmiştir. BPEI derişiminin ve çözelti pH'sının NP boyutuna etkileri incelenmiştir. BPEI ile kaplı Au NP'ler ile TA veya polistiren sülfonat (PSS)

polianyonlar kullanılarak hazırlanan filmler CV molekülünün Raman saçılma şiddetini tek katman NP içeren filmlere göre yaklaşık 3 kat arttırmıştır. Çok katmanlı sistemlerin ikisi de (NPs/TA, NPs/PSS) tek katman NP içeren filmlere göre daha tekrarlanabilir Raman sinyali sağlamıştır.

Son olarak, çok katmanlı filmler (PAH/TA, PAH/PAA, BPEI/TA) hem Au hem de Ag NP'lerinin fotokimyasal oluşumları için kullanılmıştır. Kristal viyole molekülünün Raman sinyalleri üzerinde kaplama koşullarının etkisi incelenmiştir. Çok katmanlı film sistemleri arasında PAH/TA Ag NP'lerinin *in situ* sentezi için Xe ışığını kullanarak daha iyi ve tekrarlanabilir sonuç vermiştir.

Anahtar Kelimeler: Raman Spektroskopisi, YGRS Alttaşı, LbL Tekniği, Polielektrolit, Nanoparçacık.

To Erhan and my little girl…

ACKNOWLEDGMENTS

I would like to express my deep appreciation and respect to my supervisor Prof. Dr. Gülay Ertaş and co-supervisor Prof. Dr. İrem Erel Göktepe for their endless guidance, support, encouragement, understanding, patience and suggestions throughout this study.

I would like to thank Prof. Dr. Zeynep Çulfaz Emecen and Assist. Prof. Dr. Erol Yıldırım for their ideas, comments and discussions during the PhD commitee meetings.

I would like to thank METU BAP for financial support during the thesis for the projects TEZ-D-103-2020-10176 and TEZ-D-103-2021-10625.

My special thanks to my dearest friends Canan Höçük Özkan, Yeliz Akpınar and Begüm Avcı for their endless help, moral support and friendship from the beginning of the study. I would also like to thank Zuhal Vanlı Güner and Merve Akpınar for their friendship.

I should thank all C-49 members, especially Deniz Yılmaz and Ayşe Efran Boz for their endless support.

I would like to thank my collegues at work Eda Bolayır, Yeşim Abacıoğlu, Begüm Erdem, Kübra Acer, Emre Bulut and Günseli Bayram for their moral support during the last year of this study.

Finally, my special thanks to my husband Erhan Özdemir and my little girl growing inside of me and all of my family members for their patience, moral support and love. I know that they are always with me and never leave me alone.

TABLE OF CONTENTS

ABSTRACT v

ÖZ vii

ACKNOWLEDGMENTS x

TABLE OF CONTENTS xi

LIST OF TABLES xv

LIST OF FIGURES xvi

LIST OF ABBREVIATIONS xxvi

CHAPTERS

1 INTRODUCTION 1

1.1 Raman Spectroscopy 1

1.2 Surface Enhanced Raman Spectroscopy and Its Related Mechanisms 3

1.2.1 SERS Substrates 8

1.3 Polyelectrolytes 8

1.3.1 Layer-by-Layer Self-Assembly Technique 9

1.4 Nanoparticles (NPs) 14

1.4.1 Synthesis Methods of Au NPs 15

1.4.2 Photochemical Synthesis of NPs and Related Mechanisms 16

1.5 NP Embedded Films for SERS Applications 20

1.5.1 Seed-mediated NPs in SERS Applications 21

1.5.2 Photochemically Synthesized NPs Embedded Films in Various Applications 22

1.6 Aim of the Study 25

2 EXPERIMENTAL 27

2.1 Materials 27

2.2 Methods and Instrumentation 28

2.3 Preparation of Citrate-Capped Au NPs..30

2.4 Multilayer Preparation of PAH/PAA, PAH/TA, PAH-PAA Complex/PAA and PAH-TA Complex/TA..30

2.4.1 LbL Self-Assembly of PAH and PAA 30

2.4.2 Preparation of PAH-PAA Complexes and LbL Self-Assembly of PAH-PAA Complexes and PAA 31

2.4.3 LbL Self-Assembly of PAH/TA..31

2.4.4 Preparation of PAH-TA Complexes and LbL Self-Assembly of PAH-TA Complexes and TA...32

2.4.5 Citrate-Capped Au NPs Loading into Multilayer Films...................32

2.4.6 LbL Self-Assembly of Citrate-Capped Au NPs and Polyelectrolytes or PECs (Sandwich Type Multilayers)..33

2.5 Seed-Mediated Synthesis of Au NPs..34

2.5.1 LbL Self-Assembly of Seed-Mediated Au NPs and TA 35

2.5.2 LbL Self-Assembly of Seed-Mediated Au NPs and PSS.................36

2.6 Photochemical Preparation of NPs 36

2.6.1 Multilayer Preparation for Post Loaded Inclusion of Au or Ag NPs 36

3 USE OF CITRATE-CAPPED AU NPS IN POLYELECTROLYE MULTILAYERS AS SERS SUBSTRATES 39

3.1 Characterization of Spherical Au NPs..39

3.2 Preparation of LbL Films..40

3.3 Au NPs Loading into Multilayers...47

3.4 SERS Characterization of Multilayers..50

3.4.1 Calculation of the Enhancement Factor 63

3.5 SERS Reproducibility 65

3.6 Sandwich vs. Au NPs Incorporated into Multilayers as SERS Substrates 65

3.7 The Effect of Concentration of CV on the SER Signals 70

4 USE OF SEED-MEDIATED AU NPS IN POLYELECTROLYTE MULTILAYERS AS SERS SUBSTRATES...73

4.1 Optimization Studies for Seed-Mediated Au NPs................................... 74

4.1.1 The Effect of BPEI Volume on NP Formation 74

4.1.2 The Effect of pH of NPs on Size Distribution 80

4.2 SERS Performance of 1-Layer Self-Assembled Substrates 82

4.3 SERS Performance of LbL Self-Assembled Substrates........................... 85

5 USE OF PHOTOCHEMICALLY SYNTHESIZED NPS IN POLYELECTROLYE MULTILAYERS AS SERS SUBSTRATES 95

5.1 The Effect of Concentration of $AgNO_3$ Solution on the Amount of Ag^+ Loading into Multilayers... 96

5.2 The Effect of Deposition Time on the Amount of Ag^+ Loading into Multilayers 101

5.3 The Effect of Layer Number on NP Formation 104

5.4 The Effect of Light Exposure on NP Formation 107

5.5 The Effect of Light on the Stability of Tannic Acid 109

5.6 The Effect of Number of Loading/Reduction Cycles on NP Formation 113

5.7 The Effect of Different Type of Lamps on NP Formation..................... 116

5.8 Au NPs Containing PAH/TA Multilayers.. 121

5.8.1 The Effect of Concentration on Au NP Formation 121

5.8.2 The Effect of Deposition Time on Au NP Formation..................... 124

5.9 Overview of Bimetallic Structures 126
5.9.1 The Effect of Film Architecture in Sandwich Structures Including Bimetallic NPs on SERS Enhancement 127
5.9.2 The Effect of Chemical Nature of Polyelectrolytes Including Monometallic and/or Bimetallic NPs on SERS Enhancement 142
6 CONCLUSION AND OUTLOOK 151
REFERENCES 157
APPENDICES
A. The Intensity and Volume Particle Size Distribution of BPEI-capped Au NPs Solution at pH 5.0 185
B. The Change of Particle Size Distribution with Increasing pH of BPEI-capped Au NPs solution 186
CURRICULUM VITAE 187

LIST OF TABLES

TABLES

Table 2.1. Polyelectrolyte couple list used in the photochemical part.................... 37

Table 5.1. List of multilayer PAH/TA substrates including *in situ* photosynthesized Au and/or Ag NPs prepared in this part of the study. 128

Table 5.2. Multilayer PAH/TA substrates including *in situ* photosynthesized Au and/or Ag NPs with 1, 2, 3, 4, 5 and 6 cycles of loading/reduction. 133

Table 5.3. Multilayer BPEI/TA substrates including *in situ* photosynthesized Au and/or Ag NPs.. 143

LIST OF FIGURES

FIGURES

Figure 2.1 Chemical structures of polyelectrolytes. 28
Figure 2.2 Citrate-capped Au NP loaded multilayers. 33
Figure 2.3 Sandwich type multilayer. 34
Figure 2.4 Seed-mediated synthesis of Au NPs. 35
Figure 2.5 BPEI-capped Au NP/TA multilayer. 36
Figure 2.6 Experimental scheme of photochemical Ag or Au NP formation. 38
Figure 2.7 Photochemical synthesis of Ag or Au NPs in sandwich LbL structures……………………………………………………………………..38
Figure 3.1 UV-vis spectrum of Au NPs synthesized by Turkevich Method. 40
Figure 3.2 LbL growth of PAH/PAA. PAH and PAA were deposited at pH 7.5 and 3.5, respectively. Multilayers were grown onto a precursor film with a thickness of ~1.9 nm. Thickness values do not include the precursor layer thickness. 41
Figure 3.3 LbL growth of PAH/TA at pH 7.0. Multilayers were grown onto a precursor film with a thickness of ~1.5 nm. Thickness values do not include the precursor layer thickness. 41
Figure 3.4 AFM height images and roughness values of 41-layer PAH/PAA and PAH/TA films. The roughness values were estimated over 2x2 μm^2 images. 42
Figure 3.5 AFM height images and roughness values of 7, 11 and 21-layers of PAH/PAA films. The roughness values were estimated over 2x2 μm^2 images. 43
Figure 3.6 Multilayer growth of PAH/PAA at (A) pH 4.0/4.0 and (B) pH 7.5/3.5. Multilayers were grown onto a precursor film with a thickness of ~ 1.8 and 1.9 nm, respectively. Thickness values given in A and B do not include the precursor layer thickness. 45
Figure 3.7 AFM height images and roughness (root mean square, rms) values of 41 layers of PAH/PAA films at pH 4.0/4.0 and pH 7.5/3.5 before and after Au NP deposition. The roughness values were recorded from 2x2 μm^2 images. 46

Figure 3.8 AFM height images and roughness values of 41-layers of PAH/TA and PAH/PAA films before and after Au NPs deposition. The roughness values were recorded from 2x2 μm^2 images. 48
Figure 3.9 UV-vis absorption spectra of Au NPs embedded in 41-layers of (i) PAH/TA, (ii) PAH/PAA. 49
Figure 3.10 SEM images of 41-layers of PAH/TA and PAH/PAA films after Au NPs deposition. 49
Figure 3.11 SER spectra of 1.0 x 10^{-5} M CV molecule adsorbed onto Au NPs containing (i) 41 layers of PAH/PAA (laser power: 5 mW) and (ii) PAH/TA multilayer films (laser power: 10 mW).. 51
Figure 3.12 UV-vis absorption spectra of Au NPs embedded in 41 layers of (i) PAH/PAA, (ii) PAH-PAA complex/PAA. 52
Figure 3.13 UV-vis absorption spectra of Au NPs embedded in 41 layers of (iii) PAH/TA, (iv) PAH-TA complex/TA multilayer films.. 53
Figure 3.14 Hydrodynamic size distributions by number of (1 mg/mL PAH- 0.8 mg/mL PAA) complexes by Dynamic Light Scattering. Each color shows the replicate measurements of these complexes. 54
Figure 3.15 Zeta potential distribution of the complexes. Each color shows the replicate measurements of these complexes. 54
Figure 3.16 Multilayer growth of PAH/PAA (A) PAH-PAA complex/PAA (B) at pH 7.5/3.5. Multilayers were grown onto a precursor film with a thickness of ~1.9 nm and 1.0 nm, respectively. Thickness values do not include the precursor layer thickness.. 55
Figure 3.17 AFM height images and root mean square values of 41 layers of PAH/PAA and PAH-PAA complex/PAA films before and after Au NP deposition. The roughness values were recorded from 2x2 μm^2 images. 56
Figure 3.18 SER spectra of 1.0 x 10^{-5} M CV molecule adsorbed on Au NP containing 41 layers of (i) PAH/PAA and (ii) PAH-PAA complex/PAA multilayer films. 57

Figure 3.19 SEM images of 41-layers of PAH/PAA and PAH-PAA complex/PAA films after Au NPs deposition. 58
Figure 3.20 Hydrodynamic size distributions by number of (1 mg/mL PAH- 0.4 mg/mL TA) complexes by Dynamic Light Scattering. Each color shows the replicate measurements of these complexes. 59
Figure 3.21 Zeta potential distributions of the complexes. Each color shows the replicate measurements of these complexes. 59
Figure 3.22 Multilayer growth of PAH/TA (A) and PAH-TA complex/TA (B) at pH 7.0. Multilayers were grown onto a precursor film with a thickness of ~1.5 nm. Thickness values do not include the precursor layer thickness. 60
Figure 3.23 AFM images and root mean square values of 41 layers of PAH/TA and PAH-TA complex/TA films before and after Au NP deposition. The roughness values were recorded from 2x2 μm^2 images. 61
Figure 3.24 SER spectra of 1.0 x 10^{-5} M CV molecule adsorbed on Au NPs containing 41 layers of (i) PAH/TA and (ii) PAH-TA complex/TA multilayer films. 62
Figure 3.25 SEM images of 41-layers of PAH/TA and PAH-TA complex/TA films after Au NPs deposition. 63
Figure 3.26 SER spectra of 1.0x10^{-5} M CV molecule from sandwich type substrate in various layer numbers. 67
Figure 3.27 SER spectra of 1.0x10^{-5} M CV molecule from post-loaded type substrate. 67
Figure 3.28 UV-vis spectra of sandwich type substrate in various layer numbers. 68
Figure 3.29 UV-vis spectrum of post-loaded type substrate. 68
Figure 3.30 Plot of absorbance maxima values in sandwich type substrate vs. layer number. 69
Figure 3.31 AFM height images and root mean square values of sandwich type substrates. The roughness values were recorded from 2x2 μm^2 images. 70

Figure 3.32 SER spectra of $1.0x10^{-4}$ (black), $5.0x10^{-5}$ (red), $1.0x10^{-5}$ (blue), $5.0x10^{-6}$ (pink) and $1.0x10^{-6}$ M (green) CV on $(PAH/TA)_{41}$ film with 12 h deposition of Au NPs. 71
Figure 3.33 Dependence of SER signal intensity at 1176 cm^{-1} on increasing CV concentration. 72
Figure 4.1 UV-vis absorption spectrum of Au NP seed. 75
Figure 4.2 Hydrodynamic size distribution by number of seed NPs by Dynamic Light Scattering. Each color shows the replicate measurements of these NPs. 76
Figure 4.3 Zeta potential distributions of seed NPs. Each color shows the replicate measurements of these NPs. 76
Figure 4.4 UV-vis absorption spectra of Au NP solutions synthesized using 50, 100 and 500 μL of BPEI and 1000 μL of seed. 77
Figure 4.5 Hydrodynamic size distributions by number of BPEI-capped NP solutions by Dynamic Light Scattering. Each color shows the replicate measurements of these NPs. 79
Figure 4.6 Zeta potential distribution of BPEI-capped NP solutions. Each color shows the replicate measurements of these NPs. 80
Figure 4.7 Number average hydrodynamic size of BPEI-capped NPs as a function of pH of NPs solution. Each color shows the replicate measurements of these NPs. 81
Figure 4.8 UV-vis absorption spectra of BPEI-capped NPs at pH 3.0, 5.0 and 7.5. 82
Figure 4.9 Photographic demonstration of 1-layer of BPEI-capped Au NPs at 30 min, 3 h, 6 h and 17 h deposition times. 83
Figure 4.10 UV-vis absorption spectra of 1-layer-coated substrates with 30 min, 3 h, 6 h and 17 h deposition times in BPEI-capped NP solution. 84
Figure 4.11 SER spectra of $1.0x10^{-5}$ M CV molecule adsorbed on 1-layer coated substrates with 30 min, 3 h, 6 h and 17 h deposition times in BPEI-capped Au NPs. 84

Figure 4.12 Relative intensity plot at 1176 cm^{-1} of 1.0 x 10^{-5} M CV molecule adsorbed on 1-layer coated, BPEI-capped Au NPs as a function of deposition times. 85
Figure 4.13 LbL growth of BPEI/TA. BPEI and TA were deposited at pH 5.0. Multilayers were grown onto a precursor film of 0.5 mg/mL BPEI for 30 min with a thickness of ~1.9 nm. Thickness values do not include the precursor layer thickness. 86
Figure 4.14 UV-vis spectra of 1-, 2-, 3-, 4-, 5-, 7-, 10-,11-, 14-, 15-layers of BPEI-Au NPs/TA. 88
Figure 4.15 SER spectra of 1.0x10^{-5} M CV molecule adsorbed on 1-, 2-, 3-, 4-, 5-, 7-, 10-,11-, 14-, 15-layers of BPEI-Au NPs and TA. 88
Figure 4.16 Relative intensity plot at 1176 cm^{-1} of 1.0 x 10^{-5} M CV molecule adsorbed on BPEI-Au NPs/TA multilayers as a function of layer number. 89
Figure 4.17 LbL growth of BPEI/PSS. BPEI and PSS (in 0.1 M NaCl) were deposited at pH 5.0. Multilayers were grown onto a precursor film with a thickness of ~1.6 nm. Thickness values do not include the precursor layer thickness. 90
Figure 4.18 UV-vis spectra of 1-, 3-, 5-, 7-, 8-, 9-, 10-,11-, 15-layers of BPEI-Au NPs/PSS. 91
Figure 4.19 SER spectra of 1.0x10^{-5} M CV molecule adsorbed on 1-, 3-, 5-, 7-, 8-, 9-, 10-,11-, 15-layers of BPEI-Au NPs/PSS. 92
Figure 4.20 Relative intensity plot at 1176 cm^{-1} of 1.0 x 10^{-5} M CV molecule adsorbed on BPEI-Au NPs/PSS multilayers as a function of layer number. 92
Figure 4.21 UV-vis spectra of 9 layers of seed NPs/PSS and 3 layers of seed NPs/TA. 93
Figure 4.22 SER spectra of 1.0x10^{-5} M CV molecule adsorbed on 9 layers of seed NPs/PSS and 3 layers of seed NPs/TA. 94
Figure 5.1 UV-vis absorption spectra of Ag NPs grown within 20 layers of PAH/TA multilayer films, prepared by immersion into 0.10, 0.25, 0.50 and 0.75 M $AgNO_3$ solutions for 6 h, rinsed, dried and followed by 1 h of Xe radiation. 98

Figure 5.2 Concentration of Ag^+ in the multilayers (ppm) as a function of concentration of $AgNO_3$. 98
Figure 5.3 SER spectra of 1.0 x 10^{-5} M CV on Ag NP grown within 20 layers of PAH/TA multilayer films, prepared by immersion into 0.10, 0.25, 0.50 and 0.75 M $AgNO_3$ solutions for 6 h, rinsed, dried and followed by 1 h of Xe radiation. 100
Figure 5.4 Relative Raman intensity plot at 1176 cm^{-1} of 1.0 x 10^{-5} M CV molecule on Ag NPs embedded 20 layers of PAH/TA multilayer films as a function of $AgNO_3$ concentration. 100
Figure 5.5 UV-vis absorption spectra of Ag NPs grown within 20 layers of PAH/TA multilayer films, prepared by immersion into 0.50 M $AgNO_3$ solution for 2, 4, 6 and 12 h, rinsed, dried and followed by 1 h of Xe radiation..................... 102
Figure 5.6 Concentration of Ag^+ into multilayers (ppm) as a function of deposition time of $AgNO_3$. 102
Figure 5.7 SER spectra of 1.0 x 10^{-5} M CV on Ag NP grown within 20 layers of PAH/TA multilayer films, prepared by immersion into 0.50 M $AgNO_3$ solutions for 2, 4, 6 and 12 h, rinsed, dried and followed by 1 h of Xe radiation..................... 103
Figure 5.8 Relative intensity plot at 1176 cm^{-1} of 1.0 x 10^{-5} M CV on Ag NPs embedded 20 layers of PAH/TA multilayer films as a function of deposition time of $AgNO_3$.. 104
Figure 5.9 UV-vis absorption spectra of Ag NPs grown within 20, 30 and 40 layers of PAH/TA multilayer films, prepared by immersion into 0.50 M $AgNO_3$ solution for 6 h, rinsed, dried and followed by 1 h of Xe radiation. Arrow shows increase of absorption and red-shift of the plasmon resonance... 105
Figure 5.10 SER spectra of 1.0 x 10^{-5} M CV on Ag NP grown within 20, 30 and 40 layers of PAH/TA multilayer films, prepared by immersion into 0.50 M $AgNO_3$ solution for 6 h, rinsed, dried and followed by 1 h of Xe radiation..................... 106
Figure 5.11 Relative intensity plot at 1176 cm^{-1} of 1.0 x 10^{-5} M CV on Ag NPs embedded PAH/TA multilayer films as a function of layer number. 106

Figure 5.12 UV-vis absorption spectra of Ag NPs grown within 20 layers of PAH/TA multilayer films, prepared by immersion into 0.50 M $AgNO_3$ solutions for 6 h, rinsed, dried and followed by 30, 60 and 90 min of Xe radiation. 108
Figure 5.13 SER spectra of 1.0 x 10^{-5} M CV on Ag NP grown within 20 layers of PAH/TA multilayer films, prepared by immersion into 0.50 M $AgNO_3$ solutions for 6 h, followed by 30, 60 and 90 min of Xe radiation. 108
Figure 5.14 Relative intensity plot at 1176 cm^{-1} of Ag NPs embedded PAH/TA multilayer films as a function of exposure time to Xe radiation. 109
Figure 5.15 UV-vis absorption spectra of 0.01 mg/mL TA solution at pH 7.0 followed by 0, 30, 60 and 90 min of Xe radiation. 112
Figure 5.16 UV-vis absorption spectra of 20 layers of PAH/TA multilayer films, rinsed, dried and followed by 0, 30, 60 and 90 min of Xe radiation. 113
Figure 5.17 The scheme for L/R cycles on LbL substrates for NP formation. 113
Figure 5.18 UV-vis absorption spectra of Ag NPs grown within 20 layers of PAH/TA multilayer films, prepared by immersion into 0.50 M $AgNO_3$ solutions for 6 h, rinsed, dried and followed by 1 h of Xe radiation with different number of loading/reduction cycles. 115
Figure 5.19 SER spectra of 1.0 x 10^{-5} M CV molecule on Ag NP grown within 20 layers of PAH/TA multilayer films, prepared by immersion into 0.50 M $AgNO_3$ solutions for 6 h, rinsed, dried and followed by 1 h of Xe radiation with different number of loading/reduction cycles. 115
Figure 5.20 Relative intensity plot at 1176 cm^{-1} of 1.0 x 10^{-5} M CV on Ag NPs embedded PAH/TA multilayer films as a function of L/R cycle number. 116
Figure 5.21 UV-vis absorption spectra of Ag NPs grown within 20 layers of PAH/TA multilayer films, prepared by immersion into 0.50 M $AgNO_3$ solutions for 6 h, rinsed, dried and followed by 1 h of Xe lamp or 5 h of UV lamp exposure. . 118
Figure 5.22 SER spectra of 1.0x10^{-5} M CV on Ag NP grown within 20 layers of PAH/TA multilayer films, prepared by immersion into 0.50 M $AgNO_3$ solutions for 6 h, rinsed, dried and followed by 1 h of Xe lamp and 5 h of UV lamp. 118

Figure 5.23 UV-vis absorption spectra of Ag NPs grown within 20 layers of PAH/PAA and PAH/TA multilayer films, prepared by immersion into 0.25 M $AgNO_3$ solutions for 6 h, rinsed, dried and followed by 1 h of Xe radiation. 120
Figure 5.24 SER spectra of $1.0x10^{-5}$ M CV on Ag NP grown within 20 layers of PAH/PAA and PAH/TA multilayer films, prepared by immersion into 0.25 M $AgNO_3$ solutions for 6 h, rinsed, dried and followed by 1 h of Xe radiation. 120
Figure 5.25 UV-vis absorption spectra of Au NPs grown within 19 layers of PAH/TA multilayer films, prepared by immersion into 2.0, 5.0, 10.0 and 15.0 mM $AuCl_4^-$ solutions for 6 h, rinsed, dried and followed by 1 h of Xe radiation. 122
Figure 5.26 SER spectra of 1.0×10^{-5} M CV on Au NP grown within 19 layers of PAH/TA multilayer films, prepared by immersion into 2.0, 5.0, 10.0 and 15.0 mM $AuCl_4^-$ solutions for 6 h, rinsed, dried and followed by 1 h of Xe radiation. 123
Figure 5.27 Relative intensity plot at 1176 cm^{-1} of Au NPs embedded 19 layers of PAH/TA multilayer films as a function of $AuCl_4^-$ concentration. 123
Figure 5.28 UV-vis absorption spectra of Au NPs grown within 19 layers of PAH/TA multilayer films, prepared by immersion into 5.0 mM $AuCl_4^-$ solutions for 15 min, 30 min, 1 h and 6 h, rinsed, dried and followed by 1 h of Xe radiation. . 125
Figure 5.29 SER spectra of 1.0×10^{-5} M CV on Au NP grown within 19 layers of PAH/TA multilayer films, prepared by immersion into 5.0 mM $AuCl_4^-$ solutions for 15 min, 30 min, 1 h and 6 h, rinsed, dried and followed by 1 h of Xe radiation. . 125
Figure 5.30 Relative intensity plot at 1176 cm^{-1} of Au NPs embedded 19 layers of PAH/TA multilayer films as a function of deposition time of $AuCl_4^-$. 126
Figure 5.31 Schematic representation of multilayer PAH/TA substrates including *in situ* photosynthesized Au and/or Ag NPs. 129
Figure 5.32 UV-vis absorption spectra of substrate a, b, c and d. 131
Figure 5.33 SER spectra of 1.0×10^{-5} M CV molecule on substrate a, b, c and d.131
Figure 5.34 Relative intensity column plot at 1176 cm^{-1} of substrates a, b, c and d. 132
Figure 5.35 Representation of multilayer PAH/TA substrates including *in situ* photosynthesized Au and/or Ag NPs with 6 cycles of loading/reduction. 133

Figure 5.36 UV-vis absorption spectra of Ag NPs grown within bilayers of PAH/TA multilayer films, prepared by immersion into 0.50 M $AgNO_3$ solutions for 6 h, rinsed, dried and followed by 1 h of Xe radiation with different number of loading/reduction cycles. Arrow shows increase of absorption and red-shift of the plasmon resonance. 136

Figure 5.37 UV-vis absorption spectra of Au NPs grown within bilayers of PAH/TA multilayer films, prepared by immersion into 5.0 mM $AuCl_4^-$ solutions for 15 min, rinsed, dried and followed by 1 h of Xe radiation with different number of loading/reduction cycles. 137

Figure 5.38 Comparison of UV-vis absorption spectra of only Ag or Au NPs grown within bilayers of PAH/TA multilayer films with 6 loading/reduction cycles and combination of Ag and Au NPs within bilayers of PAH/TA multilayer films with 6 total loading/reduction cycles. 137

Figure 5.39 SER spectra of 1.0 x 10^{-5} M CV molecule on Ag NPs grown within bilayers of PAH/TA multilayer films, prepared by immersion into 0.50 M $AgNO_3$ solutions for 6 h, rinsed, dried and followed by 1 h of Xe radiation with different number of loading/reduction cycles. 139

Figure 5.40 SER spectra of 1.0 x 10^{-5} M CV molecule on Au NPs grown within bilayers of PAH/TA multilayer films, prepared by immersion into 5.0 mM $AuCl_4^-$ solutions for 15 min, rinsed, dried and followed by 1 h of Xe radiation with different number of loading/reduction cycles. 140

Figure 5.41 Comparison of SER spectra of 1.0 x 10^{-5} M CV molecule on only Ag or Au NPs grown within bilayers of PAH/TA multilayer films with 6 loading/reduction cycles and combination of Ag and Au NPs within bilayers of PAH/TA multilayer films with 6 total loading/reduction cycles. 141

Figure 5.42 Relative intensity column plot at 1176 cm^{-1} of the substrates of only Ag or Au NPs grown within bilayers of PAH/TA multilayer films with 6 loading/reduction cycles and combination of Ag and Au NPs within bilayers of PAH/TA multilayer films with 6 total loading/reduction cycles. 142

Figure 5.43 Schematic representation of multilayer BPEI/TA substrates including *in situ* photosynthesized Au and/or Ag NPs. 143
Figure 5.44 UV-vis absorption spectra of substrate e ($(BPEI/TA)_{10}Ag_1$), f ($(BPEI/TA)_{10}Ag_1/(BPEI/TA)_9Au_1$), g ($(BPEI/TA)_9Au_1$) and h ($(BPEI/TA)_9Au_1/(BPEI/TA)_{10}Ag_1$). 146
Figure 5.45 SER spectra of 1.0 x 10^{-5} M CV molecule on substrate e, f, g and h substrates. 146
Figure 5.46 Relative intensity column plot at 1176 cm^{-1} of substrates e, f, g and h. 147
Figure 5.47 UV-vis absorption spectra of $(PAH/TA)_{10}Ag_1$, $(BPEI/TA)_{10}Ag_1$, $(PVCL/TA)_{10}Ag_1$, $(PEO/TA)_{10}Ag_1$ substrates. 149
Figure 5.48 UV-vis absorption spectra of $(PAH/TA)_9Au_1$, $(BPEI/TA)_9Au_1$, $(PVCL/TA)_9Au_1$, $(PEO/TA)_9Au_1$ substrates. 149
Figure 5.49 SER spectra of 1.0 x10^{-5} M CV molecule on $(PAH/TA)_{10}Ag_1$, $(BPEI/TA)_{10}Ag_1$, $(PVCL/TA)_{10}Ag_1$, $(PEO/TA)_{10}Ag_1$ substrates. 150
Figure 5.50 SER spectra of 1.0 x10^{-5} M CV molecule on $(PAH/TA)_9Au_1$, $(BPEI/TA)_9Au_1$, $(PVCL/TA)_9Au_1$, $(PEO/TA)_9Au_1$ substrates. 150

LIST OF ABBREVIATIONS

BPEI: Branched poly(ethyleneimine)

CV: Cystal violet

DI: Deionized

EF: Enhancement factor

EM: Electromagnetic mechanism

EMR: Electromagnetic radiation

LbL: Layer-by-layer

LSPR: Localized surface plasmon resonance

NP: Nanoparticle

PAA: Poly(acrylic acid)

PAH: Poly(allylamine hydrochloride)

PDADMAC: Poly(diallydimethyl ammonium chloride)

PEC: Polyelectrolyte complex

PEO: Poly(ethylene oxide)

PSS: Poly(styrene sulfonate)

PVCL: Poly(vinyl caprolactam)

SERS: Surface enhanced Raman spectroscopy

TA: Tannic acid

CHAPTER 1

INTRODUCTION

1.1 Raman Spectroscopy

Electromagnetic radiation (EMR) interacts in a variety of ways with atoms and/or molecules. These atoms and molecules have the ability to either absorb UV and IR light or scatter it.[1] When a photon is scattered, it can be absorbed and then a new photon is emitted. This new photon is called the scattered photon. The majority of photons are scattered from a molecule with the same energy as the incident photon (elastically scattered radiation or Rayleigh scattering). The elastic scattering occurs when a photon enters a medium consisting of particles whose dimensions are significantly smaller than the wavelength of the incident photon. However, a wavelength shift is caused by a small percentage of the scattered radiation, which differs in energy (or wavelength) from the incident EMR and this shift depends on the chemical structure of the molecule. Raman scattering is the name given to this inelastic scattering which is first discovered by C. V. Raman in 1928 and he was awarded the Nobel prize in physics for this discovery in 1931.

Polarizability change of molecules, momentary distortions of electrons or the ability for an EMR to induce a dipole moment on the molecule, is necessary to observe Raman scattering. The electric field of incoming light causes the electron cloud surrounding the molecules to oscillate with irradiance. Therefore, polarization of the electron cloud of the molecules occurs. The oscillating electrons will then emit an optical field that is associated with Rayleigh and Raman scattering. As a result of Raman scattering process, excitation of molecule occurs through the virtual states (the level of an induced dipole moment). Energy levels of Raman and Rayleigh scattering processes are shown in Figure 1.1.

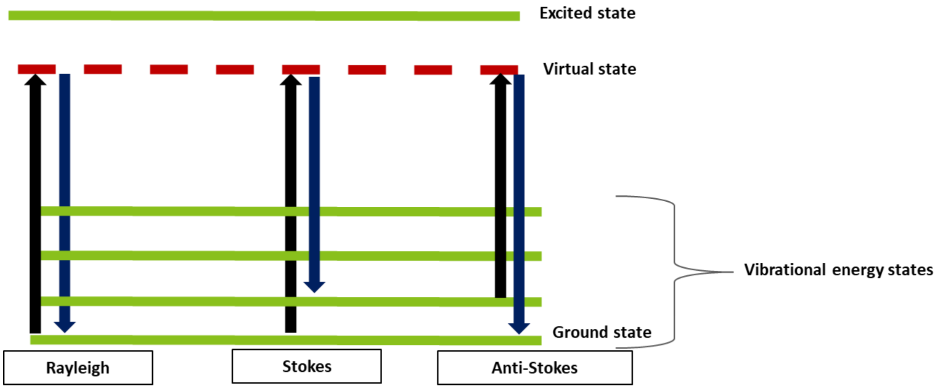

Figure 1.1 Energy levels of Stokes, Rayleigh and anti-Stokes scattering processes.

Stokes and anti-Stokes scattering are the two main sub-groups of Raman scattering. Stokes scattering occurs when the scattered radiation has a lower frequency than the excitation radiation. In other words, in the case of Stokes scattering, the molecule should be excited from its ground state to a virtual energy state before relaxing into an excited vibrational state. The intensity of the anti-Stokes line is lower than that of the Stokes line because the number of molecules is larger in the lowest energy level of the ground state compared to higher energy levels at room temperature. As a result, Stokes scattering is primarily measured in Raman spectroscopy.[2]

The lost or gained amount of energy in the inelastic scattering process by a photon is called Raman shift and is calculated as equation given below.

$$\Delta E = \frac{1}{\lambda_{incident}} - \frac{1}{\lambda_{scattered}}$$

where; $\lambda_{\text{incident}}$ is the wavelength of incoming light in centimeters, and $\lambda_{\text{scattered}}$ is the wavelength of scattered light in centimeters.[2] Raman spectroscopy offers easy instrumentation with a fast measurement time. The technique is useful for structural identification. Moreover, water has low Raman scattering providing usage of water as solvent for preparation of samples.[3] Additionally, little or no sample preparation is required. Although the technique is advantageous in these respects, Raman scattering has smaller cross section (10^{-29}-10^{-32} cm^2) compared to fluorescence (10^{-16} cm^2).[4] Low intensity of excitation sources and low sensitivity of detectors have limited the applications of Raman spectrometry for many years. Generally, one can use a powerful laser source and/or increase the exposure time to increase the intensity of Raman signals.[5]

1.2 Surface Enhanced Raman Spectroscopy and Its Related Mechanisms

Surface-enhanced Raman spectroscopy (SERS) is a widely used surface sensitive technique to increase low Raman intensities for detection of many molecules at relatively low concentrations in the order of 10^{-5} M or less. This technique has been used in chemical and biological sensing, imaging and single molecule detection applications in recent years.[6] SERS experiments were firstly conducted by Fleischmann and coworkers for the determination of pyridine adsorbed onto a roughened silver electrode to increase the electrode surface area.[7] Enhancement in Raman signal of pyridine molecules was reported by 10^5-10^6 factors through the amplification of electromagnetic fields generated by the excitation of localized surface plasmons (LSPs).[7] Electromagnetic enhancement mechanism accounted for this dramatic increase in Raman signal.[8,9] Large surface area was considered to result in high binding capacity of molecules to metallic surfaces due to more space on the surface for adsorption with etching of the surfaces at that time.[7–10] The primary contribution to SERS enhancement mechanisms is electromagnetic mechanism. It is directly related to LSPs, which are generated as a result of confinement of surface plasmons in conductive nanostructures significantly smaller than the incident laser wavelength. When LSP resonance (LSPR) is excited in a nanostructure, it leads to two main effects. The first one includes absorption and scattering of resonant radiation and the second one is the creation of very strong electromagnetic fields on the surface of the structure.[11] In case of SERS, the plasmonic nanostructure is in close proximity to the analyte. Therefore, the electromagnetic field includes not only the incident field but also the field generated by the LSPR. Thus, SERS intensity is directly related with the strength of the electromagnetic field outside the nanoparticle and is significantly amplified for a specific excitation wavelength. An illustration of the LSP effect is shown in Figure 1.2.

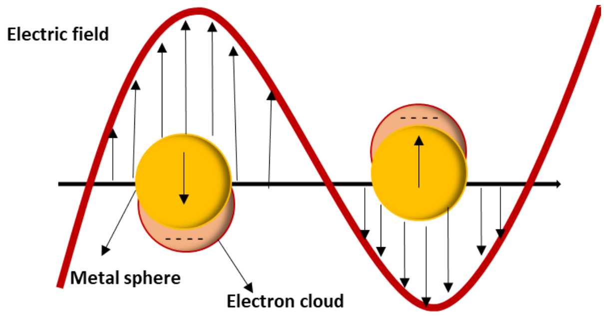

Figure 1.2 Localized surface plasmon effect.

Electromagnetic enhancement is affected by laser excitation wavelength, size and shape of NPs, nanoscale roughness, distance between neighboring NPs and distance between probe molecule and NPs.[12] Roughened surfaces are thought to be more applicable for localized enhancement of Raman signal due to strong and favorable interaction of molecules with radiation field in case of surface bumps in nanostructures,[13] resulting in amplification of the electromagnetic fields near the surface.[14] Surface bumps are formed as a result of roughening of metallic surface and free electrons of metals move in these regions in a restricted mobility.[15] Nanoscale roughness in a metal surface provides generation of high density of highly localized regions (hot spots) in which extraordinary SER signal enhancement occurs.[16–18] Hot spots can be defined as highly concentrated areas of strong electromagnetic fields. They are created by LSPRs and they are thought to provide a significant boost to SER signal. This enhancement is extremely large and it is concentrated in areas much smaller than the wavelength of light.[19] That means specific gaps between particles can generate very high magnetic fields due to coupling between their plasmon resonances. Therefore, it is important to increase the density of hot spots on a surface to increase the enhancement in SER signal. For example, approximately 10^5 times higher enhancement factors were calculated while increasing surface roughness of Ag films from 0.83 nm to 7.14 nm with the attribution of increase in the number of hot spots.[20] Furthermore, enhancement of SER signals on Ag substrates on glass and polydimethylsiloxane (PDMS) templates were evaluated in terms of both thickness and roughness by Lee and coworkers.[21] For the same thickness value of Ag films on the substrates, SER signal of 4-aminothiophenol (4-ATP) on flat PDMS structure was reported to be approximately 66% of the SER signal on porous PDMS structures. Therefore, SERS activity was mainly attributed to the density of bumps and wrinkles on variably roughened PDMS templates at 10-nm thick Ag layer.[21] Besides nanoscale roughness, important contribution to electromagnetic enhancement is distance-dependent behavior of the molecule and the surface.[22] The distance between the surface and the molecule, *r*, is proportional to r^{-12} and can increase up to r^{-10} by addition of surface molecules for electromagnetic enhancement based on calculations.[22–24] Moreover, the distance between the molecule and the surface should be within 1–30 nm for a reasonable SERS enhancement depending on the type of (Au, Ag, Cu etc.) metallic surface and probe molecule.[23,25,26] Size of NPs is another significant parameter to be controlled for optimum signal enhancement. NPs smaller than 5 nm do not provide Raman signal enhancement.[4,14,27] Although local electromagnetic field enhances with largening of particle size,[28–30] less absorption of light and less inelastic scattering by very large particles result in decrease in SER signal.[31,32] Therefore, optimal size of metal NPs is critical in terms of balancing electromagnetic field and inelastic scattering efficiency of incoming radiation.[33] It was reported that optimal size of spherical gold NPs in solution was around 50 nm for maximum SERS enhancement of 4-aminothiophenol and 4-nitrothiophenol[32] and optimal size was also similar for spherical silver NPs in solution using rhodamine-6G (R6G) as probe molecule.[33] Higher enhancement factors can be achieved at hot spots in the junctions between NPs compared to isolated single NPs.[34] When the particles are close to each other, it is favorable for generation of hot spots to achieve larger signal enhancements. When Raman-active molecules are located within these hot spots, their signals can be increased by a factor of 10^9 to 10^{11}. Therefore, spacing between NPs should be diminished, but this distance strongly depends on shape and type of NPs and probe molecules for generation of efficient hot spots.[35–37] For example, 1 nm gap (determined by the length of the probe molecule) between Au substrate and Au nanostar tips achieved twice larger enhancement factor for 1,5-naphtalenedithiol (15NAT) molecule as compared to Au nanospheres on the substrate.[36] Since nanostar particles were facilitated by highly localized plasmons in each tips, the enhancement at the 1 nm gap between the substrate and nanostar tips enhanced the signal. Another factor affecting electromagnetic enhancement is the choice of excitation wavelength of laser. For a long time, it was believed that the most effective way to stimulate a particular LSPR was by using light with a wavelength precisely matched the LSPR maximum.[11] After that, Van Duyne and coworkers demonstrated that the best excitation for a given LSPR is slightly blue-shifted from the LSPR maximum.[38] In their study, silver thin films with different optical responses were coated with a monolayer of benzenethiol (BT) and irradiated with 13 different excitation wavelegths. The results showed that the best excitation was consistently blue-shifted in relation to the LSPR maximum, and this is consistent with the electromagnetic mechanism that predicts the maximum SERS intensity is obtained when the LSPR strongly enhances both the incident and scattered photon intensities.[38] On the other hand, a good SERS spectrum of 1-naphtalenethiol (1NAT) can be obtained when LSPR of Ag NPs (between 400 and 600 nm) on exponentially grown films and excitation lines (785 and 830 nm) are far away from each other.[39] A slight red shift occurred by the addition of the probe molecule (1NAT) to NP including films. The most likely explanation for intense SER signals is the creation of hot spots that are randomly distributed within the films.[39]

The second enhancement mechanism is due to chemical mechanism including charge transfer between metal and the adsorbed molecule. It is a less understood mechanism compared to electromagnetic one. Contribution of it is less than electromagnetic mechanism, which is only enhanced the signal by a factor of 10 or 100 since the chemical mechanism should include direct contact of molecule and metal surface.[10] Mechanism of the interaction of NPs and orientation of molecule on the surface can be explained in terms of chemical mechanism. Moreover, shift of SER spectrum compared to Raman spectrum is caused by chemical enhancement mechanism.[40] Experimentally measured signal increase is a result of both combination of electromagnetic and chemical enhancement.[41]

The enhancement factor (EF) as a result of both mechanisms is calculated by the following formula as a SERS substrate point of view.[38,42]

$$EF = \left(\frac{I_{SERS}}{I_{Raman}}\right) \Big/ \left(\frac{N_{SERS}}{N_{Raman}}\right)$$

where I_{SERS} and I_{Raman} stand for observed intensities of a vibrational modes of probe molecules in SERS and Raman, respectively. Additionally, N_{Raman} and N_{SERS} symbolize number of probe molecules adsorbed on bulk and SERS substrate excited by laser radiation, respectively. Another important approximation of EF calculation is using analytical chemistry point of view. It is applicable when the matter is determination of the extent of enhancement in SERS as compared to Raman spectroscopy under specific experimental conditions.[42] Analyte solution with concentration of c_{Raman} and c_{SERS} produces the signals I_{Raman} and I_{SERS}, respectively and the formula is defined as analytical enhancement factor (AEF). AEF is heavily influenced by adsorption properties and surface coverage of the probe molecule, which may not be fully characterized by c_{SERS}. Additionally, AEF is strongly dependent on the sample preparation method. Therefore, the AEF may not fully characterize SERS substrate. The last approach for EF calculation is the single molecule EF (SMEF). It is generally influenced by probe molecule orientation on the SERS substrate, as well as the orientation of the substrate with respect to the incident laser polarization and direction. It is therefore necessary to precisely define the geometry of the SERS substrate and the position and orientation of the probe on it. Due to these limitations, this definition is more suitable for theoretical estimations of the enhancement factor rather than experimental measurements.[42] SMEF can be calculated by ratio of SERS intensity of the single molecule under consideration to average Raman intensity per molecule for the same probe.

1.2.1 SERS Substrates

When deciding if a substance is a consistent and highly promoting SERS substrate, many criteria must be considered. Desired features of SERS substrates proposed by Natan[43] and Lin and coworkers [44] are high average enhancement (>10^5), uniformity (variations <20%), reproducibility (variations <20%), large area (some mm^2), stability, ease of fabrication and cleanliness of the surface.

Many types of SERS substrates have been reported in the literature including colloidal NPs,[45–47] electrochemically roughened metal electrodes,[48,49] solid nanopatterned substrates with controllable roughness and thickness prepared by lithography[50–52] and atomic layer deposition.[53,54] Silver, gold and copper NPs are mostly used as SERS substrates due to tunable localized surface plasmon resonance (LSPR) values.[6] Copper and Ag NPs are less commonly used due to their instability in air compared to Au NPs.[6] Although using colloidal NPs as SERS substrates is easy and practical, aggregation of the particles upon analyte addition results in irreproducible SER signals.[55,56] On the other hand, nanopatterned structures provide high reproducibility due to well-controlled geometric parameters of nanostructures, however its use is limited due to expensive instrumentation and long production time of nanopatterns.[57–59]

1.3 Polyelectrolytes

Polyelectrolytes (PE) can be defined as charged polymers having ionizable groups. Strong polyelectrolytes are completely charged regardless of the pH of the solution, whereas weak polyelectrolytes have dissociation constants, meaning that they are partially ionized depending on their pK_a values. Polystyrene sulfonate (PSS), poly(3,4ethylenedioxythiophene) (PEDOT), and poly(diallyldimethyl ammonium chloride) (PDADMAC) are some examples of strong polyelectrolytes. On the other hand, some weak polyelectrolytes are polyethylene imine (branched/linear) (PEI), polyaniline (PANI), poly-*L*-lysine (PLYS), poly(amidoamine) (PAMAM), poly(methyl methacrylate) (PMMA). One of the common weak polyelectrolyte pair to prepare polyelectrolyte multilayer (PEM) is poly(allylamine hydrochloride (PAH)/poly(acrylic acid) (PAA).[60,61] By using PAH and PAA polyelectrolytes at various pHs, different conformations may be formed, and the thicknesses of multilayers can be adjusted.

1.3.1 Layer-by-Layer Self-Assembly Technique

Layer-by-Layer (LbL) technique is one of most efficient homogenous coating method with immersion of the substrate into oppositely charged polyelectrolytes which are commonly used in the literature.[60–65] This technique was developed by Gero Decher and coworkers[66] after the preliminary studies of R. K. Iler in which oppositely charged microparticles were prepared.[67] The technique enables control of the properties of a thin film on different surfaces by incorporation and immobilization various components such as NPs on the solid substrates.[68,69] Homogenous and intense coating of the LbL films with NPs is critical in terms of obtaining reproducible SERS substrate.

In LbL technique, silicon wafer, glass and quartz are used as substrates. Properties of the film can be adjusted by the chemical nature of polyelectrolytes, concentration, pH, temperature and salt concentration of the polymer solutions. LbL technique of dip-coating is summarized in Figure 1.3.

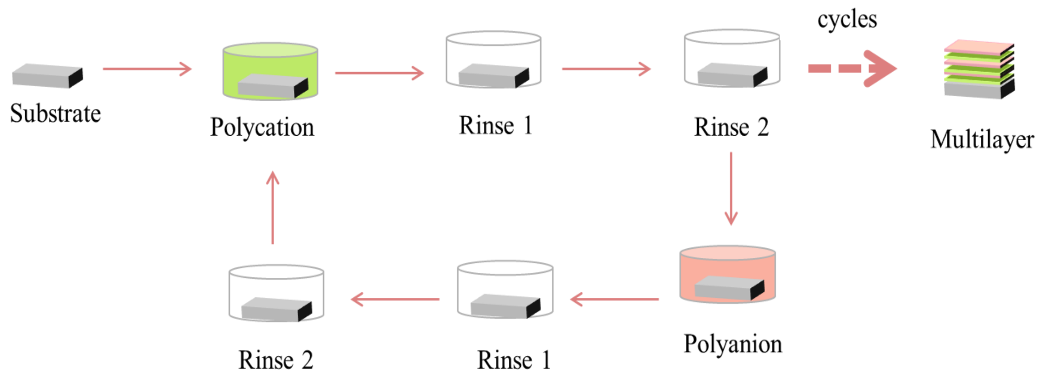

Figure 1.3 Schematic representation of layer-by-layer technique.

The films are formed by depositing oppositely charged polymers on the surface. Briefly, a substrate is immersed into a polycation solution, followed by two sequential rinsing steps to remove loosely bound polymers. Then, the substrate is dipped into a polyanion solution, followed again by two rinsing steps. This cycle is repeated until the desired number of layers is obtained. The main driving force for the formation of multilayer film is electrostatic interaction between polyanions and polycations.[70,71] Additionally, hydrogen bonds,[72] van der Waals forces,[62] covalent bonds[73] and hydrophobic interactions are contributed for LbL film formation.

1.3.1.1 Growth Mechanisms in LbL Assembly

LbL film growth patterns are broadly classified into two types as linear growth and exponential growth. The thickness of each layer increases linearly or exponentially with the increase in the number of PE layers, in linear and exponential growth, respectively. Exponential growth regime results in either an increase in surface roughness resulting in greater surface area for polymer deposition[74] or in and out diffusion of at least one of the polymers resulting in greater amount of polymer deposition with increasing number of layers.[64,65] A complex forms between polyanions and polycations, so exponential growth occurs. For example, during the growth of poly-*L*-lysine (PLL) and hyaluronic acid (HA), the PLL was observed to diffuse both into and out of the film.[64] The PLL chains that diffused out of the film formed complexes with the HA at the outermost layer of the film. As a result, the thickness of the outer layer was directly proportional to the amount of PLL chains that diffused out of the film in the presence of HA. Additionally, the growth mechanism of LbL assembly was also affected by molecular weight of PEs. Sun and coworkers reported difference in film thickness due to molecular weight of PAA.[75] When pHs of PAH and PAA solutions were adjusted to 7.5 and 3.5, respectively, exponential growth regime was observed with low molecular weight PAA. Low molecular weight PAA was shown in and out diffusion into the films extensively during assembly process. Linear growth arised due to inability of diffusion of the PAA into the film since mobility of the higher molecular weight PAA was lower. It was possible that assembly of higher molecular weight of PAA into these films might affect internal structures of the films. This effect could reduce the impact of PAA diffusion on the film thickness.[75]

1.3.1.2 Factors Affecting LbL Growth

Experimental parameters including nature of the polyanion, pH, ionic strength and concentration of polyelectrolytes have critical effect on LbL assembly of polymer. The pH of the environment can influence the charge density of weak polyelectrolytes. For instance, Shiratori and coworkers showed pH dependence of multilayer films consisting of PAH and PAA.[61] When the pH values of both PAH and PAA are 6.5, they are fully charged and behave like strong polyelectrolytes, resulting in formation of thin films (~1 nm for a bilayer)[61] due to effective ionic crosslinking between PAH and PAA layers. At pH 7.5, PAH is expected to be protonated by ~95%, whereas PAA is ~10% ionized at pH 3.5. The film has a loop and tail structure resulting from long average distances between electrostatic crosslinks. As a result, thicker films (up to 8 nm for a bilayer)[61] could be obtained with interpenetrated PAH layers among the PAA chains. The other important parameter influencing LbL growth is ionic strength resulting in structural changes. Kharlampieva and coworkers observed that when using salt-free solutions, the multilayers had more stratified structure. However, when salt ions were added, polyelectrolytes changed into coiled conformation.[76] Moreover, the thickness of multilayers were shown to be increased with increasing salt concentration.[77] In order to obtain stable deposition of layers and enable charge inversion in multilayers systems, it is essential to have sufficiently high PE concentration. The specific minimum concentration needed to form multilayers depends on the properties and characteristics of the PEs involved.[78] Moreover, thicker multilayers could be obtained as a result of using higher concentrations of PEs.[79] The growth of LbL and the composition of multilayers can be changed depending on chemical nature of the polyelectrolytes. For instance, Taketa and coworkers demonstrated that when chitosan and alginate were used for LbL, the resulting multilayers had relatively lower thickness as compared to hyaluronic acid/chitosan multilayers under the same pH and ionic strength conditions. On the other hand, hyaluronic acid was used instead of alginate, thicker LbL films were obtained.[80] Additionally, the chemical nature of the polyelectrolytes also influence the growth regime of the multilayers as linear and exponential.

1.3.1.3 Polyelectrolyte Complexes (PECs) Containing LbL Films

Polyelectrolyte complexes (PECs) are three dimensional macromolecular structures forming spontaneously via interaction of positively and negatively charged polyelectrolytes in solution. Polymer complexation leads to (i) water soluble PECs, (ii) complex precipitation, or (iii) quasi-soluble PECs in which aggregates of colloidal dimensions produced from polymers with less than 10^{-3} g/mL concentration level.[81] The main driving force for PECs formation is based on electrostatic interactions between the oppositely charged groups of polyanions and polycations. Additionally, other weak interactions like hydrogen bonding, van der Waals, or hydrophobic ones have also role in it.[82] PE multilayers (PEM) including sequential deposition of polyanions and polycations can be considered as subclasses of PECs. The basic principle for PEM corresponds to the PEC formation. There are some common properties of PEC and PEM. Both of them minimize free energy after counterion release. Their formation kinetics are based on electrostatic adsorption followed by rearrangement processes by changing conformation for both PECs and PEM. The type of complex in PECs is related with the growth mechanism in PEMs. Linearly growing PEMs have highly charged PE pairs resembling to PECs that precipitate. Exponentially growing PEMs have a gel-like structure due to PE diffusion, similar to loosely bounded, liquid-like PECs.[81]

PECs can have diverse structures which can be tailored by using various parameters in each formation such as mixing ratio, concentration, solution pH, ionic strength and temperature.[83] Moreover, the structure of the polyelectrolyte itself, like chain rigidity, topography, charge density and molecular weight, is an important parameter for the formation of the PECs.[82] LbL films containing PECs can be used in various applications such as production of robust free-standing film,[83] stable antireflection and antifogging coatings,[84] and rapid fabrication of micrometer thick films.[85] In these films, surface roughness values of the films were reported to be increased with the increase in size of PECs and number of deposition cycles attributed to accumulation of PECs to form more islands and increase in surface area for deposition of PECs.[83,85,86] PECs in LbL can result in rigid and porous film surface depending upon mixing molar ratio of polyanions and polycations in PECs which affects strength of complexation,[86] so self-adjustment of PECs conformation is not possible in case of strong interaction between the oppositely charged groups in PECs.[87] Liu and coworkers studied LbL with poly(methyl methacrylate) (PMMA) and complex of poly(vinylpyrrolidone) (PVPON)/PAA at various ratios for superhydrophobic coating applications.[85] It was reported that PVPON/PMMA multilayer film (~500 nm) was much thinner compared to PVPON-PAA complex/PMMA multilayer (~few microns). Moreover, it was shown that roughness of the film surface prepared from complexes increased with increase in number of layers based on the results of SEM images. Therefore, complexation of PVPON and PAA contributes not only for film thickness increase but also for surface roughness. Guo and coworkers used PECs of PAH and PAA in various mixing molar ratios together with PSS as multilayer film blocks for producing robust free-standing films, which are existing without solid substrates either in solution or in a dried state. Based on the results of structural morphology of PSS/PAH-$PAA_{0.75}$ (in which the feed monomer molar ratio of PAH to PAA is 1:0.75), root mean square (rms) roughness values of 39 and 40 layers of the films were shown to be similar. In the study of McAloney and coworkers, grain size, roughness and film thickness increased as the added NaCl concentration increases in a PDADMAC/PSS multilayer system. This can be interpreted as a conformation alternation of PEs from extended rod to globular coil in the polymer solution as a function of salt concentration.[88]

1.4 Nanoparticles (NPs)

Due to their enormous surface area and exceptional electrical, optical, magnetic, and catalytic properties, NPs differ from their bulk equivalent in terms of their chemical and physical characteristics.[89–92] The preparation of NPs for specific applications is currently an expanding area. Physical, chemical, and biological techniques of synthesis have all been developed in response to the persistent and ever-increasing demand for nanomaterials.[92–94] Three alternative methods including biological, chemical and physical ones are frequently used to generate inorganic NPs.[95,96] In order to facilitate the synthesis of NPs, biological approaches rely on biomolecules. On the other hand, chemical approaches typically require a large number of substances, whereas other methods frequently require sophisticated equipment such as electron beam and laser ablation.[97,98] Environmentally friendly techniques, including NP photoinduced synthesis, are becoming more popular as a way to avoid employing chemical compounds and producing hazardous byproducts.[99] Ag NPs and Au NPs have undergone substantial studies during the past few decades. They can be used in a variety of biological and biomedical fields. High electron conductivity,[89] high colloidal stability,[100], excellent surface plasmon resonance (SPR) properties, diverse surface bioconjugation[101] and low toxicity[102] are all characteristics of Au NPs. Similar to other metal NPs, Ag NPs have a distinctive SPR band, optical properties,[103] good electrical conductivity and catalytic properties,[104] as well as remarkable antibacterial activity.[105]

1.4.1 Synthesis Methods of Au NPs

Michael Faraday presented the first scientific technique for producing colloidal Au NPs in 1857.[106] The aqueous reduction of a gold salt by white phosphorous and stabilization with carbon disulfide resulted in fine particles. Some years later, Zsimondy observed anisotropic NPs[107] and he received the Nobel's Prize in 1925. He invented the ultramicroscope, which enabled him to see the shape of the Au NPs. In 1951, sodium citrate was utilized in a well-known Turkevich process as a reducing and capping agent.[108] This method has become popular, in which chloroauric acid ($HAuCl_4$) is often reduced to Au^o in a synthetic process employing several well-known reducing agents, like sodium borohydride and sodium citrate dihydrate as the boiling gold solution proceeds. When Au NPs are produced, temperature and gold salt to citrate ratio determine the size of NPs. After some years, seed-mediated growth methods for the production of large spherical as well as nonspherical Au NPs were established, allowing control over the nucleation and growth processes, resulting in improved monodispersity.[109] Citrate-based techniques make up the majority of these synthesis approaches created for seed-mediated synthesis of Au NPs.[110–112] Seed-mediated growth involves the use of a seed, or a small Au NP, as a nucleus for the growth of larger Au NPs. To synthesize Au NPs using this method, a seed solution is firstly prepared by dissolving a small amount of gold salt, such as tetrachloroaurate, in a solvent. A reducing agent, such as sodium borohydride, is then added to the seed solution to reduce the gold salt to gold metal. The seed solution is then used to grow larger Au NPs by adding a gold-precursor solution. The gold-precursor solution contains a higher concentration of gold salt and a mild reducing agent such as ascorbic acid. As the gold-precursor solution and reducing agent are added to the seed solution, the gold ion is reduced to gold metal and begins to deposit onto the surface of the seed NPs, resulting in the growth of larger Au NPs. The amount and nature of the reducing and capping agent as well as their proportion to the Au precursor control the size, shape, and surface properties. Pioneers of seed-mediated synthesis for producing nanorod-shaped particles using reductants and surfactants are Murphy and El-Sayed and their coworkers.[113,114]

Since the charge of Au NPs plays a significant role in electrostatic interaction-based adsorption, it is imperative to create Au NPs using an appropriate stabilizing agent during the seed-mediated synthesis process. Polyethylene imine (PEI)-capped Au NPs are coated with a layer of PEI which is a polymer that carries a positive charge. PEI is often used as a capping agent for Au NPs due to its ability to stabilize the NPs and modify their surface properties.[115] Using electrostatic interaction, it was shown that PEI-capped Au NPs may be used to quickly decorate a variety of silicon oxide support materials.[116,117] PEI-capped Au NPs have a number of potential applications. Due to their positive charge, they can be used as drug delivery agents, as they can interact with negatively charged biomolecules and cells.[118] They can also be used as catalysts, as the PEI layer can modify the surface properties of the Au NPs and enhance their catalytic activity.[119,120]

1.4.2 Photochemical Synthesis of NPs and Related Mechanisms

The photoinduced synthetic strategies can be divided into two categories, which are photophysical (top down) and photochemical (bottom up). The former creates NPs by subdividing bulk metals, whereas the latter creates NPs from zero-valent metal (M^o) derived from molecular or ionic precursors. Direct photoreduction of a metal source (metal salt or complex) or photochemically produced intermediates, such as excited molecules and radicals, used to reduce metal ions results in the formation of M^o.[121] The direct photoreduction in which M^o formed through the direct excitation of a metal source, has been recognized as a key technique for NP synthesis. As a result of the benefit of not including reducing agents, it has been widely used in a variety of mediums, such as polymer films, glasses and cells.[121]

Direct photoreduction has been studied to show the photochemical production of Ag NPs in an aqueous medium.[122,123] Hada and coworkers explored the synthesis of Ag NPs in aqueous and alcoholic solutions by the direct excitation of $AgClO_4$ and proposed a synthesis mechanism.[122] They suggest that the excitation of Ag^+ results in an electron transfer from the water molecule to Ag^+, by the subsequent decomposition of H_2O^+ into H^+ and $OH^·$ radical. In case of using alcohol (ethanol) as a solvent, H_2O^+ is replaced by RCH_2OH^+. The equations (1 and 2) show the photochemical reaction between solvent molecules and Ag^+. Both reactants and products are surrounded by solvent molecules in these reactions. As a final step, the solvent molecules surrounding the products of Eqns. 1 and 2 break down, causing the silver atoms to turn into colloidal silver outside of the structure. That means Ag^o associates in order to create Ag NPs (Eqn.3). $OH^·$ and $RCHOH^·$ radicals were observed to turn into O_2 and acetaldehyde, respectively. In addition, using 2-propanol as a solvent, α-hydrogen of it can be easily released, so reaction between radicals formed and 2-propanol is accelerated. $RCHOH^·$ radical in Eqn.2 has the ability to reduce additional Ag^+ and provide Ag NP formation (Eqn. 4). As a result, quantum yield of this reaction including 2-propanol is higher as compared to the reaction with ethanol.[121,122]

$$\mathrm{Ag^+ + H_2O \xrightarrow{hv} Ag^o + H^+ + OH^·}\ (1)$$

$$\mathrm{Ag^+ + RCH_2OH \xrightarrow{hv} Ag^o + H^+ + RCHOH^·}(2)$$

$$\mathrm{nAg^o \rightarrow (Ag^o)n}\ (3)$$

$$\mathrm{Ag^+ + RCHOH^· \xrightarrow{hv} Ag^o + H^+ + RCHO}\ (4)$$

Au NPs are also produced by the direct photoreduction of $AuCl_4^-$ in an aqueous solution. Numerous studies have shown the presence of an intermediate during the creation of Au NPs since the yellow color of Au^{3+} vanishes before the formation of

Au NPs.[124,125] An intermediate can be defined as a molecule that is produced during a reaction and exists for only a brief period of time. It is highly reactive and contains a lot of energy, but it is not very stable, so it quickly transforms into a more stable molecule. From this definition, excited radical in Eqn. 5 $(HAu^{3+}Cl_4)^{\cdot}$, Au^{2+} complex in Eqn. 6 $(HAu^{2+}Cl_3....Cl)$, $HAu^{2+}Cl_3$ and $HAu^{+}Cl_2$ (in Eqns. 7 and 8) can be intermediates. However, Gachard and coworkers hypothesized that Au^{+} is the most likely intermediate based on the stability with respect to disproportionation.[125] Additionally, Kurihara studied Au NP synthesis mechanism in water and water in oil emulsions.[126] When Au^{3+} is exposed to UV light in both media, it becomes excited (Eqn. 5) and forms a caged Au^{2+} complex (Eqn. 6). This complex later dissociates (Eqn. 7), and the unstable Au^{2+} further decomposes into Au^{+} and Au^{3+} (Eqn. 8). Au^{+} then absorbs another photon to become Au^{o} (Eqn. 9). It eventually combines to form nuclei and subsequently the Au NPs (Eqn. 10).

$$\mathrm{HAu^{3+}Cl_4} \xrightarrow{\mathrm{hv}} ((\mathrm{HAu^{3+}Cl_4}))^{\cdot}\ (5)$$

$$((\mathrm{HAu^{3+}Cl_4}))^{\cdot} \rightarrow (\mathrm{HAu^{2+}Cl_3} \ldots.\mathrm{Cl})\ (6)$$

$$(\mathrm{HAu^{2+}Cl_3} \ldots.\mathrm{Cl}) \rightarrow \mathrm{HAu^{2+}Cl_3} + \mathrm{Cl}\ (7)$$

$$2\mathrm{HAu^{2+}Cl_3} \rightarrow \mathrm{HAu^{3+}Cl_4} + \mathrm{HAu^{+}Cl_2}\ (8)$$

$$\mathrm{HAu^{+}Cl_2} \xrightarrow{\mathrm{hv}} \mathrm{Au^{o}} + \mathrm{HCl} + \mathrm{Cl}\ (9)$$

$$\mathrm{Au^{o}} \rightarrow (\mathrm{Au^{o}})\mathrm{n}\ (10)$$

1.4.2.1 Bimetallic (Au-Ag) NPs and Their Photochemical Synthesis

Bimetallic NPs have received significant interest because of their intriguing optical, electrical, catalytic, and magnetic properties that can be markedly different from those of their corresponding monometallic counterparts.[127–130] Since the size and shape of monometallic NPs affect their properties, numerous studies have concentrated on various NP morphologies.[131–133] Core-shell, heterostructure and alloyed nanostructures are the categories for bimetallic NPs.[134–136] These bimetallic NPs materials possess a distinct collection of qualities arising from the more sophisticated shape and composition, in addition to a mixture of properties originating in each individual element.

The optical characteristics of Au-Ag alloy NPs are greatly influenced by the Au-to-Ag ratio.[137,138] In specifically, the appearance of only one corresponding plasmon band changes with an increase in Ag concentration, shifting from about 520 nm (Au NPs) to 400 nm (Ag NPs). Since the outer electrons in Au (core)-Ag (shell) NPs are polarized in two separate electronic domains, two plasmon resonances are visible.[138] The thickness of the shell material (Ag NPs) that has been deposited also has an impact on these plasmon resonances of Au and Ag NPs.[139] For instance, in case of Au(core)-Ag (shell), increasing the amount of Ag caused shifts in the Au plasmon-band to higher energies and improves the extinction coefficient of the material. Gonzalez and coworkers studied the photochemical synthesis of Au-Ag alloys in sodium dodecyl sulfate (SDS) micelles as well as Au(core)-Ag(shell) NPs in hexadecyltrimethylammonium chloride (CTAC) micelles.[138] Using a ketyl radical as a reductant called Irgacure-2959 (I-2959), $HAuCl_4$ and $AgNO_3$ reduced to Au^o and Ag^o in aqueous surfactant solutions.[92] This reaction produces Au-Ag bimetallic NPs with various compositions and architectures depending on the type of surfactant. In another study, acetone/isopropanol mixture was used as a source for ketyl radical and UV light (260-400 nm range) to synthesize bimetallic NPs in a mixture of $NaAuCl_4$, $AgNO_3$ and CTAB system.[139] As a result, a core-shell structure could be produced while using a less UV intensity, whereas higher radiation intensity favored the synthesis of Au-Ag alloys. Xu and coworkers show the synthesis of branched Ag@Au bimetallic nanodendrites by using 532 nm pulse laser-induced photochemistry for the preparation of SERS substrate.[140] The controlled fabrication involves the photooxidation of ethanol solution by laser light, followed by the reduction of Ag^+ via pulsed laser irradiation onto precursors including $HAuCl_4$ and ascorbic acid. The final multi-branched Ag@Au nanodendrites demonstrate excellent SERS activities of 4-ATP probe molecule with an EF of 10^{11} due to the controlled architectures and composition of the nanodendrites. In a recent study, Kazancioglu and coworkers reported creating bimetallic Au-Ag alloy NPs less than 10 nm in size using a novel photoinitiator called 2-thioxanthone thioacetic acid-dioxide for the application of their catalytic activity.[141] Saha and coworkers obtained the deposition of Au on Ag NPs (Au@Ag NPs) and silver on Au NPs (Ag@Au NPs) after getting alginate beads modified with Ag NPs and Au NPs due to the action of cyclic UV irradiation. Applications for SERS of 2-aminothiophenol and 1,10-phenanthroline were studied on these hybrids, resulting in efficiency of SER signals increasing in the order of Ag@Au <Au@Ag < Au-coated beads.[142]

1.5 NP Embedded Films for SERS Applications

It is crucial and challenging to attach NPs homogenously to a solid surface. In literature, LbL deposition enables precise manipulation of the characteristics of a film on various types of substrates by combining different materials, such as NPs, nanosheets, nanoshells, nanowires with polymers. S. Abalde-Cela and coworkers used Ag NP loaded poly(diallyldimethyl ammonium chloride) (PDADMAC)/poly(acrylic acid) (PAA) multilayers as SERS substrate for detection of dioxins at concentration down to $1.0x10^{-8}$ M.[39] In another study, Zhou and coworkers adsorbed Ag^+ into PDADMAC/PAA multilayers and prepared Ag NP embedded films through in-situ reduction of Ag cations using $NaBH_4$. The SERS EF provided by these films was recorded as $\sim10^9$ for Rhodamine 6G (R6G) probe molecule.[143] Au NP including PEI/PAA coated SERS substrates were shown to have superior SERS activity for 4-nitrobenzenethiol compared to vacuum evaporated and electrochemically roughened Au substrates.[144] All these examples showed homogenous, reproducible and sensitive LbL-based SERS substrates in which either Au or Ag NPs were included within the multilayers at the post-assembly step.[39,143–

[147] There are also studies reporting the use of Au or Ag NPs as building blocks together with polyelectrolytes in the LbL film construction. These multilayers, so called the "sandwich model", are formed through sequential adsorption of polyelectrolytes and NPs.[70,148–156] SER signal obtained from sandwich-like LbL assemblies was found to enhance as the number of NP layers increased due to enhanced local electromagnetic field arising from close proximity and strong coupling interactions among neighboring NPs.[70]

1.5.1 Seed-mediated NPs in SERS Applications

Philip and coworkers demonstrated use of three distinct silicon oxide supports to explore the SERS properties of PEI-capped Au NPs.[115] A unique PEI-assisted seed-mediated growth technique was used to produce the large-sized (varied from 35 nm to 130 nm) Au NPs for the SERS applications. It was shown that PEI and seed amounts had an impact on the size control of the Au NPs during a seed-mediated synthesis. During the deposition and infiltration of the NPs to fabricate SERS substrates, Au NPs were adhered to the silicon oxide materials using electrostatic contact and capillary forces. The highest SERS performance of 4-ATP among the three SERS substrates was the Au-SiO_2 photonic crystal substrate, which utilized the synergistic effects of the photonic crystal and Au NP clusters. When it comes to Au-photonic crystals and Au-glass plate substrates, the nanoscale separations (1–15 nm) between the Au NPs in the clusters are proof of SERS hotspots, where the electromagnetic field is considerably boosted, enhancing the SERS performance of this type of substrates.[115] On the other hand, in citrate-based seed-mediated synthesis method, it was shown that citrate could be used to control the growth of NPs into unique geometries and seed-mediated growth approach could be employed to induce branching of Au NPs.[157] Branching in Au NPs increased their SERS activity of 4-ATP compared to unbranched ones, which made them particularly desirable for SERS applications. In addition, Leng and coworkers achieved room temperature seed-mediated synthesis of Au NPs using citrate ion and gold salt.[158] When compared to Au NPs synthesized at 100 °C, Au NPs synthesized at room temperature showed twice higher Raman enhancement. They credited the increased surface roughness of the Au NPs at room temperature for this improvement.[158] The particles prepared at ambient temperature displayed more edges and corners than equivalent particles prepared at 100 °C, as demonstrated in TEM imaging. In another work, a seed-mediated growth method was described to prepare Au NPs with multiple branches that eventually resembled sea urchins.[159] Their size was controlled between 40-180 nm by varying the concentrations of gold seeds, $HAuCl_4$, and hydroquinone as a reductant for optimization of SER signals of Nile Blue A with uniform morphology and monodispersity. By increasing concentration of hydroquinone and $HAuCl_4$, larger particles with sea-urchin shapes were obtained together with red-shifting of extinction spectra of NPs. On the other hand, concentration of gold seed increase resulted in smaller NPs.

1.5.2 Photochemically Synthesized NPs Embedded Films in Various Applications

Metal NPs can be generated on the surface and also inside multilayer thin films by applying physical, chemical or photochemical ways with reduction of metal cations. In this method, multilayer films were dipped into aqueous metal salt solutions allowing ion exchange process between counterions in the film and metal cations from the solution.[160] Then, NPs can be synthesized with proper routes. There are some advantages of *in situ* synthesis such as well dispersion of NPs within the film and better control over NP concentration because of the better tuning of metal content by variation of PE deposition pH and number of ion exchange and reduction cycles.[160] By this way, weight fractions of metals and size of synthesized NPs are determined.

In the study of Machado and coworkers, Ag NPs in multilayers of PAH/PAA (at pH 3.5) films were synthesized by dipping of the films into silver acetate ($AgCH_3CO_2$, 5.0 mM, pH 6.5) by UV and ambient light.[161] Smaller NPs (2-4 nm in diameters) were produced within multilayers of PAH/PAA film under UV light (365 nm) as compared to particles (4 to 50 nm) synthesized using ambient light (40 W, fluorescent lamp). Therefore, choice of excitation wavelength led to size variation and distribution of Ag NPs in the film. In another study, *in situ* Ag NP growth in PAH/PAA and polyethylene imine (PEI)/PAA multilayers were investigated by combinatorial approach by changing variables such as pH of multilayers, $AgNO_3$ concentration and dipping time in silver salt solution.[160] In this study, spherical NPs (3-5 nm) were photochemically produced in multilayer films. As concentration of $AgNO_3$ increased, absorbance at λ_{max} also increased which can be explained by the increasing binding capacity of Ag^+ cation to PE in the film for the production of NPs.[160] In another study, Shen and coworkers produced Au NPs which were formed by dipping exponentially growing poly(*L*-lysine)/hyaluronan (PLL/HA) multilayers (7.5 and 8 bilayers) at pH 9.5/2.9 into Au salt solutions of varying pH and subsequent UV irradiation of the films.[162] When pH of $AuCl_4^-$ containing solution was 3.0, amine groups of PLL were primarily protonated while carboxyl groups of HA in the multilayer structure were slightly ionized (the pK_a of PLL and HA are of 9 and 3, respectively). This resulted in a greater amount of free NH_3^+ groups in the multilayer film and led to maximum interactions for binding $AuCl_4^-$ ions. Fewer NPs with larger (~9 nm) diameters as compared to pH 6 and pH 9 were produced at pH 3.0, which were shown in SEM images. The amine and carboxyl groups were fully ionized in multilayer film when pH of $AuCl_4^-$ solution was 6. In this pH condition, number of interactions with $AuCl_4^-$ anions of these groups was reduced due to reduced number of protonated NH_3^+ groups. At pH 6, $Au^+Cl_2^-$ ions were formed, which accelerated the nucleation of $Au^+Cl_2^-$ to Au^o process as compared to pH 3. Au NPs formed in greater numbers throughout the entire film, although they could only be as big as 3 nm in diameter. When pH of $AuCl_4^-$ was 9, the COO^- groups of HA were totally ionized and nearly half of the amine groups of PLL were protonated, allowing for even fewer interactions with $AuCl_4^-$. The concentration of $AuCl_2^-$ form was reduced and there were more gold nuclei to form NPs when the pH was high.[126] However, the amine groups quickly stabilized the Au NPs, limiting their diameter to 2 nm.[162] Rubner's group *in situ* synthesized Au NPs in PAH/PAA (at pH:7.5/3.5) and PAH/poly(styrene sulfonate) (PSS) (at pH 9.3) multilayers by immersing the films into gold salt solution (at pH levels 1.8-6.1), followed by exposure to UV light.[163] Based on the UV-vis absorption spectra of Au NPs, larger numbers of free amine groups were available at pH values below of 2.5 for PAH/PAA and pH value below of 5.0 for PAH/PSS for binding of $AuCl_4^-$ anion to the film structure for the formation of Au NPs. At these pH values, this significant change in gold binding capacity is due to changes in the structure of the films. In addition, structure of the films is affected by changes in porosity and swelling of the films depending on the pH. By controlling the conditions of film assembly, such as the pH and post-assembly process, it is possible to control the size and distribution of Au NPs in the multilayers.[163] Jang and coworkers reported a hybrid multilayered film with photoinduced Ag NP for application as a sensing platform for microarray-based immunoassays.[164] Using UV-initiated photoreduction techniques, multilayer films of PEI and hyaluronic acid (HA) were used as a template for the *in situ* synthesis of Ag NPs. HA contains negatively charged carboxyl groups and they have the ability to bind to Ag^+ ions by serving as a reductant, catalyst and stabilizing agent during the synthesis of Ag nanostructures, the numbers of HA layers determined the Ag NPs distribution inside the multilayer film. The thickness of the PEI/HA multilayer film increased with the number of bilayers, which led to increasing the ability of reduction and subsequent storage of more amount of Ag NPs within the films. In another study, Zhang and coworkers showed hydrogen bonded LbL (PVPON/PAA) assemblies as nanoreactors for NP synthesis.[165] They reported that uncrosslinked hydrogen-bonded PVPON/PAA films remained stable Ag^+ loading. Based on the results of FTIR and XPS studies, Ag^+ binds to carbonyl group of PVPON via coordination interaction while also binding to PAA via electrostatic interaction. As a result, the films do not disintegrate when the hydrogen bonds between PVPON and PAA are broken.[165] Cui and coworkers presented a straightforward *in situ* method to fabricate Ag NP arrays in a LbL assembled between negatively charged hyaluronan (HA) and positively charged PDADMAC multilayer structure.[166] The number of bilayers has a significant impact on the morphology of the arrays, and the number of irradiation/drying cycles during fabrication allows for easy customization of the surface density of the NPs in the arrays. For LSPR absorption spectrum-based biosensors, the implanted Ag NP arrays provide improved stability. The LbL method was used to build PAA/PDADMAC multilayers on silk, which were then used as a 3-dimensional matrix for the *in situ* production of Ag NPs in the work by Meng and coworkers.[167] The multilayer coated silk fibers could be used to manufacture Ag NPs, and the amount of these Ag NPs could be controlled by varying the number of bilayers. The prepared silk had antibacterial action since it could effectively stop the formation of new germs and kill any existing ones.

1.6 Aim of the Study

In this thesis, the main aim was to develop sensitive and reproducible SERS substrates using LbL technique. Homogenous and intense coating of NPs on solid substrates was aimed to be provided by LbL technique, resulting in reproducible SER signals on multilayer surfaces.

In the first part of the study, it was aimed to understand the relationship between LbL film structure (PAH/PAA and PAH/TA) with surface morphology and SER signals of the probe molecule in NP containing polymer multilayers. Post-loading incorporation of citrate-capped Au NPs and sandwich type inclusion of the NPs were also explored to show film architecture effect on SER signal intensity. Although there were both post-loaded incorporation[39,143–147] and sandwich type multilayers[70,148–156] in literature for SERS applications, observation of SERS enhancement using highly rough structures in TA including multilayers was newly studied in this thesis.

In the second part of the study, it was aimed to synthesize large-sized and seed-mediated (BPEI-capped) Au NPs in the solution media and self-assemble these NPs at the surface as a single layer or multilayer using TA or PSS. Then, the films containing BPEI-capped Au NPs were aimed to increase SER signals. Since size of NPs is one of the critical parameters to be controlled for SER signal enhancement, this part was planned to optimize size of NPs in solution. Accordingly, size of NPs in solution was explored by variation of pH of the growth solution and concentration of BPEI to find out the effect of size on SER signal intensity. Although the synthesis method was modified from literature,[115] incorporation of these large-sized NPs into multilayer films were firstly applied in this thesis for obtaining more reproducible SERS substrates.

In the final part, monometallic and bimetallic Ag and/or Au NPs in LbL films were aimed to be *in situ* photosynthesized for observation of SERS enhancement with using light for reduction of metal cations. By this way, homogenous dispersion of NPs with a more controllable way as compared to post-loading of NP solutions was aimed to contribute for obtaining reproducible SER signals from surfaces. In literature, there are some applications of LbL including monometallic or bimetallic *in situ* photosynthesized NPs,[160-167] but none of them is applicable for SERS enhancement in the multilayers.

CHAPTER 2

EXPERIMENTAL

2.1 Materials

Polyallylamine hydrochloride (PAH, M_w=15,000), polyacrylic acid (PAA, M_w=1,800), branched polyethylene imine (BPEI, M_w=25,000), polystyrene sulfonate (PSS, M_w=70,000), polyethylene oxide (PEO, M_w=200,000), hydrochloric acid (HCl), sulfuric acid (H_2SO_4), sodium hydroxide (NaOH), trisodium citrate dihydrate ($C_6H_5Na_3O_7.2H_2O$), silver nitrate ($AgNO_3$) and crystal violet ($C_{25}N_3H_{30}Cl$) were purchased from Sigma-Aldrich. Polyvinyl caprolactam (PVCL, M_w=1,800) was purchased from Polymer Source Inc. Tris hydroxymethyl aminomethane hydrochloride (Tris HCl- $C_4H_{11}NO_3{\cdot}HCl$) was purchased from Scharlau. Sodium dihydrogen phosphate dihydrate ($NaH_2PO_4{\cdot}2H_2O$), sodium borohydride ($NaBH_4$) and tannic acid (TA, M_w=1,701) were purchased from Merck. Sodium chloroaurate ($NaAuCl_4.2H_2O$) was purchased from BDH Chemicals Ltd. Sodium chloride (NaCl) was purchased from Surechem Products Ltd. L-ascorbic acid ($C_6H_8O_6$) was purchased from Carlo Erba. All chemicals were used without further purifications. All aqueous solutions were prepared using Milli-Q water (18.2 MΩ cm). The chemical structures of the polyelectrolytes used in this thesis are as follows in Figure 2.1.

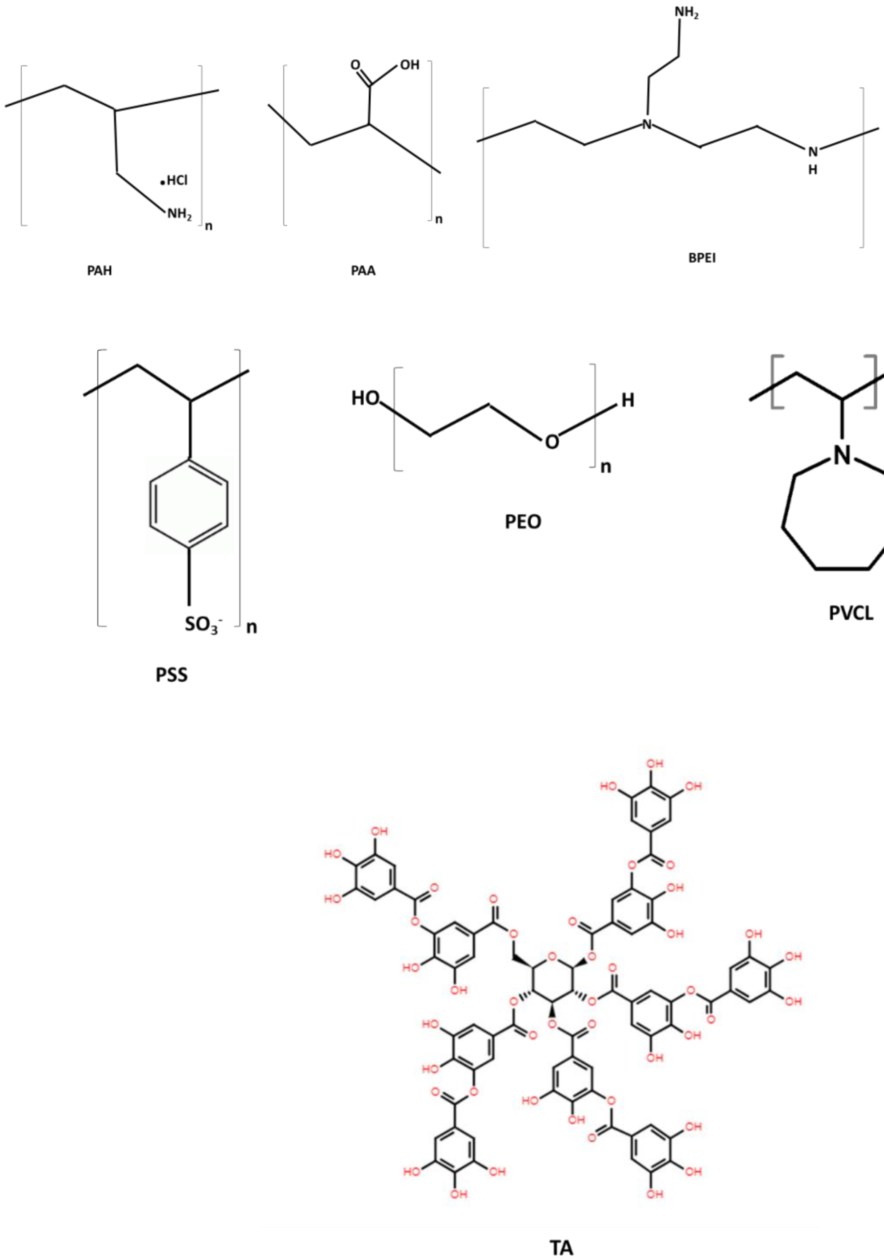

Figure 2.1 Chemical structures of polyelectrolytes.

2.2 Methods and Instrumentation

Ellipsometry: Thickness of dried films was measured using an ellipsometer of Optosense, USA (OPT-S6000).

Atomic Force Microscopy (AFM): Surface morphology was followed by AFM using NT-MDT Solver P47 AFM in tapping mode using Si cantilevers.

Scanning Electron Microscopy (SEM): Surface morphology was also followed by SEM using high resolution QUANTA 400F Field Emission SEM.

SERS Measurements: SERS spectra were recorded with Raman spectrometer using HORIBA-Jobin Yvon LabRam equipped with charge-coupled device (CCD) detector and He-Ne laser (632.8 nm, 10 mW or 5 mW) as the excitation source. Spectra were obtained using 50x objective and 600 g/mm grating with 10 s acquisition time. Each spectrum was recorded twice and then averaged. For SERS measurements, 25.0 μL of 1.0 x10^{-5} M CV solution were drop-casted onto the SERS substrate. Measurements were performed at 5 points of the substrate. The intensity of the CV band at 1176 cm^{-1} was selected as analytical signal and used for quantification.

Dynamic Light Scattering (DLS) and Zeta-Potential Measurements: Particle size and zeta potential measurements were recorded using a Zetasizer NanoZS.

UV-vis measurements: Growth of the dried films was tracked using UV-vis spectroscopy of T80+ UV-vis spectrometer PG Instruments Ltd.

ICP-MS measurements: Total Ag in multilayers were recorded by Thermo X2 Series Inductively Coupled Plasma Mass Spectrometer.

For ellipsometry, AFM and SEM measurements, LbL films were constructed onto 1 cm x 1 cm silicon wafers and for Raman and UV-vis Spectroscopy measurements were done onto 2 cm x 2 cm glass slides. Of note, in addition to horizontal position, glass slides were dipped into polyelectrolyte solutions in the vertical position to provide homogenous coating in both sides of wafers and slides. No difference in film thickness was recorded on Si wafers with respect to position of the templates in the polymer solutions.

2.3 Preparation of Citrate-Capped Au NPs

Au NPs having maximum absorption at around 520 nm were synthesized by Turkevich method.[108] Briefly, 10.0 mL of 5.0×10^{-3} M gold (III) chloride hydrate stock solution (prepared in deionized water (DI)) was diluted to 100.0 mL with DI water. This intermediate solution was heated under constant stirring until it started to boil. Afterwards, 5.0 mL of 1.0% (w/w) warm sodium citrate solution was added dropwise to the boiled solution as a reducing and capping agent. The mixture was heated for an additional 15 minutes (min) under continuous stirring. The color of the solution turned from pale yellow to ruby red, indicating the formation of Au NPs.

2.4 Multilayer Preparation of PAH/PAA, PAH/TA, PAH-PAA Complex/PAA and PAH-TA Complex/TA

Silicon wafers/glass slides were dipped in concentrated H_2SO_4 solution for 85 m and thoroughly rinsed with DI water. Afterwards, silicon wafers/glass slides were soaked in 0.25 M NaOH solution for 10 min, thoroughly rinsed with DI water and finally dried under nitrogen flow. To deposit a precursor layer, substrates were immersed into 0.5 mg/mL BPEI solution (prepared in 10 mM phosphate buffer) at pH 4.0 for 1 h, followed by rinsing of twice (1 min for each) in phosphate buffer solution (10 mM, pH 4.0). The pH of polymer and rinsing solutions were adjusted using 0.5 M HCl or 0.5 M NaOH. In all film systems, each layer was deposited for 5 min and rinsed for 1 min.

2.4.1 LbL Self-Assembly of PAH and PAA

Exponentially grown $(PAH/PAA)_n$ films, where n is number of layers, were prepared by alternatingly dipping the substrates in PAA (0.8 mg/mL in 10 mM phosphate buffer, pH 3.5) and in PAH (1.0 mg/mL in 10 mM Tris buffer, pH 7.5) solutions. After each deposition step, substrates were rinsed twice using either 10 mM phosphate buffer at pH 3.5 (after PAA deposition) or 10 mM Tris buffer at pH 7.5 (after PAH deposition). Multilayer films were dried under N_2 flow. In linearly grown PAH/PAA films, similar deposition procedure was followed except the deposition pH which was 4.0 for both PAA and PAH.

2.4.2 Preparation of PAH-PAA Complexes and LbL Self-Assembly of PAH-PAA Complexes and PAA

A 50.0 µL of 0.8 mg/mL PAA (pH 3.5) solution was added dropwise at two increments as 25.0 µL onto 10.0 mL of 1.0 mg/mL PAH (pH 7.5) solution under vigorous stirring continued for 15 min. The pH was readjusted to 7.5 upon mixing of the polyelectrolyte solutions using 0.5 M NaOH or 0.5 M HCl solutions. The final concentrations of PAH and PAA in the complexes were 1.0 mg/mL and 0.004 mg/mL, respectively.

For multilayer deposition, BPEI-coated slides were alternately immersed into PAA (0.8 mg/mL in 10 mM phosphate buffer, pH 3.5) and PAH-PAA complex (1.0 mg/mL or 0.8 mg/mL in 10 mM Tris buffer, pH 7.5) solutions. Each deposition step was followed by two rinsing steps (1 min for each rinsing) using 10 mM phosphate buffer (pH 3.5) for PAA and in 10 mM Tris HCl buffer (pH 7.5) for PAH-PAA complex layers. Of note, PAH-PAA complex solutions were refreshed every 1 hour (h) to avoid precipitation during LbL self-assembly.

2.4.3 LbL Self-Assembly of PAH/TA

BPEI coated substrates were alternatingly immersed into PAH (1.0 mg/mL in 10 mM Tris buffer, pH 7.0) and TA solutions (0.4 mg/mL in 10 mM phosphate buffer, pH 7.0), followed by two rinsing steps (each for 1 min) using either 10 mM phosphate buffer (pH 7.0) for TA layer or 10 mM Tris HCl buffer (pH 7.0) for PAH layer.

2.4.4 Preparation of PAH-TA Complexes and LbL Self-Assembly of PAH-TA Complexes and TA

PAH-TA complexes were prepared by adding 500 µL of 0.4 mg/mL TA solution (pH 7.0) at once into 5.0 mL of 1.0 mg/mL PAH solution (pH 7.0) under vigorous stirring continued for 15 min. The final concentrations of PAH and TA in complex solutions were 0.91 mg/mL and 0.036 mg/mL, respectively.

For multilayer deposition, BPEI-coated substrates were alternately immersed into TA (0.4 mg/mL in 10 mM phosphate buffer, pH 7.0) and in PAH-TA complex (1.0 mg/mL or 0.4 mg/mL in 10 mM Tris buffer, pH 7.0) solutions. Each deposition step was followed by two rinsing steps (each for 1 min) in 10 mM phosphate buffer (pH 7.0) for TA layer and 10 mM Tris HCl buffer (pH 7.0) for PAH-TA complex layer.

2.4.5 Citrate-Capped Au NPs Loading into Multilayer Films

Multilayer films with positively charged outmost layer (PAH or PAH-PAA complex or PAH-TA complex) were immersed into citrate-capped Au NPs solution for 12 h. Then, the films were dipped into deionized water for 1 min twice and dried with N_2 gas. The schematic representation of these 4 polyelectolyte multilayers are shown in Figure 2.2.

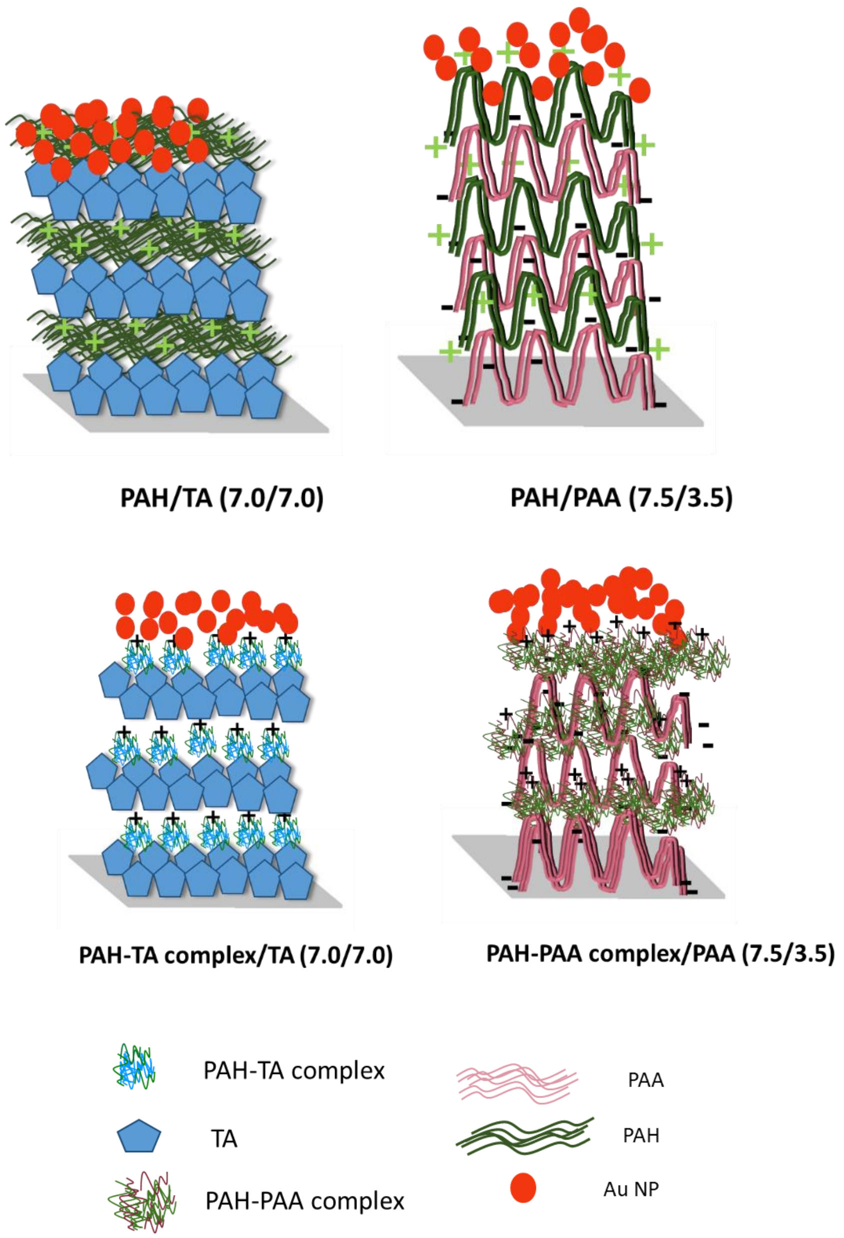

Figure 2.2 Citrate-capped Au NP loaded multilayers.

2.4.6 LbL Self-Assembly of Citrate-Capped Au NPs and Polyelectrolytes or PECs (Sandwich Type Multilayers)

BPEI-coated substrates were immersed into Au NPs solution and rinsed twice in deionized water for 1 min. Then, the substrates were immersed into PAH (1.0 mg/mL, pH 7.5) solution, followed by rinsing with 10 mM Tris HCl buffer (pH 7.5) for 1 min twice. This procedure was repeated until the desired layer number was reached. Sandwich type multilayer of PAH/Au NPs is shown in Figure 2.3.

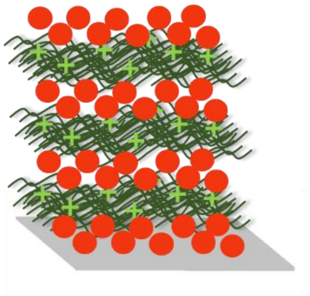

Figure 2.3 Sandwich type multilayer.

2.5 Seed-Mediated Synthesis of Au NPs

It was performed by modifying the study of Philip and coworkers[115] with changing source of $AuCl_4^-$, volume of BPEI in seeded growth solution and pH of final solution. Firstly, a solution of 0.5 mM $NaAuCl_4.3H_2O$ in deionized water (15 mL) was stirred in a flask under ice-cold conditions. To this gold salt solution, 10 µL of 0.6 mM of BPEI was added under stirring. The reaction mixture was mixed for 5 min and then 600 µL of 10 mM of ice-cold solution of $NaBH_4$ was added. The resulting solution was stirred for another 15 min prior to use. This solution corresponds to Au NP seeds.

For seeded growth of Au NPs, 60 mL of 0.5 mM $NaAuCl_4.3H_2O$ in deionized water was stirred in a 100 mL Erlenmeyer flask. To this stirring solution 1.0 mL of seed solution was added. After stirring for 2 min, different volumes of 0.6 mM of BPEI (50, 100, 500 µL) were added to the reaction mixture. The added concentration of these BPEI solutions were corresponded to 0.5, 1.0 and 5.0 µM, respectively. After stirring the reaction mixture for another 2 min, 3.0 mL of 10 mM of ascorbic acid was added. The resulting growth solution was stirred for another 30 min. Then, the solution pH was brought to 5.0 using 0.5 M NaOH and it was centrifuged for 60 min at 2,000 rpm. Supernatant was removed from the solution and NPs were dispersed in deionized water. Experimental scheme for seed-mediated synthesis is summarized in Figure 2.4.

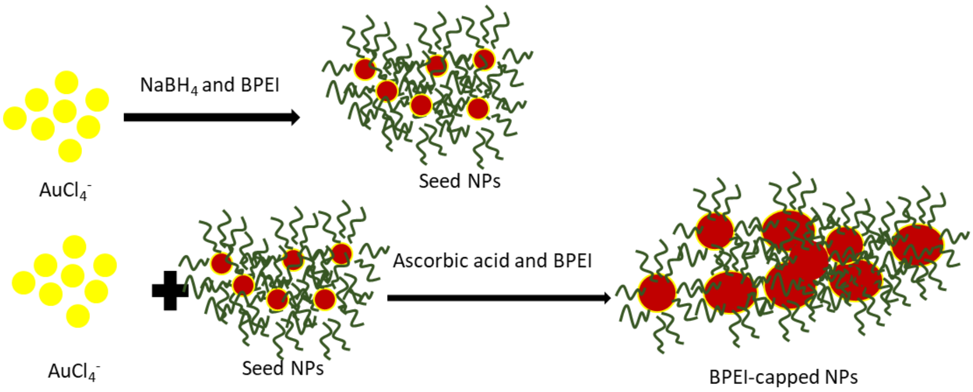

Figure 2.4 Seed-mediated synthesis of Au NPs.

The synthesized BPEI-capped Au NPs were loaded into negatively charged glass substrate as either 1-layer or LbL self-assembled with TA (or PSS).

2.5.1 LbL Self-Assembly of Seed-Mediated Au NPs and TA

Acid and base-treated glasses were immersed into BPEI-capped Au NP solution (60±8 nm measured by DLS in size at pH 5.0) for 30 min and rinsed twice in deionized water for 1 min. Then, the substrates were immersed into TA solution (1.0 mg/mL, pH 5.0) for 30 min, followed by rinsing with 10 mM phosphate buffer (pH 5.0) for 1 min twice. This procedure was repeated until the desired layer number was reached. The schematic representation of the multilayer is shown in the following Figure 2.5.

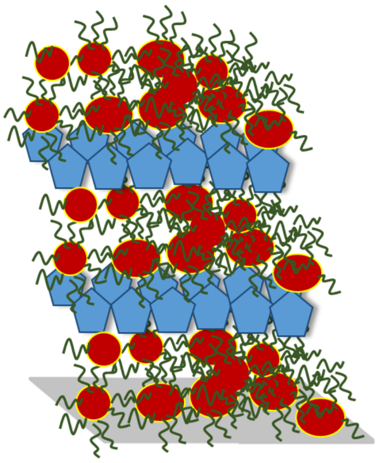

Figure 2.5 BPEI-capped Au NP/TA multilayer.

2.5.2 LbL Self-Assembly of Seed-Mediated Au NPs and PSS

Acid and base-treated glasses were immersed into BPEI-capped Au NP solution (60±8 nm measured by DLS in size at pH 5.0) for 30 min and rinsed twice in deionized water for 1 min. Then, the substrates were immersed into PSS solution (1.0 mg/mL in 0.1 M NaCl, pH 5.0) for 30 min, followed by rinsing with 10 mM phosphate buffer (pH 5.0) for 1 min twice. This procedure was repeated until the desired layer number was reached.

2.6 Photochemical Preparation of NPs

2.6.1 Multilayer Preparation for Post Loaded Inclusion of Au or Ag NPs

Glass slides were dipped in concentrated sulfuric acid for 85 min and thoroughly rinsed with DI water. Afterwards, they were soaked in 0.25 M NaOH solution for 10 min, thoroughly rinsed with DI water and finally dried under nitrogen flow. To deposit a precursor layer, substrates were immersed into 0.5 mg/mL BPEI solution (prepared in 10 mM phosphate buffer) at pH 4.0 for 1 h, followed by rinsing twice

(1 min for each) in phosphate buffer solution (10.0 mM, pH 4.0). The pH of polyelectrolyte and rinsing solutions were same with each other and adjusted using 0.5 M HCl or 0.5 M NaOH to bring it to the desired value. The concentration of the polymer solutions was 1.0 mg/mL for LbL assembly. The duration of deposition and rinsing steps were 5 min and 1 min, respectively. The polymer pairs together with deposition pH and rinsing solutions used in LbL assembly are shown in Table 2.1.

Table 2.1. Polyelectrolyte couple list used in the photochemical part.

Polyelectrolyte couple (1 mg/mL)	**Deposition pH**	**Rinsing buffer type**	**Rinsing pH**
PAH/PAA	7.5/3.5	Tris buffer (PAH)/ Phosphate buffer (PAA)	7.5/3.5
PAH/TA	7.0/7.0	Tris buffer (PAH)/ Phosphate buffer (TA)	7.0/7.0
BPEI/TA	5.0/5.0	Phosphate buffer for both BPEI and TA	5.0/5.0
PAH/PSS	9.3/9.3	Tris buffer (PAH)/ Phosphate buffer (PSS)	9.3/9.3
BPEI/PSS	5.0/5.0	Phosphate buffer for both BPEI and PSS	5.0/5.0
PEO/TA	2.0/2.0	Phosphate buffer for both PEO and TA	2.0/2.0
PVCL/TA	2.0/2.0	Phosphate buffer for both PVCL and TA	2.0/2.0

The LbL procedure was repeated until desired layer number of polymer layers was reached. It was critical to provide polycation at the topmost layer of the multilayer for $AuCl_4^-$ immersion (5.0 mM, 15 min) while topmost layer was polyanion in case of $AgNO_3$ (0.5 M, 6 h) loading. After that, films were rinsed with DI water for 1 min twice and dried with N_2 gas. Then, these films were exposed to Xe light (500

Watt) for 1 h. The scheme of photochemical NP formation on LbL substrates is shown in Figure 2.6.

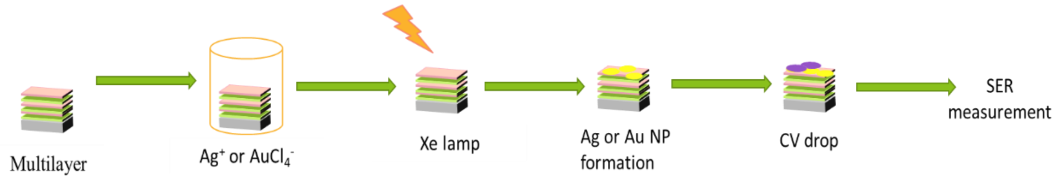

Figure 2.6 Experimental scheme of photochemical Ag or Au NP formation.

Additionally, the scheme of photochemical NP formation in sandwich structures is as follows in Figure 2.7.

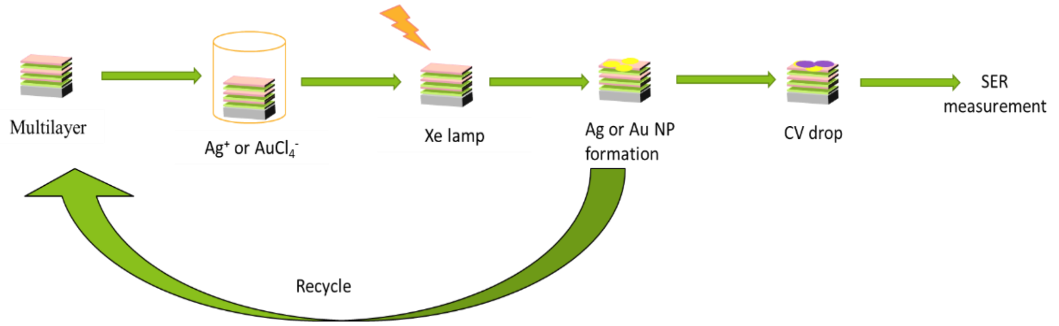

Figure 2.7 Photochemical synthesis of Ag or Au NPs in sandwich LbL structures.

CHAPTER 3

USE OF CITRATE-CAPPED AU NPS IN POLYELECTROLYE MULTILAYERS AS SERS SUBSTRATES

In this part, the effect of the chemical nature of the polyanion, surface morphology and film architecture on the SER signal was explored. In this respect, various SERS substrates were prepared through electrostatic LbL deposition of PAH with either PAA or TA, followed by post-loading of Au NPs. Additionally, water-soluble PECs were also included into the multilayers. Sandwich type multilayers including PAH and Au NPs were also investigated for SER signal enhancement. The performance of Au NPs post-loaded PAH/TA, PAH/PAA, PAH-TA complex/TA, PAH-PAA complex/PAA films and sandwich type films as SERS substrates was assessed using crystal violet (CV) as the model probe molecule.

3.1 Characterization of Spherical Au NPs

Au NPs have distinctive optical properties in the visible region of the electromagnetic spectrum because of their free electrons' localized surface plasmon resonances (LSPR).[168] The LSPR band of Au NPs synthesized in this study using the Turkevich method is shown in Figure 3.1 at approximately 520 nm. This method yields Au colloids with dimensions of 10±2 nm.

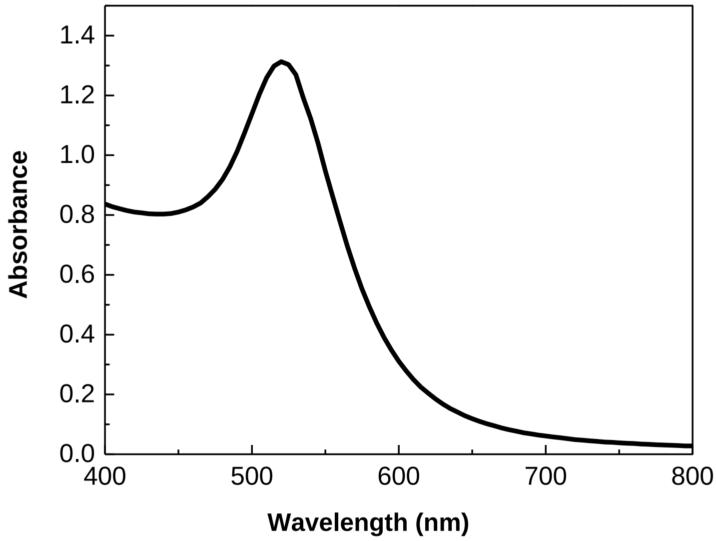

Figure 3.1 UV-vis spectrum of Au NPs synthesized by Turkevich Method.

3.2 Preparation of LbL Films

Two different multilayer films were prepared through LbL deposition of either PAH and PAA or PAH and TA. Both films were constructed onto a BPEI precursor layer for a more robust film growth. The first layer was either TA or PAA. Multilayer growth of PAH/PAA and PAH/TA films was followed by ellipsometry technique through measuring the dry film thickness after each layer deposition.

LbL deposition of PAH and PAA provided exponentially grown multilayers when PAH and PAA were deposited at pH 7.5 and pH 3.5, respectively. The driving force for multilayer deposition was electrostatic interactions between the protonated amino groups of PAH and carboxylate groups of PAA. Figure 3.2 and Figure 3.3 show evolution of ellipsometric film thickness as a function of layer number. The error in thickness measurements increased with further increasing of the layer number and film thickness reached 130 nm at 12th layer and. Therefore, LbL growth could be followed up to 12th layer using ellipsometry.

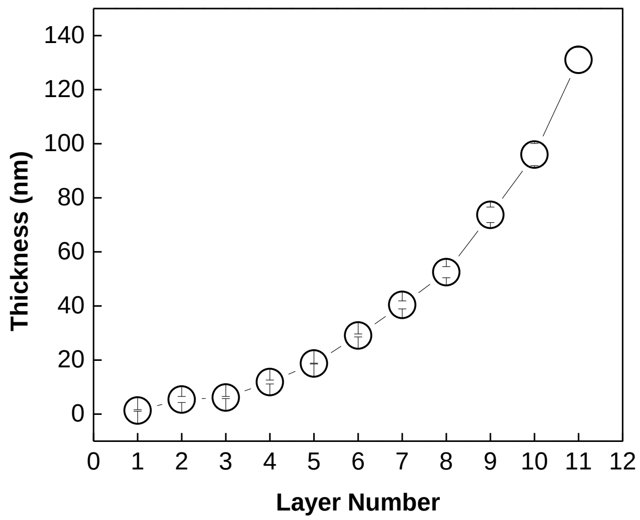

Figure 3.2 LbL growth of PAH/PAA. PAH and PAA were deposited at pH 7.5 and 3.5, respectively. Multilayers were grown onto a precursor film with a thickness of ~1.9 nm. Thickness values do not include the precursor layer thickness.

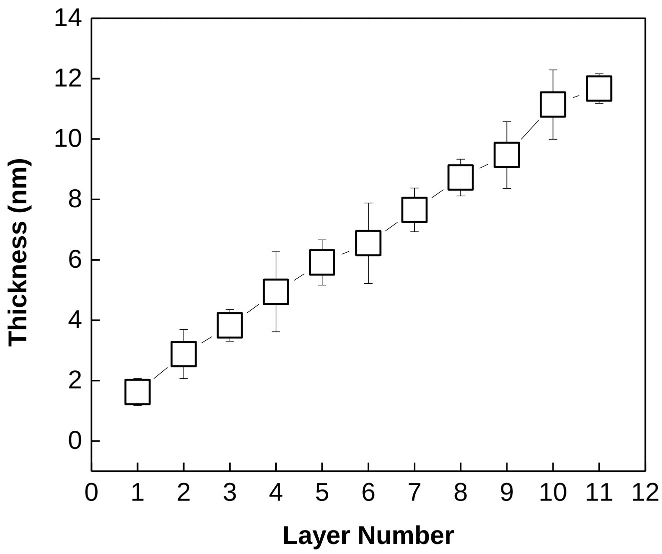

Figure 3.3 LbL growth of PAH/TA at pH 7.0. Multilayers were grown onto a precursor film with a thickness of ~1.5 nm. Thickness values do not include the precursor layer thickness.

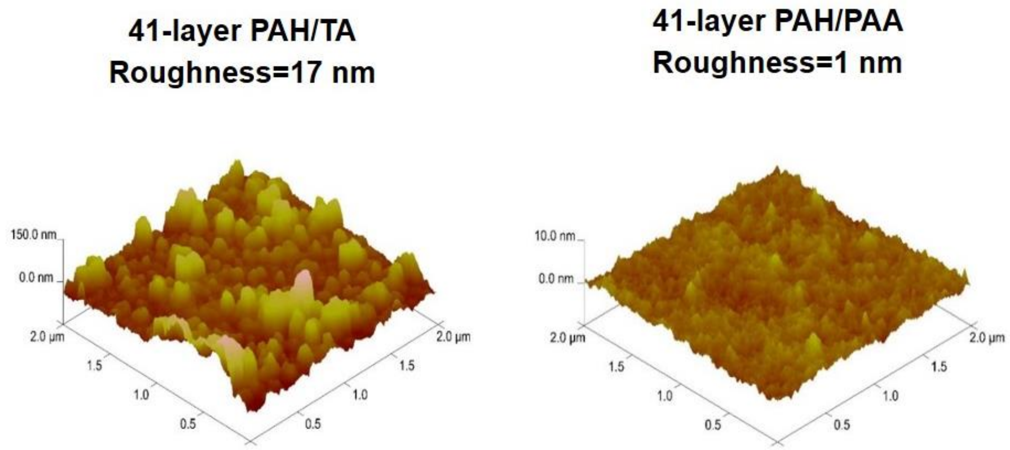

Figure 3.4 AFM height images and roughness values of 41-layer PAH/PAA and PAH/TA films. The roughness values were estimated over 2x2 μm^2 images.

Exponential growth regime results from either an increase in surface roughness with increasing number of layers resulting in greater surface area for polymer deposition[74] or in and out diffusion of at least one of the polymers resulting in greater amount of polymer deposition with increasing number of layers.[64,65] PAH/PAA multilayers were smooth and the roughness values for 7, 11 and 21- layer films were comparable (~1 nm, Figure 3.5).

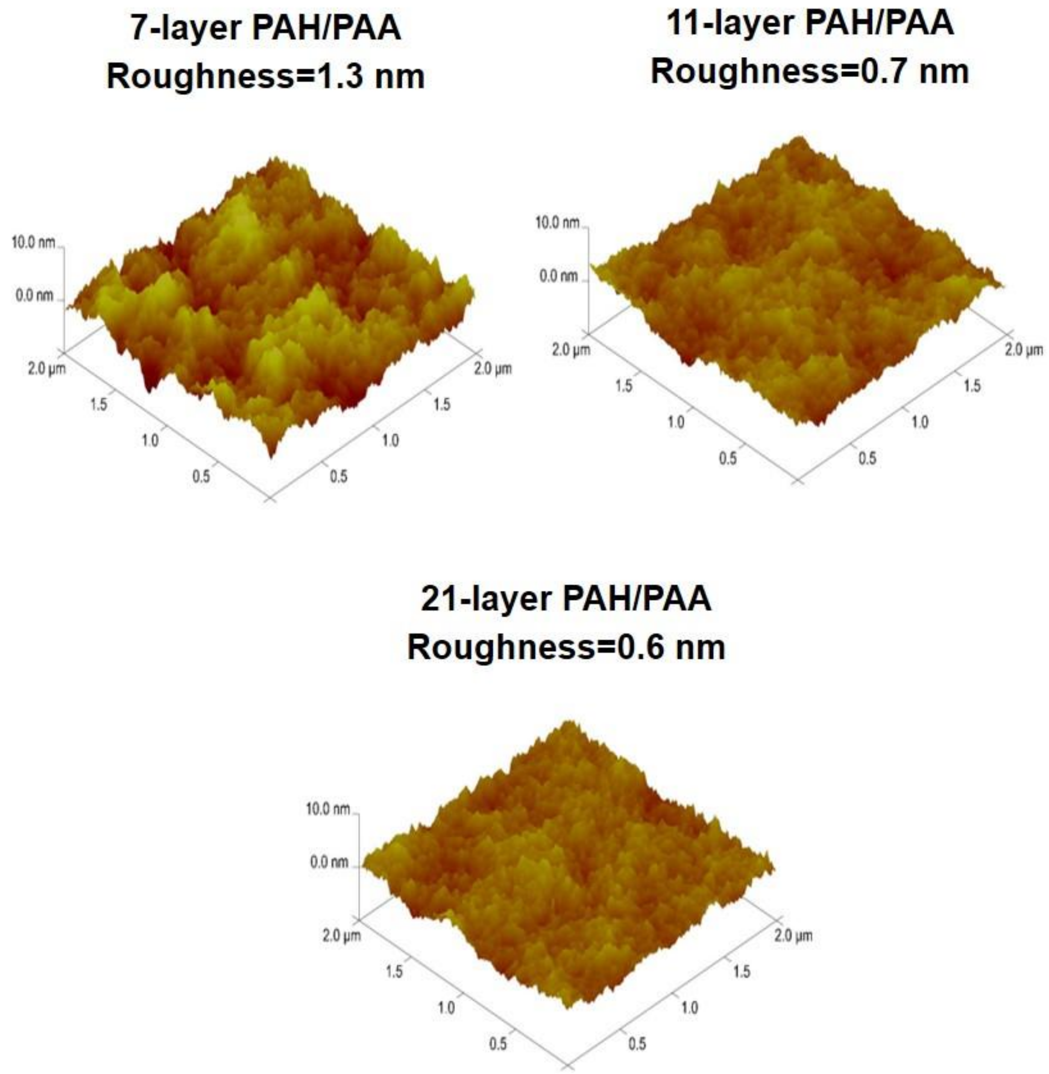

Figure 3.5 AFM height images and roughness values of 7, 11 and 21-layers of PAH/PAA films. The roughness values were estimated over 2x2 μm^2 images.

Considering the minor difference in roughness values, the exponential growth was attributed to regime to in and out diffusion of highly hydrophilic PAA with relatively low molecular weight. At pH 7.5, PAH is expected to be protonated by 95 % (pK_a of PAH is ~ 8.7),[169] whereas PAA (pK_a of PAA is ~ 4.5)[62] is 10% ionized at pH 3.5. The lower number of ionic association among PAH and PAA possibly led to weakly associating layers and enabled in and out diffusion of relatively short PAA chains resulting in exponential growth of multilayers.[75] Of note, PAH and PAA multilayers were also prepared at pH 4.0. PAH and PAA exhibited linear growth at pH 4.0 when carboxylic acid (COOH) groups of PAA was ionized by ~ 25 % and PAH was almost fully charged. Linear growth at pH 4.0 was correlated with the higher charge density on PAA and stronger association among the layers, preventing in and out diffusion of polymer chains. Figure 3.6 and Figure 3.7 contrast the LbL growth and AFM images and the corresponding surface roughness values of PAH and PAA deposited at pH 7.5 (PAH)/pH 3.5 (PAA) and pH 4.0 (PAH)/pH 4.0 (PAA). Roughness values of linearly grown films were higher for before and after deposition of Au NPs as compared to exponentially grown ones. High initial roughness value before deposition increased the possibility of deposition of NPs on higher parts of linearly grown film. Importantly, linearly grown PAH/PAA films did not provide a SER signal, therefore could not be further considered as a SERS substrate. Although roughness values of linearly grown films were higher than exponentially grown ones, lower thickness of linearly grown films deposited less amount of Au NPs, resulting in no SER signal.

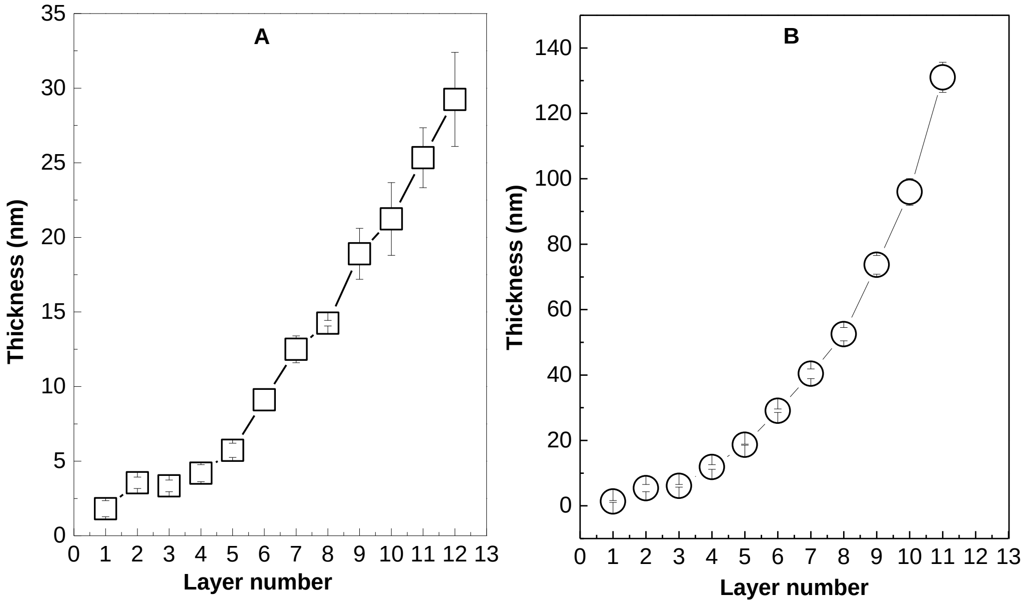

Figure 3.6 Multilayer growth of PAH/PAA at (A) pH 4.0/4.0 and (B) pH 7.5/3.5. Multilayers were grown onto a precursor film with a thickness of ~ 1.8 and 1.9 nm, respectively. Thickness values given in A and B do not include the precursor layer thickness.

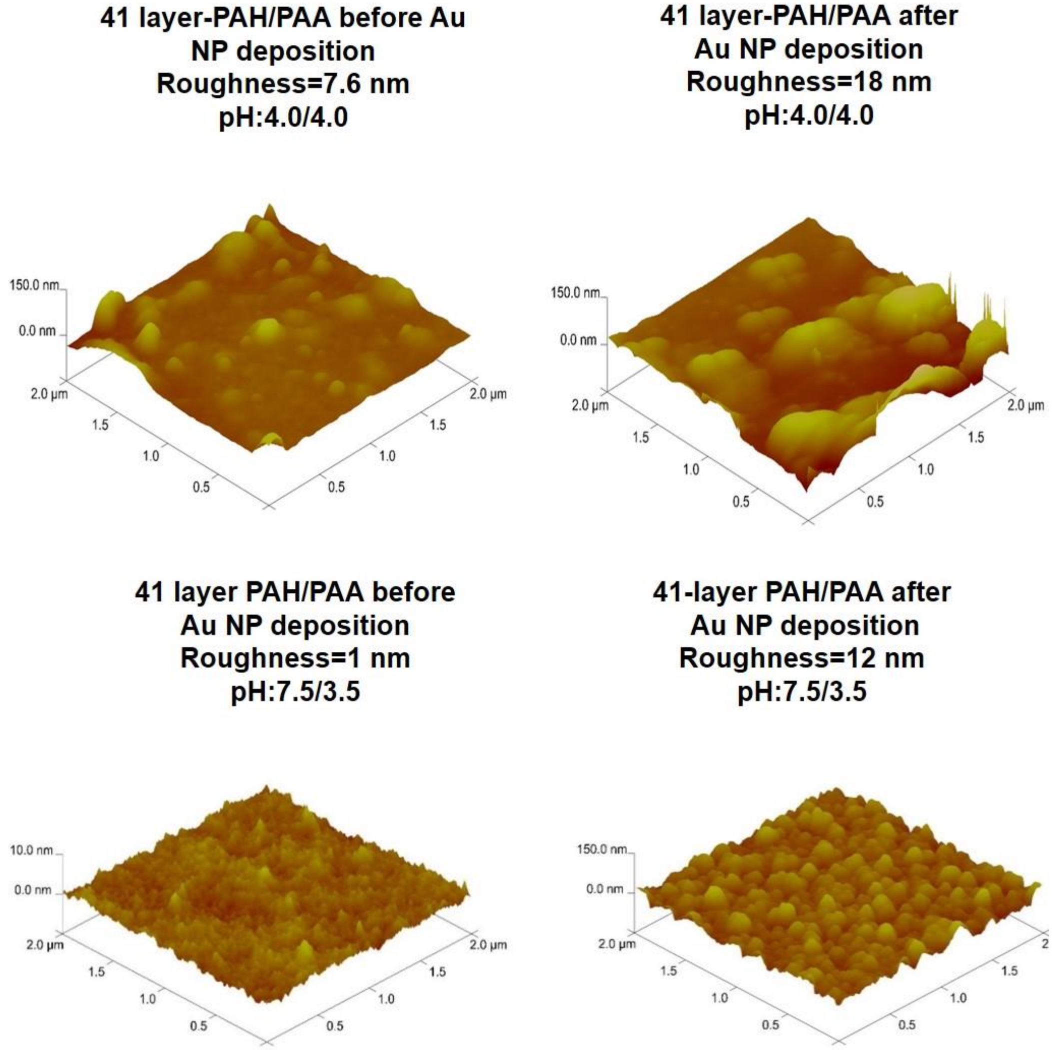

Figure 3.7 AFM height images and roughness (root mean square, rms) values of 41 layers of PAH/PAA films at pH 4.0/4.0 and pH 7.5/3.5 before and after Au NP deposition. The roughness values were recorded from 2x2 μm^2 images.

PAH and TA multilayers were constructed at pH 7.0 through electrostatic interactions among protonated amino groups of PAH and phenolate groups of TA. PAH and TA films showed linear growth profile with ~1.7 nm increment per bilayer (Figure 3.3). TA is a natural polyphenol with 25 hydroxyl groups per molecule. TA has two pK_a values, i.e. p$K_{a,1}$ ~ 6.5 and p$K_{a,2}$ ~ 8.0.[170] At pH 7.0, TA is expected to have both phenolic hydroxyl and phenolate groups. Findings in this study are in good agreement with the study of Lvov and coworkers who reported a bilayer thickness ranging between 1.6 to 2.7 nm for PAH and TA films constructed under similar pH conditions and is maximum at pH 7.0.[71]

As seen in Figure 3.4, the roughness of 41-layer PAH/TA films was ~ 17 nm estimated from 2x2 μm^2 images and PAH/PAA films with similar number of layers were rather smooth with a surface roughness of ~ 1 nm. PAH/TA films were rough, exhibiting circular islands at the surface. These circular objects were possibly due to self-aggregation of TA molecules in the solution and deposition at the surface in the aggregated form. Self-association of TA has been reported earlier.[71]

3.3 Au NPs Loading into Multilayers

For SERS measurements, PAH/PAA and PAH/TA multilayers were coated with Au NPs by exposing 41 layers of films to Au NPs solution for 12 h. Of note, 11, 21, and 31 layers of films for PAH/PAA multilayers were also examined. However, the SER signals of these 11, 21 and 31 multilayers were too weak, so that Au NPs loaded 41 layers of films were used for the rest of the study. Figure 3.8 contrasts the surface morphology of PAH/PAA and PAH/TA multilayers before and after Au NPs loading. Both multilayers showed an increase in surface roughness upon deposition of Au NPs. However, the remarkable roughness increment recorded for PAH/TA multilayers after Au NPs loading was possibly due to high initial roughness of PAH/TA films and deposition of Au NPs probably on higher parts of the multilayers.

UV-vis absorption spectrum of Au NPs loaded PAH/PAA multilayers (Figure 3.9) showed that LSPR peak associated with NPs broadened and red-shifted indicating deposition of NPs on the multilayers in the aggregated form.[143,171] On the other hand, the LSPR band obtained from PAH/TA multilayers remained in the same position as native Au NPs demonstrating deposition of Au NPs as isolated particles on multilayer films (Figure 3.9). These results are in good agreement with the SEM images of 41 layers of PAH/PAA and PAH/TA multilayer films (Figure 3.10). PAH/PAA film exhibited accumulation of relatively small particles on the film, indicating aggregation of Au NPs. The aggregates on top of PAH/TA multilayers were rather large and sparsely distributed, thus were correlated with the self-associated TA aggregates. The small and isolated particles were associated with isolated Au NPs.

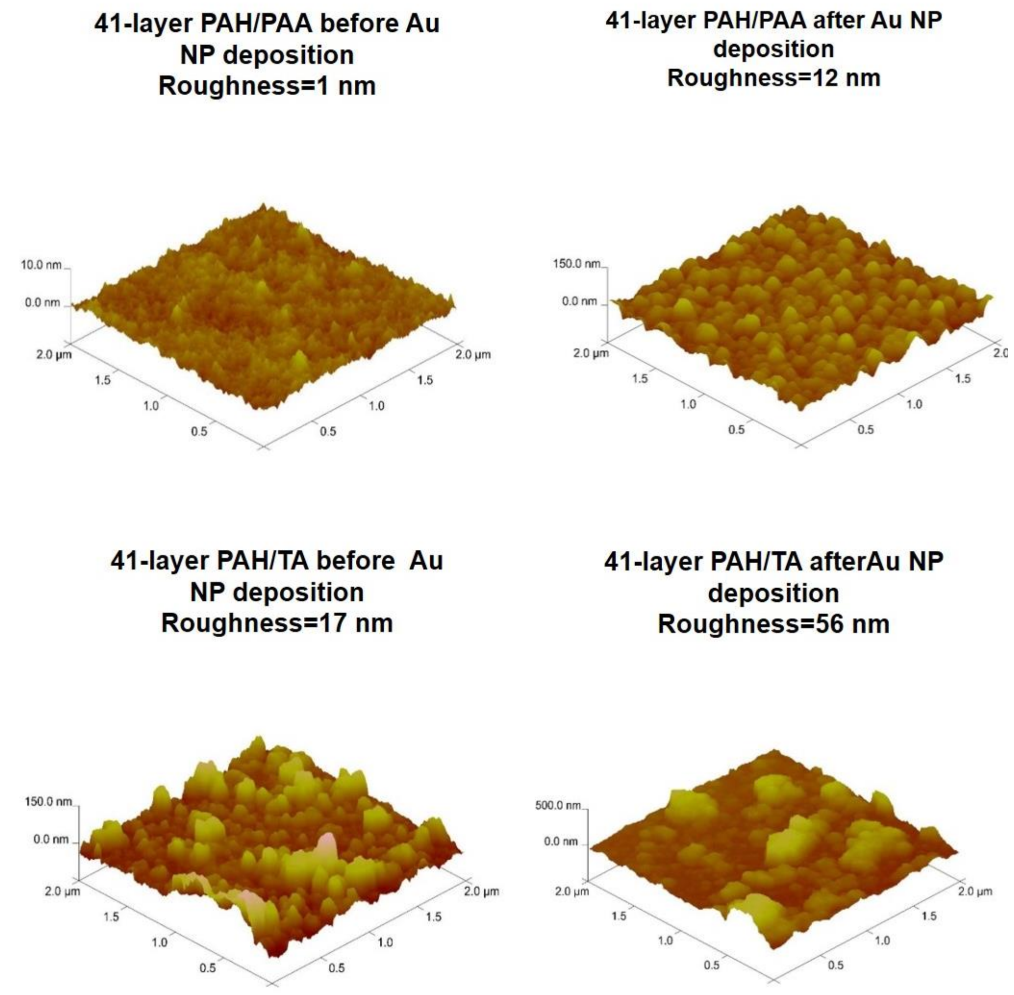

Figure 3.8 AFM height images and roughness values of 41-layers of PAH/TA and PAH/PAA films before and after Au NPs deposition. The roughness values were recorded from 2x2 μm^2 images.

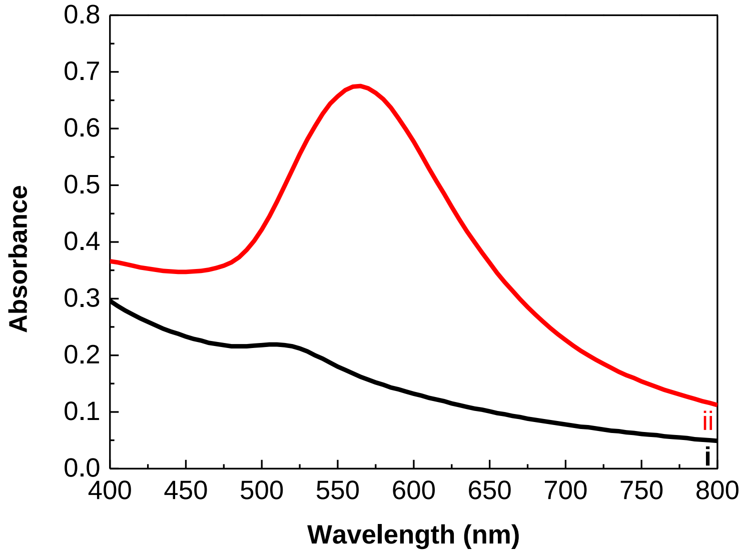

Figure 3.9 UV-vis absorption spectra of Au NPs embedded in 41-layers of (i) PAH/TA, (ii) PAH/PAA.

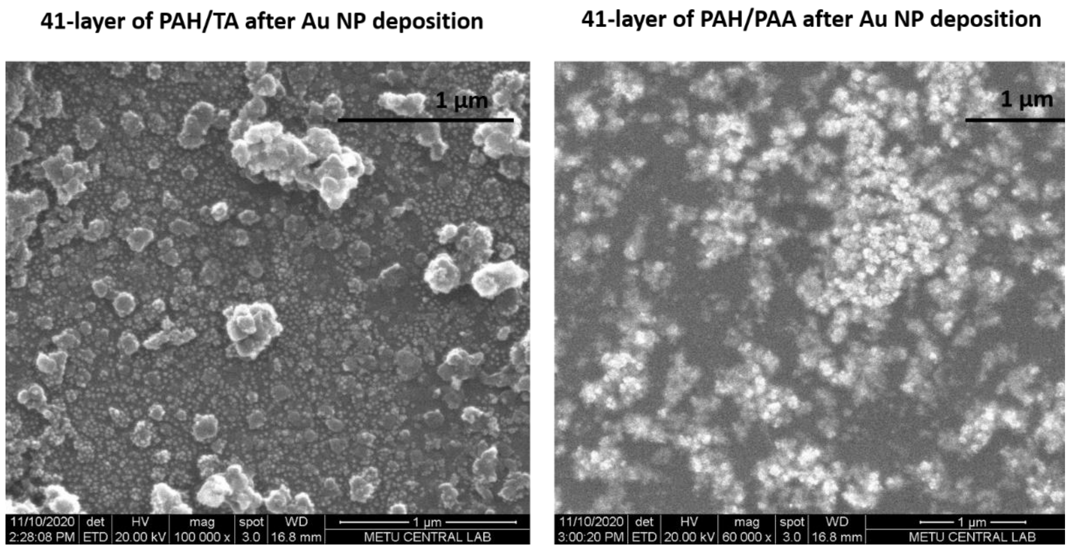

Figure 3.10 SEM images of 41-layers of PAH/TA and PAH/PAA films after Au NPs deposition.

3.4 SERS Characterization of Multilayers

CV was used as a probe molecule to compare the performance of multilayers as SERS substrates. CV molecule has a central carbonium ion (CH_5^+) with three benzene rings around the center and each benzene ring is connected to $–N(CH_3)_2$ group. The observed main characteristic vibrational bands of CV molecule at around 449, 526, 800, 916, 1176, 1376, 1576 and 1618 cm^{-1}, corresponding to out-of-plane bending mode of $C–C_{center}–C$, bending mode of C–N–C, phenyl-H out-of-plane antisymmetric bending, out-of-plane aromatic C–C deformation, C–N–C symmetric stretching vibration, C–H out-of-plane bending modes, C–H in-plane bending mode, stretching vibration of nitrogen and phenyl ring, stretching vibration of nitrogen and phenyl ring and in-plane aromatic C–C, respectively.[172–176] As seen in Figure 3.11, when CV was deposited onto multilayers, the observed peak positions were due to interaction between CV molecules and Au NPs distributed on the surface of the substrate. The orientation of CV molecule on the surface of Au nanostructures has significant effect on the SERS intensity, resulting that no enhancement occurs in Raman vibrational bands if adsorption of CV molecules is not at right sites of the substrate surface at desired angles.[175]

SER signal obtained from PAH/TA films was significantly greater than that obtained from PAH/PAA films as can be seen from Figure 3.11. In literature, Raman signal enhancements were shown to be correlated with increase in surface roughness on solid substrates.[20,21,69,177] Nanoscale roughness in a metal surface provides generation of high density of highly localized regions (hot spots) in which extraordinary SER signal enhancement occurs.[16–18] Hot spots can be defined as highly concentrated areas of strong electromagnetic fields. They are created by LSPRs and they are thought to provide a significant boost to SER signal. This enhancement is extremely large and it is concentrated in areas much smaller than the wavelength of light.[19] When probe molecules are located in between these neighboring areas, a significant increase in SER signal could be obtained in comparison to the signal obtained from isolated areas. It has been reported that highly localized electric field regions are formed between the numerous neighboring islands on rough surfaces.[20] Intersection angle between neighboring islands describes surface roughness, so that when the angle is sharper, larger surface roughness is obtained. Moreover, rough surfaces provide a large surface area resulting in an increased binding capacity as compared to flat surfaces.[143] Since molecules between two localized regions exhibit the greatest SERS enhancement, a rougher surface can increase the likelihood that probe molecules will become adsorbed on two nanoislands. As a result, a rougher nanoislands-deposited substrates were shown to exhibit a stronger SERS effect.[178] Additionally, an increase in surface roughness enables greater confinement of NPs, so a rough surface was shown to display a higher density of NPs.[179] This led to formation of localized regions, where the distance separated these NPs allows to obtain a localized surface plasmons couplings.[179] In the light of these findings, the higher SER signal obtained from PAH/TA multilayers can be explained by the higher surface roughness of PAH/TA films compared to PAH/PAA.

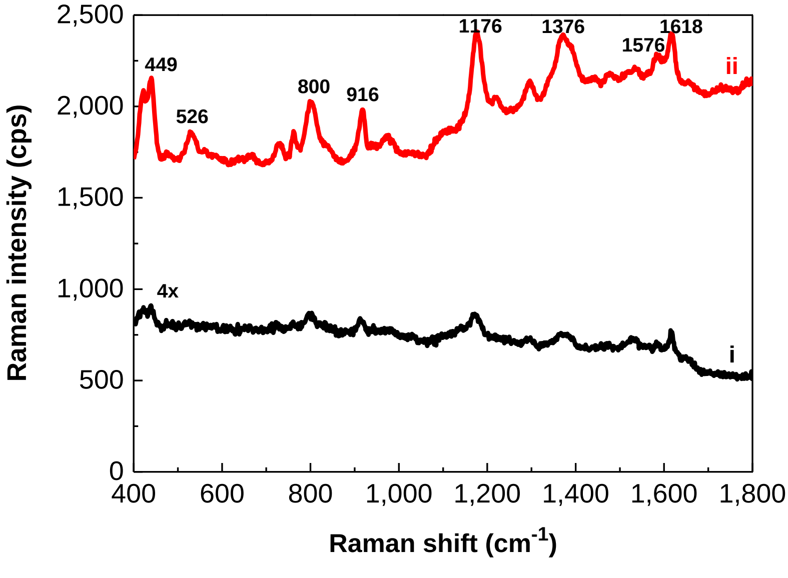

Figure 3.11 SER spectra of 1.0 x 10^{-5} M CV molecule adsorbed onto Au NPs containing (i) 41 layers of PAH/PAA (laser power: 5 mW) and (ii) PAH/TA multilayer films (laser power: 10 mW).

To further understand the effect of surface roughness on SER signal, water-soluble complexes of PAH with PAA or TAA were prepared and LbL deposited at the surface using PAA or TA as the polyacid counterpart. In this way, surface roughness was aimed to control through deposition of interpolyelectrolyte aggregates on the surface. The difference between UV-vis absorption spectra of Au NPs including multilayers of PAH/PAA and PAH-PAA complex/PAA (Figure 3.12) and PAH/TA and PAH-TA complex/TA are seen in Figure 3.13.

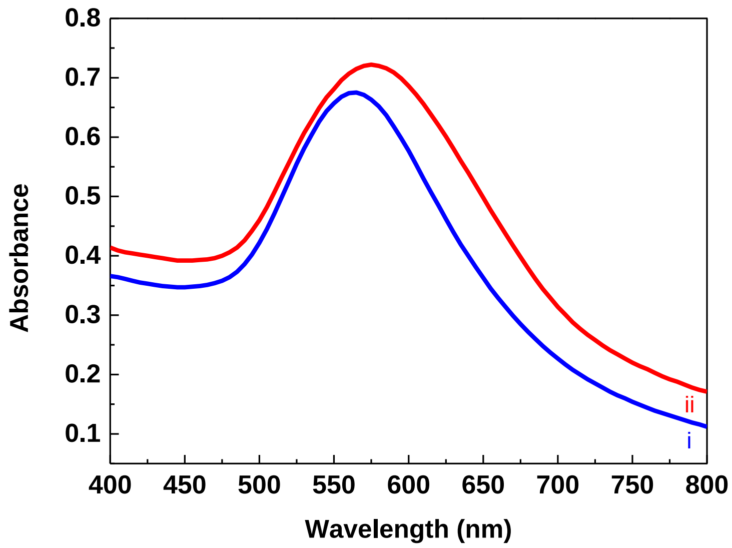

Figure 3.12 UV-vis absorption spectra of Au NPs embedded in 41 layers of (i) PAH/PAA, (ii) PAH-PAA complex/PAA.

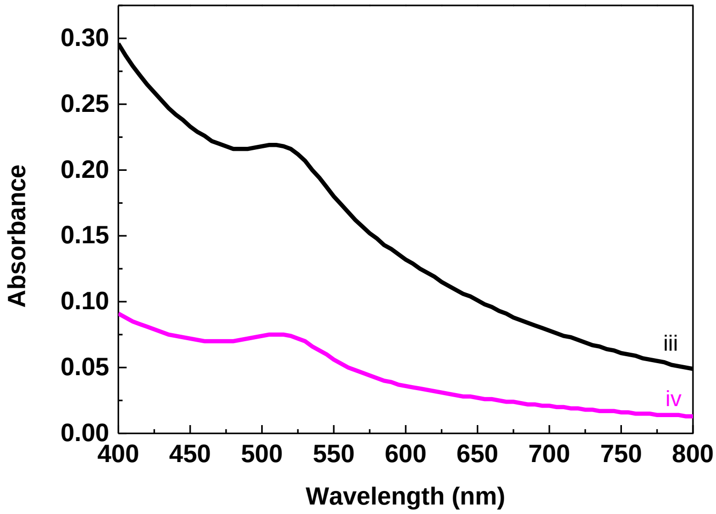

Figure 3.13 UV-vis absorption spectra of Au NPs embedded in 41 layers of (iii) PAH/TA, (iv) PAH-TA complex/TA multilayer films.

Water-soluble complexes of PAH and PAA were simply prepared by adding PAA solution into PAH solution. The number average particle size of PAH-PAA complexes measured using dynamic light scattering (DLS) technique was 142.8±14.9 nm (Figure 3.14) and the zeta potential of the PAH-PAA complexes was measured as 60.7±2.2 mV (Figure 3.15).

To prepare larger complexes, the amount of PAH was kept constant and that of PAA was increased. Increasing the amount of PAA in the complexes resulted in formation of larger and but less stable complexes. Therefore, PAH:PAA ratio was not changed for further studies. Another reason for not increasing the amount of PAA in the complexes was to leave enough functional groups on PAH chains to drive LbL self-assembly. LbL deposition of PAH-PAA complexes and PAA were performed under similar conditions with PAH/PAA films, i.e. pH 7.5 for PAH-PAA complexes and pH 3.5 for PAA. No significant differences in film thickness and roughness values (before and after Au NPs loading) between PAH/PAA and PAH-PAA complexes/PAA were measured (Figure 3.16 and Figure 3.17).

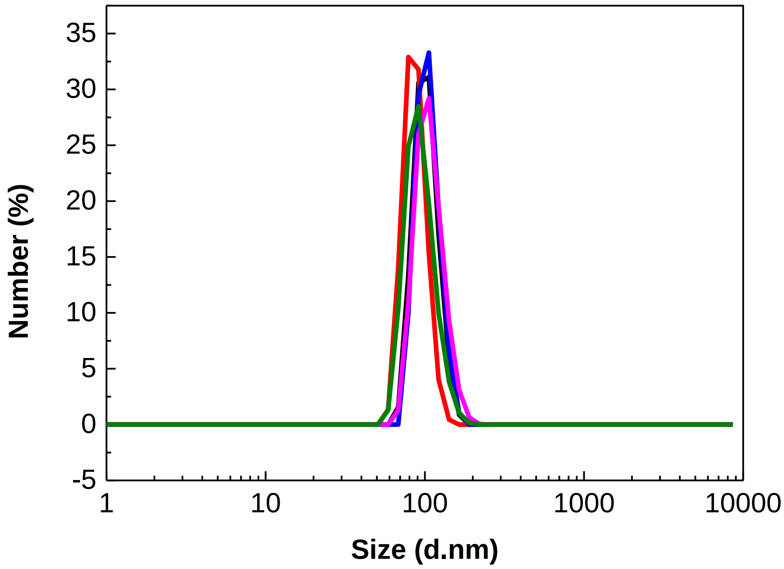

Figure 3.14 Hydrodynamic size distributions by number of (1 mg/mL PAH- 0.8 mg/mL PAA) complexes by Dynamic Light Scattering. Each color shows the replicate measurements of these complexes.

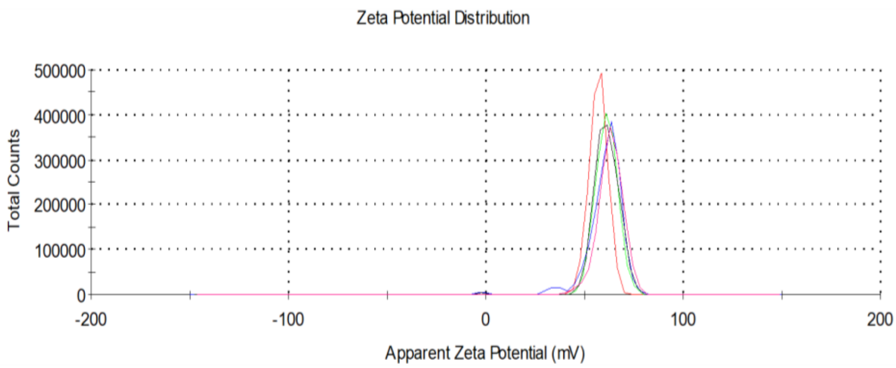

Figure 3.15 Zeta potential distribution of the complexes. Each color shows the replicate measurements of these complexes.

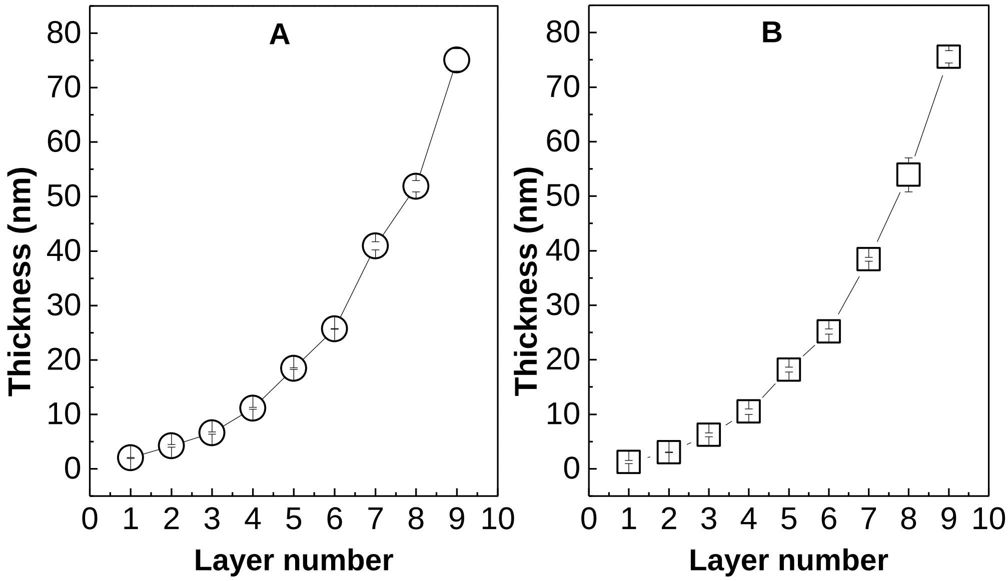

Figure 3.16 Multilayer growth of PAH/PAA (A) PAH-PAA complex/PAA (B) at pH 7.5/3.5. Multilayers were grown onto a precursor film with a thickness of ~1.9 nm and 1.0 nm, respectively. Thickness values do not include the precursor layer thickness.

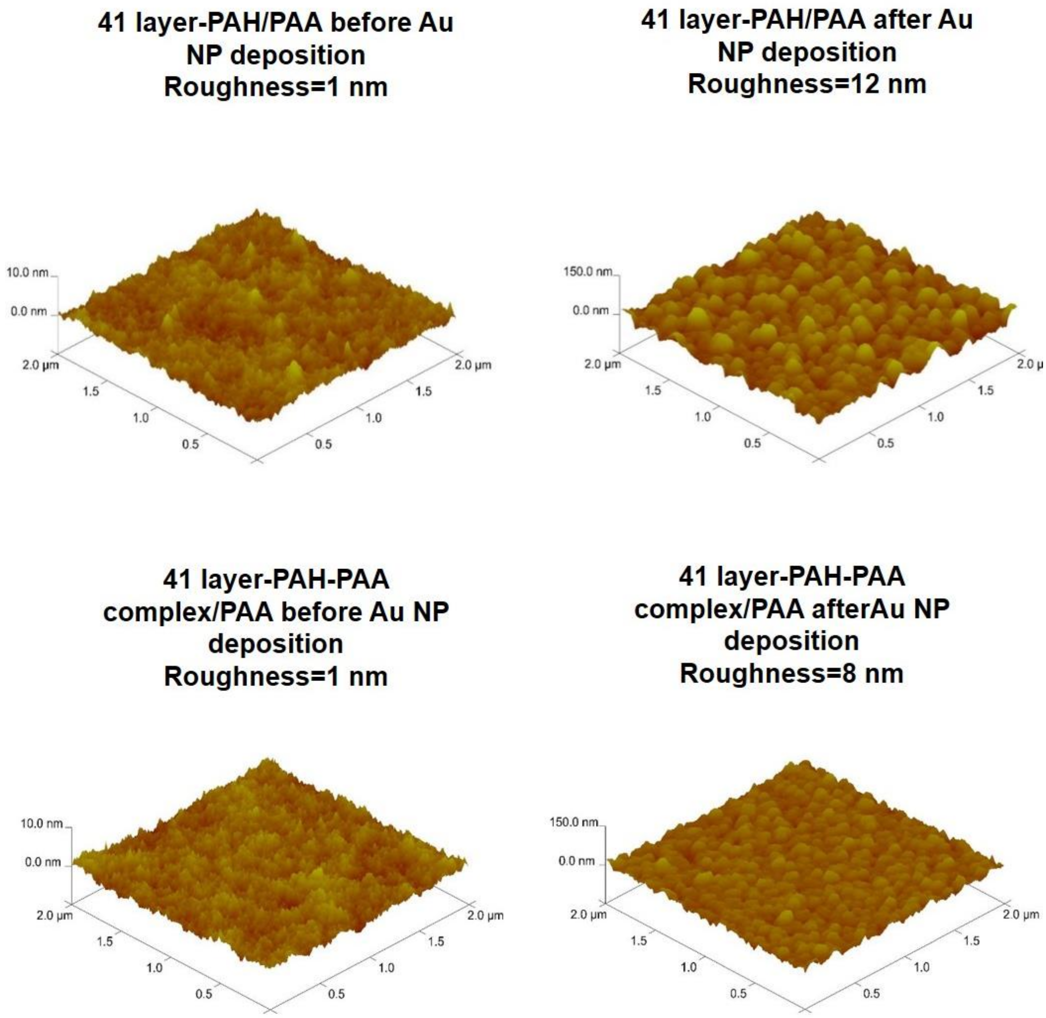

Figure 3.17 AFM height images and root mean square values of 41 layers of PAH/PAA and PAH-PAA complex/PAA films before and after Au NP deposition. The roughness values were recorded from 2x2 μm^2 images.

Accordingly, a significant enhancement in the Raman signal was not observed as shown in Figure 3.18.

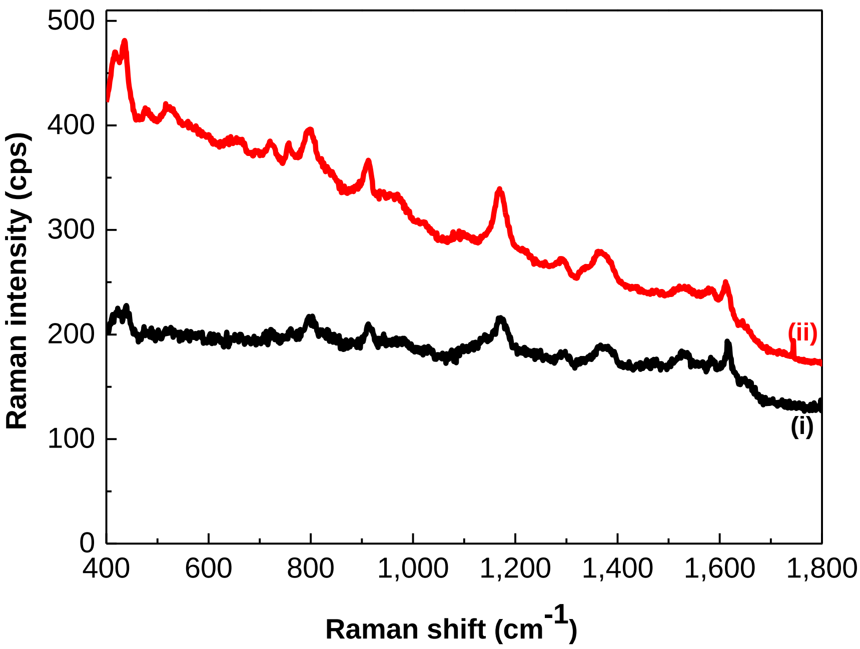

Figure 3.18 SER spectra of 1.0 x 10^{-5} M CV molecule adsorbed on Au NP containing 41 layers of (i) PAH/PAA and (ii) PAH-PAA complex/PAA multilayer films.

As seen in SEM images of 41-layers of PAH/PAA and PAH-PAA complex/PAA (Figure 3.19), Au NPs adsorbed unevenly and in the aggregated form onto PAH/PAA multilayers, whereas Au NPs arranged with high density and less space between the particles in multilayers of PAH-PAA complex/PAA. This result was also consistent with UV-vis absorption spectra of these multilayers with significant aggregation of NPs for both multilayers (Figure 3.12). Additionally, similar roughness results of PAH/PAA and PAH-PAA complex/PAA multilayers resulted in comparable SER signals of CV molecule.

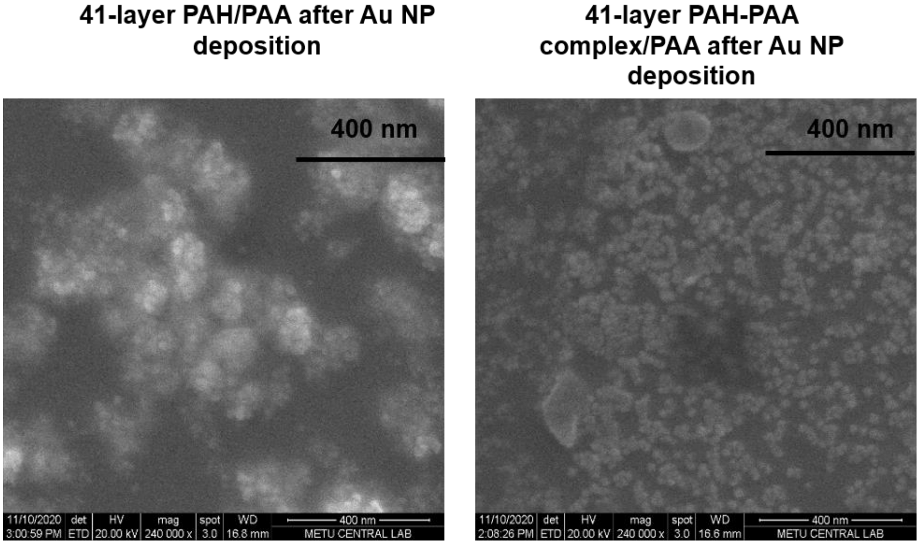

Figure 3.19 SEM images of 41-layers of PAH/PAA and PAH-PAA complex/PAA films after Au NPs deposition.

A similar experiment was also conducted through LbL deposition of PAH/TA complexes and TA. Water-soluble complexes of PAH and TA were simply prepared by adding TA solution into PAH. The number average size of PAH-TA complexes was recorded as 67.2 ± 2.2 nm with an average zeta potential value of 16.9 ±1.1 mV (Figure 3.20 and Figure 3.21). Although the thicknesses of PAH/TA and PAH-TA complexes/TA were similar, the roughness of PAH-TA complexes/TA was lower than that of PAH/TA films both before and after Au NPs deposition (Figure 3.22 and Figure 3.23). This might be due to a decrease in the extent of self-association of TA molecules due to complexation with PAH resulting in lower surface roughness.

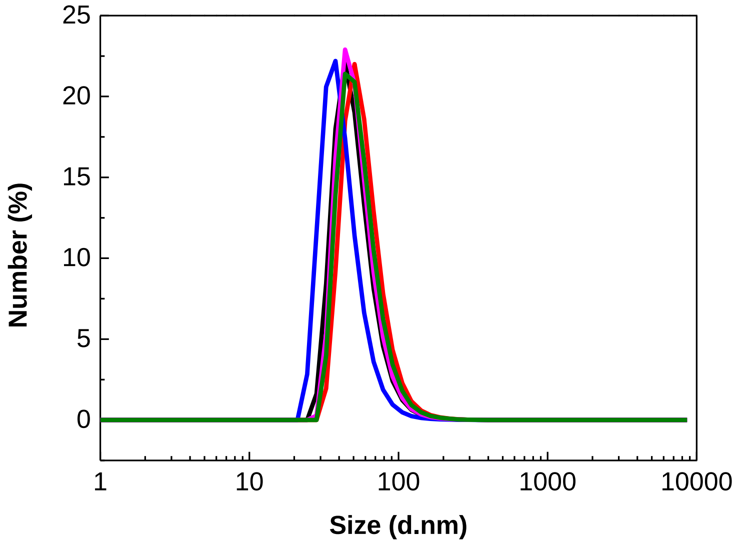

Figure 3.20 Hydrodynamic size distributions by number of (1 mg/mL PAH- 0.4 mg/mL TA) complexes by Dynamic Light Scattering. Each color shows the replicate measurements of these complexes.

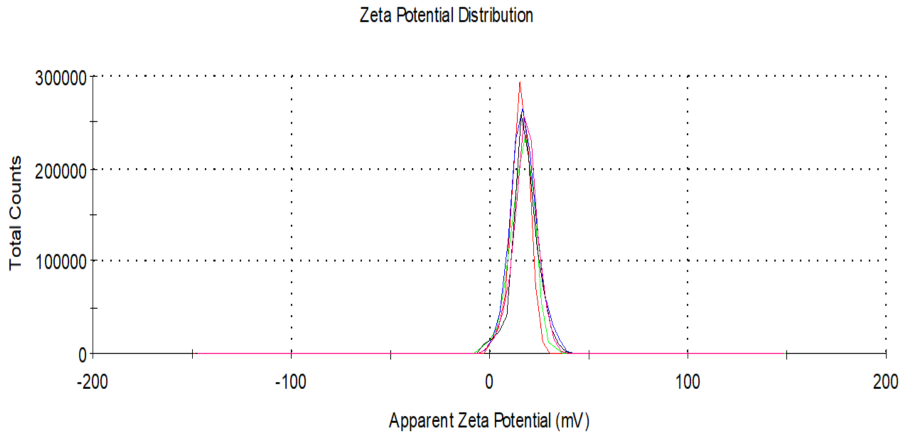

Figure 3.21 Zeta potential distributions of the complexes. Each color shows the replicate measurements of these complexes.

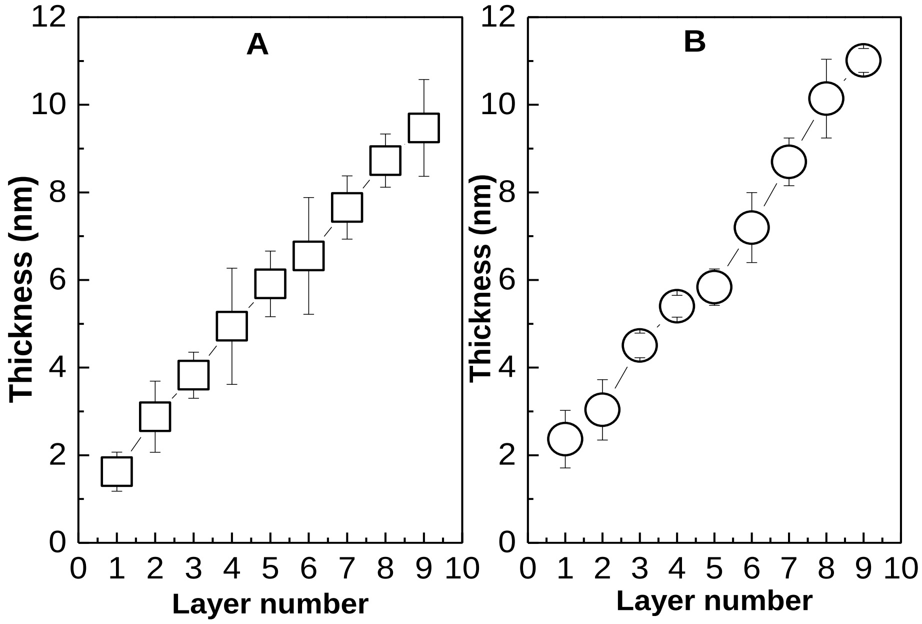

Figure 3.22 Multilayer growth of PAH/TA (A) and PAH-TA complex/TA (B) at pH 7.0. Multilayers were grown onto a precursor film with a thickness of ~1.5 nm. Thickness values do not include the precursor layer thickness.

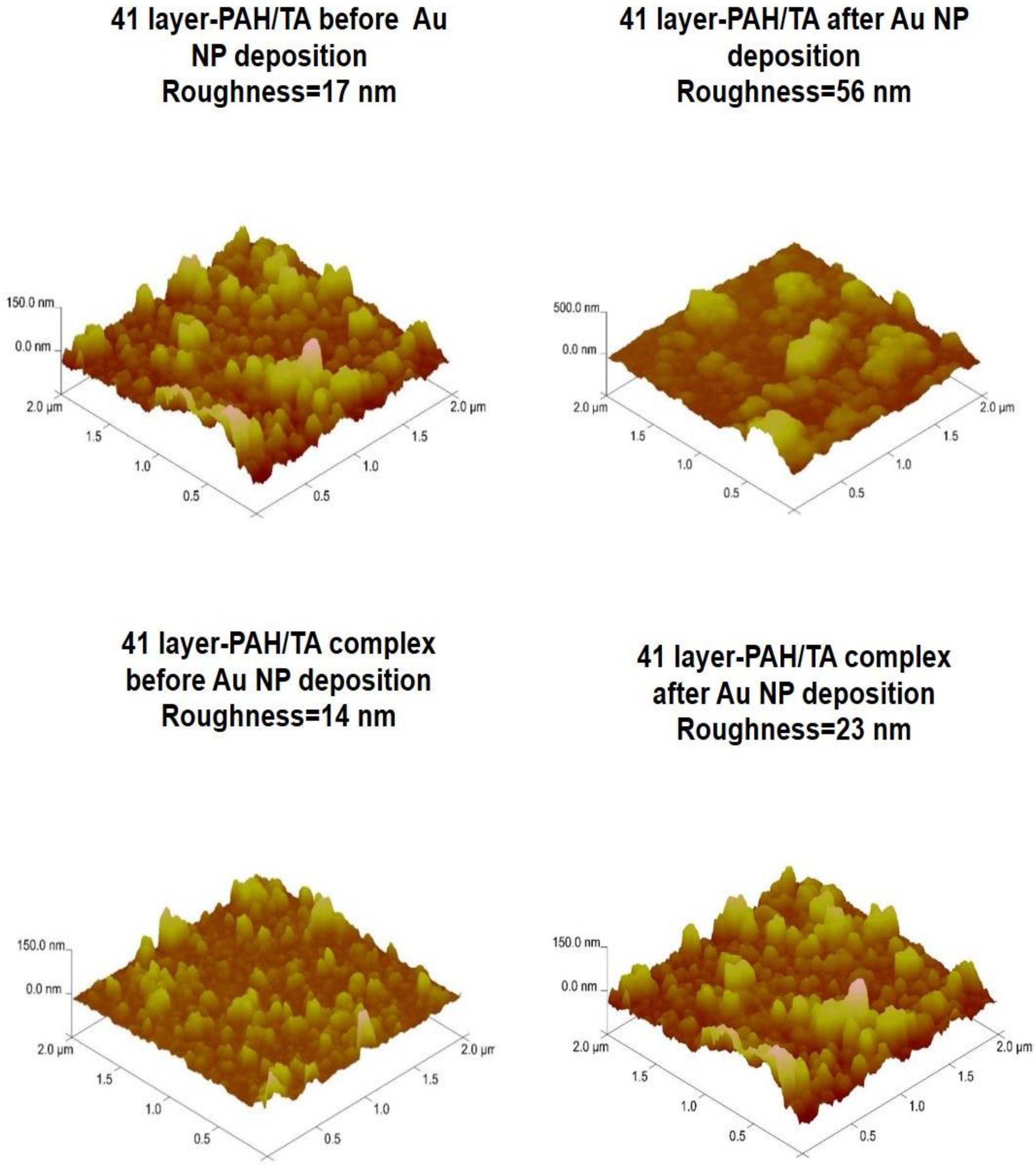

Figure 3.23 AFM images and root mean square values of 41 layers of PAH/TA and PAH-TA complex/TA films before and after Au NP deposition. The roughness values were recorded from 2x2 μm^2 images.

A decrease in Raman signal of $1.0x10^{-5}$ M CV by a factor of ~3 was recorded for multilayers of PAH-TA complexes/TA compared to PAH/TA multilayers (Figure 3.24). The decrease in the intensity of the Raman signal upon deposition of PAH-TA complexes can be correlated with the decrease in surface roughness compared to PAH/TA films. The relatively smooth surface of PAH-TA complex/TA multilayers is also confirmed by SEM images (Figure 3.25).

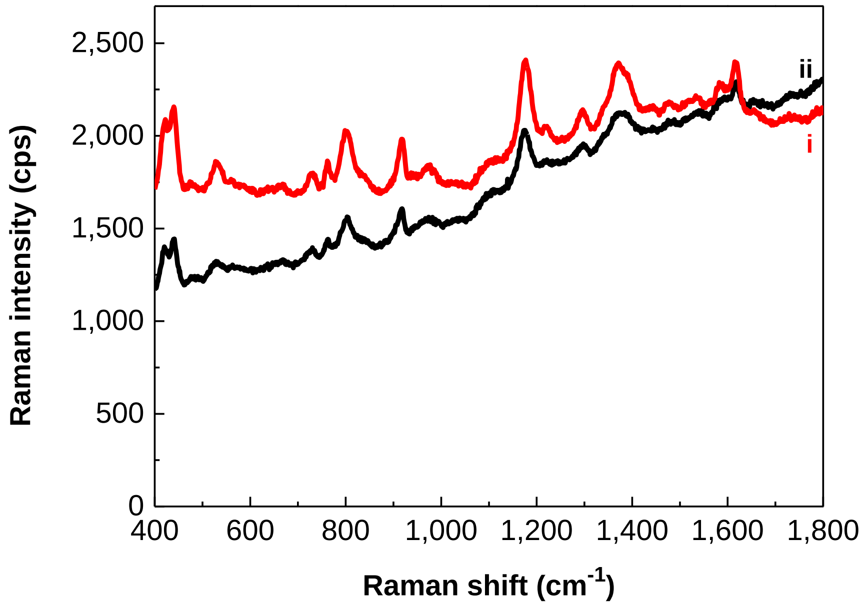

Figure 3.24 SER spectra of 1.0 x 10^{-5} M CV molecule adsorbed on Au NPs containing 41 layers of (i) PAH/TA and (ii) PAH-TA complex/TA multilayer films.

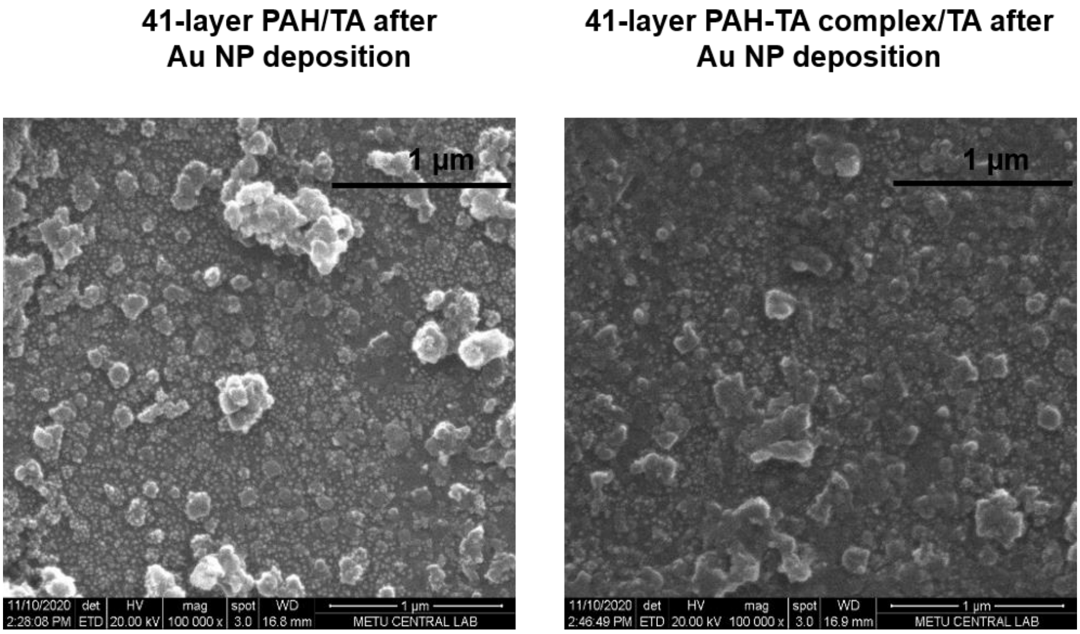

Figure 3.25 SEM images of 41-layers of PAH/TA and PAH-TA complex/TA films after Au NPs deposition.

3.4.1 Calculation of the Enhancement Factor

The enhancement factor (EF) of multilayer substrates was estimated by comparing Raman and SERS peak intensities at 1176 cm^{-1} using the formula,[42]

$$EF = \left(\frac{I_{SERS}}{I_{Raman}}\right) \Big/ \left(\frac{N_{SERS}}{N_{Raman}}\right)$$

where I_{SERS} and I_{Raman} stand for observed intensities of a vibrational mode in SERS for 10^{-5} M CV and Raman for 10^{-3} M CV. Additionally, N_{Raman} and N_{SERS} symbolize number of CV molecules adsorbed on bulk and SERS substrate excited by laser radiation, respectively.

CV molecule was assumed as a complete monolayer on Au NP surfaces and the surface area of each CV molecule (A_{cv}) is 1.2 nm^2.[180] A_{laser} is area of laser spot which has 1 µm diameter. Au NPs were spherical with a radius of ~5 nm and spaces between NPs were neglected.

$$A_{laser} = \pi\, r_{laser}{}^2 = 2.5\ x\ 10^5 \pi\ (nm^2)$$

Accordingly, the number of NPs (n_{NPs}) in the area of laser spot was calculated by,

$$n_{NPs} = \frac{A_{laser}}{A_{NP\ cross\ section}} = 10^4$$

A_{NP} corresponded to the surface area for each NP (A_{NP}) and total surface area of NPs ($A_{plasmonic}$) were calculated as follows.

$$A_{NP} = \frac{1}{2} 4\pi r_{NP}{}^2 = 200\pi\ (nm^2)$$

$$Total\ surface\ area\ (A_{plasmonic}) = n_{NPs}\ x\ A_{NP} = 2\ x\ 10^6 \pi\ (nm^2)$$

Accordingly, N_{SERS} was calculated by,

$$N_{SERS} = \frac{A_{plasmonic}}{A_{CV}} = 1.7\ x\ 10^6 \pi$$

Effective volume (V_{CV}) and moles of CV (n_{cv}) corresponding to this volume were calculated by using the following equations.

$$V_{CV} = \pi r_{laser}{}^2 h = 5\ x\ 10^8\ \pi (nm^3)$$

$$n_{CV} = \frac{V_{CV} d_{CV}}{M_{CV}} = 4.58\ x\ 10^{-15}\ mol$$

where h is penetration depth of the laser (2 μm), d_{CV} is the density of solid CV molecule (1.19 g/cm^3) and M is molecular weight of CV molecule (407.9 g/mol).

Accordingly, N_{Raman} can be expressed as

$N_{Raman} = N_A n_{CV} = 2.76\ x\ 10^9$, where N_A is Avogadro's number.

In conclusion, EF is calculated as $1.05\ x\ 10^6$ for PAH/TA multilayer system.

Similarly, EF value of PAH/PAA multilayer system was calculated as $6.5\ x\ 10^4$.

3.5 SERS Reproducibility

Finally, 41 layers of PAH/TA film was selected as a model to evaluate the SERS reproducibility of the substrates. Two approaches were used. First, fluctuation in SERS enhancement across the substrate was measured from SERS spectra of CV ($1.0x10^{-5}$ M) at five randomly selected spots on same $(PAH/TA)_{41}$ substrate at 1176 cm^{-1} peak. The percent relative standard deviation (%RSD) of SER signal at 1176 cm^{-1} peak was calculated as 12%, indicating homogenous coating on the film surface. Second, %RSD of SER signals collected from five replicate $(PAH/TA)_{41}$ films to show variation of SER signal from substrate to substrate was calculated as 18%.

3.6 Sandwich vs. Au NPs Incorporated into Multilayers as SERS Substrates

In this part of the study, Au NPs were used as building blocks together with PAH to prepare so called 'sandwich-model LbL films. The SER signal intensity of PAH/Au NPs multilayers was contrasted with that of 41 layers of PAH/TA multilayers post-loaded with Au NPs. First, the absorbance of PAH/Au NPs films at 520 nm was followed as a function of layer number with UV-vis spectroscopy. The absorbance increased as the layer number increased at the surface, indicating successful LbL growth of PAH and Au NPs. The shift of the LSPR band resulted from aggregation of AuNPs on the surface and interaction of NPs by closing to each other with increasing deposition number of NPs layers.[181] While the number of NPs dipping increased, extinction of multiple-NP resonance also increased, resulting in NP aggregate size growth. Dense packing and greater coverage of increased immobilized NPs contribute to shifts of the band to longer wavelengths.[70] Moreover, the extent of coupling interaction becomes more pronounced, leading to a higher peak intensity with the NPs layer deposition.[150]

In general, SER signals would be expected to increase with increasing number of immobilized NPs layers. This is explained by generation of more localized regions via small interparticle distances and junction formation between the neighboring NPs with increasing dipping cycles.[70,150,182] SER signal intensities of $1.0x10^{-5}$ M CV molecule on $(PAH/TA)_{41}$ and $(PAH/Au\ NPs)_{40}$ multilayers were shown in Figure 3.26 and Figure 3.27 and the post-loaded one was higher than $(PAH/Au\ NPs)_{40}$ based on these figures. Additionally, LSPR band of sandwich type multilayers shifted to longer wavelengths with increasing in layer numbers (as seen in Figure 3.28 and Figure 3.30) due to possibly larger surface coverage and tighter packing of immobilized NPs. Moreover, LSPR band of post-loaded type substrate was shown in Figure 3.29 with no significant shift of the plasmon peak ~520 nm. One possible reason of decrease in SER signal intensity through 40 layers can be explained by shifting of plasmon band of NPs aggregates to longer wavelengths (650 nm- Figure 3.28 and Figure 3.29) than excitation wavelength of the laser (632.8 nm). This situation was also consistent with previous studies in which SERS intensity became weaker with multiple deposition steps of Au and Ag colloid particles in case of exceeding excitation wavelength.[171,181] Additionally, AFM images of the sandwich multilayers are shown in Figure 3.31. Based on this figure, more accumulation of particles was observed with layer number increase. Moreover, surface roughness values increased from 6 layers (4 nm) to 30 layers (14 nm) and decreased a bit for 40 layers (11 nm) of PAH/Au NPs in Figure 3.31. Relatively larger SER signal observed for 30 layers (Figure 3.26) might be due to larger surface roughness and larger aggregates seen in the image (Figure 3.31 for 30 layers). As a result, highly rough surfaces of PAH/TA with post-loaded NPs (56 nm) contributed greater SER signals as compared to sandwich structures of PAH/Au NPs with smoother surfaces.

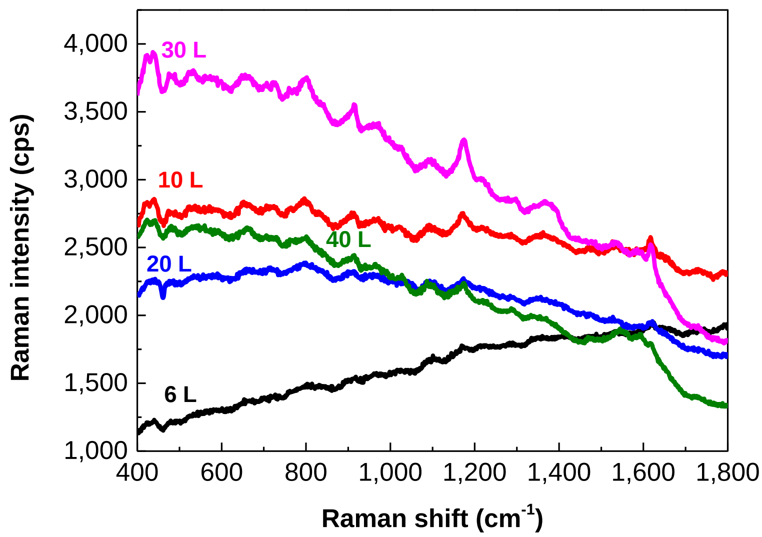

Figure 3.26 SER spectra of 1.0x10^{-5} M CV molecule from sandwich type substrate in various layer numbers.

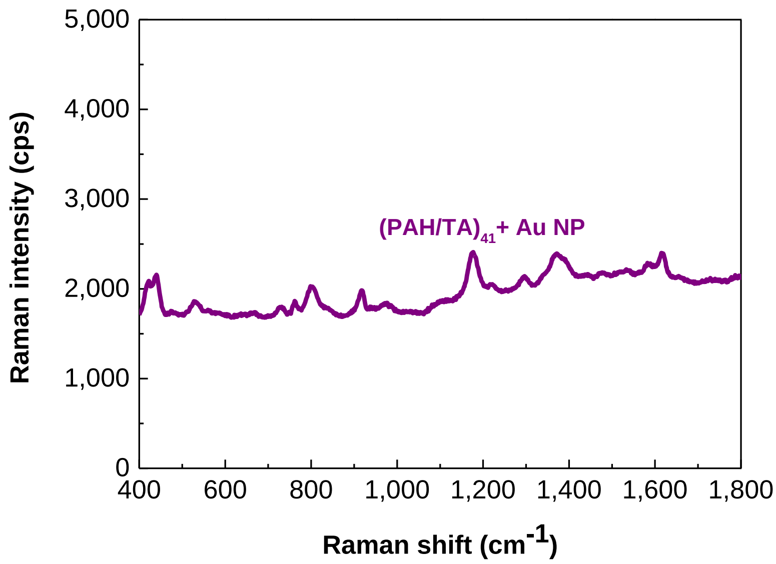

Figure 3.27 SER spectra of 1.0x10^{-5} M CV molecule from post-loaded type substrate.

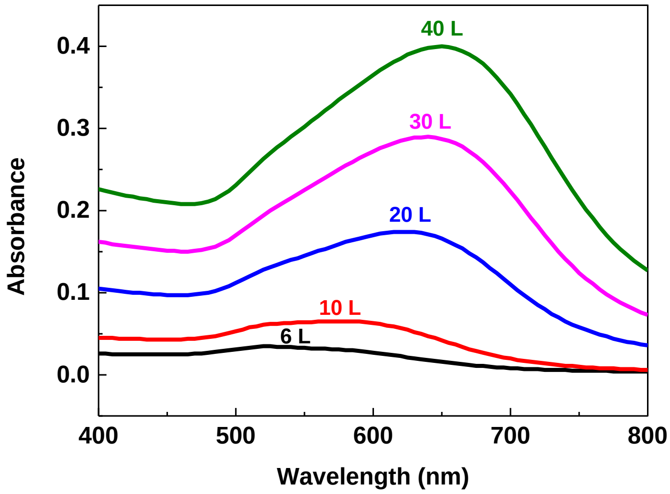

Figure 3.28 UV-vis spectra of sandwich type substrate in various layer numbers.

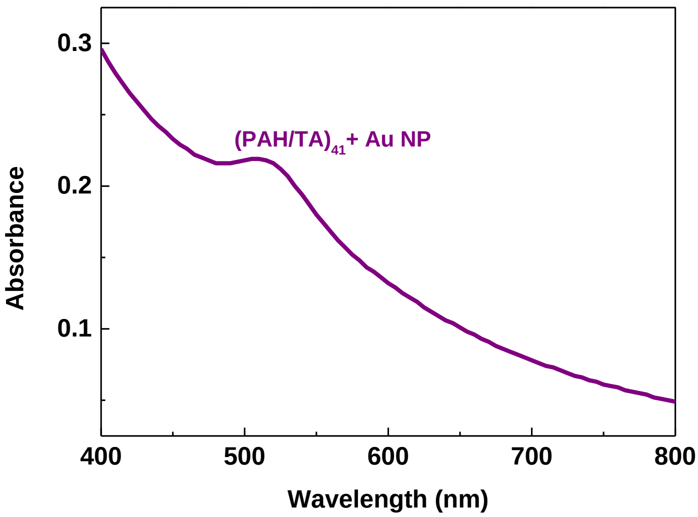

Figure 3.29 UV-vis spectrum of post-loaded type substrate.

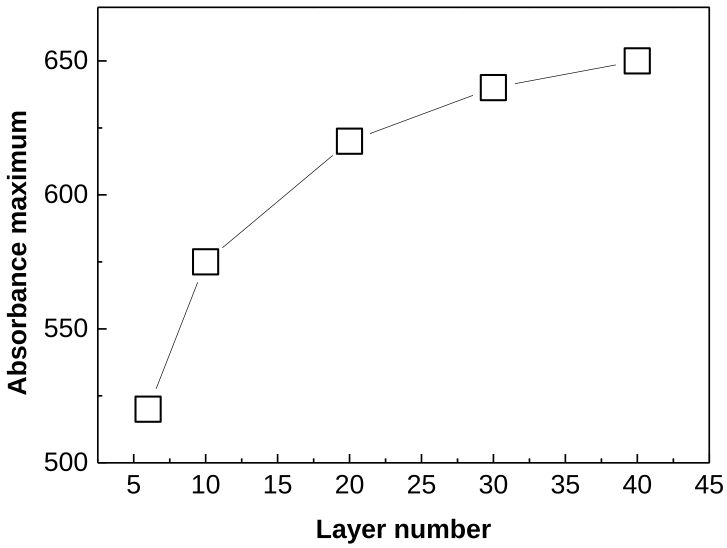

Figure 3.30 Plot of absorbance maxima values in sandwich type substrate vs. layer number.

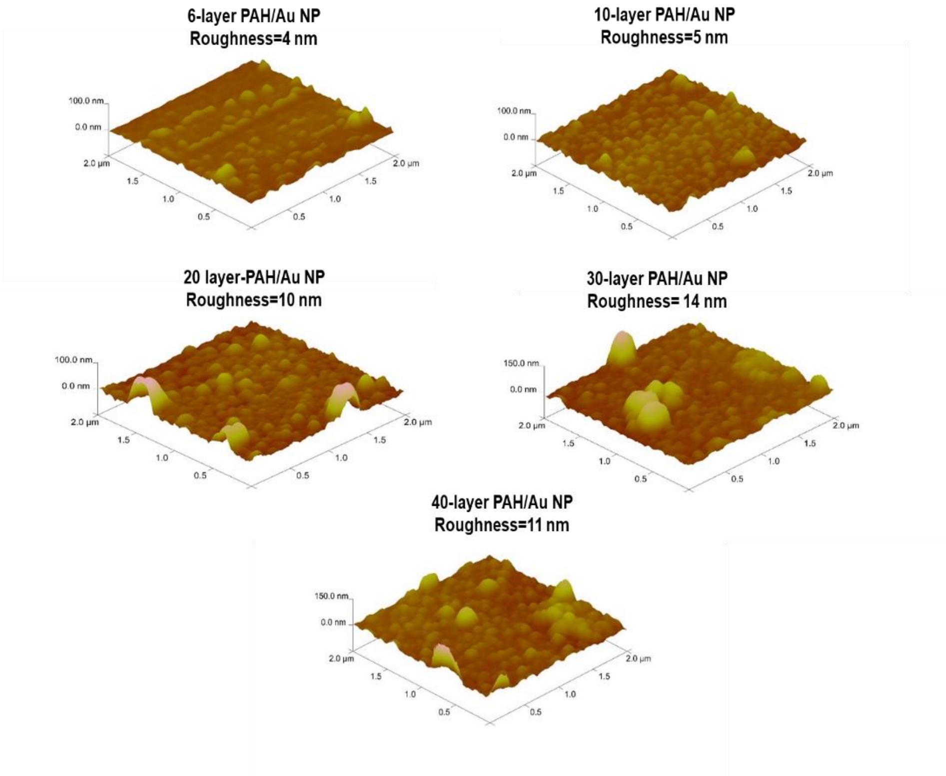

Figure 3.31 AFM height images and root mean square values of sandwich type substrates. The roughness values were recorded from 2x2 μm^2 images.

Of note, SERS substrates prepared by LbL deposition of Au NPs and PAH-PAA complexes or Au NPs and PAH-TA complexes were also examined as SERS substrates. However, none of them produced reproducible signal, which could be attributed to nonuniform accumulation of NPs within multilayers.

3.7 The Effect of Concentration of CV on the SER Signals

To evaluate the effect of concentration of CV on the SER signal intensity, 41 layers of PAH/TA multilayer film was selected as a model. Figures 3.32 and 3.33 show SER spectra of various concentrations of CV on $(PAH/TA)_{41}$ films and the change in SER signal intensity at 1176 cm^{-1} with increasing CV concentration. The SER signal decreased as the concentration of CV decreased in the range of $1.0x10^{-4}$–$1.0x10^{-6}$ M. Limit of detection was determined as $1.0x10^{-6}$ M for CV molecule by signal to noise ratio of ~4. In a recent paper, CV detection was 10^{-8} M on a conductive surface covered with monolayer Au seeds by electrodeposition method.[183] Since seed-assisted electrodeposition helps to generate three dimensional (3D) SERS substrate in the paper, larger number of hot spots can be formed as compared to two dimensional (2D) substrates like in this thesis, resulting in lower detection limits with 3D substrates. In another 3D substrate including microhemisphere array PDMS films with Au NPs, CV molecule detection as low as 10^{-12} M.[184] High density and highly ordered hot spots in this 3D substrate contributed significant SERS enhancement with reducing the detection limit of probe molecules.

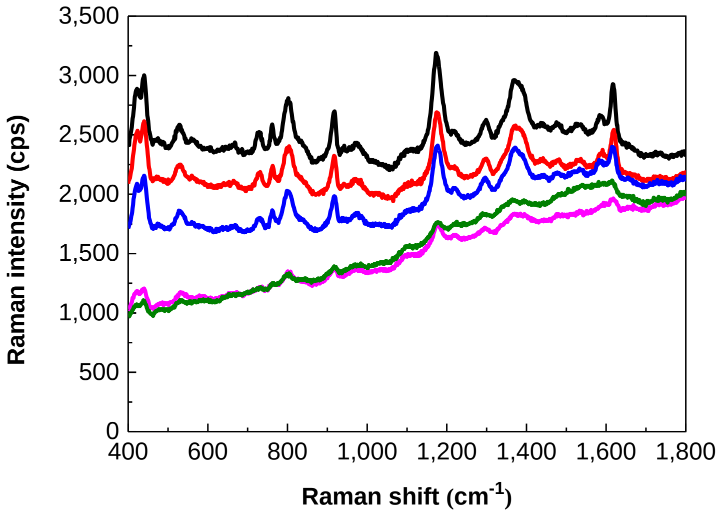

Figure 3.32 SER spectra of $1.0x10^{-4}$ (black), $5.0x10^{-5}$ (red), $1.0x10^{-5}$ (blue), $5.0x10^{-6}$ (pink) and $1.0x10^{-6}$ M (green) CV on $(PAH/TA)_{41}$ film with 12 h deposition of Au NPs.

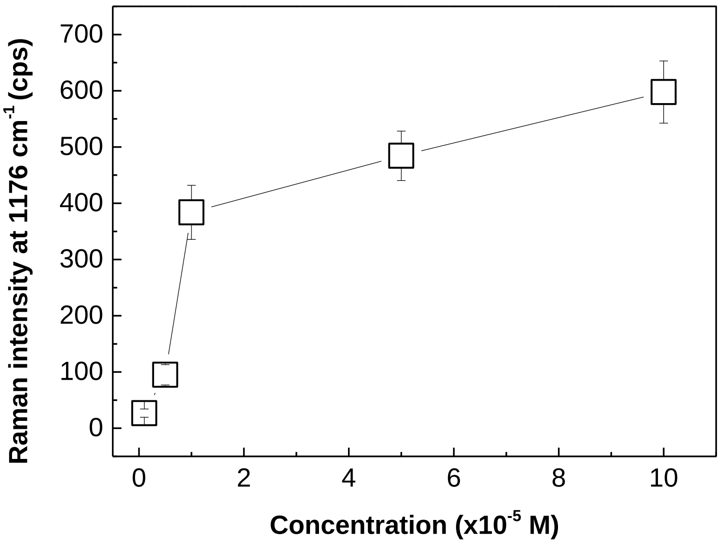

Figure 3.33 Dependence of SER signal intensity at 1176 cm^{-1} on increasing CV concentration.

CHAPTER 4

USE OF SEED-MEDIATED AU NPS IN POLYELECTROLYTE MULTILAYERS AS SERS SUBSTRATES

This part of the study aimed to prepare large-sized and seed-mediated (BPEI-capped) Au NPs in the solution media and these NPs assembled onto glass surfaces as single layer or multilayer using TA or PSS. The films containing (BPEI-capped) Au NPs were compared with respect to SERS performance using CV as a probe molecule.

The use of polyelectrolytes, especially BPEI, is common in the stabilization and modification of Au NPs formed through the reduction of Au^{3+} ions in water.[185] BPEI is promising for this due to its dendrimer-like structure, which provides high surface to volume ratio and physicochemical stability.[186] The self-assembled Au-PEI NPs have recently been used in SERS studies to show different silicon oxide materials as substrates for binding of NPs[115] and to show interparticle-distance-dependent properties of the films by varying alkyl chains on the substrates.[187] Interparticle distance, which is gap between neighboring NPs, can be controlled by self-assembly techniques. It was reported that higher SER signals and greater red-shift of SPR bands due to electromagnetic coupling between NPs were obtained with smaller interparticle distances.[187]

The exact mechanism behind the nucleation and stabilization of polymer-capped Au NPs is not clear yet. Cho and coworkers reported that BPEI with a molecular weight of 25,000 g/mol was the best choice for the preparation of these particles, and the stability and size of the Au-BPEI NPs were found to be dependent on the ratio of BPEI to Au^{3+} ions.[188] Sun and coworkers conducted a study where they mixed BPEI and $HAuCl_4$ at room temperature in different molar ratios.[189] They found that as the molar ratio of PEI to Au^{3+} ($AuCl_4^-$) increased, the particle size of the resulting Au-PEI preparations increased proportionally.

Achieving precise control over the size of particles can be challenging, as even small variations in the experimental parameters used in the NP synthesis can result in significant differences in size distribution.[190] Additionally, it can be difficult to maintain a low degree of polydispersity (narrow distribution in particle sizes) when attempting to increase the size of the particles by changing the reaction parameters such as the concentration of BPEI in the reaction medium. In this part of the thesis, BPEI–capped Au NPs were synthesized to be used in SERS applications. While Philip and coworkers used $HAuCl_4$ as a source of Au seeds and seeded growth solution, $NaAuCl_4$ was used in this study.[115] Moreover, volumes of BPEI (75 μL) and seed (100 μL) in the growth solution for SERS study were changed to 100 and 1000 μL, respectively in order to get relatively big NPs (~50-60 nm) in solution. Centrifuge conditions in the paper (5,300 rpm for 10 min) were also changed (2,000 rpm for 60 min to provide complete separation of NPs) due to usage different volumes of BPEI and seed in this study. In the paper, NPs were dispersed in ethanol after centrifugation before attachment of NPs as a 1-layer to photonic crystal, glass plate and halloysite nanotubes for SERS analysis of 4-aminothiophenol (4-ATP) molecule. On the other hand, NPs were dispersed in deionized water in this study to prevent collapse of polyelectrolyte containing films with ethanol treatment. Then, the NPs were assembled directly on either bare glass substrate or LbL-coated substrate for investigation of SERS enhancement of CV molecule.

4.1 Optimization Studies for Seed-Mediated Au NPs

4.1.1 The Effect of BPEI Volume on NP Formation

When Au NPs are synthesized, adding a long chain polymer can help to keep the particles stable by creating strong repulsion forces that prevent them from aggregation.[191] Moreover, the polymer can also provide a surface modification. By this way, BPEI can stabilize Au NPs by capping them through its amino groups and imparting positive charge by again the amino groups to NPs. During seed formation,

$NaBH_4$ reduced the gold ions, which was indicated by a color change from yellow to wine-red. Seeds produced by this method showed surface plasmon resonance (SPR) band at 518 nm in the absorption spectrum (Figure 4.1). The number average particle size of seeds measured using DLS technique was 6.0±1.4 nm (Figure 4.2) and the zeta potential value of these Au NP seeds was measured as 22.3±0.3 mV (Figure 4.3). These results were in good agreement with the findings reported by Philip and coworkers.[115]

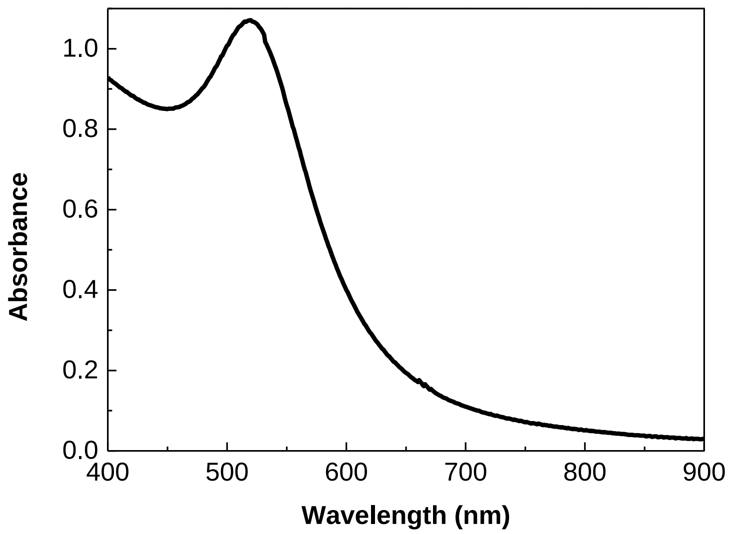

Figure 4.1 UV-vis absorption spectrum of Au NP seed.

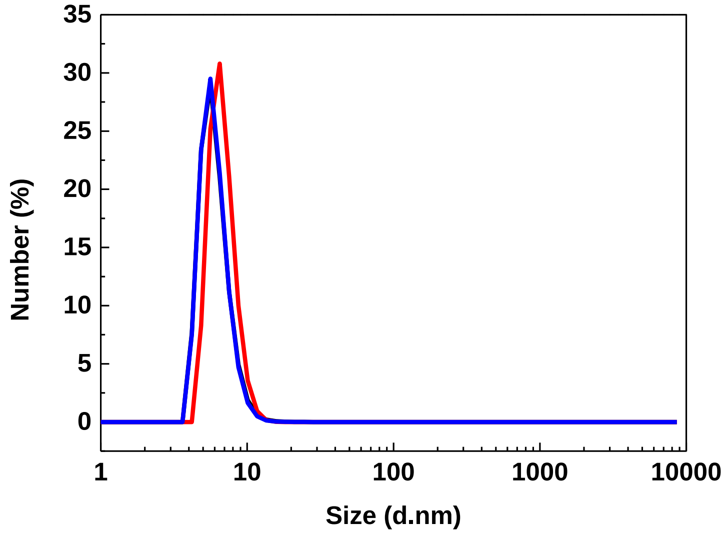

Figure 4.2 Hydrodynamic size distribution by number of seed NPs by Dynamic Light Scattering. Each color shows the replicate measurements of these NPs.

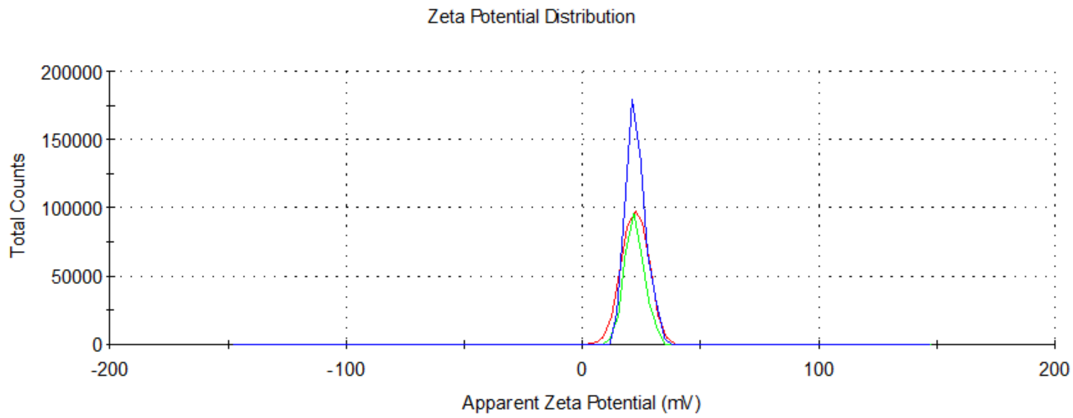

Figure 4.3 Zeta potential distributions of seed NPs. Each color shows the replicate measurements of these NPs.

In the seed growth step, the concentrations of both BPEI and seed solutions affect the size of Au NPs. A red shift in SPR along with a peak broadening was observed with decreasing volumes of BPEI solutions from 500 µL to 100 µL and 50 µL when the volume of seeds in the growth solution were held constant at 1000 µL (Figure 4.4). Red shift in the wavelength of the SPR and the broad shape of the peak indicated that larger NPs were obtained with the decrease in volume of BPEI and they have become more varied in size.[157,192] Variation in size depends on full width at half maximum (FWHM), which is the width of absorbance distribution at half maximum absorbance value. Since FWHM of SPR band of NPs broadened from 500 µL to 50 µL, size of NPs was varied. Ascorbic acid used in the growth step functions as a mild reducing agent, while Au seeds account for the nucleation centers.[193] With a lower BPEI amount, there was more chances for agglomeration and aggregation of the NPs, which resulted polydispersed Au NPs and a red shift in LSPR.[115] BPEI possibly plays a role in regulating the size of Au NPs by covering the surfaces of the growing NPs and preventing further growth. As a result, it allows for the formation of Au NPs that are spherical and uniform in shape.[115] When large number of seeds are added, it results in more nucleation sites for new particles to form, which leads to the formation of smaller Au NPs.[194]

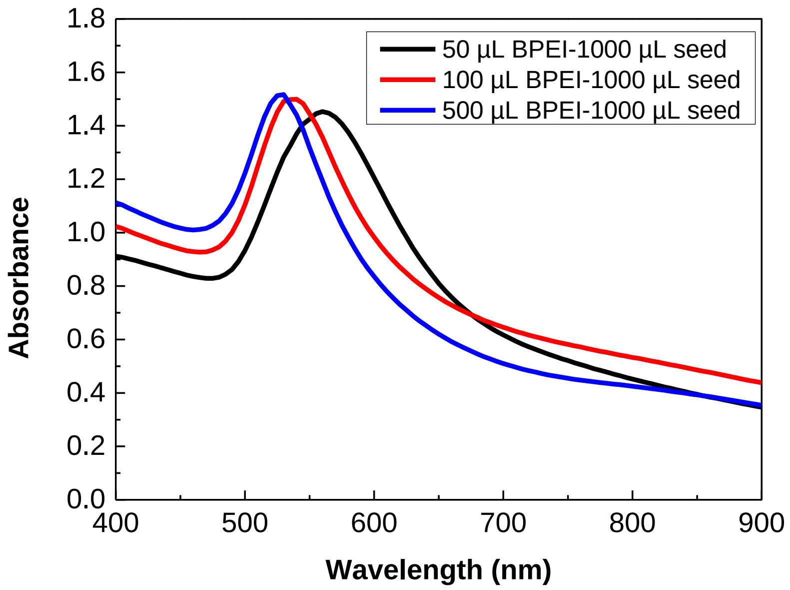

Figure 4.4 UV-vis absorption spectra of Au NP solutions synthesized using 50, 100 and 500 µL of BPEI and 1000 µL of seed.

In the light of these information about BPEI and seed amounts, 100 μL as an intermediate volume of the trials was selected as the BPEI volume at constant seed volume (1000 μL) to prevent agglomeration and to provide large-sized particles as understood from red-shifting and broadening of the spectrum (Figure 4.4) as compared to UV-vis absorption spectrum of seed in Figure 4.1. While size variation was more for 50 μL BPEI, blue-shift and narrower SPR band in 500 μL suggested smaller size of NPs as compared to 100 μL of BPEI. SPR maximum of the NPs corresponded to approximately 535 nm with average particle size of 60 ± 8 nm. (Figure 4.5). Additionally, intensity and volume size distribution curves of these particles were also shown in Appendix A, showing consistency with each other in terms of sizes. Moreover, the zeta potential of the NPs was measured as 7.9±0.5 mV (Figure 4.6). The zeta potential is one of the multiple indicators for physical stability of the NPs. Although BPEI has been known to provide stabilization of NPs, this low zeta potential value indicated colloidal unstability of NPs possibly related with concentration of BPEI. If the concentration of polyelectrolyte used to coat particles is too low, the particles may not be completely covered by BPEI which functions as stabilization agent for Au NPs.[195] On the other hand, if the concentration is too high, the polyelectrolyte molecules may absorb onto multiple particles at the same time, causing them to aggregate.[196] Unsaturated layers of polyelectrolytes on NPs leads to low and unstable zeta potentials. This means that attractive van der Waals forces become stronger than repulsive electrostatic forces.[195] As a result, the NPs get closer to each other due to charge neutralization and this leads to an unstable suspension and aggregation of the particles.[197] In the light of these findings, large-sized synthesis of NPs was achieved, but physical stability of NPs was not provided in these experimental conditions. After centrifugation, NPs were clearly separated from the growth solution and redispersed easily in deionized water. However, a precipitate formation occurred after waiting one day.

When UV-vis absorption spectrum of Au NP seed (Figure 4.1) and BPEI-capped (seed-mediated) Au NP solutions (Figure 4.4) were compared to each other, NP size increase can be clearly seen from red shifting of the spectrum from 518 nm to 535 nm. In addition, significant broadening of the spectrum of BPEI-capped NPs indicated larger size distribution. Since spectral intensity was related with the number of NPs, the number of seed NPs was greater than that of BPEI-capped NPs. Significant background increase of the BPEI-capped NPs might be due to higher scattering of light by larger-sized NPs.

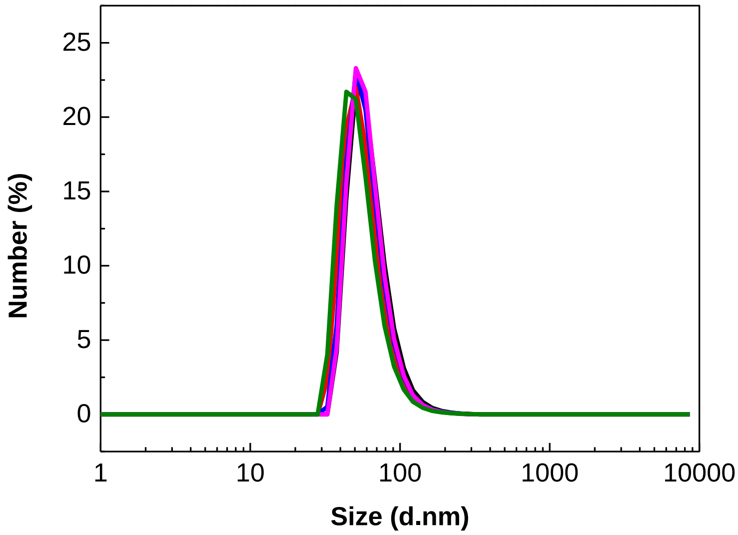

Figure 4.5 Hydrodynamic size distributions by number of BPEI-capped NP solutions by Dynamic Light Scattering. Each color shows the replicate measurements of these NPs.

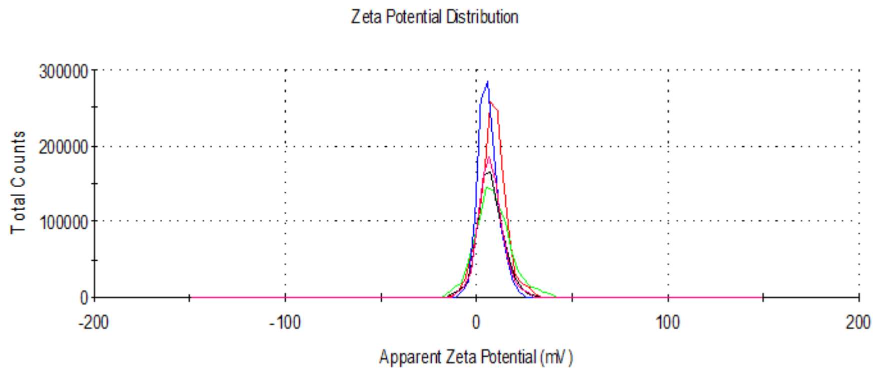

Figure 4.6 Zeta potential distribution of BPEI-capped NP solutions. Each color shows the replicate measurements of these NPs.

4.1.2 The Effect of pH of NPs on Size Distribution

Dissociation of functional groups on the surface of self-assembled monolayers and the binding of NPs to the substrates are affected by pH of NPs solution which eventually affects the immobilization of NPs on the surface.[198] pH studies on this part were performed in the solution, not on the surface. Since synthesized NP solution was at the pH of ~3.0 as a starting point, we investigated growth solution pH with increasing increments at 3.0, 5.0 and 7.5. Size distribution of the NPs prepared at pH 3.0, pH 5.0 and pH 7.5 is shown in Figure 4.7. Increasing pH of NPs solution to 7.5 resulted in agglomeration accompanied by instability and fluctuation of the NP size. Figure 4.8 shows absorption spectra of NP solutions at pH 3.0, 5.0 and 7.5. Moreover, their number size distribution graphs can also be observed in Appendix B, showing higher fluctuation at pH 7.5 as compared to pH 3.0 and 5.0. Although SPR maxima were same at all pH values, larger size distribution and lower amounts of NPs as evidenced by lower spectral intensities were obtained at pH 7.5 (Figure 4.8). When the metal NPs are very large, the Au colloids offer only a small number of nucleation sites[199] and they tend to aggregate. The original absorption peak will typically broaden or form a secondary peak at longer wavelengths, ~720 nm as shown in Figure 4.8 when the particles destabilize. This resulted in decrease in peak signal intensity due to the depletion of stable NPs. Therefore, spectral intensity at pH 7.5 was smaller than the intensities at pH 3.0 and 5.0. Moreover, large-sized NPs at pH 5.0 led to larger background in their absorption spectra as compared to NPs at pH 3.0, but their absorption signals are comparable to each other as seen in Figure 4.8.

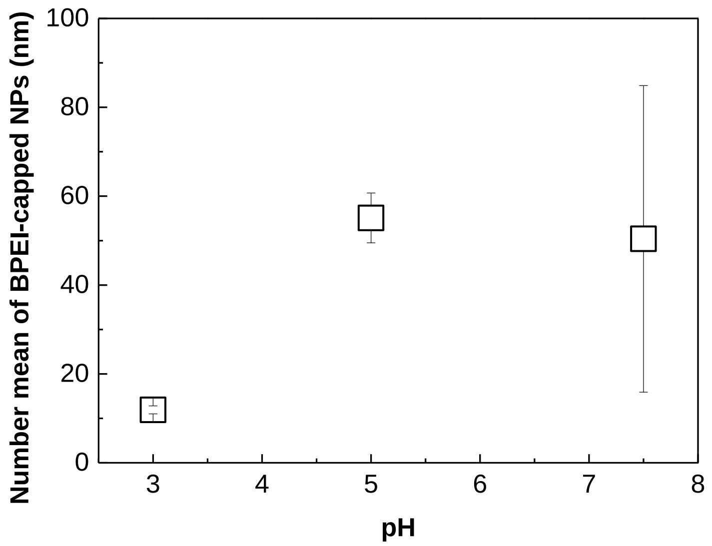

Figure 4.7 Number average hydrodynamic size of BPEI-capped NPs as a function of pH of NPs solution. Each color shows the replicate measurements of these NPs.

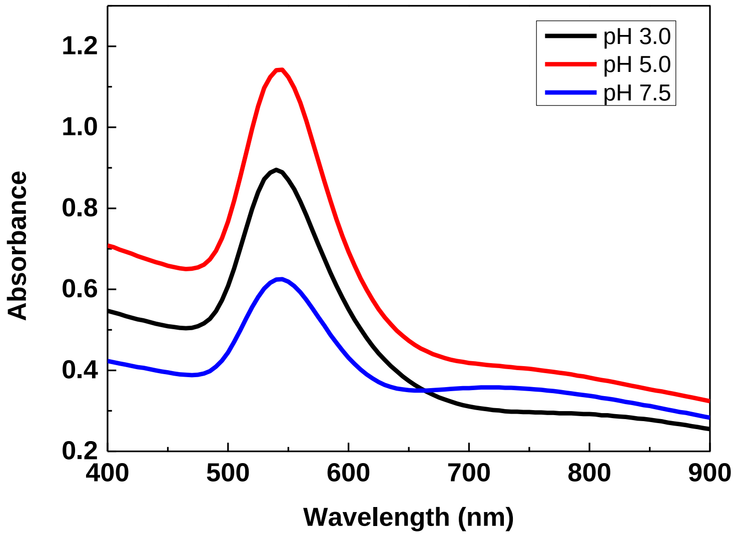

Figure 4.8 UV-vis absorption spectra of BPEI-capped NPs at pH 3.0, 5.0 and 7.5.

4.2 SERS Performance of 1-Layer Self-Assembled Substrates

SER signal of CV molecule on BPEI-capped Au NP-coated substrates were measured in this section. First, the glass slides were immersed into Au NP solution synthesized using 100 μL BPEI and 1000 μL seed solution to deposit 1-layer film.[115] Since the surface charge of the glass is negative, electrostatic attraction occurs between negatively charged silicon dioxide groups and positively charged BPEI-capped Au NPs. Although NPs were stabilized by BPEI, nonuniform distribution of NPs on the substrates was observed on the surface with increasing deposition time of NPs as shown in Figure 4.9.

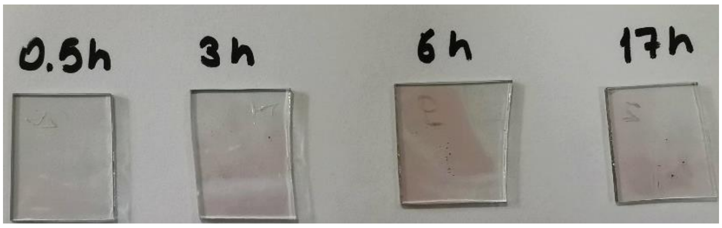

Figure 4.9 Photographic demonstration of 1-layer of BPEI-capped Au NPs at 30 min, 3 h, 6 h and 17 h deposition times.

UV-vis absorption spectra of these 1-layer films prepared at varying deposition times (Figure 4.10) suggested that weak S/N ratio was obtained from all substrates. This could be attributed to attachment of low number of NPs in negatively charged glass slides. After 0.5 h of deposition, SPR maxima could be hardly observed around 530-535 nm. Immersion time of glass substrate in BPEI- capped Au NPs resulted in increased up to 17 h but the SPR signals was not drastic compared to very long exposure times as seen in Figure 4.10. The SER signals of CV molecule recorded for BPEI-capped Au NPs coated substrates prepared at different deposition times and relative intensity signal at 1176 cm^{-1} are given in Figures 4.11 and Figure 4.12, respectively. Nonhomogeneous coating of Au NPs resulted in irreproducible SER signals with %RSD values around 50% from the same substrate. In spite of very low absorbance values measured from these substrates, relatively large SER signals were measured. As the NP size increases, its surface area become larger and local electromagnetic field enhancement around NPs increases. This leads to an increase in the quantity of the probe molecules that can be adsorbed onto the surface. Consequently, SER intensity rises.[32]

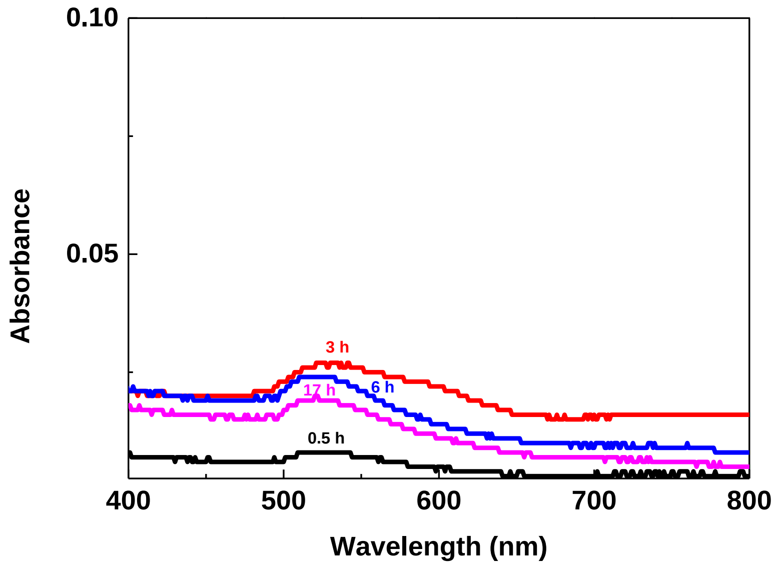

Figure 4.10 UV-vis absorption spectra of 1-layer-coated substrates with 30 min, 3 h, 6 h and 17 h deposition times in BPEI-capped NP solution.

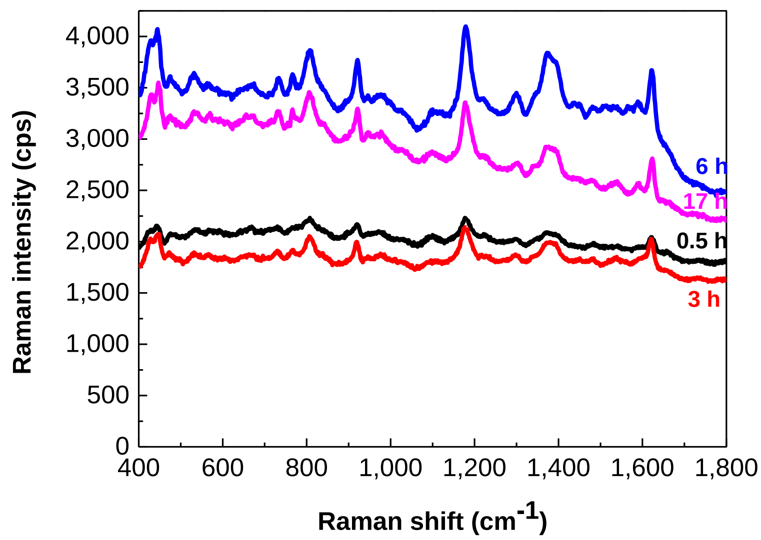

Figure 4.11 SER spectra of $1.0x10^{-5}$ M CV molecule adsorbed on 1-layer coated substrates with 30 min, 3 h, 6 h and 17 h deposition times in BPEI-capped Au NPs.

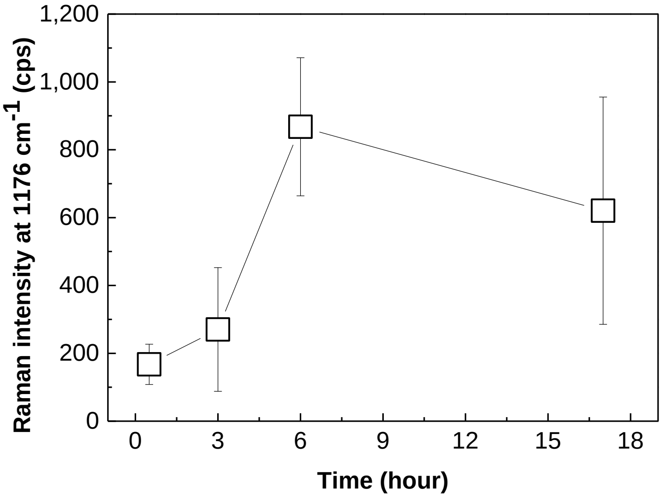

Figure 4.12 Relative intensity plot at 1176 cm^{-1} of 1.0 x 10^{-5} M CV molecule adsorbed on 1-layer coated, BPEI-capped Au NPs as a function of deposition times.

4.3 SERS Performance of LbL Self-Assembled Substrates

Since aggregation and irreproducibility problems with 1-layer BPEI-capped Au NPs coated SERS substrates, preparation of multilayers of BPEI-capped Au NPs was examined. As mentioned in introduction part (Section 1.3.1), LbL method enables control of the properties of a film on surfaces by incorporation and immobilization of NPs on the solid substrates. Homogenous coating of the LbL films with NPs is also critical in terms of obtaining reproducible SERS substrate. For this purpose, positively charged BPEI-capped Au NPs were alternatingly deposited with negatively charged TA at pH 5.0. Since TA was known to provide roughness increase from the previous chapter, it was expected to contribute for not only increase of SER signals but also reproducibility of the signals with inclusion into LbL films. Prior to multilayer deposition of BPEI-capped Au NPs, LbL growth of BPEI and TA were followed at pH 5.0 using ellipsometry as shown in Figure 4.13. For ellipsometry measurements, Au NPs were not included in film preparation step. Thickness of colored NPs on thin films could not be tracked using ellipsometry due to absorption of light by NPs. Light beam travelling through the layer has to return back to the surface for accurate thickness measurement. As a result, it is difficult to accurately measure layer thickness of the films with NPs using ellipsometry. From ellipsometry measurements, LbL deposition of BPEI and TA provided linearly grown multilayers with ~2 nm increase per layer. The driving force for multilayer growth was hydrogen bonding association among amino groups of BPEI and phenolic hydroxyl groups of TA multilayers.

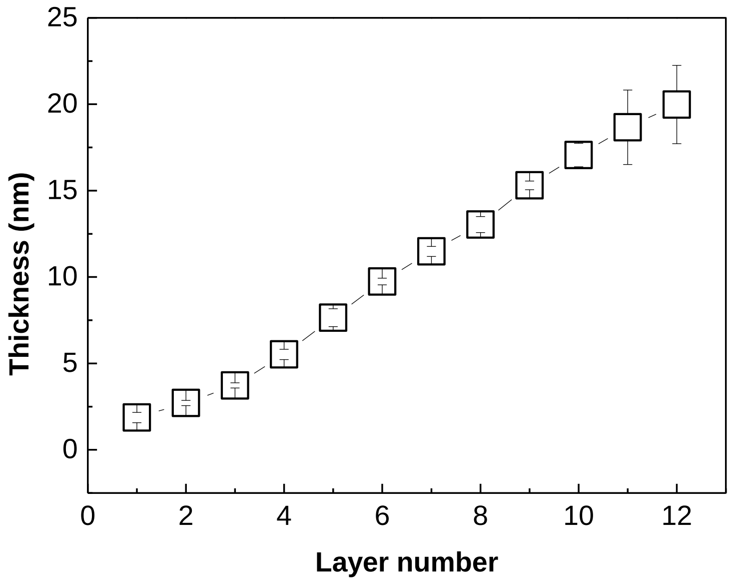

Figure 4.13 LbL growth of BPEI/TA. BPEI and TA were deposited at pH 5.0. Multilayers were grown onto a precursor film of 0.5 mg/mL BPEI for 30 min with a thickness of ~1.9 nm. Thickness values do not include the precursor layer thickness.

UV-vis absorption spectra of multilayers of BPEI-capped NPs and TA with increasing layer number are given in Figure 4.14. The absorbance at 535 nm associated with Au NPs became visible as the layer number increase. At pH 5.0, both TA (~96%) and BPEI (~100%) were almost in protonated form. Therefore, phenolic hydroxyl groups of TA interacted with amino groups of BPEI-capped Au NPs via hydrogen bonding instead of electrostatic attraction at pH 5.0. Additionally, the interaction and attachment of NPs through TA molecules might be weak so that absorbance values in LbL structures were very low. The increasing background with increasing layer number was possibly due to enhanced scattering of light from the coated surfaces. The SER spectra of 1.0×10^{-5} M CV molecule on these substrates and relative intensity plot at 1176 cm^{-1} with respect to layer number are plotted in Figure 4.15 and Figure 4.16, respectively. SER signal was observed to decrease with increasing layer number. The expectation was to obtain enhanced SER signals with increasing number of BPEI-capped Au NPs layers due to more localized areas with small interparticle distances and the junctions between neighboring NP layers.[70,150,182] The decrease in signal after 7 layers, as shown in Figure 4.16, can be explained by the interaction of LbL composition and CV molecule. The laser used for excitation needs to reach the Au NPs present on the glass slide, and interact with CV molecules adsorbed at the Au NPs. There needs to be a balance between the thickness of the NP layers and the arrangement of the nanostructures to create the necessary enhanced fields for SERS.[200] The increase in SER intensity from 1 to 3-layer depositions could be attributed to increasing number of enhanced field accessible to the adsorbed CV molecules. However, after 7-layer deposition, the NP layer might be thicker, which might reduce the efficiency of both excitation and scattering of light from the film, leading to a decrease in SER signal. LbL assembly enables to develop more reproducible SER signals from the film surfaces (Figures 4.15 and 4.16) as compared to 1-layer coated films (Figures 4.11 and 4.12). Moreover, multilayers using BPEI-capped Au NPs and TA increased SERS signal approximately 3 times as compared to 1-layer NP including films.

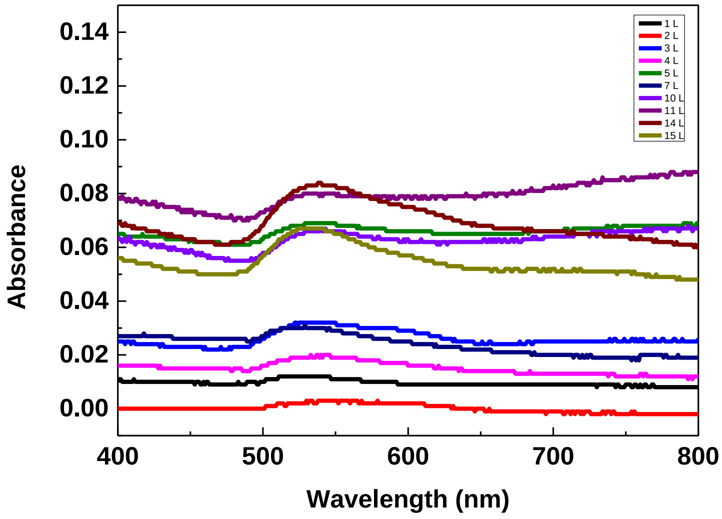

Figure 4.14 UV-vis spectra of 1-, 2-, 3-, 4-, 5-, 7-, 10-,11-, 14-, 15-layers of BPEI-Au NPs/TA.

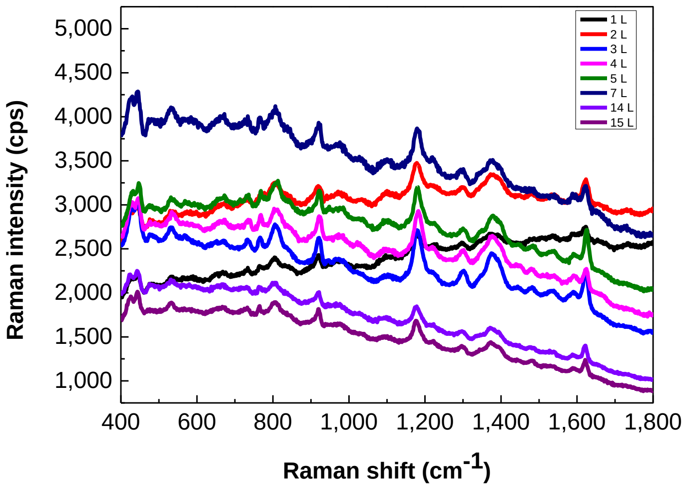

Figure 4.15 SER spectra of 1.0×10^{-5} M CV molecule adsorbed on 1-, 2-, 3-, 4-, 5-, 7-, 10-,11-, 14-, 15-layers of BPEI-Au NPs and TA.

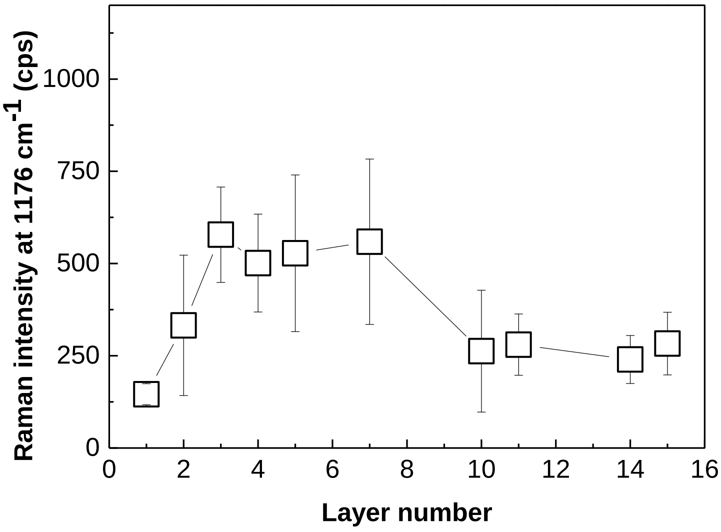

Figure 4.16 Relative intensity plot at 1176 cm^{-1} of 1.0 x 10^{-5} M CV molecule adsorbed on BPEI-Au NPs/TA multilayers as a function of layer number.

BPEI-capped Au NPs was also LbL-deposited using PSS, a strong polyanion which is fully ionized within a wide pH range. Similarly, LbL growth of BPEI and PSS was first assured at pH 5.0. BPEI and PSS showed linear growth of multilayers through electrostatic interactions between protonated amine groups of BPEI and sulfonate groups of PSS as shown in Figure 4.17.

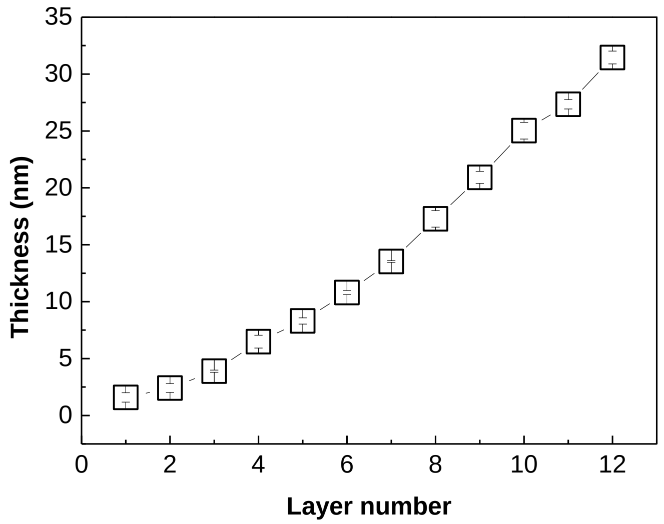

Figure 4.17 LbL growth of BPEI/PSS. BPEI and PSS (in 0.1 M NaCl) were deposited at pH 5.0. Multilayers were grown onto a precursor film with a thickness of ~1.6 nm. Thickness values do not include the precursor layer thickness.

Positively charged BPEI-capped Au NPs were deposited alternatingly with negatively charged PSS at pH 5.0. UV-vis absorption spectra of multilayers at varying layer numbers were given in Figure 4.18. The absorbance at 530 nm associated with Au NPs did not differ significantly from 3 to 9 layers. The SER spectra of $1.0x10^{-5}$ M CV molecule recorded for LbL-coated substrates prepared at different multilayer numbers and relative intensity signal at 1176 cm^{-1} against layer number were plotted in Figures 4.19 and 4.20. SER signal increased up to 10 layers and then decreased till 15 layers. Largest signal could be obtained from 9-layers of films within reasonable reproducibility from the surface (~20% RSD). The possible reasons of SER signal increase until 9 depositions and decrease after 10 layers from these surfaces discussed above (BPEI-Au NPs/TA part) were also valid for this multilayer system. Higher S/N ratio from SER signals were recorded in this multilayer system as compared to BPEI-Au NPs/TA. This might be due to the presence of NaCl in PSS layers, resulting in larger aggregation of NPs on the surface. Increasing the salt concentration in PE solution leads to a larger Debye length, which quantifies the overall electrostatic effect of a charged particle within a solution. This extended length diminishes the repellent electrostatic interactions, resulting in a dominance of Van der Waals forces. Consequently, this promotes the aggregation of NPs.[201] As a result of that, SER signals were enhanced compared to BPEI-Au NPs/TA multilayers.

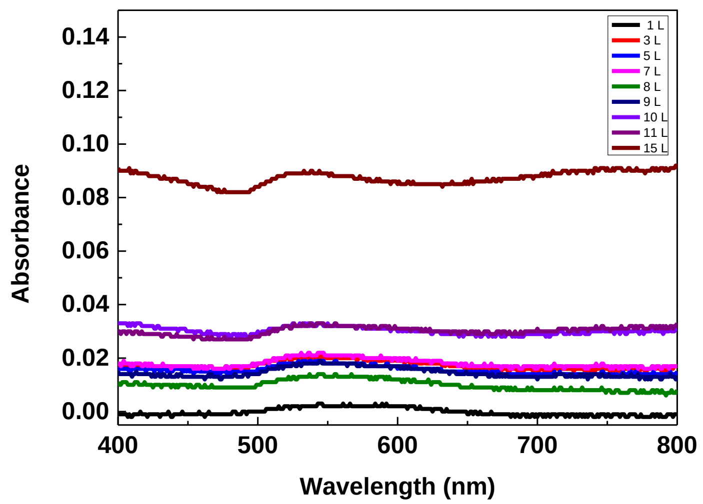

Figure 4.18 UV-vis spectra of 1-, 3-, 5-, 7-, 8-, 9-, 10-,11-, 15-layers of BPEI-Au NPs/PSS.

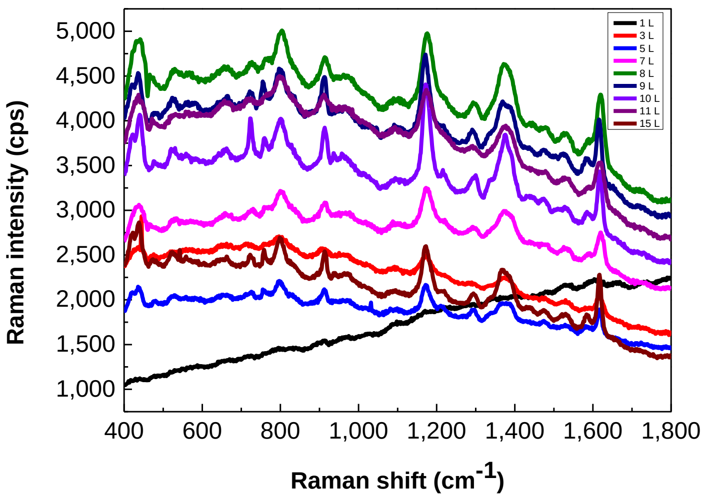

Figure 4.19 SER spectra of 1.0x10^{-5} M CV molecule adsorbed on 1-, 3-, 5-, 7-, 8-, 9-, 10-,11-, 15-layers of BPEI-Au NPs/PSS.

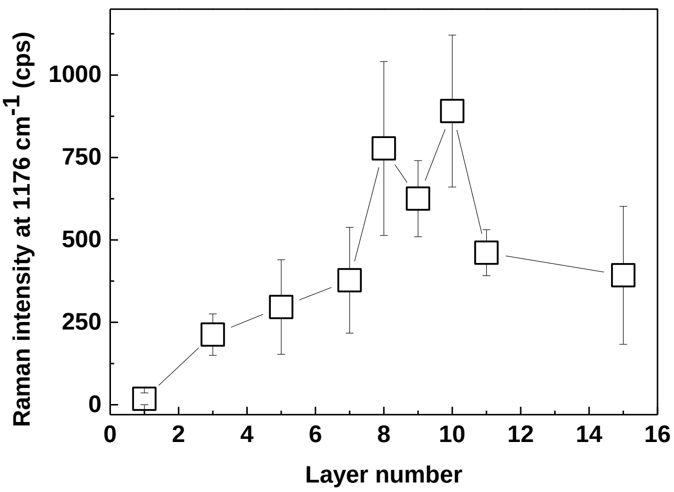

Figure 4.20 Relative intensity plot at 1176 cm^{-1} of 1.0 x 10^{-5} M CV molecule adsorbed on BPEI-Au NPs/PSS multilayers as a function of layer number.

LbL substrates consisting of seed particles (pH 5.0) having better stability due to carrying more negative charge than BPEI-capped NPs (as seen in Figure 4.1) and polyanions (TA and PSS) were also investigated as SERS substrates. 3-layers of seed/TA and 9-layers of seed/PSS were prepared to investigate the seed Au NPs and BPEI-capped Au NPs. UV-vis absorption spectra of these substrates are illustrated in Figures 4.21 and 4.22. There was not recorded any SERS enhancement for both seed including substrates.

The particle size of seeds (~5 nm) was too small compared to BPEI-capped Au NP (~60 nm). As mentioned in the introduction part (Section 1.2), NPs smaller than 5 nm do not show Raman signal enhancement.[4,14,27] That is, small-sized NPs quantum effects become noticeable and surface-related electronic scattering becomes prominent. This causes a decrease in electrical conductivity. Consequently, the quality of plasmon resonance and SERS enhancement decrease.[27]

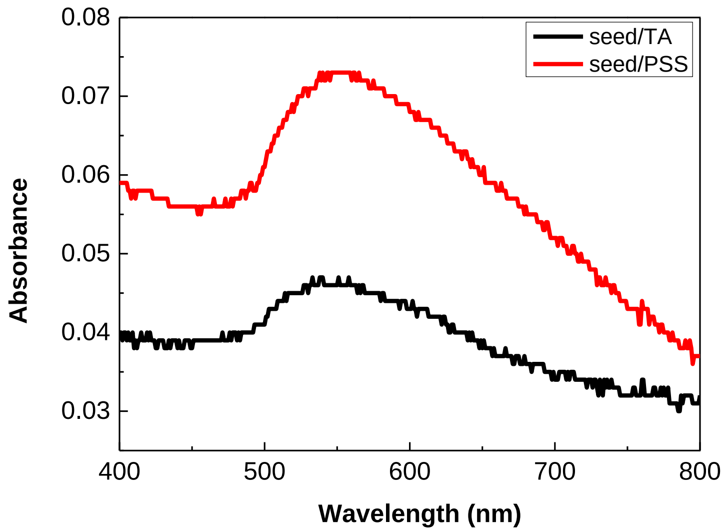

Figure 4.21 UV-vis spectra of 9 layers of seed NPs/PSS and 3 layers of seed NPs/TA.

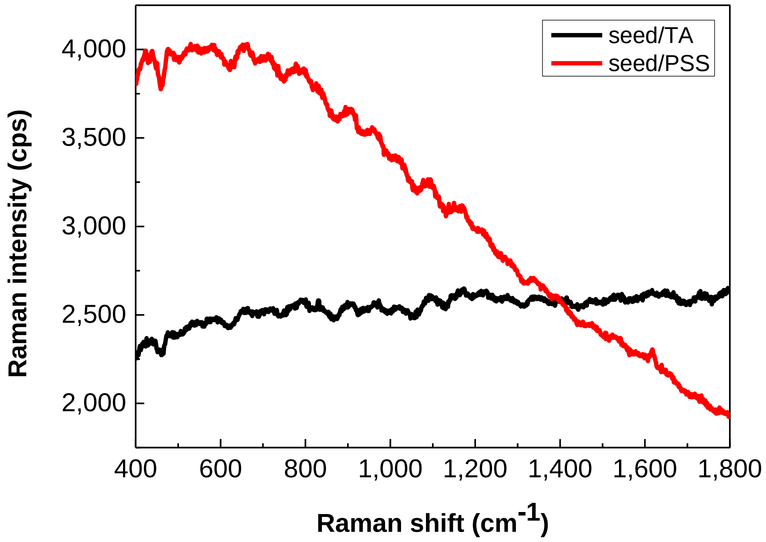

Figure 4.22 SER spectra of $1.0 x 10^{-5}$ M CV molecule adsorbed on 9 layers of seed NPs/PSS and 3 layers of seed NPs/TA.

CHAPTER 5

USE OF PHOTOCHEMICALLY SYNTHESIZED NPS IN POLYELECTROLYE MULTILAYERS AS SERS SUBSTRATES

The aim of this part was to investigate the potential of LbL assembled polyelectrolyte multilayer films as a platform to immobilize Ag and/or Au NPs. These films were prepared by consecutive adsorption of polyelectrolytes from aqueous solutions, and they include functional groups such as phenolic hydroxyls and amines that can bind to either Ag^+ or $AuCl_4^-$ through ion exchange with acid protons or create Ag^+-amine as well as $AuCl_4^-$ -amine coordination complexes.[160] The Ag^+ or $AuCl_4^-$ including films can then be reduced photochemically to produce Ag or Au NPs that are dispersed within PEM films. Direct photoreduction of a metal source (metal salt or complex) or photochemically produced intermediates, such as excited molecules and radicals which are enrolled in reduction of metal ions results in the formation of zerovalent metal which is M°.[121] The excited molecules are generated as a result of electron transfer from the solvent molecule to Ag^+ or absorption of a photon by $HAuCl_4$ molecule.[122,125] The mechanisms of Au and Ag NPs formation and the corresponding reactions are explained in the Introduction part (Section 1.4.2). For NP formations and incorporations of multilayers, Ag^+ ions bind to the functional sites (such as carboxylic acid, phenolic hydroxyl or amine groups) within the film at low salt concentrations. At sufficiently high concentration of $AgNO_3$ solution, the polymer segments might have been separated, providing more sites for binding of Ag^+ ions. The following relationship between polymers and $AgNO_3$ could be expressed as follows.[160]

Pol^-Pol^+(multilayer) + Ag^+(aq) + NO_3^-(aq) $\leftrightarrow$ Pol^-Ag^+ (multilayer) + $Pol^+NO_3^-$ (multilayer)

In this part, various PEs such as PAH, BPEI, PAA, and TA were used as the building blocks for the multilayer film formation. The effects of Ag^+ or $AuCl_4^-$ concentration,

Ag^+ or $AuCl_4^-$ absorption time and the number of PE layers on the amount, size and aggregation of NPs were followed using UV-vis absorption spectroscopy. Moreover, the enhancement of Raman signal of CV molecule on these multilayer substrates was followed using Raman Spectrometer. The formation of NPs was monitored using UV-vis absorption spectroscopy, and their presence was confirmed by the characteristic SPR absorbance of metal NPs. The SPR, which results from the collective oscillations of the conduction electrons of metals, is influenced by factors such as particle shape, size, and aggregation of NPs.[28] In PAH/TA multilayer thin films, the polyanion TA presents phenolate groups at the working pH (7.0) where these groups are responsible for the electrostatic attraction with the protonated amine groups of the PAH, forming ion pairs to build sequentially adsorbed multilayers in the LbL assembly. Then, *in situ* photochemical reduction of the loaded Ag^+ in multilayers to Ag NPs by photochemical reduction.

5.1 The Effect of Concentration of $AgNO_3$ Solution on the Amount of Ag^+ Loading into Multilayers

The aim of the following experiments was to study the effect of Ag^+ concentration on the formation of NPs within PAH/TA multilayer films. $AgNO_3$ solutions were prepared at concentrations ranging from 0.10 M to 0.75 M. Twenty layers of PAH/TA films were immersed into $AgNO_3$ solution at varying concentrations. The substrates were rinsed, dried and then exposed to light from Xe lamp. UV-vis absorption spectra of Ag NPs formed within PAH/TA multilayers are shown in Figure 5.1. SPR band of Ag NPs was observed at all concentrations of $AgNO_3$ solution. The absorbance of the peak at 435 nm (λ_{max}) was increased with the increase in the concentration of Ag^+. The increase in the width of the plasmon peak at especially 0.10 M and 0.25 M concentrations suggests a wider NP size distribution. Increasing concentration of silver ions might have resulted in loading greater amounts of Ag^+ from the solution and resulted in an increase in the absorbance value at λ_{max}. To strengthen this argument, the amount of Ag^+ loaded within the multilayers was indirectly quantified through Inductively-coupled Plasma-Mass Spectrometry (ICP-MS). Multilayers were immersed into $AgNO_3$ solution at various concentrations for 6 h. Then, the films were removed from the solution and the concentration of Ag remaining in the solution was determined using ICP-MS. The difference in the concentration of Ag^+ ions in the solution before and after loading was attributed to the amount of Ag^+ ions loaded into the multilayers. It was found that the amount of Ag^+ ions loaded within the multilayers increased as the concentration of $AgNO_3$ solution was increased up to 0.75 M. It was found that ~30-40% of the total Ag^+ ions were loaded into the multilayers at all concentrations and the concentration of Ag^+ loaded into multilayers was found to increase with increasing $AgNO_3$ concentration (Figure 5.2). These results were in good agreement with the increasing absorbance value of the peak at 435 nm, obtained from Ag NP containing multilayers from 0.10 to 0.50 M (Figure 5.1). On the other hand, spectra of multilayers obtained with 0.50 M and 0.75 M loading solutions were not significantly different from each other. At high salt concentrations, i.e. 0.75 M might have resulted in disruption of electrostatic interactions between the oppositely charged polymer layers. Segmented polymers (Pol^-Pol^+, representing positively or negatively charged PE units in the multilayer) might provide additional loading of Ag^+, but possible instability to multilayers due to disruption of electrostatic interactions which might be responsible from the decrease in absorbance value in 0.75 M $AgNO_3$ compared to that measured in 0.5 M $AgNO_3$.

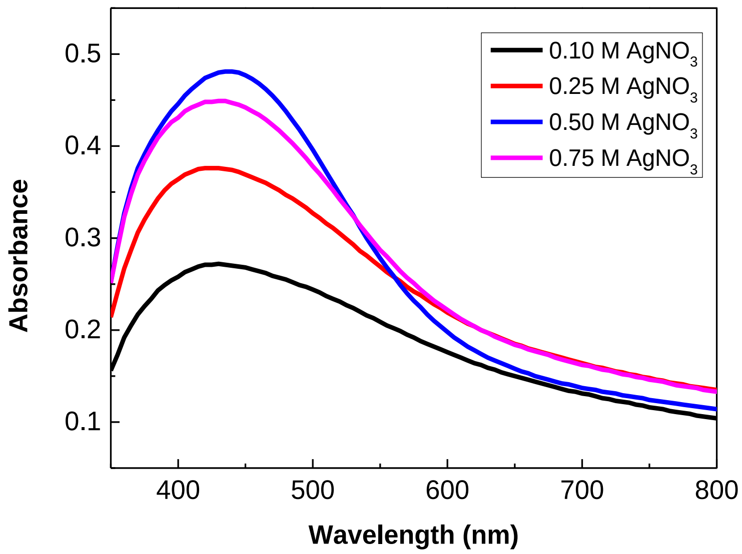

Figure 5.1 UV-vis absorption spectra of Ag NPs grown within 20 layers of PAH/TA multilayer films, prepared by immersion into 0.10, 0.25, 0.50 and 0.75 M $AgNO_3$ solutions for 6 h, rinsed, dried and followed by 1 h of Xe radiation.

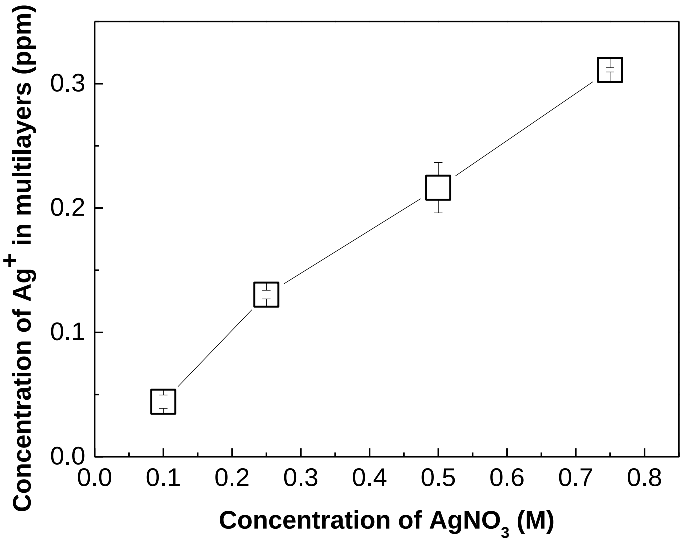

Figure 5.2 Concentration of Ag^+ in the multilayers (ppm) as a function of concentration of $AgNO_3$.

Additionally, SER spectra of 1.0 x10^{-5} M CV drop-coated on these multilayers and relative Raman intensity of the peak at 1176 cm^{-1} with respect to concentration of $AgNO_3$ solution are shown in Figures 5.3 and 5.4, respectively. Even though it seemed that there was a decreasing trend with increasing concentration values of $AgNO_3$ solution, SER signals statistically remained same from 0.10 M to 0.50 M $AgNO_3$–treated samples. Electrostatic attractions might have disrupted with using high concentration of $AgNO_3$ such as 0.75 M in this study, resulting in loading less amount of Ag^+ and obtaining poorer SERS performance compared to 0.1, 0.25 and 0.50 M $AgNO_3$-treated samples. As mentioned in Section 1.2, smaller distance between NPs resulted in more localized regions as indicated by stronger Raman signals. Additionally, formation of highly localized regions is influenced by some factors such as shape and size of NPs and roughness on the surface of substrate. NPs show a characteristic surface plasmon resonance (SPR) absorbance that arises due to the collective oscillations of conduction electrons in the metal. Spherical metal NPs have strong single surface plasmon bands.[202] Since only a single λ_{max} is observed from all substrates, shape of all NPs was spherical. Furthermore, an increase in the width of the SPR at especially 0.10 M and 0.25 M $AgNO_3$ concentrations suggests a wider range of particle sizes, which possibly led to Raman signal as high as the substrate immersed into 0.50 M Ag NPs.

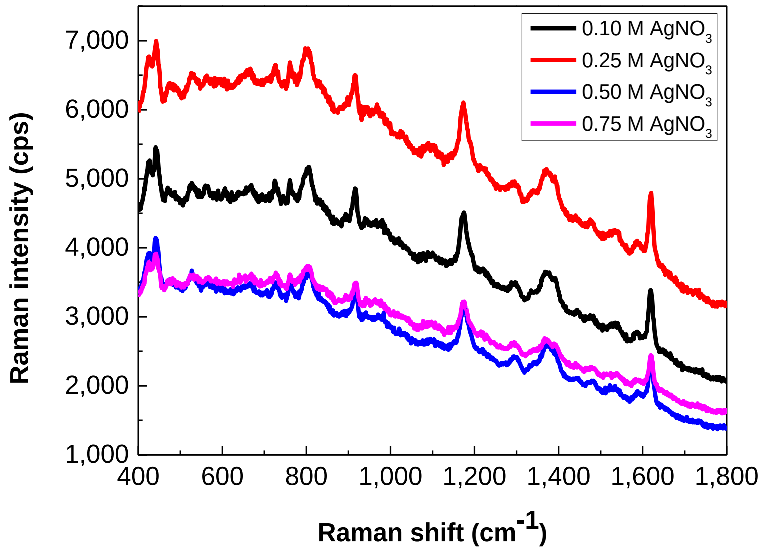

Figure 5.3 SER spectra of 1.0 x 10^{-5} M CV on Ag NP grown within 20 layers of PAH/TA multilayer films, prepared by immersion into 0.10, 0.25, 0.50 and 0.75 M $AgNO_3$ solutions for 6 h, rinsed, dried and followed by 1 h of Xe radiation.

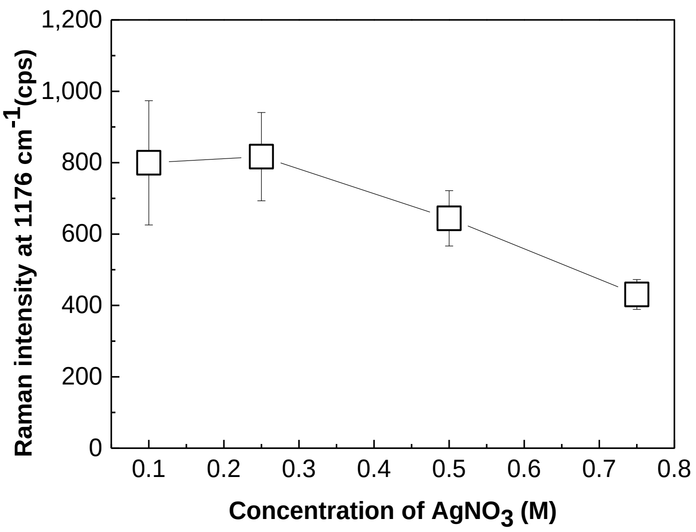

Figure 5.4 Relative Raman intensity plot at 1176 cm^{-1} of 1.0 x 10^{-5} M CV molecule on Ag NPs embedded 20 layers of PAH/TA multilayer films as a function of $AgNO_3$ concentration.

Based on these results, 0.50 M $AgNO_3$ was selected for the following studies with respect to minimum signal fluctuation for the same concentration of the CV molecule at randomly selected regions on the same substrate.

5.2 The Effect of Deposition Time on the Amount of Ag^+ Loading into Multilayers

The effect of deposition time on the amount of Ag^+ ions loaded into twenty layers of PAH/TA multilayers was examined by immersing the LbL films into 0.50 M $AgNO_3$ solution for 2, 4, 6 and 12 h, followed by rinsing, drying and exposure to Xe radiation for 1 h. Absorbance values at 435 nm increased with increasing exposure time to $AgNO_3$ solution (Figure 5.5). However, increase in background signals which probably resulted from the increase in surface roughness with increasing deposition time led to higher scattering from the substrates.

The amount of Ag^+ ions loaded in PE multilayer films as a function of time was quantified through ICP-MS. As discussed earlier, the multilayers were immersed into $AgNO_3$ solution and the concentration of Ag^+ in the multilayers was determined. The difference in the concentration of Ag^+ ions in the solution before and after loading was attributed to the concentration of Ag^+ ions loaded into the multilayers. It was found that ~35-40% of the total Ag^+ ions were loaded into the multilayers at all deposition times and the concentration increased slightly with increasing loading time from 2 h to 12 h (Figure 5.6). These results were in good agreement with the UV-vis absorption spectra of multilayers loaded with $AgNO_3$ with increasing deposition times (Figure 5.5).

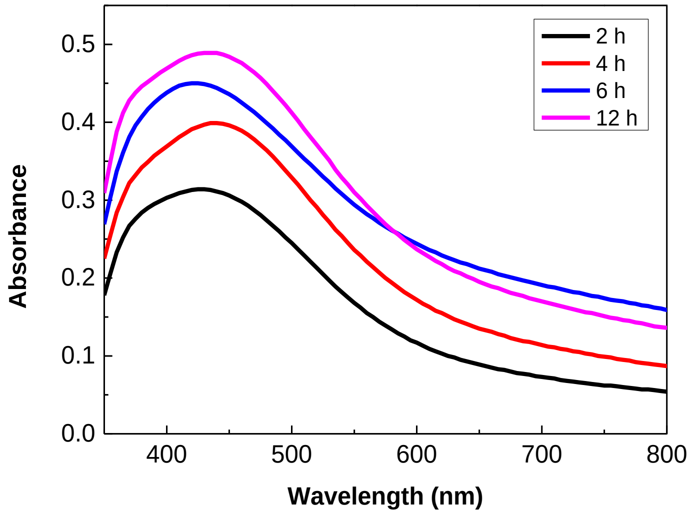

Figure 5.5 UV-vis absorption spectra of Ag NPs grown within 20 layers of PAH/TA multilayer films, prepared by immersion into 0.50 M $AgNO_3$ solution for 2, 4, 6 and 12 h, rinsed, dried and followed by 1 h of Xe radiation.

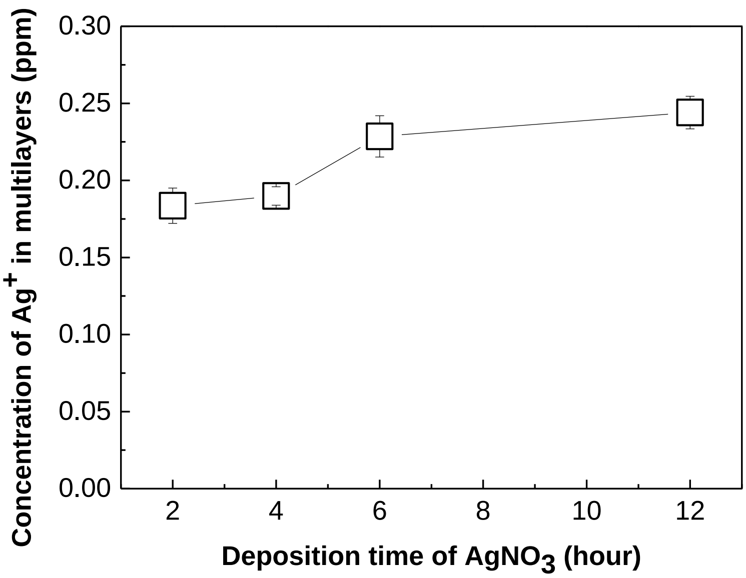

Figure 5.6 Concentration of Ag^+ into multilayers (ppm) as a function of deposition time of $AgNO_3$.

SER signal would be expected to enhance with increasing growth time of NPs due to possible decrease in gaps between adjacent NPs with a denser NP distribution.[203,204] SER spectra of 1.0 x10^{-5} M CV on these multilayers and relative Raman intensity of the peak at 1176 cm^{-1} with respect to deposition time of $AgNO_3$ solution are shown in Figures 5.7 and 5.8, respectively. There were no significant signal difference and enhancement between multilayers with increasing deposition time of $AgNO_3$ from 2 h to 6 h. However, the signal enhanced by approximately 1.3 times when the deposition time was increased from 6 h to 12 h. This was not a significant rise to wait two times more time for loading of Ag^+ within the films. Therefore, 6 h deposition time of $AgNO_3$ was decided to be adequate for further studies. Furthermore, multilayer films were found to be loaded with slightly higher amount of Ag^+ at 6 h of deposition time compared to shorter deposition times.

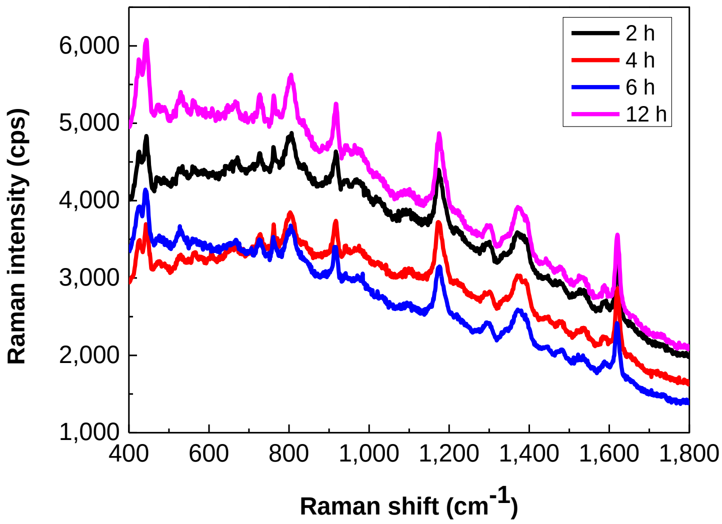

Figure 5.7 SER spectra of 1.0 x 10^{-5} M CV on Ag NP grown within 20 layers of PAH/TA multilayer films, prepared by immersion into 0.50 M $AgNO_3$ solutions for 2, 4, 6 and 12 h, rinsed, dried and followed by 1 h of Xe radiation.

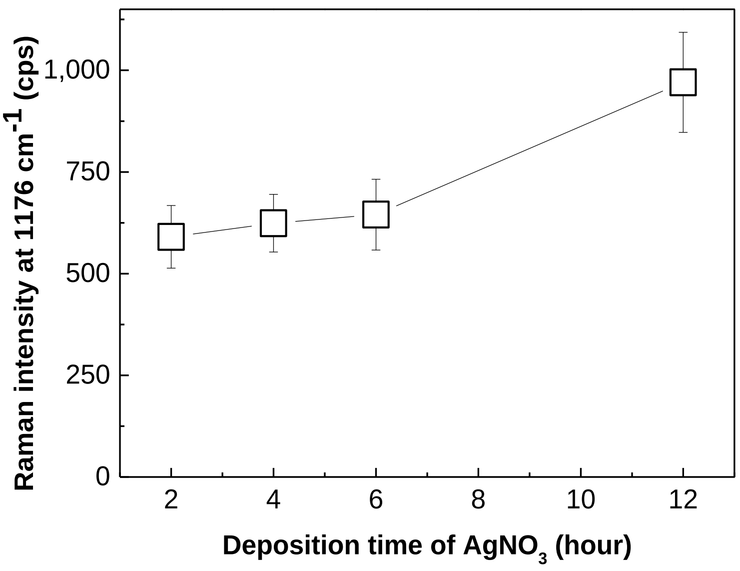

Figure 5.8 Relative intensity plot at 1176 cm^{-1} of 1.0 x 10^{-5} M CV on Ag NPs embedded 20 layers of PAH/TA multilayer films as a function of deposition time of $AgNO_3$.

5.3 The Effect of Layer Number on NP Formation

The influence of the number of PE layers in the LbL films on NP formation was examined. 20, 30 and 40 PAH/TA layers were prepared and exposed to 0.50 M $AgNO_3$ solution, rinsed, dried and exposed to 1 h of Xe irradiation. The absorbance at 435 nm associated with Ag NP increased with increasing layer number, suggesting incorporation of higher amounts of Ag^+ ions and then Ag NPs within the multilayers (Figure 5.9) Additionally, maximal wavelength position of the LSPR absorption bands shifted by approximately 30 nm as going from 20 to 40 layers together with an increase in FWHM of the SPR band. This showed that aggregation of Ag NPs incorporated into multilayer films increased with increasing number of layers.[143,171] This increase in aggregation of NPs can be explained by increase in loaded amount of Ag^+ with the increase in the layer number from 20 to 40 PAH/TA layers.

Results of SER signals of 1.0×10^{-5} M CV drop-coated on Ag NPs on 20, 30, and 40 layers of films and evolution of Raman intensity at 1176 cm^{-1} of 1.0×10^{-5} M CV as a function of layer number are seen in Figures 5.10 and 5.11, respectively. There was no change in the signal when the layer number increased from 20 to 30. The average signal decreased by 1.3 times for 40-layer films. However, the signals of these three multilayers were not statistically different from each other considering the range of signals measured on the same substrate. As a result, deposition of twenty layers of PAH and TA was chosen for further studies.

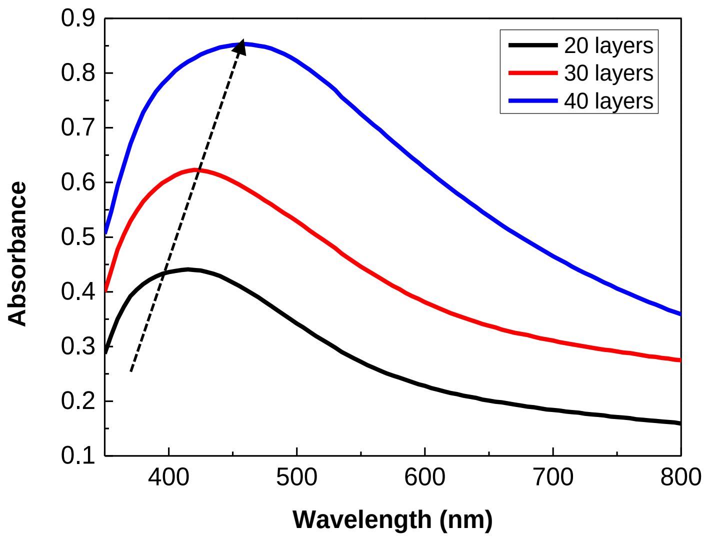

Figure 5.9 UV-vis absorption spectra of Ag NPs grown within 20, 30 and 40 layers of PAH/TA multilayer films, prepared by immersion into 0.50 M $AgNO_3$ solution for 6 h, rinsed, dried and followed by 1 h of Xe radiation. Arrow shows increase of absorption and red-shift of the plasmon resonance.

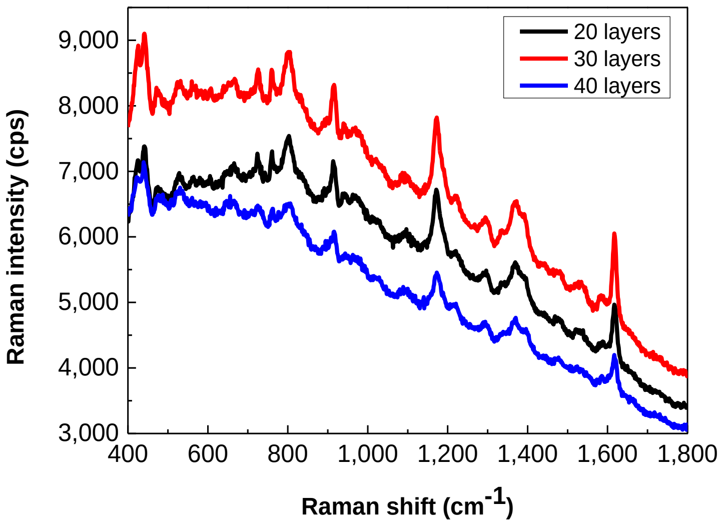

Figure 5.10 SER spectra of 1.0 x 10^{-5} M CV on Ag NP grown within 20, 30 and 40 layers of PAH/TA multilayer films, prepared by immersion into 0.50 M $AgNO_3$ solution for 6 h, rinsed, dried and followed by 1 h of Xe radiation.

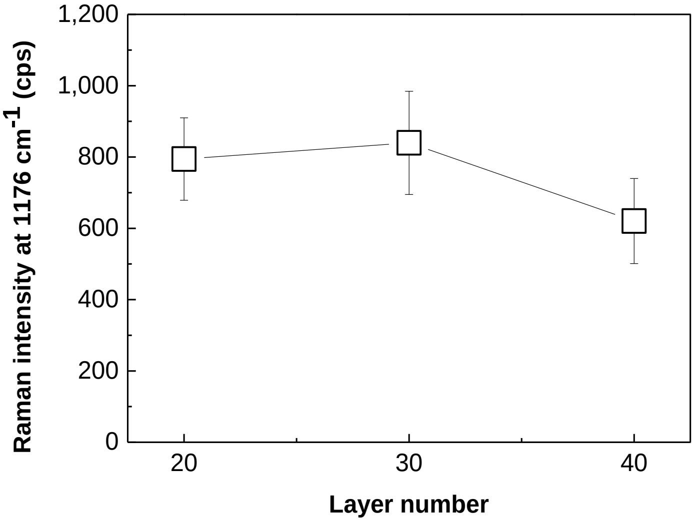

Figure 5.11 Relative intensity plot at 1176 cm^{-1} of 1.0 x 10^{-5} M CV on Ag NPs embedded PAH/TA multilayer films as a function of layer number.

5.4 The Effect of Light Exposure on NP Formation

Twenty layers of PAH/TA multilayers were exposed to 0.50 M $AgNO_3$ solution for 6 h, followed by rinsing, drying and exposing to Xe radiation for 30, 60 and 90 min. UV-vis spectra of these films are shown in Figure 5.12. Although the characteristic SPR band of Ag NPs with a maximum at 435 nm (λ_{max}) were obtained, no direct relation between the absorbance values and exposure time of the lamp could be revealed. Probably, Ag NPs are formed within 30 min of the exposure of Xe lamp and further exposure time does not affect the composition of Ag NPs on the surface of the film.

Figure 5.13 shows the SER spectra of CV molecule, drop coated onto twenty layers of PAH/TA films, exposed to 0.50 M $AgNO_3$ solution, rinsed, dried and irradiated using a Xe lamp for 30, 60 or 90 min. In Figure 5.14, Raman intensity at 1176 cm^{-1} of 1.0 x 10^{-5} M CV as a function of Xe light exposure time is shown. The intensity of Raman signals increased with increasing exposure time from 30 min to 60 min. However, no significant difference in the signal was recorded when the exposure time increased from 60 to 90 min. Therefore, 60 min Xe radiation exposure time was selected for further studies.

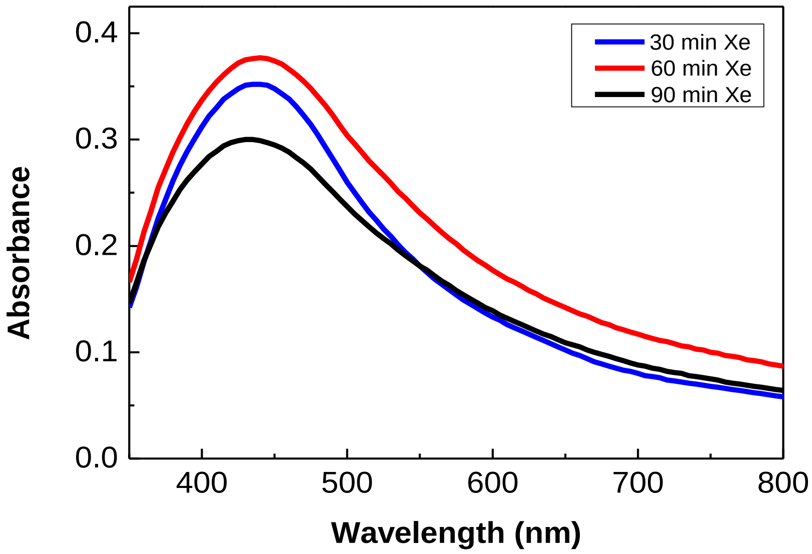

Figure 5.12 UV-vis absorption spectra of Ag NPs grown within 20 layers of PAH/TA multilayer films, prepared by immersion into 0.50 M $AgNO_3$ solutions for 6 h, rinsed, dried and followed by 30, 60 and 90 min of Xe radiation.

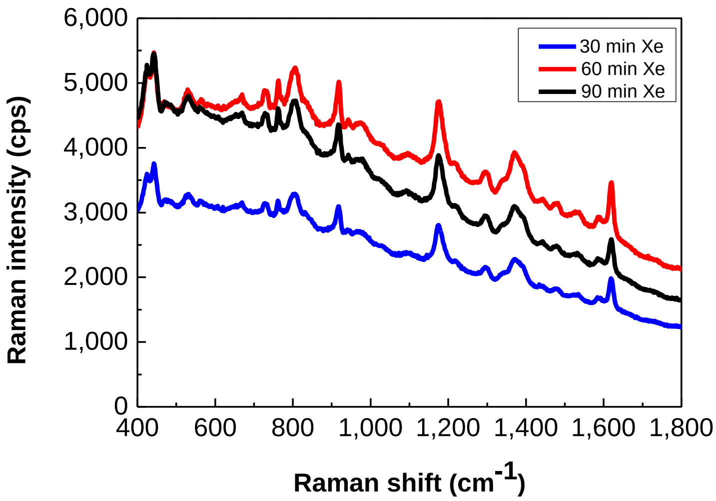

Figure 5.13 SER spectra of 1.0 x 10^{-5} M CV on Ag NP grown within 20 layers of PAH/TA multilayer films, prepared by immersion into 0.50 M $AgNO_3$ solutions for 6 h, followed by 30, 60 and 90 min of Xe radiation.

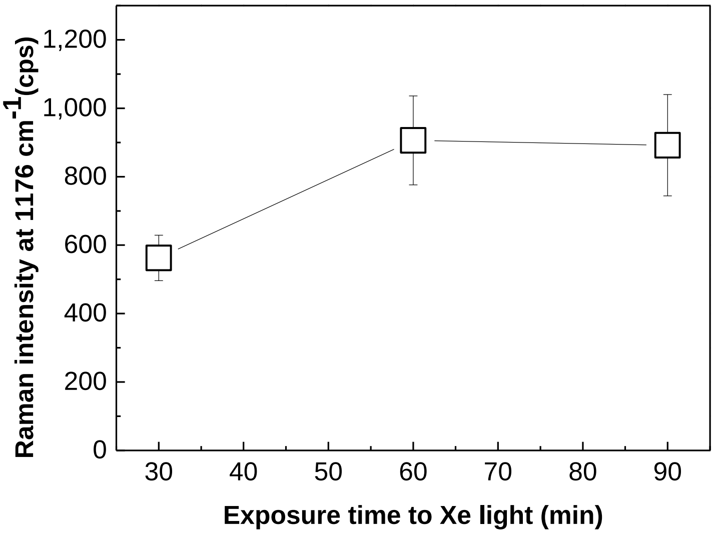

Figure 5.14 Relative intensity plot at 1176 cm^{-1} of Ag NPs embedded PAH/TA multilayer films as a function of exposure time to Xe radiation.

5.5 The Effect of Light on the Stability of Tannic Acid

Before the discussion of stability of TA in both solution and film, pK_a values and aqueous solution behavior of the molecule identifying ionization of molecule depending on pH were summarized. The acidity strength (pK_a) of molecules depends on the stability of conjugate bases of the molecules. Therefore, factors affecting the stability of phenolic hydroxyl groups in TA molecule determines pK_a of it. The pK_a value of TA has been varied from 2.5 to 8.5 in different literature sources. The variation in pK_a values is due to the usage of different sources of tannins.[71,170,205] Haktaniyan and coworkers studied to examine the behavior of TA in aqueous solutions at pH levels ranging from 2.0 to 9.5 using UV-visible spectroscopy.[170] They observed that at pH 2.0, TA had two absorption peaks at 214 nm and 276 nm, associated with the neutral form of TA. As the pH increased, the intensities of these peaks decreased and two new peaks at 245 nm and 322 nm emerged. These new peaks corresponded to the ionized form of TA, which were due to ionization of the phenolic hydroxyl groups on TA.[170,205–207] In order to estimate pK_a value associated with phenolic hydroxyl groups of TA, the ratio of absorbance values at 322 nm to 276 nm was plotted. The ratio remained relatively constant between pH 2-4, gradually increased between pH 4.0-7.0, and then sharply increased between pH 7.0-9.5. By analyzing the second-order derivative of the absorbance ratio, they estimated pK_a values of 6.5 and 8.0 for the phenolic hydroxyl groups of TA.[170] There are also other studies reported different pKa values for TA in the literature.[208,209] Lin and Constadinnova with their coworkers reported two pK_a values as varied between ~4.0-5.0 and ~6.0-7.4 correlating them with the phenolic hydroxyl groups of TA.[209,210] However, there were incompatibilities in the interpretation of the pK_a values in the literature. Simon and coworkers associated the first pK_a value with acidic groups originating from digallic acids bound to the glucose core,[208] while Lin and Constadinnova an coworkers linked both pK_a values to the phenolic hydroxyl groups as mentioned above.[209,210] Furthermore, different pK_a values reported for TA were explained by variations in the composition of TA samples, because TA is a natural product and may contain tannin molecules with different numbers of galloyl groups. Although some studies also reported a single pK_a value for TA varied between 2.5 to 8.5, all of them agreed that ionizable units on TA were due to phenolic hydroxyl groups of TA.[71,205,206,211]

In this section, the stability of TA within the film was examined due to possible degradation of TA during Xe lamp exposure of the films. The absorption band at 276 nm is corresponded to $\pi \rightarrow \pi^*$ transition in aromatic ring. This band can be used as a way to determine percentages of aromatics by investigating absorbance values of TA at 276 nm with increasing exposure time of the light. TA absorbs UV light due to its phenolic groups suggesting that UV light has slight effect on its degradation.[212] In order to show the efficiency of UV process on degradation of TA in wastewater, Bensalah and coworkers used UV irradiation alone, H_2O_2 alone and UV/H_2O_2 combination for comparison in order to treat wastewaters contaminated with natural organic compounds like TA.[212] Use of H_2O_2 together with UV light provides the production of highly reactive radicals such as $OH^{\cdot}$ and $HO_2^{\cdot}$ which are successfully used in wastewater treatment. Based on the results of variations of absorbance at 276 nm with time, only 10% of aromatics were depleted by UV light while removal of aromatics was 55% by UV/H_2O_2 combination. The enhanced efficiency is due to the generation of hydroxyl radicals during the UV treatment of H_2O_2. The large amount of hydroxyl radicals is mainly resulted from photodecomposition of H_2O_2 while a minor amount of the radicals is produced by using UV photolysis of water. As a result of that, significant degradation of TA solution is not expected in this part of this thesis. In this respect, stability of TA was investigated in solution phase firstly. TA exhibited two peaks at 210 and 277 nm in 0.01 M phosphate buffer solution at pH 7.0 as shown in Figure 5.15. In acidic aqueous solution of TA, these two peaks were assigned to its neutral form as mentioned in the previous paragraph. Emergence of new peaks and decrease of the absorption of the new peaks are expected at higher pH levels such as pH 7.0 in this study, and these new peaks are attributed to ionization of polyphenols.[213] However, usage of different tannins and variations in the sample compositions with different ionizable units of TA might affect the aqueous behavior of TA solution at pH 7.0 in this study as compared to literature sources. As a result of that, Figure 5.15 suggests that the stability TA in solution was not affected by Xe radiation as indicated with no significant change of the peaks belonged to TA in terms of both positions and intensities.

To assure multilayer stability, twenty layer of PAH/TA films were deposited onto quartz slides and exposed to Xe radiation for 30, 60 and 90 min. Assembly of TA with PAH resulted in shift of peak positions of TA through higher wavelengths (215 nm and 300 nm) compared to the peaks recorded when TA was in the solution form (210 nm and 277 nm). The shift in the positions of the peaks in the multilayer spectra can be attributed to the alteration of the distribution of charges in the enhanced ionized TA molecules when they are conjugated with the amine groups of PAH.[71] Figure 5.16 shows UV-vis absorption spectra of the films before and after exposure to Xe radiation. The absorbance spectra of multilayers showed two peaks at 215 nm and 300 nm before the radiation. The peak at 300 nm shifted to lower wavelength (275 nm) upon exposure to Xe radiation. As a result, two absorption bands at 215 nm and 275 nm resembled to TA peaks obtained in the solution form (210 nm and 277 nm), suggesting that enhanced ionized TA molecules turned into neutral form with the radiation. Additionally, the intensities of the absorption peaks were not affected by the duration of radiation. As a result of all these findings, TA in multilayers might be changed its ionization but the molecule kept its integrity in the presence of Xe light for 1-h duration

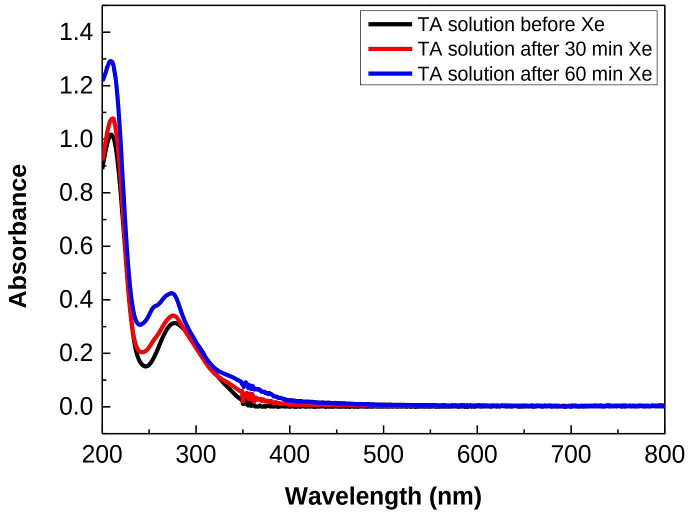

Figure 5.15 UV-vis absorption spectra of 0.01 mg/mL TA solution at pH 7.0 followed by 0, 30, 60 and 90 min of Xe radiation.

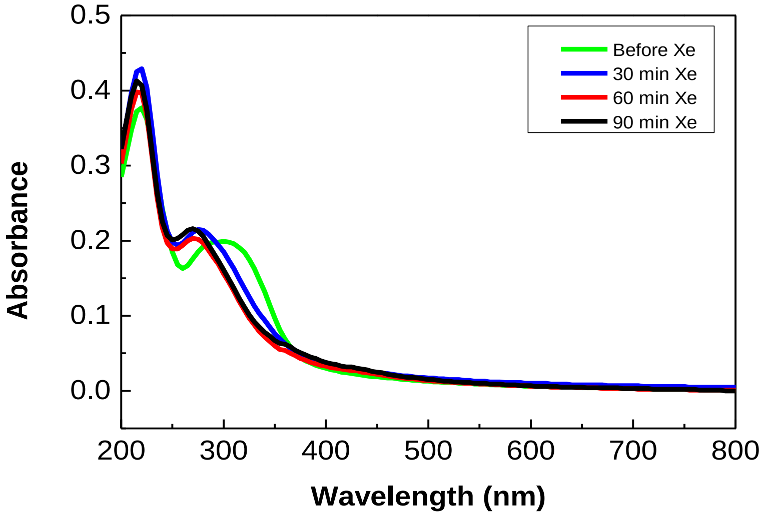

Figure 5.16 UV-vis absorption spectra of 20 layers of PAH/TA multilayer films, rinsed, dried and followed by 0, 30, 60 and 90 min of Xe radiation.

5.6 The Effect of Number of Loading/Reduction Cycles on NP Formation

Number of cycles can be repeated for *in-situ* growth of NPs in order to densify NPs distribution on the surface, so that SERS-active spaces between adjacent NPs can be increased.[204,214,215] For this purpose, the loading/reduction (L/R) cycles were repeated up to 4 times on the multilayer surface. The schematic representation of the procedure of this part is given in the following Figure 5.17.

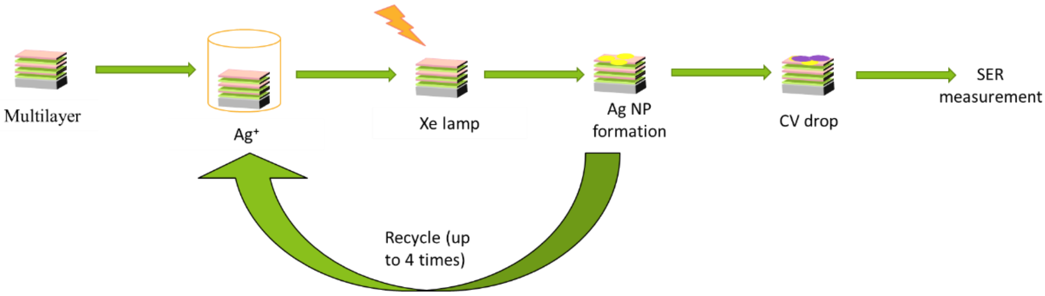

Figure 5.17 The scheme for L/R cycles on LbL substrates for NP formation.

UV-vis absorption spectra of these multilayer films are shown in Figure 5.18. Applying 2 L/R cycle increased the amount of Ag NPs formed in the multilayers. Further increasing L/R cycles did not result in a significant difference in the amount of Ag NP. Moreover, broadening of the spectra with increasing cycle numbers showed densified size distribution and aggregation of NPs within multilayers.[143,171]

No significant change in SER signals of 1.0×10^{-5} M CV was observed as shown in Figures 5.19 and 5.20. As NP density and NP size on the surface increase, the gaps between adjacent NPs decrease, leading to the formation of more nanoscale spaces at the connection points of NPs.[214] However, it might be possible that closely spaced Ag NPs were densified not only on multilayer surface but also deep inside multilayer films with increasing L/R cycles. Since the number of NPs and their distribution on the substrate surface is critical for Raman signal enhancement, possible NPs inside the multilayers might not have increased the signals as expected. As a result of that 1 cycle of loading/reduction was chosen to immobilize Ag ions in multilayer films for further studies.

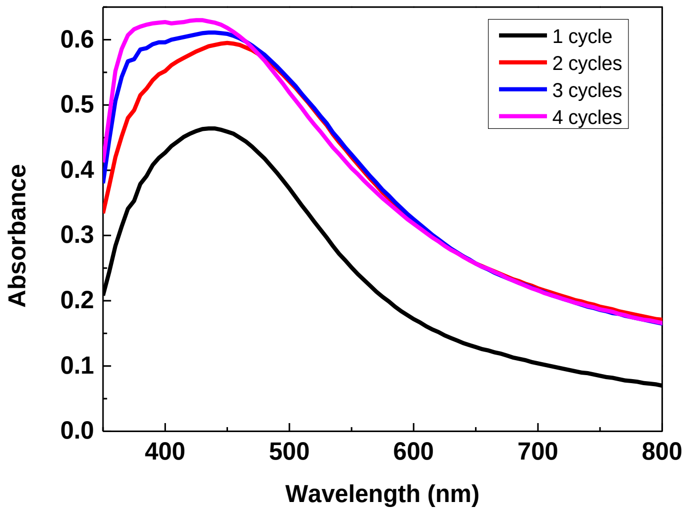

Figure 5.18 UV-vis absorption spectra of Ag NPs grown within 20 layers of PAH/TA multilayer films, prepared by immersion into 0.50 M $AgNO_3$ solutions for 6 h, rinsed, dried and followed by 1 h of Xe radiation with different number of loading/reduction cycles.

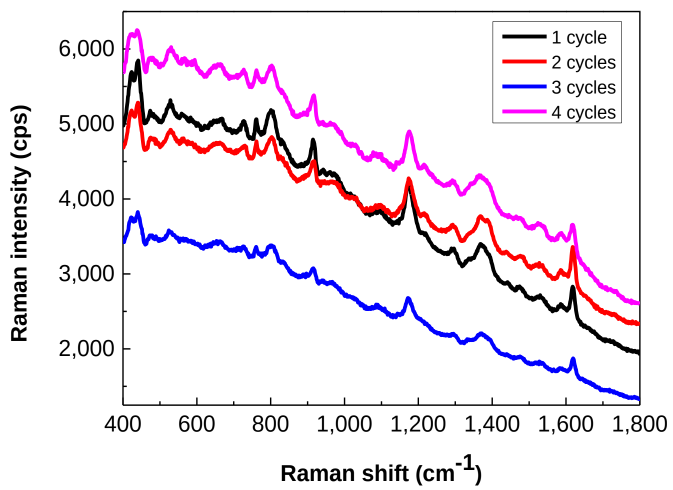

Figure 5.19 SER spectra of 1.0 x 10^{-5} M CV molecule on Ag NP grown within 20 layers of PAH/TA multilayer films, prepared by immersion into 0.50 M $AgNO_3$ solutions for 6 h, rinsed, dried and followed by 1 h of Xe radiation with different number of loading/reduction cycles.

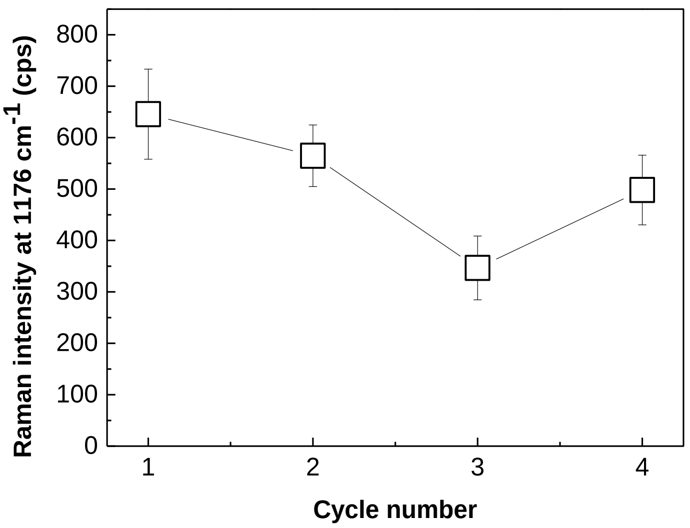

Figure 5.20 Relative intensity plot at 1176 cm^{-1} of 1.0 x 10^{-5} M CV on Ag NPs embedded PAH/TA multilayer films as a function of L/R cycle number.

5.7 The Effect of Different Type of Lamps on NP Formation

The aim of the following experiments was to examine the effect of lamp type, particularly Xe lamp (500 W) and UV lamp (254 nm, 6 W), on the formation of NPs within PAH/TA multilayer films. As mentioned in Section 1.4.2, silver ion photoreduction depends on intensity and wavelength of incident radiation promoting electron transfer from water molecule to Ag^+ by the subsequent decomposition of H_2O^+ into H^+ and OH· radical.[216] Finally, Ag^o associates to form Ag NPs. Machado and coworkers compared photoreduction methods of Ag NPs with UV light (365 nm) with conventional fluorescent light in PAH/PAA multilayers.[161] Substrate including PEM and silver ions was exposed to different amounts of light, when it was illuminated with conventional fluorescent light. This implies that larger NPs (ranging from 4-50 nm) can be obtained as compared to smaller NPs synthesized by UV reduction (2-4 nm).[161] Machado and coworkers claimed that size, concentration and crystalline structure type of NPs were affected by choice of excitation light.

Since fluorescent light was consisted of many wavelengths including visible and UV light, reduction of NPs retarded so that larger NPs could be obtained.[161] Since UV light used in this thesis has lower power as compared to Xe lamp, 5 h of irradiation time was applied to assure formation and completeness of NP formation on the surface. On the other hand, Xe light exposure was kept at 1 h due to its higher power (500 W). When the exposure time was increased, the film surfaces heated because of high power of the lamp. In order to minimize the danger of destroying film surfaces with heat, light exposure was limited to 1 h in this study. UV-vis absorption spectra of multilayer films obtained by these two light sources are shown in Figure 5.21. Accordingly, size distribution of NPs was comparable to each other as understood from the spectra with width of spectral distribution. Additionally, the higher background of the NPs formed by Xe radiation was the indications of higher scattering of light from the surface as compared to the UV-photoinduced one.

SER spectra of CV recorded on these films are shown in Figure 5.22. This result is in good agreement with UV-vis absorption spectra shown in Figure 5.21 suggesting NPs with broader size distribution. The broader size distribution together with higher scattering probability from the surface resulted in enhancement of the signal. S/N ratio was better for multilayers exposed to Xe lamp for the reduction of Ag^+ ions embedded into the films.

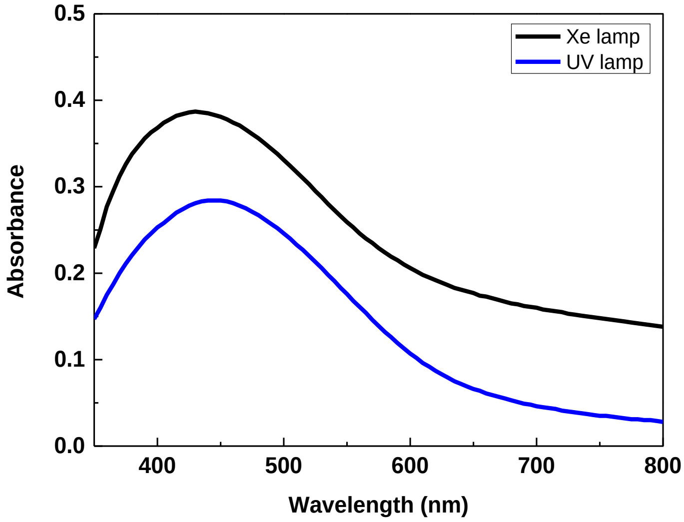

Figure 5.21 UV-vis absorption spectra of Ag NPs grown within 20 layers of PAH/TA multilayer films, prepared by immersion into 0.50 M $AgNO_3$ solutions for 6 h, rinsed, dried and followed by 1 h of Xe lamp or 5 h of UV lamp exposure.

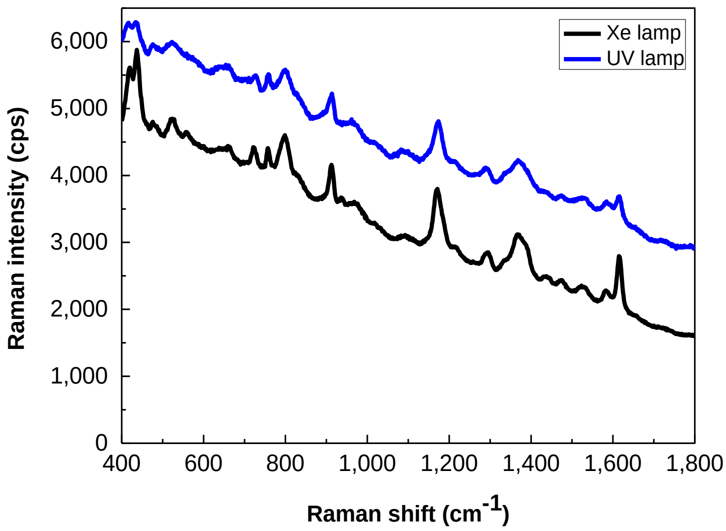

Figure 5.22 SER spectra of $1.0x10^{-5}$ M CV on Ag NP grown within 20 layers of PAH/TA multilayer films, prepared by immersion into 0.50 M $AgNO_3$ solutions for 6 h, rinsed, dried and followed by 1 h of Xe lamp and 5 h of UV lamp.

As an alternative to PAH/TA, PAH/PAA polyelectrolyte pair was also examined for Ag NP formation with respect to Ag^+ concentration, deposition time, layer numbers and different types of lamps. Veletanlic and Machado with their coworkers used PAH/PAA multilayers to investigate for *in situ* synthesis of Ag NPs by UV light-induced photoreduction. They showed that the size of the NPs varied between 2-5 nm, depending on the pH of the multilayer deposition and UV light used at 254 or 365 nm.[160,161] For the samples of PAH/PAA which were exposed to 0.50 M or 0.75 M $AgNO_3$ solution, Ag NPs distributed inhomogeneously by disassembling from the surface of the films in this study. Therefore, 0.25 M $AgNO_3$ was used for the rest of the experiments of this part.

The optimization studies of experimental parameters mentioned above such as Ag^+ concentration, deposition time, layer numbers and different types of lamps were not provided significant enhancement for the Raman signal of CV molecule, deposited onto PAH/PAA LbL films. As an example, UV-vis absorption spectra of Ag NPs grown within twenty layers of PAH/PAA and PAH/TA multilayer films are presented in Figure 5.23. Number of Ag NP on PAH/PAA multilayer is apparently higher than PAH/TA multilayers based on higher absorbance spectrum obtained in Figure 5.23. Moreover, narrower size distribution of PAH/PAA as compared to PAH/TA was obtained due to sharper SPR band measured in PAH/PAA films compared to PAH/TA films as shown in Figure 5.23. These findings found here is consistent with literature results of photochemically prepared Ag NPs sizes on PAH/PAA multilayers.[160,161] Comparison of SER spectra of CV molecule on these multilayers is shown in Figure 5.24. No signal could be obtained from the surface of PAH/PAA multilayers suggesting that small-sized NPs could not lead to enhanced electromagnetic field.[4] On the other hand, Ag NPs having wider size distribution at PAH/TA multilayers (Figure 5.23) might result in higher SER signal as shown in Figure 5.24.

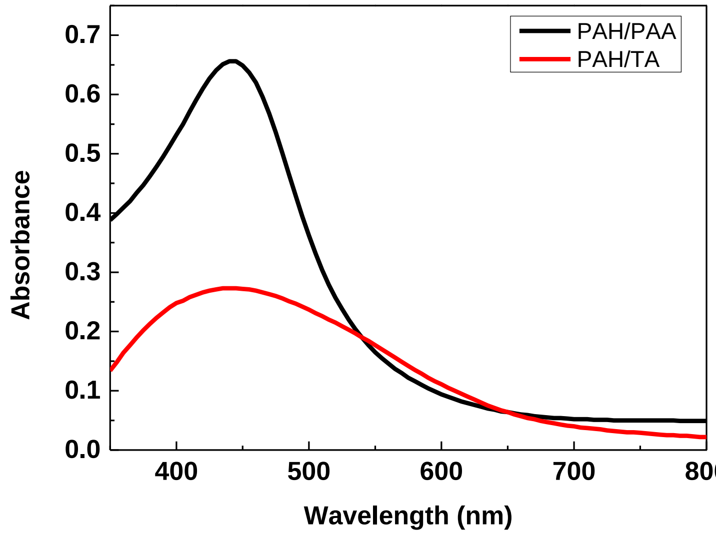

Figure 5.23 UV-vis absorption spectra of Ag NPs grown within 20 layers of PAH/PAA and PAH/TA multilayer films, prepared by immersion into 0.25 M $AgNO_3$ solutions for 6 h, rinsed, dried and followed by 1 h of Xe radiation.

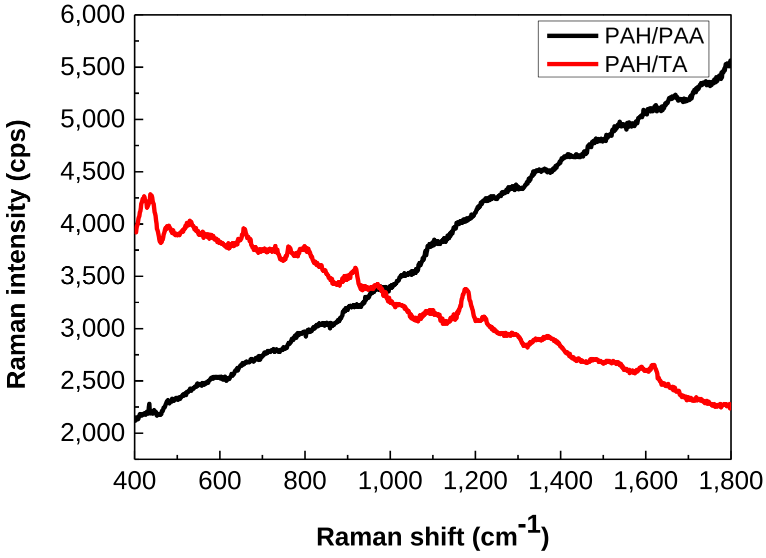

Figure 5.24 SER spectra of 1.0×10^{-5} M CV on Ag NP grown within 20 layers of PAH/PAA and PAH/TA multilayer films, prepared by immersion into 0.25 M $AgNO_3$ solutions for 6 h, rinsed, dried and followed by 1 h of Xe radiation.

5.8 Au NPs Containing PAH/TA Multilayers

Au NPs were also synthesized with photochemical reduction of $AuCl_4^-$ anions in PAH/TA multilayer films (post-loading structure). Optimization parameters including concentration and deposition time of $AuCl_4^-$ were studied for Au NPs formation.

Au NPs show a characteristic surface plasmon resonance (SPR) absorbance (at ~550 nm) that arises due to the collective oscillations of conduction electrons in the metal. Spherical metal NPs were formed in these experiments, evidenced by single resonance peaks in UV-vis absorption spectra. Detectable absorption bands in the spectra were attributed to NPs with confirmation of attachment of gold complex anions to multilayers. The following experimental parameters were investigated for *in situ* preparation of Au NPs in PAH/TA multilayers by photochemical reduction method.

5.8.1 The Effect of Concentration on Au NP Formation

Association of $AuCl_4^-$ anion within the multilayer films was affected by the concentration of metal salt ($NaAuCl_4$). $AuCl_4^-$ solutions with concentrations ranging from 2.0 mM to 15.0 mM were prepared to investigate the effect of concentration of $AuCl_4^-$ solution on NP formation. Deposition concentration selection was based on adequate binding of $AuCl_4^-$ and reducing of Au NPs. In literature, loading concentration values of $AuCl_4^-$ into amine containing polymers was varied between 2.0 mM to 40.0 mM.[162,163,214] Nineteen layers of PAH/TA films were immersed into $AuCl_4^-$ solution at varying concentrations. The substrates were rinsed, dried and exposed to Xe radiation. UV-vis absorption spectra of Au NPs formed within PAH/TA multilayers are shown in Figure 5.25. Characteristic absorbance spectra of Au NPs were observed at all concentrations having very similar spectra for 2.0 and 5.0 mM with a λ_{max} value of ~550 nm. Higher baseline and larger width of the peaks for the multilayers which were immersed in 10.0 and 15.0 mM $AuCl_4^-$ showing larger distribution of Au NPs sizes in these substrates.

SER spectra of 1.0 x10^{-5} M CV drop-coated on these multilayers and relative Raman intensity of the peak at 1176 cm^{-1} with respect to concentration of $AuCl_4^-$ solution are shown in Figures 5.26 and 5.27, respectively. SER signals statistically remained same for 2.0 and 5.0 mM-treated samples with a little increase at higher concentration values of $AuCl_4^-$. This could be attributed to having higher scattering abilities of enlarged NPs with increasing concentration. However, irreproducible SERS performance measured especially on 10.0 mM-treated sample, which might be due to stacking of Au NPs on the surface. Since no remarkable difference between the signals of four concentrations was recorded, 5.0 mM $AuCl_4^-$ was selected to continue for the following experiments.

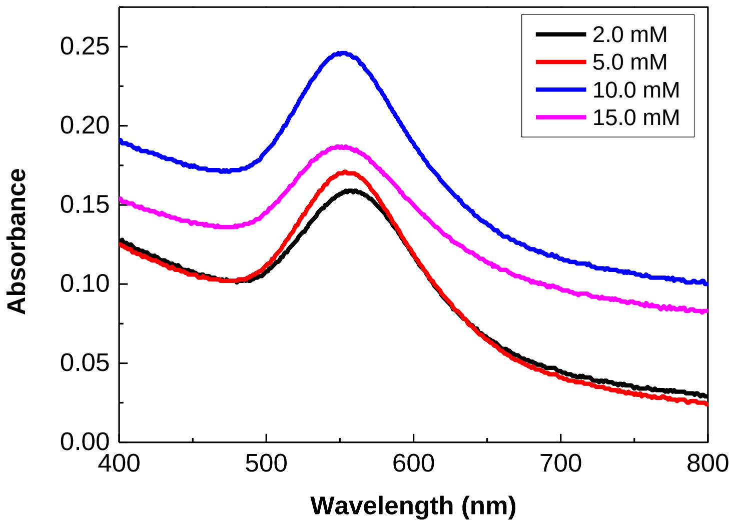

Figure 5.25 UV-vis absorption spectra of Au NPs grown within 19 layers of PAH/TA multilayer films, prepared by immersion into 2.0, 5.0, 10.0 and 15.0 mM $AuCl_4^-$ solutions for 6 h, rinsed, dried and followed by 1 h of Xe radiation.

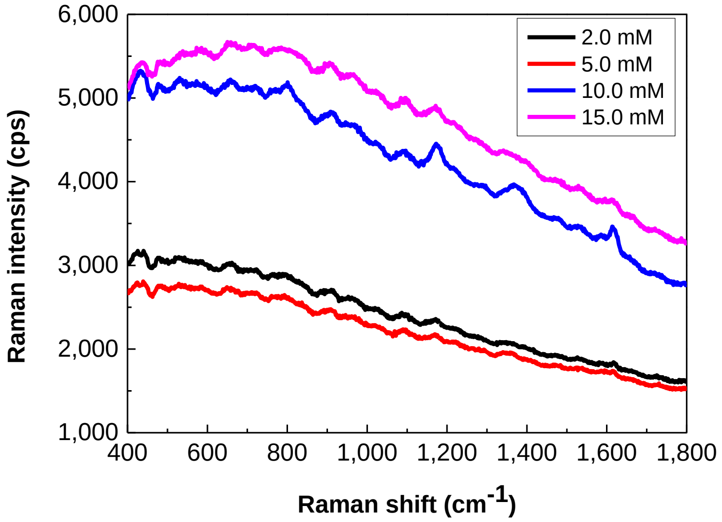

Figure 5.26 SER spectra of 1.0 x 10^{-5} M CV on Au NP grown within 19 layers of PAH/TA multilayer films, prepared by immersion into 2.0, 5.0, 10.0 and 15.0 mM $AuCl_4^-$ solutions for 6 h, rinsed, dried and followed by 1 h of Xe radiation.

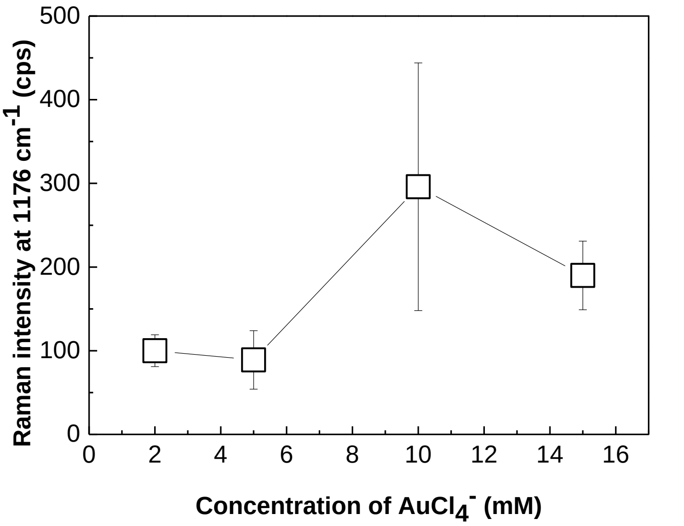

Figure 5.27 Relative intensity plot at 1176 cm^{-1} of Au NPs embedded 19 layers of PAH/TA multilayer films as a function of $AuCl_4^-$ concentration.

5.8.2 The Effect of Deposition Time on Au NP Formation

Au NPs distribution on the substrate was aimed to be densified with increasing immersion time in $AuCl_4^-$ solution. For this purpose, 19 layers of PAH/TA multilayers was examined by immersing the LbL films into 5.0 mM $AuCl_4^-$ solution for 15 min, 30 min, 1 h, 2 h or 6 h, followed by rinsing, drying and exposure to Xe radiation for 1 h. Absorbance values at 550 nm did not show an increasing trend with increase in exposure time of $AuCl_4^-$ ions as shown in Figure 5.28. For example, Au NPs containing multilayers prepared with 1 and 6 h of deposition had almost the same spectra. Deposition time of 15 min was shown to be adequate for the formation of NPs at the surface with wider size distribution as evidenced from the peak width. Increasing deposition time resulted in an increase in the number of NPs number at 30 min of immersion time, but further increasing of the immersion time led to a decrease in λ_{max} intensity which was related with the number of NPs at the surface.[163] Binding of $AuCl_4^-$ anions within the multilayers might have increased the number of NPs to some limit (30 min), but longer deposition times might have resulted in dislodging the anions from the substrates.

SER spectra of 1.0 x10^{-5} M CV on these multilayers and relative Raman intensity of the peak at 1176 cm^{-1} with respect to deposition time of $AuCl_4^-$ solution are shown in Figures 5.29 and 5.30, respectively. There were no significant signal differences and enhancement between multilayers with increasing deposition time of $AuCl_4^-$ from 15 min to 6 h. Therefore, 15 min deposition time was selected for further studies due to higher reproducibility on the same surface for *in-situ* formation of Au NPs.

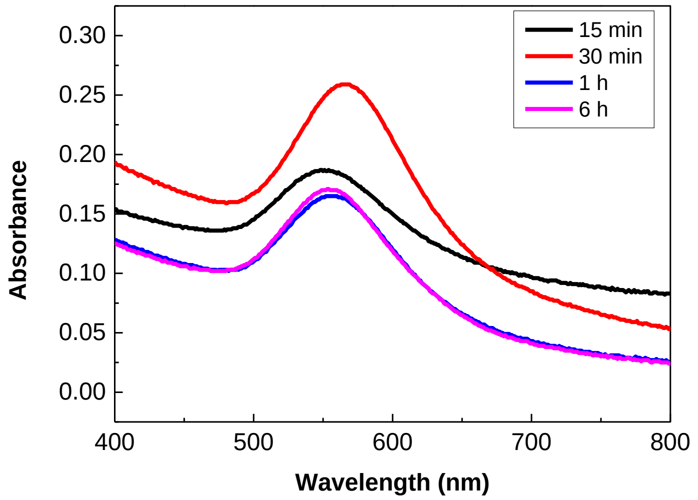

Figure 5.28 UV-vis absorption spectra of Au NPs grown within 19 layers of PAH/TA multilayer films, prepared by immersion into 5.0 mM $AuCl_4^-$ solutions for 15 min, 30 min, 1 h and 6 h, rinsed, dried and followed by 1 h of Xe radiation.

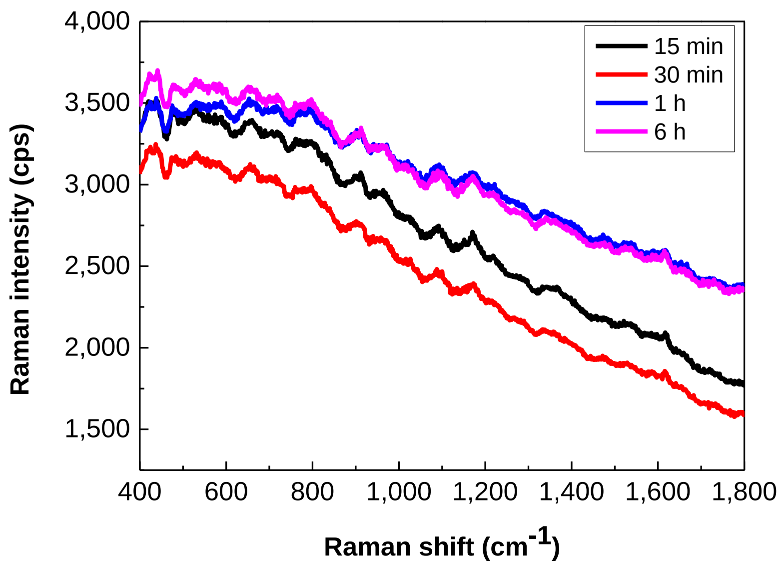

Figure 5.29 SER spectra of 1.0 x 10^{-5} M CV on Au NP grown within 19 layers of PAH/TA multilayer films, prepared by immersion into 5.0 mM $AuCl_4^-$ solutions for 15 min, 30 min, 1 h and 6 h, rinsed, dried and followed by 1 h of Xe radiation.

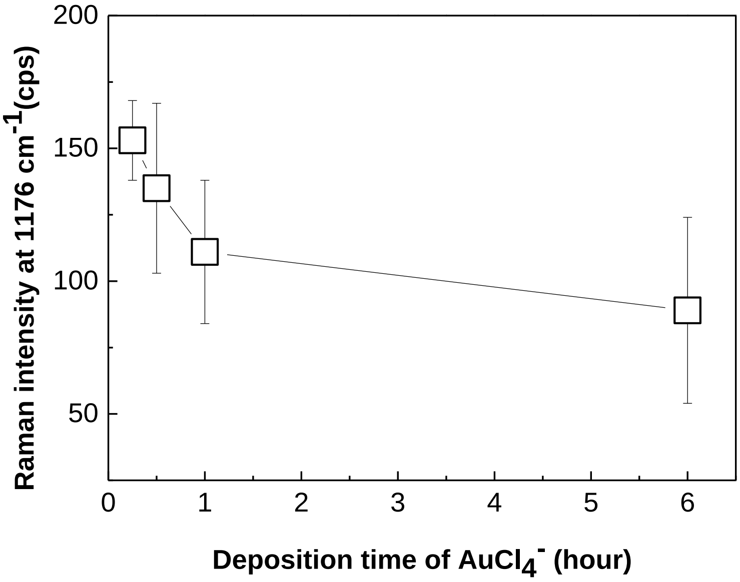

Figure 5.30 Relative intensity plot at 1176 cm^{-1} of Au NPs embedded 19 layers of PAH/TA multilayer films as a function of deposition time of $AuCl_4^-$.

5.9 Overview of Bimetallic Structures

Au-Ag bimetallic nanostructures include alloys and core@shell NPs such as (Ag@Au indicating Ag NP in the inner core and Au NP in the outer shell), and have been employed in literature mostly as catalysts and SERS substrates.[217,218] As mentioned in Section 1.10, they have received special interest due to their exceptional optical, electrical, catalytic and magnetic properties.[127] Especially core@shell and alloyed NPs have unique properties due to their sophisticated shape and composition, as well as the combination of properties from each individual element. However, both monometallic and bimetallic NPs in solution can aggregate without using an appropriate support. Therefore, immobilization of these NPs onto solid supports such as polymer matrices including polyelectrolyte multilayer were used to prevent aggregation of NPs.[219] Synthesis of bimetallic NPs as both core@shell and alloy in polyelectrolyte multilayers was explored in literature especially using thermal[220,221] and chemical reduction methods.[127,219,222] In this part of the study, photochemical synthesis of bimetallic nanostructures (Au and Ag NPs) on various types of multilayers and use of these polymer/bimetallic nanostructure platforms as SERS substrates have been investigated. In this context, sandwich-like structures consisting of sequential adsorption of PE multilayers and in-situ photosynthesized Au and/or Ag NPs were constructed. SERS activities of these multilayers have been studied.

5.9.1 The Effect of Film Architecture in Sandwich Structures Including Bimetallic NPs on SERS Enhancement

In situ post-synthesis of NPs were applied on PAH/TA multilayer films. Briefly, Ag^+/$AuCl_4^-$ ions were loaded into multilayer films and then these films were exposed to Xe light for the formation of Ag/Au NPs. Different from *in situ* post-synthesis, this part includes PAH/TA multilayer formation, loading of Ag^+/$AuCl_4^-$ ions, exposure of the Ag^+/$AuCl_4^-$-loaded films to Xe light for NP formation. After NP formation, a sequential coating of PAH/TA multilayers was applied, followed by loading of Ag^+ and $AuCl_4^-$ ions onto the new multilayers. The films were once again exposed to Xe light for NP formation on the same substrate, as illustrated in Figure 2.7. 0.5 M $AgNO_3$ and 5.0 mM $AuCl_4^-$ were continued to use as deposition concentration values for loading of these ions into the films such as explained in Section 5.1 to obtain reproducible SER signal from different points of the same substrate. Moreover, 6 h and 15 min deposition times were used as immersion periods for Ag^+ and $AuCl_4^-$, respectively such as in Section 5.2. The experimental design of the substrates is explained as follows. Briefly, 10 layers of PAH/TA were immersed into 0.5 M $AgNO_3$ for 6 h and then,1 h Xe radiation was exposed to the substrate (Substrate ‘a’- including only Ag NPs). An additional 9 layers of PAH/TA was coated onto this substrate and then it was immersed into 5.0 mM $AuCl_4^-$ followed by 1 h Xe lamp radiation (Substrate ‘b’-including Au NPs onto Ag NPs). Substrate ‘c’ included only Au NPs on 9 layers of PAH/TA and substrate ‘d’ corresponded to reverse order of substrate ‘b’. A summary of the components of the substrates is shown in Table 5.1.

Prepared films loaded with NPs are denoted shortly as $(PAH/TA)_nAg_m$ or $(PAH/TA)_nAu_m$, where n and m is the number of deposited PAH/TA layer number and number of loading/reduction cycles for NP formation, respectively. Thereafter, schematic representation of the substrates is given in Figure 5.31.

Table 5.1. List of multilayer PAH/TA substrates including *in situ* photosynthesized Au and/or Ag NPs prepared in this part of the study.

Substrate **a**, $(PAH/TA)_{10}Ag_1$	10 L PAH/TA+ 6 h $AgNO_3$+ 1 h Xe
Substrate **b**, $(PAH/TA)_{10}Ag_1/(PAH/TA)_9Au_1$	10 L PAH/TA+ 6 h $AgNO_3$ + 1 h Xe +9 L PAH/TA+ 15 min $AuCl_4^-$+ 1 h Xe
Substrate **c**, $(PAH/TA)_9Au_1$	9 L PAH/TA+ 15 min $AuCl_4^-$+ 1 h Xe
Substrate **d**, $(PAH/TA)_9Au_1/(PAH/TA)_{10}Ag_1$	9 L PAH/TA+ 15 min $AuCl_4^-$ + 1 h Xe +10 L PAH/TA+ 6 h $AgNO_3$+ 1 h Xe

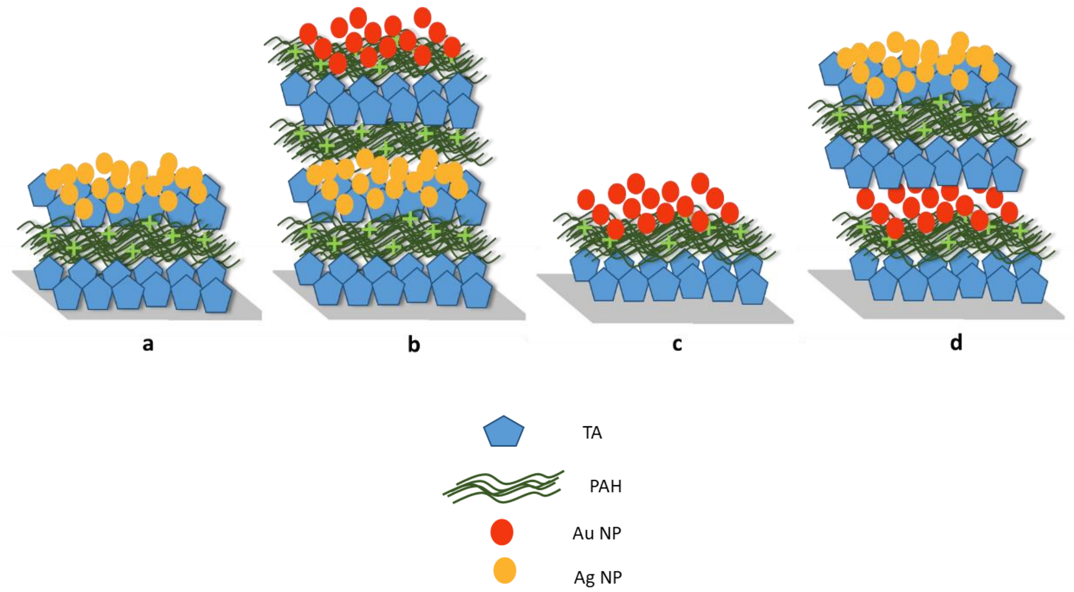

Figure 5.31 Schematic representation of multilayer PAH/TA substrates including *in situ* photosynthesized Au and/or Ag NPs.

Figure 5.32 shows UV-vis absorption spectra of the substrates listed in Table 5.1. $(PAH/TA)_{10}Ag_1$ shows its characteristic surface plasmon peak of Ag NPs at around 420 nm. In Section 5.1, Ag NPs on twenty layers of PAH/TA was shown to have surface plasmon resonance (SPR) at 435 nm (Figure 5.1). Therefore, decrease in multilayer number resulted in ~15 nm blue shift in the spectra showing smaller size of NP formation and lower amount of Ag NPs as understood from lower absorbance values as shown in Figures 5.32 than Figure 5.1. On the other hand, broadening of spectrum as compared to twenty layers of PAH/TA led to aggregated NPs. Additional coating of $(PAH/TA)_{10}Ag_1$ with 9 layers of PAH/TA and immersion of it into $AuCl_4^-$ dominated broad-sized Au NP formation. SPR peak related to Ag NPs around 420 nm in this $(PAH/TA)_{10}Ag_1/(PAH/TA)_9Au_1$ substrate were not measured in UV-vis absorption spectrum of this film (Figure 5.32). Moreover, substrate $(PAH/TA)_9Au_1$ included characteristic surface plasmon peak of Au NPs, and additional coating of it with PAH/TA and immersion into $AgNO_3$ resulted in formation of Ag NPs together with Au NPs in substrate $(PAH/TA)_9Au_1/(PAH/TA)_{10}Ag_1$. The spectrum of substrate 'd' in Figure 5.32

displayed approximately double-peak spectral line shape, which a feature of Au@Ag (core@shell) NPs and is indicative of their plasmonic properties.[223,224] The presence of the new bands at around 410 nm and 540 nm might indicate the formation of Ag shell on the Au core (Figure 5.32, d). The combined optical characteristics of the bimetallic core-shell NPs might result in the emergence of both high-energy and low-energy SPRs.[127] On the other hand, when creating NPs from a mixture of gold and silver (Au−Ag alloy NPs), there is a single SPR band. The position of this band falls between the plasmon positions of pure Au and Ag NPs with the exact location depending on the composition of the alloy.[225] Zhang and coworkers also reported that impact of covering Au cores with Ag shells on the plasmon spectrum is visible through a shift towards the blue end of the spectrum for the low-energy plasmon resonance and the appearance of a new high-energy peak around 420 nm for PDADMAC/PSS multilayers.[127]

SER spectra of substrate ‘a’, ‘b’, ‘c’ and ‘d’ are shown in Figure 5.33. There were 3 times increase in SER signal as going from substrate ‘c’, $(PAH/TA)_9Au_1$ to ‘d’, $(PAH/TA)_9Au_1/(PAH/TA)_{10}Ag_1$ in Table 5.1. On the other hand, there was no difference between signals of ‘a’, $(PAH/TA)_{10}Ag_1$ and ‘b’, $(PAH/TA)_{10}Ag_1/(PAH/TA)_9Au_1$. Besides, reproducibility of SER signal on substrate ‘b’ was observed to be poor. In substrate ‘b’, effect of Ag NPs was seen on the surface which could be related to penetration depth of laser through Ag NPs. Since thickness of 10 layers of PAH/TA multilayer was found to be around ~10 nm, laser might have the ability to reach to Ag NPs for SERS ability of the substrate ‘b’. Same situation might be valid for substrate ‘d’, $(PAH/TA)_9Au_1/(PAH/TA)_{10}Ag_1$. That means laser can penetrate through Au NPs. However, plasmonically more active Ag NPs on top of the substrate might have more contribution on the SER signal of substrate ‘d’. SER signal intensities at 1176 cm^{-1} of substrates a to d were shown in Figure 5.34. Substrate ‘a’ was specified as a better SERS substrate in terms of larger S/N and better RSD values, because Ag NPs were plasmonically more active than Au NP due to proper electronic structure and dielectric function of Ag.[226]

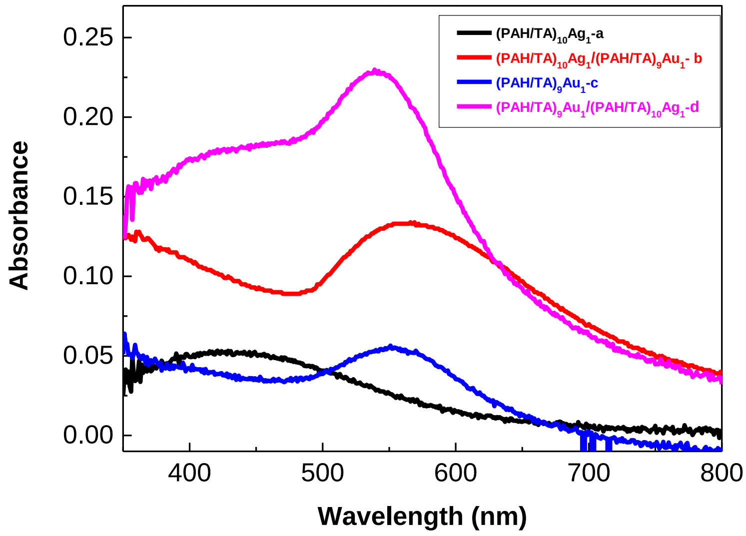

Figure 5.32 UV-vis absorption spectra of substrate a, b, c and d.

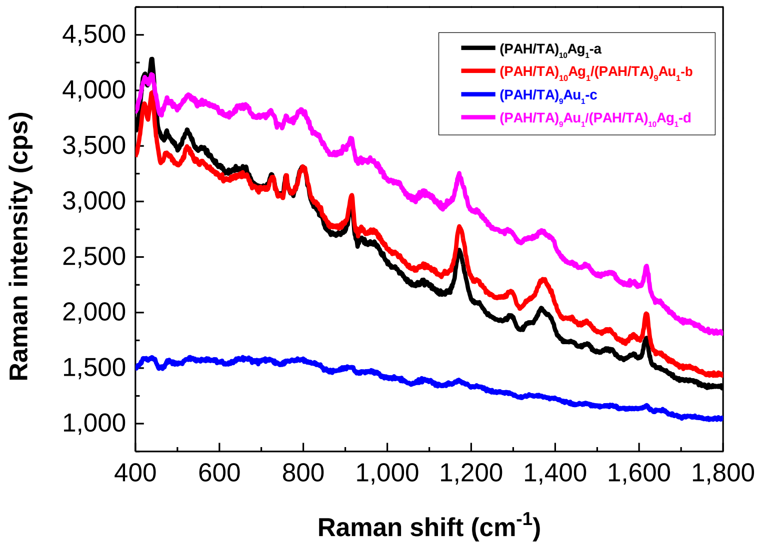

Figure 5.33 SER spectra of 1.0 x 10^{-5} M CV molecule on substrate a, b, c and d.

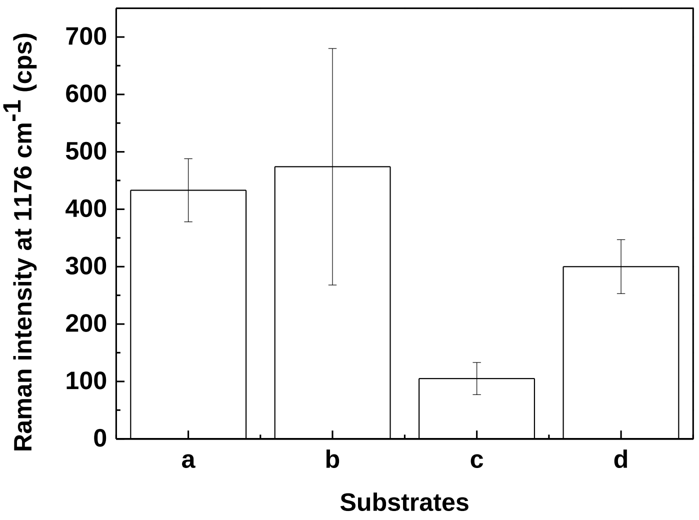

Figure 5.34 Relative intensity column plot at 1176 cm^{-1} of substrates a, b, c and d.

In Section 5.6, increasing of loading/reduction cycles on top of twenty layers of PAH/TA multilayer did not provide any additional enhancement in Raman signal (Figure 5.19) despite the increasing number of NP layers within PE multilayers. In this part of the study, instead of increasing of L/R cycle numbers on top of multilayers, these cycle numbers were increased within PAH/TA bilayers. For this purpose, PAH/TA bilayer were constructed on the glass slide and Ag^+ or $AuCl_4^-$ ions were loaded into the bilayer films and then these films were exposed to Xe light for the formation of Ag or Au NPs. This corresponds to 1 cycle of L/R of Ag/Au NPs and it is symbolized by 1c-Ag shown as ($(PAH/TA)_2Ag_1$) or 1 c-Au shown as ($(PAH/TA)_2Au_1$) in the text. In the same manner, (including bilayer coating of PAH/TA, loading of Ag^+/$AuCl_4^-$ ions and Xe exposure), these cycle numbers were repeated up to 6 times on the same substrate. Summary of the structures is represented in Table 5.2.

Table 5.2. Multilayer PAH/TA substrates including *in situ* photosynthesized Au and/or Ag NPs with 1, 2, 3, 4, 5 and 6 cycles of loading/reduction.

1 c-Ag	$(PAH/TA)_2Ag_1$
2 c-Ag	$[(PAH/TA)_2Ag_1]_2$
3 c-Ag	$[(PAH/TA)_2Ag_1]_3$
4 c-Ag	$[(PAH/TA)_2Ag_1]_4$
5 c-Ag	$[(PAH/TA)_2Ag_1]_5$
6 c-Ag	$[(PAH/TA)_2Ag_1]_6$
1 c-Au	$(PAH/TA)_2Au_1$
2 c-Au	$[(PAH/TA)_2Au_1]_2$
3 c-Au	$[(PAH/TA)_2Au_1]_3$
4 c-Au	$[(PAH/TA)_2Au_1]_4$
5 c-Au	$[(PAH/TA)_2Au_1]_5$
6 c-Au	$[(PAH/TA)_2Au_1]_6$
3 c-Au+ 3 c-Ag	$[(PAH/TA)_2Au_1]_3/ [(PAH/TA)_2Ag_1]_3$
3 c-Ag+ 3 c-Au	$[(PAH/TA)_2Ag_1]_3/ [(PAH/TA)_2Au_1]_3$

The schematic representation of 6c-Ag, 6c-Au, 3c-Au+3c-Ag and 3c-Ag+3c-Au was demonstrated in Figure 5.35.

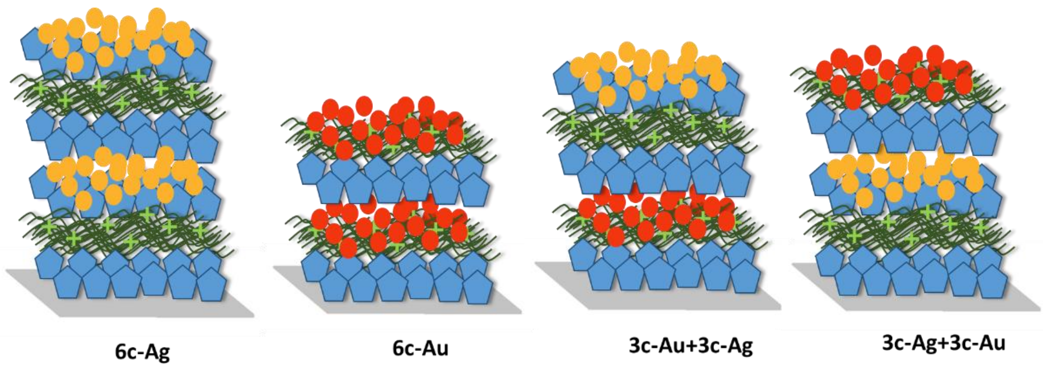

Figure 5.35 Representation of multilayer PAH/TA substrates including *in situ* photosynthesized Au and/or Ag NPs with 6 cycles of loading/reduction.

Each substrate was analyzed after each L/R cycle was completed in order to observe the effect of the cycle number on SER signals in these structures. UV-vis absorption spectra of sandwich structures including 1 to 6 L/R cycles within bilayers of PAH/TA are shown in Figure 5.36 (including only L/R cycles for formation of *Ag NPs*) and Figure 5.37 (including only L/R cycles for formation of *Au NPs*).

Application of each L/R cycle increased the amount of Ag NPs formed at the sandwich structures with red-shifting and broadening in SPR band of Ag NPs (Figure 5.36). Figure 5.37 also shows that the intensity of SPR band signatures of absorption spectra are in accordance with the increase size of Ag NPs. It is obvious that with the increase in L/R cycle and more Ag^+ are reduced, captured by LbL films and this results in the increase size of Ag NPs. Furthermore, increased coverage of immobilized NPs, the absorption band shifts towards longer wavelengths as the LbL assembly continues.[227] On the other hand, Au NP numbers were densified with increasing cycles without affecting the maximum wavelength (Figure 5.37). This is because the plasmon resonance of Au NPs within the size range of 3 to 40 nm is observed nearly at the fixed wavelength.[127] Additionally, 6 L/R cycles including only Au (6c-Au) or only Ag NPs (6c-Ag) and bimetallic NPs (3c-Au+3c-Ag and 3c-Ag+3c-Au) in these sandwiches were compared to observe SPR band and SERS characteristics of multilayers. These four multilayers include same number of polyelectrolyte layers (PAH/TA), but they have different order and different composition of NPs. Figure 5.38 shows the comparison of UV-vis absorption spectra of 6c-Ag, 6c-Au, 3c-Ag+3c-Au and 3c-Ag+3c-Au substrates. Selected concentration and deposition time in this study were 0.5 M and 6 h for $AgNO_3$, respectively based on SER intensity and minimum fluctuation on the substrate. Negatively charged phenolate groups in TA were used for attachment of Ag^+ cations. On the other hand, positively charged amine groups were used as binding sites for $AuCl_4^-$ complex anions. Deposition concentration and time for $AuCl_4^-$ were selected in this study as 5.0 mM and 15 min, respectively for adequate binding and reducing of NPs. In literature, loading concentration values of $AuCl_4^-$ into amine containing polymers was varied between 2.0 mM to 40.0 mM.[162,163,214] On the other hand, Velentanlic and coworkers used deposition concentration values of Ag^+ cations in polycarboxylic acid films as high as 0.5 M.[160] Therefore, deposition concentration values were selected based on the literature experimental conditions for loading of the ions in multilayer films. Thereafter, deposition time studies were continued.

When UV-vis absorption spectra of 6c-Ag and 6c-Au substrates (Figure 5.38) were compared, it was observed that more Ag^+ ions were held by negatively charged TA molecules. As a result, more Ag NPs were formed on the surface as compared to limited binding of gold complex ion to amine groups to form Au NPs. Additionally, bimetallic NPs in between bilayers led to significant background increase and that might be attributed to light scattering properties of the NP-dense substrates. When observing 3c-Ag+3c-Au substrate, ($[(PAH/TA)_2Ag_1]_3/[(PAH/TA)_2Au_1]_3$), Au NPs were seen (Figure 5.38), but not as dominant as in the substrate of $(PAH/TA)_{10}Ag_1/(PAH/TA)_9Au_1$ (Figure 5.32). This could be attributed to lower loading capacity of $AuCl_4^-$ ions into thinner PAH/TA bilayers as compared to 9-layers of PAH/TA. Moreover, there were also no SPR peak related with Ag NPs in 3c-Ag+3c-Au (Figure 5.38). The other bimetallic substrate in Figure 5.38 corresponded to (3c-Au+3c-Ag, $[(PAH/TA)_2Au_1]_3/[(PAH/TA)_2Ag_1]_3$). The amount of NPs related with SPR peak intensities of 3c-Au+3c-Ag were higher than that of 3c-Ag+3c-Au substrate based on Figure 5.38. Since only one peak was observed as SPR peaks (~550 nm and ~530 nm for 3c-Ag+3c-Au and 3c-Au+3c-Ag substrates, respectively) and it was present in between only Ag and only Au NPs range for both substrates, alloy NPs might be formed.[228] Four substrates (6c-Ag, 6c-Au, 3c-Ag+3c-Au, 3c-Au+3c-Ag) are composed of same number of PAH/TA however, the difference in NP composition and order of NPs might lead to difference in NP amounts, NP arrangements and light scattering abilities from the surfaces of these substrates.

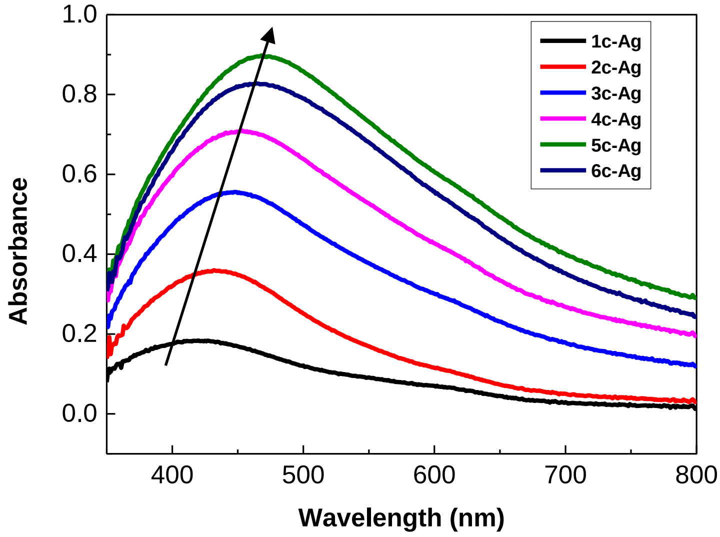

Figure 5.36 UV-vis absorption spectra of Ag NPs grown within bilayers of PAH/TA multilayer films, prepared by immersion into 0.50 M $AgNO_3$ solutions for 6 h, rinsed, dried and followed by 1 h of Xe radiation with different number of loading/reduction cycles. Arrow shows increase of absorption and red-shift of the plasmon resonance.

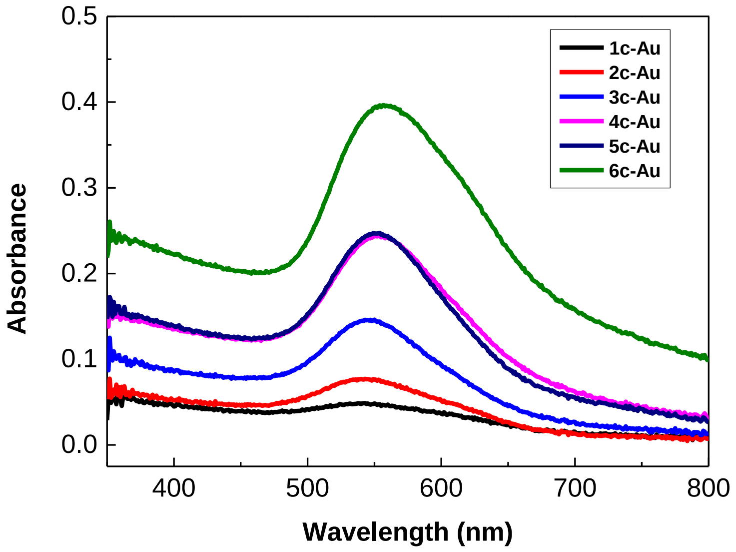

Figure 5.37 UV-vis absorption spectra of Au NPs grown within bilayers of PAH/TA multilayer films, prepared by immersion into 5.0 mM $AuCl_4^-$ solutions for 15 min, rinsed, dried and followed by 1 h of Xe radiation with different number of loading/reduction cycles.

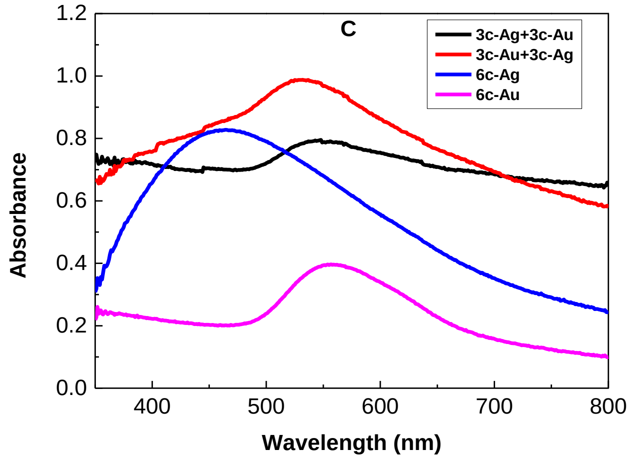

Figure 5.38 Comparison of UV-vis absorption spectra of only Ag or Au NPs grown within bilayers of PAH/TA multilayer films with 6 loading/reduction cycles and combination of Ag and Au NPs within bilayers of PAH/TA multilayer films with 6 total loading/reduction cycles.

SER spectra of CV molecule on only Ag NPs (substrates from 1c-Ag to 6c-Ag, shown in Figure 5.39), only Au NPs (substrates from 1c-Au to 6c-Au, shown in Figure 5.40) and bimetallic NPs (substrates of 3c-Ag+3c-Au and 3c-Au+3c-Ag) are shown in Figure 5.41. Although both number and aggregation of Ag NPs increased with each L/R cycles (Figure 5.36), intensity in SER signal increase was recorded approximately 1.5 times from 1 to 4 cycles together with similar intensities for 2, 3 and 4 cycle numbers (Figure 5.39). Increase in L/R cycles might have resulted in significant stacking of particles with relatively poor SERS performance. On the other hand, increase of Au NPs resulted in important increase of SER signal only for 6 cycles of Au NPs between bilayers (Figure 5.40). Number of Au NPs were densified with little broadening as shown in Figure 5.37, so loading of them without stacking provided increase in SER signal. Since loading of $AuCl_4^-$ was lower as compared to $AgNO_3$ for same cycle numbers, 6 cycles of L/R might be required for loading of enough NPs for enhancement in SER signal. Bimetallic NPs in these bilayer sandwich structures (3c-Ag+3c-Au and 3c-Au+3c-Ag) did not result in any significant increase in SER signal as shown in Figure 5.41 and their corresponding relative intensities at 1176 cm^{-1} in Figure 5.42. Instead of using 6 cycles of possibly aggregated Ag NPs (6c-Ag), 3 cycles of the Ag NPs with Au NPs (3c-Ag+ 3c-Au) might become beneficial to increase SER signal as shown in Figure 5.41. Lower amount of using Ag NPs with homogenous distribution might result in enhancement of the signal. However, 6 cycles of Au NPs (6c-Au) on the substrate were observed as more homogenously distributed and better signal were obtained as compared to other three substrates (Figure 5.42). Accordingly, hybrid system was seemed to have no advantage also here for Raman signal enhancement.

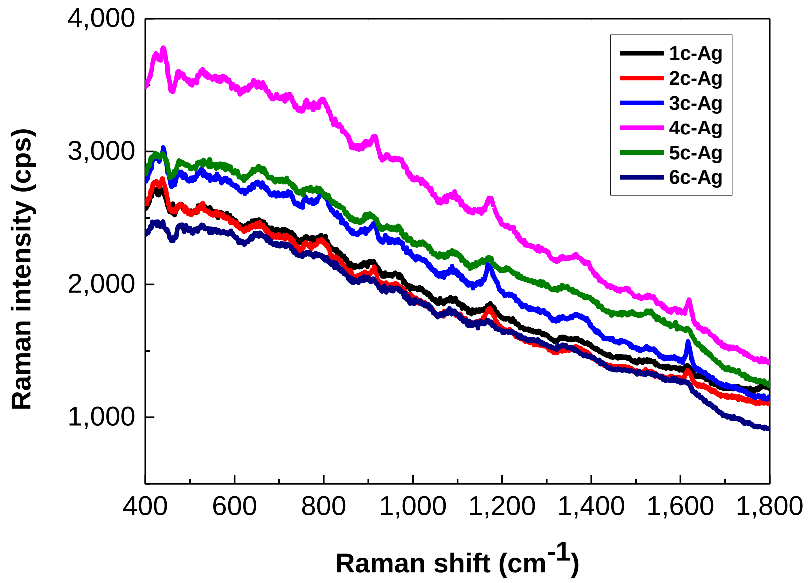

Figure 5.39 SER spectra of 1.0 x 10^{-5} M CV molecule on Ag NPs grown within bilayers of PAH/TA multilayer films, prepared by immersion into 0.50 M $AgNO_3$ solutions for 6 h, rinsed, dried and followed by 1 h of Xe radiation with different number of loading/reduction cycles.

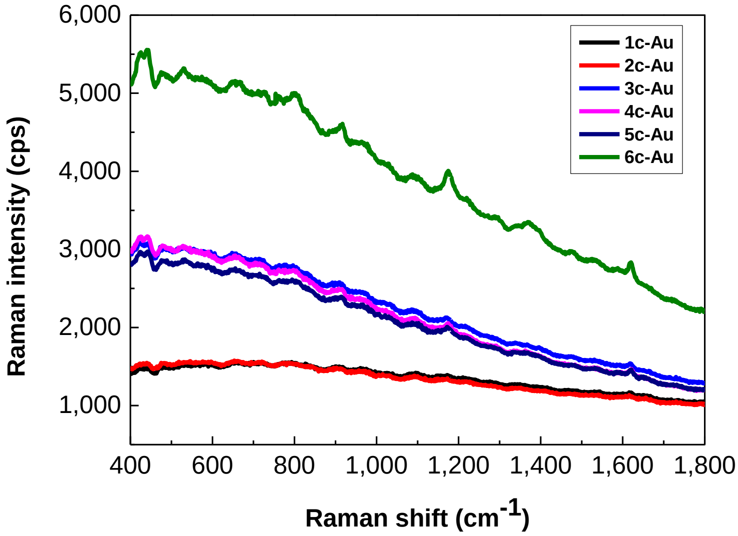

Figure 5.40 SER spectra of 1.0 x 10^{-5} M CV molecule on Au NPs grown within bilayers of PAH/TA multilayer films, prepared by immersion into 5.0 mM $AuCl_4^-$ solutions for 15 min, rinsed, dried and followed by 1 h of Xe radiation with different number of loading/reduction cycles.

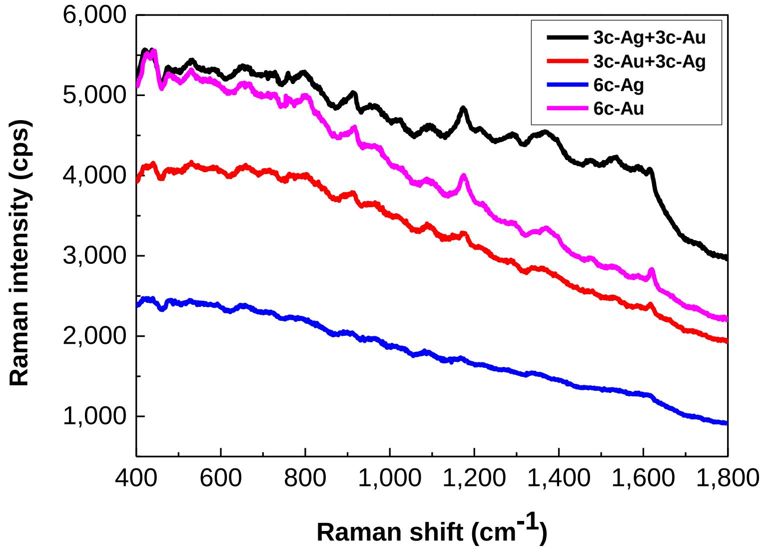

Figure 5.41 Comparison of SER spectra of 1.0 x 10^{-5} M CV molecule on only Ag or Au NPs grown within bilayers of PAH/TA multilayer films with 6 loading/reduction cycles and combination of Ag and Au NPs within bilayers of PAH/TA multilayer films with 6 total loading/reduction cycles.

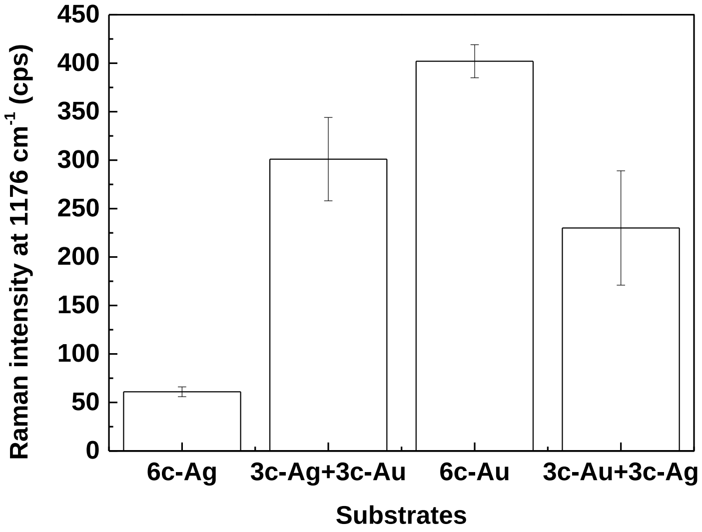

Figure 5.42 Relative intensity column plot at 1176 cm^{-1} of the substrates of only Ag or Au NPs grown within bilayers of PAH/TA multilayer films with 6 loading/reduction cycles and combination of Ag and Au NPs within bilayers of PAH/TA multilayer films with 6 total loading/reduction cycles.

5.9.2 The Effect of Chemical Nature of Polyelectrolytes Including Monometallic and/or Bimetallic NPs on SERS Enhancement

The effect of film architecture including bimetallic NPs on SER intensities was discussed for PAH/TA multilayers in Section 5.9.1. In this part, BPEI/TA pair was studied as SERS substrate. BPEI is expected to have more ion binding capacity resulting in higher loading of ions and reduction of more NPs.[160] Summary of the components of the substrates is shown in Table 5.3.

Table 5.3. Multilayer BPEI/TA substrates including *in situ* photosynthesized Au and/or Ag NPs.

Substrate **e**, $(BPEI/TA)_{10}Ag_1$	10 L BPEI/TA+ 6 h $AgNO_3$+ 1 h Xe
Substrate **f**, $(BPEI/TA)_{10}Ag_1/(BPEI/TA)_9Au_1$	10 L BPEI/TA+ 6 h $AgNO_3$ + 1 h Xe +9 L BPEI/TA+ 15 min $AuCl_4^-$+ 1 h Xe
Substrate **g**, $(BPEI/TA)_9Au_1$	9 L BPEI/TA+ 15 min $AuCl_4^-$+ 1 h Xe
Substrate **h**, $(BPEI/TA)_9Au_1/(BPEI/TA)_{10}Ag_1$	9 L BPEI/TA+ 15 min $AuCl_4^-$ + 1 h Xe +10 L BPEI/TA+ 6 h $AgNO_3$+ 1 h Xe

The schematic demonstration of these substrates was given in Figure 5.43.

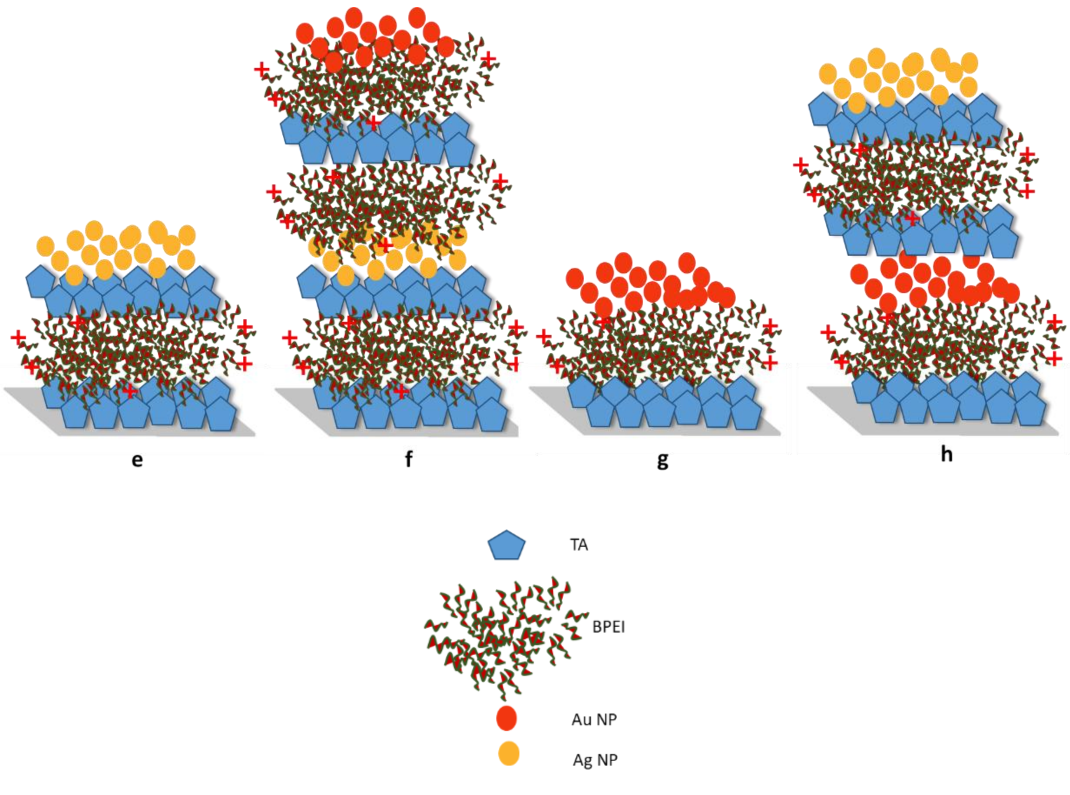

Figure 5.43 Schematic representation of multilayer BPEI/TA substrates including *in situ* photosynthesized Au and/or Ag NPs.

Figure 5.44 shows UV-vis absorption spectra of the 4 substrates including $(BPEI/TA)_{10}Ag_1$, $(BPEI/TA)_{10}Ag_1/(BPEI/TA)_9Au_1$, $(BPEI/TA)_9Au_1$ and $(BPEI/TA)_9Au_1/(BPEI/TA)_{10}Ag_1$. This system exhibited higher absorbance values for 4 substrates as compared to PAH/TA system. This could be attributed to ability of BPEI for higher ion binding capacity due to complexation of its amine groups with transition metal cations.[160,229] Higher loading of ions as compared to PAH and then reducing of the ions into NPs contributed increase of number of NPs on the films. $(BPEI/TA)_{10}Ag_1$ indicates its characteristic surface plasmon peak of Ag NPs at around 420 nm. Additional coating of $(BPEI/TA)_{10}Ag_1$ with BPEI/TA and immersion into $AuCl_4^-$ formed $(BPEI/TA)_{10}Ag_1/(BPEI/TA)_9Au_1$ substrate. Au NPs formation was dominated and no SPR peaks belonged to Ag NPs could be seen just like in $(PAH/TA)_{10}Ag_1/(PAH/TA)_9Au_1$ substrate (Figure 5.32). However, the spectrum of $(BPEI/TA)_{10}Ag_1/(BPEI/TA)_9Au_1$ showed significant broadening and red shifting compared to $(BPEI/TA)_9Au_1$ substrate (Figure 5.44), which only contained Au NPs. This suggests that $(BPEI/TA)_{10}Ag_1/(BPEI/TA)_9Au_1$ was able to accommodate a greater amount of Au NPs with a wider range of size distribution on its surface. In addition, Au NPs might be in the shell in $(BPEI/TA)_{10}Ag_1/(BPEI/TA)_9Au_1$ as understood from the red-shifted and broadened spectrum.[142] That means the possible core@shell structure of Ag@Au NPs ($(BPEI/TA)_{10}Ag_1/(BPEI/TA)_9Au_1$) shows an absorption band at 560 nm which is characteristics of grown Au NPs. On the other hand, bare Au NPs on $(BPEI/TA)_9Au_1$ substrate exhibits the band at 540 nm (Figure 5.44). This 20 nm shifting through longer wavelength with broadening might indicate the formation of Au NP shell dominated core-shell structure. As the thickness of the Au NP shell becomes thick, the intensity of Ag NP becomes broader, eventually reaching a point where it cannot be differentiated anymore.[230] This situation might occur in the $(BPEI/TA)_{10}Ag_1/(BPEI/TA)_9Au_1$ substrate. Additional coating of $(BPEI/TA)_9Au_1$ substrate with BPEI/TA and immersion into $AgNO_3$ produced spectrum of $(BPEI/TA)_9Au_1/(BPEI/TA)_{10}Ag_1$ (Figure 5.44). Since only one peak was observed for maximum wavelength and it was in between only Ag and only Au NPs range, this might be interpreted as alloy NPs formation.[228]

Figure 5.45 shows SER spectra of these 4 sandwich multilayers including $(BPEI/TA)_{10}Ag_1$, $(BPEI/TA)_{10}Ag_1/(BPEI/TA)_9Au_1$, $(BPEI/TA)_9Au_1$ and $(BPEI/TA)_9Au_1/(BPEI/TA)_{10}Ag_1$. Approximately 15 times increase in SER signal was recorded as going from substrate $(BPEI/TA)_9Au_1$ to $(BPEI/TA)_9Au_1/(BPEI/TA)_{10}Ag_1$. This can be explained by both a significant increase in the loading amount of NPs and greater size distribution on the substrate. This also agrees with greater SPR intensities and broadening of the spectrum belonged to substrate $(BPEI/TA)_9Au_1/(BPEI/TA)_{10}Ag_1$ in comparison to $(BPEI/TA)_9Au_1$ as seen in Figure 5.44. On the other hand, there were no significant differences between SER signals of substrates of $(BPEI/TA)_{10}Ag_1$ and $(BPEI/TA)_{10}Ag_1/(BPEI/TA)_9Au_1$, like in case of PAH/TA multilayers consisting of similar multilayers. Although UV-vis absorption spectra of substrates of $(BPEI/TA)_{10}Ag_1$ and $(BPEI/TA)_{10}Ag_1/(BPEI/TA)_9Au_1$ are different from each other (Figure 5.44), effect of Ag NPs could be observed on the surface related with penetration depth of laser through Ag NPs which is plasmonically more active than Au NPs.[226] SER signal intensities of substrates at 1176 cm^{-1} were summarized in Figure 5.46. Accordingly, BPEI/TA including bimetallic system consisting of Ag NPs on top of Au NPs ($(BPEI/TA)_9Au_1/(BPEI/TA)_{10}Ag_1$)) was seemed to be very beneficial to use not only for signal enhancement but also for high reproducibility of the SER signal on the same substrate. On the other hand, higher ion binding capacity of BPEI as compared to PAH might have a dominant effect for this SER signal increase in substrate of $(BPEI/TA)_9Au_1/(BPEI/TA)_{10}Ag_1$) as compared to $(BPEI/TA)_9Ag_1$. Therefore, 3-fold signal increase observed here was not accounted for the substrate going from $(PAH/TA)_9Ag_1$ to ($(PAH/TA)_9Au_1/(PAH/TA)_{10}Ag_1$).

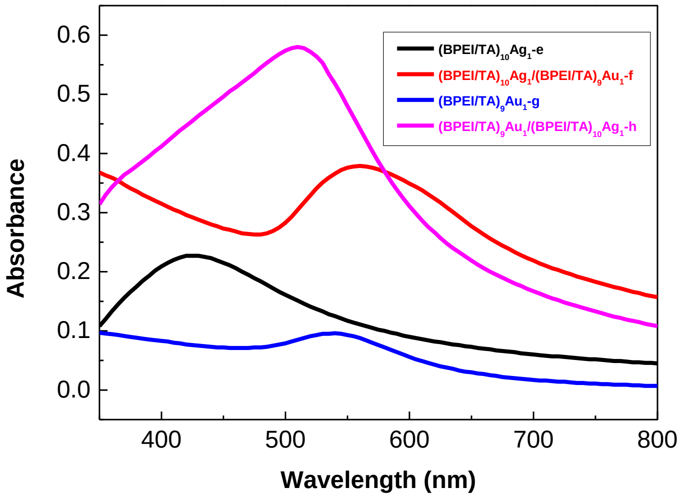

Figure 5.44 UV-vis absorption spectra of substrate e ($(BPEI/TA)_{10}Ag_1$), f ($(BPEI/TA)_{10}Ag_1/(BPEI/TA)_9Au_1$), g ($(BPEI/TA)_9Au_1$) and h ($(BPEI/TA)_9Au_1/(BPEI/TA)_{10}Ag_1$).

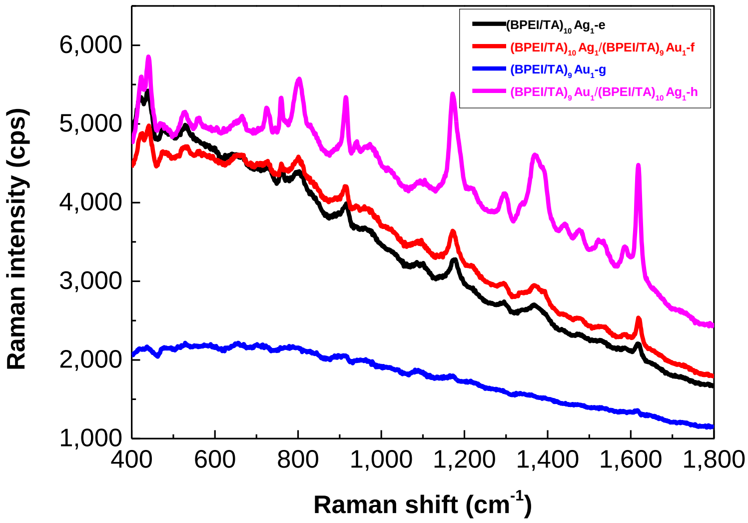

Figure 5.45 SER spectra of 1.0 x 10^{-5} M CV molecule on substrate e, f, g and h substrates.

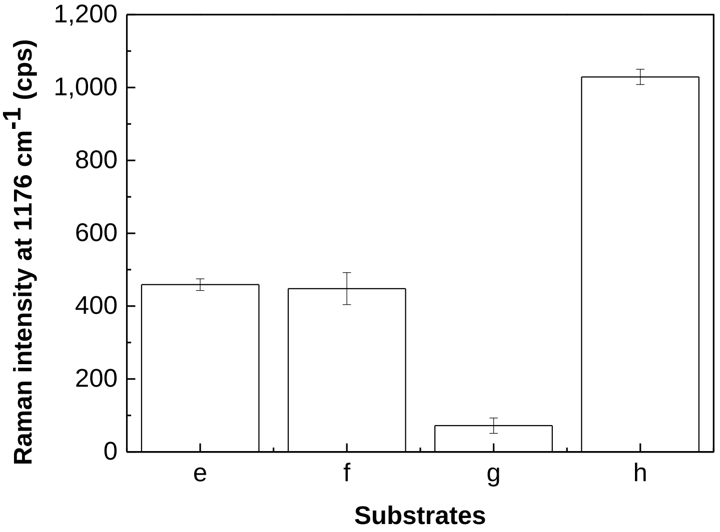

Figure 5.46 Relative intensity column plot at 1176 cm^{-1} of substrates e, f, g and h.

Of note, PAH/PSS and BPEI/PSS polyelectrolyte pairs with in-situ photoreduced NPs were also studied as SERS substrates. However, CV molecule on these substrates could not produce any SER signals. Therefore, further studies were not conducted with these substrates.

Using a nanoreactor to create metal NPs, hydrogen-bonded LbL assembled films might be a better option compared to electrostatic ones as they offer more uncharged groups to bind to metal ions.[165] In order to investigate this effect on SER signal, hydrogen-bonded multilayers with exponentially grown (PEO/TA) and linearly grown (PVCL/TA) were studied for photochemical formation of NPs. UV-vis absorption spectra of Ag and Au NPs including hydrogen-bonded (PEO/TA, PVCL/TA) and electrostatically formed multilayers (PAH/TA, BPEI/TA) are shown in Figures 5.47 and 5.48. The difference in internal film structures and loading capacity for ions to multilayers might be the primary factor affecting SPR intensities. Since PEO/TA films grow exponentially, higher Ag and Au loadings in thicker multilayers were expected as shown in both Figures 5.47 and 5.48. Ag NPs on PEO/TA multilayers were broader in size as compared to other multilayers as seen in Figure 5.47. On the other hand, Ag NPs on PVCL/TA might not have spherical shape or size distribution of Ag NPs on the surface are distributed in two regions as understood from two plasmon peaks of its spectrum. In this film system, PVCL and PEO behaved as hydrogen acceptor while TA was hydrogen donor while loading of Ag^+. While most of the hydrogens in TA groups are replaced by Ag^+ (seen in Figure 5.47), interaction of $AuCl_4^-$ groups with PVCL groups was not successful for Au NP formation on PVCL/TA substrate (Figure 5.48), because number of uncharged PVCL groups at pH 2.0 might not be enough for loading of $AuCl_4^-$ into linearly grown and hydrophobically interacted PVCL/TA multilayers. Since exponentially grown, rougher and thicker PEO/TA could offer more capability to immobilize $AuCl_4^-$, Au NP formation on its surface could be seen. In addition, higher ion binding capacity due to complexation of amine groups of BPEI with Ag^+ might contribute to obtain higher SPR intensities than that of PAH.[160] As a result, absorption signals of both NPs were higher in BPEI/TA than PAH/TA substrates.

SER signals of CV molecule on these 4 types of NP immobilized multilayers (PEO/TA, PVCL/TA, PAH/TA and BPEI/TA) are illustrated in Figure 5.49 and 5.50. Signals of Ag NP including substrates were not significantly different from each other (Figure 5.49). The signal belonged to $(PVCL/TA)_{10}Ag_1$ might be enhanced due to broad size distributed, Ag NPs as shown in Figure 5.47. Moreover, Ag NPs on PAH/TA substrates were also significantly broadened, and this contributed to the signal of $(PAH/TA)_{10}Ag_1$. Larger number of Ag NPs were loaded on BPEI/TA compare to PAH/TA substrates, but smaller size distribution on $(BPEI/TA)_{10}Ag_1$ might limit the increase in SER signal. Higher number and broader size distributed Ag NPs on the substrate $(PEO/TA)_{10}Ag_1$ did not increase the signal effectively as expected. This might be related to possibly excessive size of roughness features as a result of exponential growth of the film. SER signals of CV molecule on Au NP containing films $(PAH/TA)_9Au_1$, $(BPEI/TA)_9Au_1$, $(PVCL/TA)_9Au_1$, $(PEO/TA)_9Au_1$ substrates) did not enhance SER signals (Figure 5.50). This possibly related to lower plasmonic activity of Au NPs as compared to Ag NPs. Moreover, lower amount of Au NPs on the substrates might negatively affect the results.

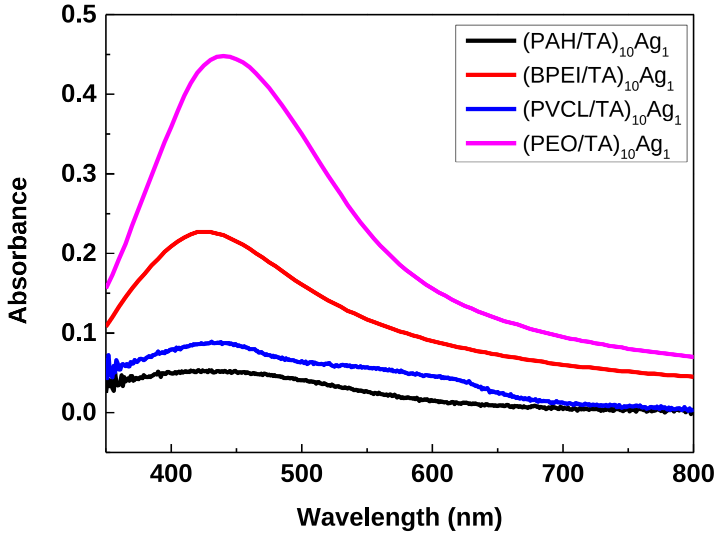

Figure 5.47 UV-vis absorption spectra of $(PAH/TA)_{10}Ag_1$, $(BPEI/TA)_{10}Ag_1$, $(PVCL/TA)_{10}Ag_1$, $(PEO/TA)_{10}Ag_1$ substrates.

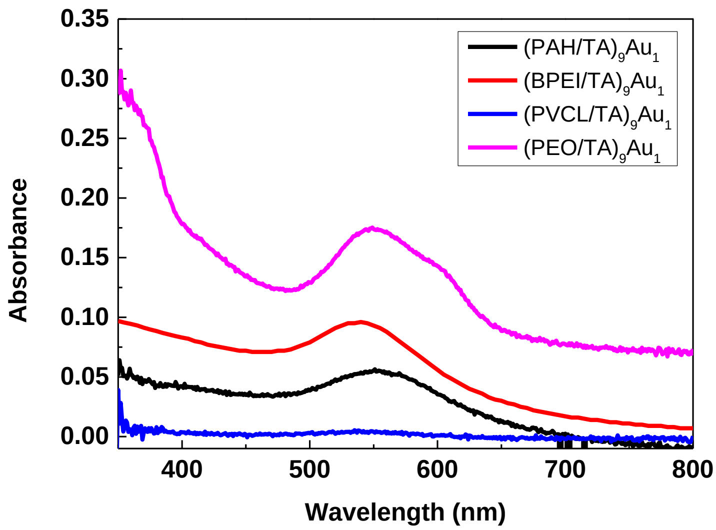

Figure 5.48 UV-vis absorption spectra of $(PAH/TA)_9Au_1$, $(BPEI/TA)_9Au_1$, $(PVCL/TA)_9Au_1$, $(PEO/TA)_9Au_1$ substrates.

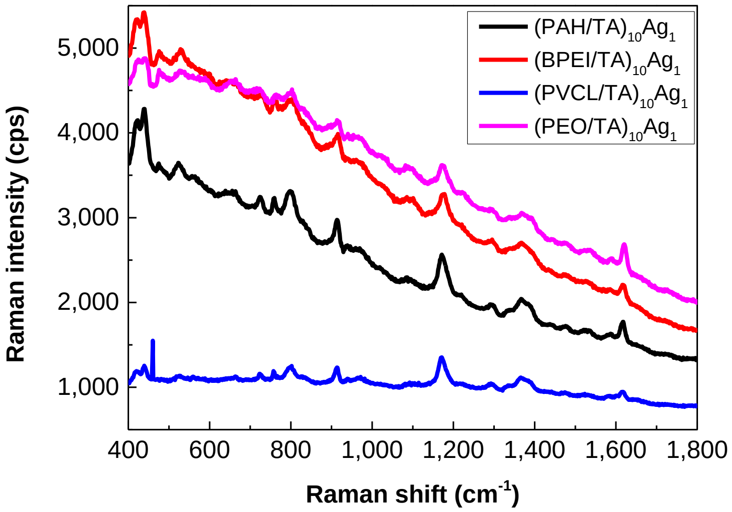

Figure 5.49 SER spectra of 1.0 x10^{-5} M CV molecule on $(PAH/TA)_{10}Ag_1$, $(BPEI/TA)_{10}Ag_1$, $(PVCL/TA)_{10}Ag_1$, $(PEO/TA)_{10}Ag_1$ substrates.

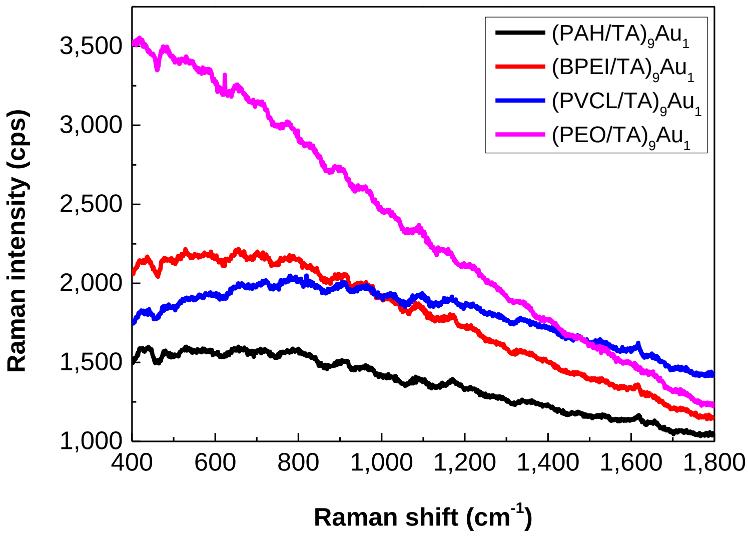

Figure 5.50 SER spectra of 1.0 x10^{-5} M CV molecule on $(PAH/TA)_9Au_1$, $(BPEI/TA)_9Au_1$, $(PVCL/TA)_9Au_1$, $(PEO/TA)_9Au_1$ substrates.

CHAPTER 6

CONCLUSION AND OUTLOOK

The main aim of this study was to develop sensitive and reproducible SERS substrates in multilayers. Moreover, the relationship between these multiayers and SER signals of the probe molecule in NP containing structures were aimed to be understood. In this concept, SER signals were examined to enhance with both post-loaded NPs and sandwich-model LbL structures, where chemically reduced Au NPs (negatively or positively charged) were included. Additionally, LbL structures were also investigated as *in situ* photochemical template for Ag and/or Au NP synthesis for SERS enhancement. All LbL self-assembled films used in this thesis study contributed homogenous distribution of NPs resulting in reproducible and repeatable SER signals on the substrates.

In chapter 3, the effect of chemical nature of polyanion, surface morphology and film architecture on SER signals were explored. The substrates were based on LbL deposition of PAH using two polyacids, i.e. PAA and TA. Furthermore, water-soluble complexes of PAH were prepared with either PAA or TA and LbL deposited at the surface using PAA or TA to control the surface morphology. PAH and PAA formed exponentially growing LbL films with smooth surface morphology, whereas PAH and TA resulted in linearly growing films with highly rough surface morphology. Both multilayers were post-loaded with chemically synthesized citrate-capped Au NPs and compared with respect to SER signal intensity using CV as the probe molecule. Au NPs containing PAH/TA multilayers provided 10 times higher SER signal intensity as compared to PAH/PAA multilayers including Au NPs. The EF of PAH/TA was calculated as 10^6. The EF for PAH/TA films was found to be ~15 times larger than EF of PAH/PAA multilayers. The increased Raman signal obtained from PAH/TA films as SER substrates can be explained by the highly localized electric field regions that are formed between the numerous neighboring islands on rough surfaces. For PAH/TA multilayers, limit of detection was determined as 1.0×10^{-6} M for CV molecule by signal to noise ratio of ~4. Importantly, higher SER signal from CV molecule was obtained with Au NPs post-loaded PAH and TA multilayers than with sandwich-like PAH/Au NPs. This was possibly due to weaker signals with multiple deposition steps of Au NPs by red-shifting of their plasmon bands (~650 nm) with exceeding excitation wavelengths of the laser (633 nm). Moreover, rougher surface of post-loaded Au NPs of PAH/TA multilayer (56 nm) contributed more enhanced signal as compared to smoother surfaces of sandwich multilayers (~5 nm to 14 nm). Au NPs post-loaded PAH/TA multilayers displayed acceptable reproducibility and homogeneity. The reproducibility of SER signal was calculated as 12% and 18% RSD for point-to-point and substrate-to-substrate variations, respectively. Of note, no significant increase in roughness values were recorded with using polyelectrolyte complex including films. As a result of that, critical SERS enhancement did not occur with using them.

In Chapter 4, BPEI-capped (seed-mediated) Au NPs were synthesized to obtain large-sized NPs in solution (~50-60 nm) before incorporating it into the films using TA or PSS for SERS enhancement. Since size of NPs is one of the critical parameters to be controlled for SER signal enhancement, this part was planned to optimize size of NPs in solution. Although local electromagnetic field enhances with increase of particle size, less absorption of light and less inelastic scattering by very large particles result in decrease in SER signal. In this respect, the basic difference of this chapter in terms of NP size from the Chapter 3 is getting large-sized NPs firstly in solution in order to get better SER signals. Citrate-capped NPs size in solution were relatively small (~10 nm) in Chapter 3. In Chapter 4, the function of BPEI was both stabilizing and size-controlling reagent of NPs. In the seed growth step, the concentrations of both BPEI and seed solutions affected the size of Au NPs and these were investigated with UV-vis absorption spectroscopy and DLS measurements.

Accordingly, decreased concentration of BPEI as compared to larger concentration of seed particles at the final growth solution pH of 5.0 were proper in terms of obtaining desired size and preventing aggregation. Depositing 1-layer of BPEI-capped NPs onto the glass slides with varying deposition times resulted in irreproducible SER signals attributed to low coverage of NPs on the surface. In order to overcome irreproducibility of SER signals, LbL deposition of BPEI-capped Au NPs with either TA or PSS was examined. Among two systems, 3 layers of BPEI-capped NPs/TA and 9 layers of BPEI-capped NPs/PSS multilayers provided better SER signal intensity as compared to other deposition layer numbers either thinner or thicker films within their own LbL systems. The increase in SER intensity might be attributed to possibly increasing density of highly localized regions accessible to the adsorbed CV molecules between neighboring NPs. Moreover, LbL assembly enabled to develop more reproducible SER signals from the film surfaces as compared to 1-layer coated films.

In Chapter 5, PE films were used as templates for *in situ* photosynthesis of Ag and/or Au NPs. Various PEs such as PAH, BPEI, PAA, and TA were used as the building blocks for the multilayer film formation. Ag^+ or $AuCl_4^-$ ions were loaded into LbL films based on the proper electrostatic attraction and these films were exposed to Xe radiation. The effects of Ag^+ or $AuCl_4^-$ concentration, Ag^+ or $AuCl_4^-$ absorption time, the number of PE layers, loading/reduction cycle and exposure time of radiation on the amount, size and aggregation of NPs were followed. Accordingly, twenty layers of PAH/TA worked well for *in situ* synthesis of Ag NPs using Xe radiation. One loading/reduction cycle on these multilayers was adequate to obtain reproducible SER signals. However, deposition of Au NPs on top of PAH/TA layers could not record any critical SER signal enhancement for CV molecule. Moreover, bimetallic NPs in between bilayers and 10-layers of PAH/TA did not provide significant SERS enhancement as compared to monometallic counterparts of PAH/TA multilayers. On the other hand, using of bimetallic sandwich structures including BPEI/TA with Ag NPs on the top of multilayer might be promising SER substrate for significant signal enhancement. Higher ion binding capacity of BPEI in comparison to PAH might have a dominant effect for 3 times increase in SER signal of the substrate including BPEI/TA with Ag NPs on the top of multilayer as compared to PAH/TA including multilayer counterpart.

All in all, post-incorporated Au NPs included PAH/TA multilayers with enabling high surface roughness was best suited system for SERS enhancement for Chapter 3. For Chapter 4, LbL system incorporating alternatively BPEI-capped NPs and TA or PSS gave best SERS enhancement for this part with providing more homogenous distribution of SER signal. For Chapter 5, *in situ* photoreduced Ag NPs in PAH/TA multilayers gave best SER signals among monometallic NPs including multilayer systems. Ag^+ deposition concentration, absorption time and exposure time of Xe light were critical parameters to be controlled in this respect. Among bimetallic systems, BPEI/TA multilayer films including Ag NPs at the top and Au NPs at the middle of multilayer provide best SER signal.

Overall, this study generated fundamental knowledge on understanding structure-property and SER signal relationship in LbL-assembled SERS substrates. Considering the potential need of reproducible substrates in various SERS applications, these results might form a basis for development of controlled substrates. LbL-self assembly enabled homogenous and intense coating of NPs on solid substrates, resulting in reproducible SER signals. On the other hand, it is still difficult to control many parameters simultaneously (such as surface morphology, number of NPs on the surface, aggregation, and distance between NPs and size of NPs) for the formation of NPs. Yet, PAH/TA multilayer system incorporated with Au NPs might be promising to further explore salt-induced aggregation and pH variation of polyelectrolyte couple for more sensitive and reproducible SERS platform production. For analytical purposes, the need for high sensitivity, efficiency and reproducibility is obvious for SERS substrates. However, optimization studies on the optical and chemical properties of substrates are crucial. In this respect, a close collaboration between theoretical modeling and practical experimentation is essential. This collaboration will be important for gaining a more profound comprehension of most relevant factors and achieving the successful adoption of SERS as a common analytical technique.

REFERENCES

1. Petry, Renate, Schmitt, Michael & Popp, Jürgen. Raman Spectroscopy—A Prospective Tool in the Life Sciences. *ChemPhysChem* **4**, 14–30 (2003).

2. Skoog, D., Holler, F. J. & Crouch, S. R. *Principles of Instrumental Analysis*. (David Harris, 2007).

3. Graham, Duncan. The next Generation of Advanced Spectroscopy: Surface Enhanced Raman Scattering from Metal Nanoparticles. *Angew. Chemie - Int. Ed.* **49**, 9325–9327 (2010).

4. Kneipp, Katrin, Kneipp, Harald, Itzkan, Irving, Dasari, Ramachandra R. & Feld, Michael S. Surface-Enhanced Raman Scattering and Biophysics. *J. Phys. Condens. Matter* **14**, R597–R624 (2002).

5. Lohumi, Santosh, Kim, Moon S., Qin, Jianwei & Cho, Byoung Kwan. Improving Sensitivity in Raman Imaging for Thin Layered and Powdered Food Analysis Utilizing a Reflection Mirror. *Sensors (Basel).* **19**, (2019).

6. Sharma, Bhavya, Frontiera, Renee R., Henry, Anne-Isabelle, Ringe, Emilie & Van Duyne, Richard P. SERS: Materials, Applications, and the Future. *Mater. Today* **15**, 16–25 (2012).

7. Fleischmann, M., Hendra, P. J. & McQuillan, A. J. Raman Spectra of Pyridine Adsorbed at a Silver Electrode. *Chem. Phys. Lett.* **26**, 163–166 (1974).

8. Jeanmaire, David L. & Van Duyne, Richard P. Surface Raman Spectroelectrochemistry. Part I. Heterocyclic, Aromatic, and Aliphatic Amines Adsorbed on the Anodized Silver Electrode. *J. Electroanal. Chem.* **84**, 1–20 (1977).

9. Albrecht, M. Grant & Creighton, J. Alan. Anomalously Intense Raman Spectra of Pyridine at a Silver Electrode. *J. Am. Chem. Soc.* **99**, 5215–5217 (1977).

10. Moskovits, Martin. Surface-Enhanced Spectroscopy. *Rev. Mod. Phys.* **57**, 783–826 (1985).

11. Álvarez-Puebla, Ramón A. Effects of the Excitation Wavelength on the SERS Spectrum. *J. Phys. Chem. Lett.* **3**, 857–866 (2012).

12. Schatz, George C., Young, Matthew A. & Van Duyne, Richard P. Electromagnetic Mechanism of SERS. *Top. Appl. Phys.* **103**, 19–46 (2006).

13. Robinson, G. W. Surface-Enhanced Raman Effect. *Chem. Phys. Lett.* **76**, 191–195 (1980).

14. Stiles, Paul L., Dieringer, Jon a, Shah, Nilam C. & Van Duyne, Richard P. Surface-Enhanced Raman Spectroscopy. *Annu. Rev. Anal. Chem* **1**, 601–626 (2008).

15. Moskovits, M. Surface Roughness and the Enhanced Intensity of Raman Scattering by Molecules Adsorbed on Metals. *J. Chem. Phys.* **69**, 4159–4161 (1978).

16. Asiala, Steven M. & Schultz, Zachary D. Characterization of Hotspots in a Highly Enhancing SERS Substrate. *Analyst* **136**, 4472–4479 (2011).

17. Alexander, Kristen D., Skinner, Kwan, Zhang, Shunping, Wei, Hong & Lopez, Rene. Tunable SERS in Gold Nanorod Dimers through Strain Control on an Elastomeric Substrate. *Nano Lett.* **10**, 4488–4493 (2010).

18. Lee, Seung Joon, Morrill, Andrew R. & Moskovits, Martin. Hot Spots in Silver Nanowire Bundles for Surface-Enhanced Raman Spectroscopy. *J. Am. Chem. Soc.* **128**, 2200–2201 (2006).

19. Maher, Robert C. SERS Hot Spots. *Raman Spectrosc. Nanomater. Charact.* **9783642206207**, 215–260 (2011).

20. Zhao, Yuda, Liu, Xin, Lei, Dang Yuan & Chai, Yang. Effects of Surface Roughness of Ag Thin Films on Surface-Enhanced Raman Spectroscopy of Graphene: Spatial Nonlocality and Physisorption Strain. *Nanoscale* **6**, 1311–1317 (2014).

21. Lee, Changwon, Robertson, Christopher S., Nguyen, An H., Kahraman, Mehmet & Wachsmann-Hogiu, Sebastian. Thickness of a Metallic Film, in Addition to Its Roughness, Plays a Significant Role in SERS Activity. *Sci. Rep.* **5:11644**, 1–10 (2015).

22. Kennedy, B. J., Spaeth, S., Dickey, M. & Carron, K. T. Determination of the Distance Dependence and Experimental Effects for Modified Sers Substrates Based on Self-Assembled Monolayers Formed Using Alkanethiols. *J. Phys. Chem. B* **103**, 3640–3646 (1999).

23. Dieringer, Jon A., McFarland, Adam D., Shah, Nilam C., Stuart, Douglas A., Whitney, Alyson V., Yonzon, Chanda R., Young, Matthew A., Zhang, Xiaoyu & Van Duyne, Richard P. Surface Enhanced Raman Spectroscopy: New Materials, Concepts, Characterization Tools, and Applications. in *Faraday Discussions* (2006).

24. Israelsen, Nathan D., Hanson, Cynthia & Vargis, Elizabeth. Nanoparticle Properties and Synthesis Effects on Surface-Enhanced Raman Scattering Enhancement Factor: An Introduction. *Sci. World J.* **2015**, 1–12 (2015).

25. Singh, Anant Kumar, Khan, Sadia Afrin, Fan, Zhen, Demeritte, Teresa, Senapati, Dulal, Kanchanapally, Rajashekhar & Ray, Paresh Chandra. Development of a Long-Range Surface-Enhanced Raman Spectroscopy Ruler. *J. Am. Chem. Soc.* **134**, 8662–8669 (2012).

26. Kukushkin, V. I., Van'kov, A. B. & Kukushkin, I. V. Long-Range Manifestation of Surface-Enhanced Raman Scattering. *JETP Lett.* **98**, 64–69 (2013).

27. Ko, Hyunhyub, Singamaneni, Srikanth & Tsukruk, Vladimir V. Nanostructured Surfaces and Assemblies as SERS Media. *Small* **4**, 1576–1599 (2008).

28. Kelly, K. Lance, Coronado, Eduardo, Zhao, Lin Lin & Schatz, George C. The Optical Properties of Metal Nanoparticles: The Influence of Size, Shape, and Dielectric Environment. *J. Phys. Chem. B* **107**, 668–677 (2003).

29. Quinten, M. The Color of Finely Dispersed Nanoparticles. *Appl. Phys. B Lasers Opt.* **73**, 317–326 (2001).

30. Pustovit, V. N. & Shahbazyan, T. V. Quantum-Size Effects in SERS from Noble-Metal Nanoparticles. *Microelectronics J.* **36**, 559–563 (2005).

31. Boca, Sanda C., Farcau, Cosmin & Astilean, Simion. The Study of Raman Enhancement Efficiency as Function of Nanoparticle Size and Shape. *Nucl. Instruments Methods Phys. Res. Sect. B Beam Interact. with Mater. Atoms* **267**, 406–410 (2009).

32. Hong, Seongmin & Li, Xiao. Optimal Size of Gold Nanoparticles for Surface-Enhanced Raman Spectroscopy under Different Conditions. *J. Nanomater.* **2013**, 1–9 (2013).

33. Stamplecoskie, Kevin G., Scaiano, Juan C., Tiwari, Vidhu S. & Anis, Hanan. Optimal Size of Silver Nanoparticles for Surface-Enhanced Raman Spectroscopy. *J. Phys. Chem. C* **115**, 1403–1409 (2011).

34. Xu, Hongxing, Aizpurua, Javier, Käll, Mikael & Apell, Peter. Electromagnetic Contributions to Single-Molecule Sensitivity in Surface-Enhanced Raman Scattering. *Phys. Rev. E - Stat. Physics, Plasmas, Fluids, Relat. Interdiscip. Top.* **62**, 4318–4324 (2000).

35. Xu, H., Bjerneld, E. J., Käll, M. & Börjesson, L. Spectroscopy of Single Hemoglobin Molecules by Surface Enhanced Raman Scattering. *Phys. Rev. Lett.* **83**, 4357–4360 (1999).

36. Rodríguez-Lorenzo, Laura, Álvarez-Puebla, Ramón A., Pastoriza-Santos, Isabel, Mazzucco, Stefano, Stéphan, Odile, Kociak, Mathieu, Liz-Marzán, Luis M. & De Abajo, F. Javier García. Zeptomol Detection through Controlled Ultrasensitive Surface-Enhanced Raman Scattering. *J. Am. Chem. Soc.* **131**, 4616–4618 (2009).

37. Li, Kuiru, Stockman, Mark I. & Bergman, David J. Self-Similar Chain of Metal Nanospheres as an Efficient Nanolens. *Phys. Rev. Lett.* **91**, 227402-1-227402–4 (2003).

38. McFarland, Adam D., Young, Matthew A., Dieringer, Jon A. & Van Duyne, Richard P. Wavelength-Scanned Surface-Enhanced Raman Excitation Spectroscopy. *J. Phys. Chem. B* **109**, 11279–11285 (2005).

39. Abalde-Cela, Sara, Ho, Szushen, Rodríguez-González, Benito, Correa-Duarte, Miguel A., Álvarez-Puebla, Ramón A., Liz-Marzán, Luis M. & Kotov, Nicholas A. Loading of Exponentially Grown LBL Films with Silver Nanoparticles and Their Application to Generalized SERS Detection. *Angew. Chemie - Int. Ed.* **48**, 5326–5329 (2009).

40. Davies, Rachel A., Chong, Ngee S. & Ooi, Beng Guat. Chemical Enhancement of the Surface Enhanced Raman Scattering Signals of Anilines via Their *Ortho*-Substituents. *Opt. Photonics J.* **2013**, 13–23 (2013).

41. Kruszewski, Stefan & Skonieczny, J. Roughness Effects in Surface Enhanced Raman Scattering - Evidence for Electromagnetic and Charge Transfer Enhancement Mechanism. *Acta Phys. Pol. A* **80**, 611–620 (1991).

42. Le Ru, E. C., Blackie, E., Meyer, M. & Etchegoint, P. G. Surface Enhanced Raman Scattering Enhancement Factors: A Comprehensive Study. *J. Phys. Chem. C* **111**, 13794–13803 (2007).

43. Natan, Michael J. Concluding Remarks. *Faraday Discuss.* **132**, 321–328 (2006).

44. Lin, Xiu Mei, Cui, Yan, Xu, Yan Hui, Ren, Bin & Tian, Zhong Qun. Surface-Enhanced Raman Spectroscopy: Substrate-Related Issues. *Anal. Bioanal. Chem.* **394**, 1729–1745 (2009).

45. Sabur, Alia, Havel, Mickael & Gogotsi, Yury. SERS Intensity Optimization by Controlling the Size and Shape of Faceted Gold Nanoparticles. *J. Raman Spectrosc.* **39**, 61–67 (2008).

46. Schwartzberg, Adam M., Grant, Christian D., Wolcott, Abraham, Talley, Chad E., Huser, Thomas R., Bogomolni, Roberto & Zhang, Jin Z. Unique Gold Nanoparticle Aggregates as a Highly Active Surface-Enhanced Raman Scattering Substrate. *J. Phys. Chem. B* **108**, 19191–19197 (2004).

47. Tian, Furong, Bonnier, Franck, Casey, Alan, Shanahan, Anne E. & Byrne, Hugh J. Surface Enhanced Raman Scattering with Gold Nanoparticles: Effect of Particle Shape. *Anal. Methods* **6**, 9116–9123 (2014).

48. Stewart, S. & Fredericks, P. M. Surface-Enhanced Raman Spectroscopy of Amino Acids Adsorbed on an Electrochemically Prepared Silver Surface. *Spectrochim. Acta - Part A Mol. Biomol. Spectrosc.* **55**, 1641–1660 (1999).

49. Szafranski, Cory A., Tanner, Weslene, Laibinis, Paul E. & Garrell, Robin L. Surface-Enhanced Raman Spectroscopy of Aromatic Thiols and Disulfides on Gold Electrodes. *Langmuir* **14**, 3570–3579 (1998).

50. Yue, Weisheng, Wang, Zhihong, Yang, Yang, Chen, Longqing, Syed, Ahad, Wong, Kimchong & Wang, Xianbin. Electron-Beam Lithography of Gold Nanostructures for Surface-Enhanced Raman Scattering. *J. Micromechanics Microengineering* **22**, 125007-1-125007–9 (2012).

51. Cinel, Neval A., Bütün, Serkan, Ertaş, Gülay & Özbay, Ekmel. 'Fairy Chimney'-Shaped Tandem Metamaterials as Double Resonance SERS Substrates. *Small* **9**, 531–537 (2013).

52. Tan, R. Z., Agarwal, A., Balasubramanian, N., Kwong, D. L., Jiang, Y., Widjaja, E. & Garland, M. 3D Arrays of SERS Substrate for Ultrasensitive Molecular Detection. *Sensors Actuators, A Phys.* **139**, 36–41 (2007).

53. Liu, Monan, Sun, Li, Cheng, Chuanwei, Hu, Hailong, Shen, Zexiang & Fan, Hong Jin. Highly Effective SERS Substrates Based on an Atomic-Layer-Deposition-Tailored Nanorod Array Scaffold. *Nanoscale* **3**, 3627–3630 (2011).

54. Yin, Guilin, Bai, Shiheng, Tu, Xinglong, Li, Zheng, Zhang, Yanpeng, Wang, Weiming, Lu, Jing & He, Dannong. Highly Sensitive and Stable SERS Substrate Fabricated by Co-Sputtering and Atomic Layer Deposition. *Nanoscale Res. Lett.* **14**, 1–7 (2019).

55. Roca, Maryuri & Haes, Amanda J. Silica-Void-Gold Nanoparticles: Temporally Stable Surface-Enhanced Raman Scattering Substrates. *J. Am. Chem. Soc.* **130**, 14273–14279 (2008).

56. Muehlethaler, Cyril, Leona, Marco & Lombardi, John R. Towards a Validation of Surface-Enhanced Raman Scattering (SERS) for Use in Forensic Science: Repeatability and Reproducibility Experiments. *Forensic Sci. Int.* **268**, 1–13 (2016).

57. Zhu, Chuhong, Meng, Guowen, Huang, Qing, Zhang, Zhuo, Xu, Qiaoling, Liu, Guangqiang, Huang, Zhulin & Chu, Zhaoqin. Ag Nanosheet-Assembled Micro-Hemispheres as Effective SERS Substrates. *Chem. Commun.* **47**, 2709–2727 (2011).

58. Abu Hatab, Nahla A., Oran, Jenny M. & Sepaniak, Michael J. Surface-Enhanced Raman Spectroscopy Substrates Created via Electron Beam Lithography and Nanotransfer Printing. *ACS Nano* **2**, 377–385 (2008).

59. Clément, Nicolas, Patriarche, Gilles, Smaali, Kacem, Vaurette, François, Nishiguchi, Katsuhiko, Troadec, David, Fujiwara, Akira & Vuillaume, Dominique. Large Array of Sub-10-Nm Single-Grain Au Nanodots for Use in Nanotechnology. *Small* **7**, 2607–2613 (2011).

60. Schönhoff, Monika & Bieker, Peter. Linear and Exponential Growth Regimes of Multilayers of Weak Polyelectrolytes in Dependence on PH. *Macromolecules* **43**, 5052–5059 (2010).

61. Shiratori, S. S. & Rubner, M. F. PH-Dependent Thickness Behavior of Sequentially Adsorbed Layers of Weak Polyelectrolytes. *Macromolecules* **33**, 4213–4219 (2000).

62. Choi, Jeeyoung & Rubner, Michael F. Influence of the Degree of Ionization on Weak Polyelectrolyte Multilayer Assembly. *Macromolecules* **38**, 116–124 (2005).

63. Elzbieciak-Wodka, Magdalena, Kolasińska-Sojka, Marta, Nowak, Paweł & Warszyński, Piotr. Comparison of Permeability of Poly(Allylamine Hydrochloride)/and Poly(Diallyldimethylammonium Chloride)/Poly(4-Styrenesulfonate) Multilayer Films: Linear vs. Exponential Growth. *J. Electroanal. Chem.* **738**, 195–202 (2015).

64. Picart, C., Picart, C., Mutterer, J., Richert, L., Luo, Y., Prestwich, G. D., Schaaf, P., Voegel, J. C. & Lavalle, P. Molecular Basis for the Explanation of the Exponential Growth of Polyelectrolyte Multilayers. *Proc. Natl. Acad. Sci. U. S. A.* **99**, 12531–12535 (2002).

65. Porcel, Claudine, Lavalle, Philippe, Ball, Vincent, Decher, Gero, Senger, Bernard, Voegel, Jean Claude & Schaaf, Pierre. From Exponential to Linear Growth in Polyelectrolyte Multilayers. *Langmuir* **22**, 4376–4383 (2006).

66. Decher, Gero. Fuzzy Nanoassemblies: Toward Layered Polymeric Multicomposites. *Science (80-.).* **277**, 1232–1237 (1997).

67. Iler, R. K. Multilayers of Colloidal Particles. *J. Colloid Interface Sci.* **21**, 569–594 (1966).

68. Dai, Jinhua & Bruening, Merlin L. Catalytic Nanoparticles Formed by Reduction of Metal Ions in Multilayered Polyelectrolyte Films. *Nano Lett.* **2**, 497–501 (2002).

69. Mhlanga, N., Domfe, T. & Skepu, A. Fabrication of Surface Enhanced Raman Spectroscopy Substrates on Solid Supports. *Appl. Surf. Sci.* **476**, 1108–1117 (2019).

70. Liu, Zhicheng, Yan, Zhaodong & Bai, Lu. Layer-by-Layer Assembly of Polyelectrolyte and Gold Nanoparticle for Highly Reproducible and Stable SERS Substrate. *Appl. Surf. Sci.* **360**, 437–441 (2016).

71. Shutava, Tatsiana, Prouty, Malcolm, Kommireddy, Dinesh & Lvov, Yuri. PH Responsive Decomposable Layer-by-Layer Nanofilms and Capsules on the Basis of Tannic Acid. *Macromolecules* **38**, 2850–2858 (2005).

72. Lu, Conghua, Möhwald, Helmuth & Fery, Andreas. Plasmon Resonance Tunable by Deaggregation of Gold Nanoparticles in Multilayers. *J. Phys. Chem. C* **111**, 10082–10087 (2007).

73. Dhar, Joydeep & Patil, Satish. Self-Assembly and Catalytic Activity of Metal Nanoparticles Immobilized in Polymer Membrane Prepared via Layer-by-Layer Approach. *ACS Appl. Mater. Interfaces* **4**, 1803–1812 (2012).

74. Ruths, J., Essler, F., Decher, G. & Riegler, H. Polyelectrolytes I: Polyanion/Polycation Multilayers at the Air/Monolayer/Water Interface as Elements for Quantitative Polymer Adsorption Studies and Preparation of Hetero-Superlattices on Solid Surfaces. *Langmuir* **16**, 8871–8878 (2000).

75. Sun, Bin, Jewell, Christopher M., Fredin, Nathaniel J. & Lynn, David M. Assembly of Multilayered Films Using Well-Defined, End-Labeled Poly(Acrylic Acid): Influence of Molecular Weight on Exponential Growth in a Synthetic Weak Polyelectrolyte System. *Langmuir* **23**, 8452–8459 (2007).

76. Kharlampieva, Eugenia, Kozlovskaya, Veronika, Chan, Jennifer, Ankner, John F. & Tsukruk, Vladimir V. Spin-Assisted Layer-by-Layer Assembly: Variation of Stratification as Studied with Neutron Reflectivity. *Langmuir* **25**, 14017–14024 (2009).

77. Tang, Kan & Besseling, Nicolaas A. M. Formation of Polyelectrolyte Multilayers: Ionic Strengths and Growth Regimes. *Soft Matter* **12**, 1032–1040 (2016).

78. Guzmán, Eduardo, Rubio, Ramón G. & Ortega, Francisco. A Closer Physico-Chemical Look to the Layer-by-Layer Electrostatic Self-Assembly of Polyelectrolyte Multilayers. *Adv. Colloid Interface Sci.* **282**, 102197 (2020).

79. Guzmán, Eduardo, Ritacco, Hernán A., Ortega, Francisco & Rubio, Ramón G. Growth of Polyelectrolyte Layers Formed by Poly(4-Styrenesulfonate Sodium Salt) and Two Different Polycations: New Insights from Study of Adsorption Kinetics. *J. Phys. Chem. C* **116**, 15474–15483 (2012).

80. Taketa, Thiago Bezerra & Beppu, Marisa Masumi. Layer-by-Layer Thin Films of Alginate/Chitosan and Hyaluronic Acid/Chitosan with Tunable Thickness and Surface Roughness. *Mater. Sci. Forum* **783**–**786**, 1226–1231 (2014).

81. Das, Biswa P. & Tsianou, Marina. From Polyelectrolyte Complexes to Polyelectrolyte Multilayers: Electrostatic Assembly, Nanostructure, Dynamics, and Functional Properties. *Adv. Colloid Interface Sci.* **244**, 71–89 (2017).

82. Thünemann, Andreas F., Müller, Martin, Dautzenberg, Herbert, Joanny, Jean-François & Löwen, Hartmut. Polyelectrolyte Complexes. *Adv. Comput. Simul. Approaches Soft Matter Sci. I* **166**, 113–171 (2004).

83. Guo, Yongmei, Geng, Wei & Sun, Junqi. Layer-by-Layer Deposition of Polyelectrolyte-Polyelectrolyte Complexes for Multilayer Film Fabrication. *Langmuir* **25**, 1004–1010 (2009).

84. Zhang, Lianbin, Li, Yang, Sun, Junqi & Shen, Jiacong. Mechanically Stable Antireflection and Antifogging Coatings Fabricated by the Layer-by-Layer Deposition Process and Postcalcination. *Langmuir* (2008).

85. Liu, Xiaokong, Dai, Boya, Zhou, Lu & Sun, Junqi. Polymeric Complexes as Building Blocks for Rapid Fabrication of Layer-by-Layer Assembled Multilayer

Films and Their Application as Superhydrophobic Coatings. *J. Mater. Chem.* **19**, 497–504 (2009).

86. Zhang, L. & Sun, J. Layer-by-Layer Deposition of Polyelectrolyte Complexes for the Fabrication of Foam Coatings with High Loading Capacity. *Chem. Commun.* **26**, 3901–3903 (2009).

87. Li, Yang, Wang, Xu & Sun, Junqi. Layer-by-Layer Assembly for Rapid Fabrication of Thick Polymeric Films. *Chem. Soc. Rev.* **41**, 5998–6009 (2012).

88. McAloney, Richard A., Sinyor, Mark, Dudnik, Vyacheslav & Cynthia Goh, M. Atomic Force Microscopy Studies of Salt Effects on Polyelectrolyte Multilayer Film Morphology. *Langmuir* **17**, 6655–6663 (2001).

89. Alaqad, Khalid & Saleh, Tawfik A. Gold and Silver Nanoparticles: Synthesis Methods, Characterization Routes and Applications towards Drugs. *J Env. Anal Toxicol* **6**, 384 (2016).

90. Khan, Ibrahim, Saeed, Khalid & Khan, Idrees. Nanoparticles: Properties, Applications and Toxicities. *Arab. J. Chem.* **12**, 908–931 (2019).

91. Lin, Sheng Kai & Cheng, Wen Tung. Fabrication and Characterization of Colloidal Silver Nanoparticle via Photochemical Synthesis. *Mater. Lett.* **261**, 127077 (2020).

92. Jara, Nicole, Milán, Nataly S., Rahman, Ashiqur, Mouheb, Lynda, Boffito, Daria C., Jeffryes, Clayton & Dahoumane, Si Amar. Photochemical Synthesis of Gold and Silver Nanoparticles—A Review. *Mol. 2021, Vol. 26, Page 4585* **26**, 4585 (2021).

93. Dahoumane, Si Amar, Wijesekera, Kushlani, Filipe, Carlos D. M. & Brennan, John D. Stoichiometrically Controlled Production of Bimetallic Gold-Silver Alloy Colloids Using Micro-Alga Cultures. *J. Colloid Interface Sci.* **416**, 67–72 (2014).

94. Bárta, J., Procházková, L., Vaněček, V., Kuzár, M., Nikl, M. & Čuba, V. Photochemical Synthesis of Nano- and Micro-Crystalline Particles in Aqueous Solutions. *Appl. Surf. Sci.* **479**, 506–511 (2019).

95. Dhand, Chetna, Dwivedi, Neeraj, Loh, Xian Jun, Jie Ying, Alice Ng, Verma, Navin Kumar, Beuerman, Roger W., Lakshminarayanan, Rajamani & Ramakrishna, Seeram. Methods and Strategies for the Synthesis of Diverse Nanoparticles and Their Applications: A Comprehensive Overview. *RSC Adv.* **5**, 105003–105037 (2015).

96. De Freitas, Lucas Freitas, Varca, Gustavo Henrique Costa, Batista, Jorge Gabriel Dos Santos & Lugão, Ademar Benévolo. An Overview of the Synthesis of Gold Nanoparticles Using Radiation Technologies. *Nanomaterials* **8**, (2018).

97. Gonzalez-Martinez, I. G., Bachmatiuk, A., Bezugly, V., Kunstmann, J., Gemming, T., Liu, Z., Cuniberti, G. & Rümmeli, M. H. Electron-Beam Induced Synthesis of Nanostructures: A Review. *Nanoscale* **8**, 11340–11362 (2016).

98. Kim, Myungjoon, Osone, Saho, Kim, Taesung, Higashi, Hidenori & Seto, Takafumi. Synthesis of Nanoparticles by Laser Ablation: A Review. *KONA Powder Part. J.* **2017**, 80–90 (2017).

99. Gabriel, Juliana S., Gonzaga, Virgínia A. M., Poli, Alessandra L. & Schmitt, Carla C. Photochemical Synthesis of Silver Nanoparticles on Chitosans/Montmorillonite Nanocomposite Films and Antibacterial Activity. *Carbohydr. Polym.* **171**, 202–210 (2017).

100. Jiang, Ke & Pinchuk, Anatoliy O. Noble Metal Nanomaterials: Synthetic Routes, Fundamental Properties, and Promising Applications. *Solid State Phys. - Adv. Res. Appl.* **66**, 131–211 (2015).

101. McNamara, Karrina & Tofail, Syed A. M. Nanoparticles in Biomedical Applications. *Adv. Phys. X* **2**, 54–88 (2017).

102. Huang, Xiaohua, Jain, Prashant K., El-Sayed, Ivan H. & El-Sayed, Mostafa A. Gold Nanoparticles: Interesting Optical Properties and Recent Applications in Cancer Diagnostics and Therapy. *Nanomedicine* **2**, 681–693 (2007).

103. Amirjani, Amirmostafa, Firouzi, Farzad & Haghshenas, Davoud Fatmehsari. Predicting the Size of Silver Nanoparticles from Their Optical Properties. *Plasmonics* **15**, 1077–1082 (2020).

104. Edison, Thomas Nesakumar Jebakumar Immanuel, Lee, Yong Rok & Sethuraman, Mathur Gopalakrishnan. Green Synthesis of Silver Nanoparticles Using Terminalia Cuneata and Its Catalytic Action in Reduction of Direct Yellow-12 Dye. *Spectrochim. Acta - Part A Mol. Biomol. Spectrosc.* **161**, 122–129 (2016).

105. Sondi, Ivan & Salopek-Sondi, Branka. Silver Nanoparticles as Antimicrobial Agent: A Case Study on E. Coli as a Model for Gram-Negative Bacteria. *J. Colloid Interface Sci.* **275**, 177–182 (2004).

106. Faraday, M. X. The Bakerian Lecture. —Experimental Relations of Gold (and Other Metals) to Light. *Philos. Trans. R. Soc. London* **147**, 145–181 (1857).

107. Szymondy, R. *The Chemistry of Colloids*. (Wiley, 1917).

108. Turkevich, John, Stevenson, Peter Cooper & Hillier, James. A Study of the Nucleation and Growth Processes in the Synthesis of Colloidal Gold. *Discuss. Faraday Soc.* **11**, 55–75 (1951).

109. Murphy, Catherine J., Sau, Tapan K., Gole, Anand M., Orendorff, Christopher J., Gao, Jinxin, Gou, Linfeng, Hunyadi, Simona E. & Li, Tan. Anisotropic Metal Nanoparticles: Synthesis, Assembly, and Optical Applications. *J. Phys. Chem. B* **109**, 13857–13870 (2005).

110. Zou, Xiangqin, Ying, Erbo & Dong, Shaojun. Seed-Mediated Synthesis of Branched Gold Nanoparticles with the Assistance of Citrate and Their Surface-Enhanced Raman Scattering Properties. *Nanotechnology* **17**, 4758–4764 (2006).

111. Kumar, Dhiraj, Mutreja, Isha & Sykes, Peter. Seed Mediated Synthesis of Highly Mono-Dispersed Gold Nanoparticles in the Presence of Hydroquinone. *Nanotechnology* **27**, 355601 (2016).

112. Bastús, Neus G., Comenge, Joan & Puntes, Víctor. Kinetically Controlled Seeded Growth Synthesis of Citrate-Stabilized Gold Nanoparticles of up to 200 Nm: Size Focusing versus Ostwald Ripening. *Langmuir* **27**, 11098–11105 (2011).

113. Jana, N. R., Gearheart, L. & Murphy, C. J. Seed-Mediated Growth Approach for Shape-Controlled Synthesis of Spheroidal and Rod-like Gold Nanoparticles Using a Surfactant Template. *Adv. Mater.* (2001).

114. Nikoobakht, Babak & El-Sayed, Mostafa A. Preparation and Growth Mechanism of Gold Nanorods (NRs) Using Seed-Mediated Growth Method. *Chem. Mater.* (2003).

115. Philip, Anish, Ankudze, Bright & Pakkanen, Tuula T. Polyethylenimine-Assisted Seed-Mediated Synthesis of Gold Nanoparticles for Surface-Enhanced Raman Scattering Studies. *Appl. Surf. Sci.* **444**, 243–252 (2018).

116. Philip, Anish, Lihavainen, Jenna, Keinänen, Markku & Pakkanen, Tuula T. Gold Nanoparticle-Decorated Halloysite Nanotubes – Selective Catalysts for Benzyl Alcohol Oxidation. *Appl. Clay Sci.* **143**, 80–88 (2017).

117. Erola, Markus O. A., Philip, Anish, Ahmed, Tanzir, Suvanto, Sari & Pakkanen, Tuula T. Fabrication of Au- and Ag–SiO2 Inverse Opals Having Both Localized Surface Plasmon Resonance and Bragg Diffraction. *J. Solid State Chem.* **230**, 209–217 (2015).

118. Zhao, Chong & Zhou, Benqing. Polyethyleneimine-Based Drug Delivery Systems for Cancer Theranostics. *J. Funct. Biomater. 2023, Vol. 14, Page 12* **14**, 12 (2022).

119. Ankudze, Bright, Philip, Anish & Pakkanen, Tuula T. Controlled Synthesis of High Yield Polyhedral Polyethylenimine-Capped Gold Nanoparticles for Real-

Time Reaction Monitoring by SERS. *Sensors Actuators B Chem.* **265**, 668–674 (2018).

120. Pandey, Prem C., Pandey, Govind & Narayan, Roger J. Controlled Synthesis of Polyethylenimine Coated Gold Nanoparticles: Application in Glutathione Sensing and Nucleotide Delivery. *J. Biomed. Mater. Res. Part B Appl. Biomater.* **105**, 1191–1199 (2017).

121. Sakamoto, Masanori, Fujistuka, Mamoru & Majima, Tetsuro. Light as a Construction Tool of Metal Nanoparticles: Synthesis and Mechanism. *J. Photochem. Photobiol. C Photochem. Rev.* **10**, 33–56 (2009).

122. Hada, Hiroshi, Yonezawa, Yoshiro, Yoshida, Akio & Kurakake, Atsuhiro. Photoreduction of Silver Ion in Aqueous and Alcoholic Solutions. *J. Phys. Chem.* **80**, 2728–2731 (1976).

123. Yonezawa, Yoshiro, Sato, Tomoo, Ohno, Masashi & Hada, Hiroshi. Photochemical Formation of Colloidal Metals. *J. Chem. Soc. Faraday Trans. 1 Phys. Chem. Condens. Phases* **83**, 1559–1567 (1987).

124. Han, M. Y. & Quek, C. H. Photochemical Synthesis in Formamide and Room-Temperature Coulomb Staircase Behavior of Size-Controlled Gold Nanoparticles. *Langmuir* **16**, 362–367 (1999).

125. Gachard, Elisabeth, Remita, Hynd, Khatouri, Jamal, Keita, Bineta, Nadjo, Louis & Belloni, Jacqueline. Radiation-Induced and Chemical Formation of Gold Clusters. *New J. Chem.* **22**, 1257–1265 (1998).

126. Kurihara, Kazue, Fendler, Janos H., Kizling, Jerzy & Stenius, Per. Laser and Pulse Radiolytically Induced Colloidal Gold Formation in Water and in Water-in-Oil Microemulsions. *J. Am. Chem. Soc.* **105**, 2574–2579 (1983).

127. Zhang, Xin, Wang, Hui & Su, Zhaohui. Fabrication of Au@Ag Core-Shell Nanoparticles Using Polyelectrolyte Multilayers as Nanoreactors. *Langmuir* **28**, 15705–15712 (2012).

128. Wei, Suying, Wang, Qiang, Zhu, Jiahua, Sun, Luyi, Lin, Hongfei & Guo, Zhanhu. Multifunctional Composite Core–Shell Nanoparticles. *Nanoscale* **3**, 4474–4502 (2011).

129. Toshima, Naoki & Yonezawa, Tetsu. Bimetallic Nanoparticles—Novel Materials for Chemical and Physical Applications. *New J. Chem.* **22**, 1179–1201 (1998).

130. Wang, Dingsheng & Li, Yadong. Bimetallic Nanocrystals: Liquid-Phase Synthesis and Catalytic Applications. *Adv. Mater.* **23**, 1044–1060 (2011).

131. Jena, Bikash Kumar & Raj, C. Retna. Synthesis of Flower-like Gold Nanoparticles and Their Electrocatalytic Activity towards the Oxidation of Methanol and the Reduction of Oxygen. *Langmuir* **23**, 4064–4070 (2007).

132. Caswell, K. K., Bender, Christopher M. & Murphy, Catherine J. Seedless, Surfactantless Wet Chemical Synthesis of Silver Nanowires. *Nano Lett.* **3**, 667–669 (2003).

133. Millstone, Jill E., Hurst, Sarah J., Métraux, Gabriella S., Cutler, Joshua I. & Mirkin, Chad A. Colloidal Gold and Silver Triangular Nanoprisms. *Small* **5**, 646–664 (2009).

134. Wang, Dingsheng & Li, Yadong. Bimetallic Nanocrystals: Liquid-Phase Synthesis and Catalytic Applications. *Adv. Mater.* **23**, 1044–1060 (2011).

135. Jiang, Hai Long & Xu, Qiang. Recent Progress in Synergistic Catalysis over Heterometallic Nanoparticles. *J. Mater. Chem.* **21**, 13705–13725 (2011).

136. Ferrando, Riccardo, Jellinek, Julius & Johnston, Roy L. Nanoalloys: From Theory to Applications of Alloy Clusters and Nanoparticles. *Chem. Rev.* **108**, 845–910 (2008).

137. Major, Kevin J., De, Chandrima & Obare, Sherine O. Recent Advances in the Synthesis of Plasmonic Bimetallic Nanoparticles. *Plasmonics* **4**, 61–78 (2009).

138. Gonzalez, Carlos Miguel, Liu, Yun & Scaiano, J. C. Photochemical Strategies for the Facile Synthesis of Gold-Silver Alloy and Core-Shell Bimetallic Nanoparticles. *J. Phys. Chem. C* **113**, 11861–11867 (2009).

139. Gonzalez, Carlos M., Martin, Benjamin & Betancourt, Tania. Photochemical Synthesis of Bimetallic and Anisotropic Au-Containing Nanoparticles Using a One-Step Protocol. *J. Mater. Chem. A* **2**, 17574–17585 (2014).

140. Xu, Linlin, Li, Shuang, Zhang, Hua, Wang, Dameng, Chen, Ming, Liu, K., Bai, Y., Zhang, L., Yang, Z., Fan, Q., Zheng, H., Yin, Y., Gao, C., Fu, S. Y., Hsu, Y. K., *et al.* Laser-Induced Photochemical Synthesis of Branched Ag@Au Bimetallic Nanodendrites as a Prominent Substrate for Surface-Enhanced Raman Scattering Spectroscopy. *Opt. Express, Vol. 25, Issue 7, pp. 7408-7417* **25**, 7408–7417 (2017).

141. Ozcelik Kazancioglu, Elif, Aydin, Meral & Arsu, Nergis. Photochemical Synthesis of Bimetallic Gold/Silver Nanoparticles in Polymer Matrix with Tunable Absorption Properties: Superior Photocatalytic Activity for Degradation of Methylene Blue. *Mater. Chem. Phys.* **269**, 124734 (2021).

142. Saha, Sandip, Pal, Anjali, Pande, Surojit, Sarkar, Sougata, Panigrahi, Sudipa & Pal, Tarasankar. Alginate Gel-Mediated Photochemical Growth of Mono- and Bimetallic Gold and Silver Nanoclusters and Their Application to Surface-Enhanced Raman Scattering. *J. Phys. Chem. C* **113**, 7553–7560 (2009).

143. Zhou, Ji, Xu, Shuping, Xu, Weiqing, Zhao, Bing & Ozaki, Yukihiro. In Situ Nucleation and Growth of Silver Nanoparticles in Membrane Materials: A Controllable Roughened SERS Substrate with High Reproducibility. *J. Raman Spectrosc.* **40**, 31–37 (2009).

144. Park, Myungchan, Shin, Kuan Soo, Lee, Ji Won & Kim, Kwan. Novel Fabrication of Au Nanoparticle Film on a Polyelectrolyte-Coated Glass for Efficient Surface-Enhanced Raman Scattering. *Bull. Korean Chem. Soc.* **36**, 743–747 (2015).

145. Rivera-Betancourt, Omar E., Sheppard, Edward S., Krause, Duncan C. & Dluhy, Richard A. Layer-by-Layer Polyelectrolyte Encapsulation of Mycoplasma Pneumoniae for Enhanced Raman Detection. *Analyst* **139**, 4287–4295 (2014).

146. Koo, Hye Young, Choi, Won San, Park, Jeong Ho & Kim, Dong Yu. Polyelectrolyte Multilayer-Mediated Growth of Gold Nanoparticle Films with Tunable Loading Density and Nanoparticle Shape. *Macromol. Rapid Commun.* **29**, 520–524 (2008).

147. Li, Xiangming, Zhang, Yihe, Wu, Yaling, Duan, Yang, Luan, Xinglong, Zhang, Qian & An, Qi. Combined Photothermal and Surface-Enhanced Raman Spectroscopy Effect from Spiky Noble Metal Nanoparticles Wrapped within Graphene-Polymer Layers: Using Layer-by-Layer Modified Reduced Graphene Oxide as Reactive Precursors. *ACS Appl. Mater. Interfaces* **7**, 19353–19361 (2015).

148. Liu, Zhicheng, Bai, Lu, Zhao, Guizhe & Liu, Yaqing. Sandwich-like Layer-by-Layer Assembly of Gold Nanoparticles with Tunable SERS Properties. *Beilstein J. Nanotechnol.* **7**, 1028–1032 (2016).

149. Zhao, Shuang, Zhang, Kai, An, Jing, Sun, Yingying & Sun, Changqing. Synthesis and Layer-by-Layer Self-Assembly of Silver Nanoparticles Capped by Mercaptosulfonic Acid. *Mater. Lett.* **60**, 1215–1218 (2006).

150. Hu, Xiaoge, Cheng, Wenlong, Wang, Tie, Wang, Yuling, Wang, Erkang & Dong, Shaojun. Fabrication, Characterization, and Application in SERS of Self-Assembled Polyelectrolyte - Gold Nanorod Multilayered Films. *J. Phys. Chem. B* **109**, 19385–19389 (2005).

151. Ruan, Weidong, Lu, Zhicheng, Zhou, Tieli, Zhao, Bing & Niu, Li. Surface Micropatterning Technique for Surface-Enhanced Raman Scattering Analysis. *Anal. Methods* **2**, 684–687 (2010).

152. Tang, Wenqiong, Chase, D. Bruce & Rabolt, John F. Immobilization of Gold Nanorods onto Electrospun Polycaprolactone Fibers via Polyelectrolyte Decoration - A 3D SERS Substrate. *Anal. Chem.* **85**, 10702–10709 (2013).

153. Zhang, Li, Shi, Hong Wei, Wang, Cong & Zhang, Ke Ying. Preparation of a Nanocomposite Film from Poly(Diallydimethyl Ammonium Chloride) and Gold Nanoparticles by in-Situ Electrochemical Reduction, and Its Application to SERS Spectroscopy and Sensing of Ascorbic Acid. *Microchim. Acta* **173**, 401–406 (2011).

154. Wang, Qiang, Bai, Xiuhui, Zhang, Yang, Zhou, Ziang, Guo, Ming, Zhang, Jiatao, Li, Chunhong, Wang, Changzheng & Chen, Shaowei. Layered Assembly of Silver Nanocubes/Polyelectrolyte/Gold Film as an Efficient Substrate for Surface-Enhanced Raman Scattering. *ACS Appl. Nano Mater.* **3**, 1934–1941 (2020).

155. Peng, C., Song, Y., Wei, G., Zhang, W., Zhuang, L. & Dong, W. Self-Assembly of λ-DNA Networks/ Ag NPs: Hybrid Architecture and Active-SERS Substrates. *J. Colloid Interface Sci.* **317**, 183–190 (2008).

156. Anderson, William J., Nowinska, Kamila, Hutter, Tanya, Mahajan, Sumeet & Fischlechner, Martin. Tuning Plasmons Layer-by-Layer for Quantitative Colloidal Sensing with Surface-Enhanced Raman Spectroscopy. *Nanoscale* **10**, 7138–7146 (2018).

157. Zou, Xiangqin, Ying, Erbo & Dong, Shaojun. Seed-Mediated Synthesis of Branched Gold Nanoparticles with the Assistance of Citrate and Their Surface-Enhanced Raman Scattering Properties. *Nanotechnology* **17**, 4758–4764 (2006).

158. Leng, Weinan, Pati, Paramjeet & Vikesland, Peter J. Room Temperature Seed Mediated Growth of Gold Nanoparticles: Mechanistic Investigations and Life Cycle Assesment. *Environ. Sci. Nano* **2**, 440–453 (2015).

159. Cao, Xiaowei, Kong, Yang & Shi, Hongcan. Sea Urchin-Like Gold Nanoparticles: Controllable Preparation and SERS Properties. *Key Eng. Mater.* **789**, 1–5 (2018).

160. Veletanlic, Emina & Cynthia Goh, M. Polyelectrolyte Multilayer Films as Templates for the in Situ Photochemical Synthesis of Silver Nanoparticles. *J. Phys. Chem. C* **113**, 18020–18026 (2009).

161. Machado, G., Beppu, M. M., Feil, A. F., Figueroa, F., Correria, R. R. B. & Teixeira, S. Silver Nanoparticles Obtained in PAH/PAA-Based Multilayers by Photochemical Reaction. *J. Phys. Chem. C.* **113**, 19005–19010 (2009).

162. Shen, Liyan, Rapenne, Laetitia, Chaudouet, Patrick, Ji, Jian & Picart, Catherine. In Situ Synthesis of Gold Nanoparticles in Exponentially-Growing Layer-by-Layer Films. *J. Colloid Interface Sci.* **388**, 56–66 (2012).

163. Chia, Khek Khiang, Cohen, Robert E. & Rubner, Michael F. Amine-Rich Polyelectrolyte Multilayer Nanoreactors for in Situ Gold Nanoparticle Synthesis. *Chem. Mater.* **20**, 6756–6763 (2008).

164. Jang, Eunji & Son, Kyung Jin. Metal-Enhanced Fluorescence Using Silver Nanoparticles-Embedded Polyelectrolyte Multilayer Films for Microarray-Based Immunoassays.

165. Zhang, Wenjing, Zhang, Aijuan, Guan, Ying, Zhang, Yongjun & Zhu, X. X. Silver-Loading in Uncrosslinked Hydrogen-Bonded LBL Films: Structure Change and Improved Stability. *J. Mater. Chem.* **21**, 548–555 (2010).

166. Cui, Xiaoqiang, Li, Chang Ming, Bao, Haifeng, Zheng, Xinting & Lu, Zhisong. In Situ Fabrication of Silver Nanoarrays in Hyaluronan/PDDA Layer-by-Layer Assembled Structure. *J. Colloid Interface Sci.* **327**, 459–465 (2008).

167. Meng, Mei, He, Huawei, Xiao, Jing, Zhao, Ping, Xie, Jiale & Lu, Zhisong. Controllable in Situ Synthesis of Silver Nanoparticles on Multilayered Film-Coated Silk Fibers for Antibacterial Application. *J. Colloid Interface Sci.* **461**, 369–375 (2016).

168. Haiss, Wolfgang, Thanh, Nguyen T. K., Aveyard, Jenny & Fernig, David G. Determination of Size and Concentration of Gold Nanoparticles from UV-Vis Spectra. *Anal. Chem.* **79**, 4215–4221 (2007).

169. Petrov, Alexander I., Antipov, Alexei A. & Sukhorukov, Gleb B. Base-Acid Equilibria in Polyelectrolyte Systems: From Weak Polyelectrolytes to

Interpolyelectrolyte Complexes and Multilayered Polyelectrolyte Shells. *Macromolecules* **36**, 10079–10086 (2003).

170. Haktaniyan, Meltem, Atilla, Suleyman, Cagli, Eda & Erel-Goktepe, Irem. PH- and Temperature-Induced Release of Doxorubicin from Multilayers of Poly(2-Isopropyl-2-Oxazoline) and Tannic Acid. *Polym. Int.* **66**, 1851–1863 (2017).

171. Li, Xiaoling, Xu, Weiqing, Zhang, Junhu, Jia, Huiying, Yang, Bai, Zhao, Bing, Li, Bofu & Ozaki, Yukihiro. Self-Assembled Metal Colloid Films: Two Approaches for Preparing New SERS Active Substrates. *Langmuir* **20**, 1298–1304 (2004).

172. Strehle, Katrin R., Cialla, Dana, Rösch, Petra, Henkel, Thomas, Köhler, Michael & Popp, Jürgen. A Reproducible Surface-Enhanced Raman Spectroscopy Approach. Online SERS Measurements in a Segmented Microfluidic System. *Anal. Chem.* **79**, 1542–1547 (2007).

173. Volný, Michael, Sengupta, Atanu, Wilson, C. Brant, Swanson, Brian D., Davis, E. James & Tureček, František. Surface-Enhanced Raman Spectroscopy of Soft-Landed Polyatomic Ions and Molecules. *Anal. Chem.* **79**, 4543–4551 (2007).

174. Cañamares, Maria Vega, Chenal, Cat, Birke, Ronald L. & Lombardi, John R. DFT, SERS, and Single-Molecule SERS of Crystal Violet. *J. Phys. Chem. C* **112**, 20295–20300 (2008).

175. Lai, Keqiang, Zhang, Yuanyuan, Du, Rui, Zhai, Fuli, Rasco, Barbara A. & Huang, Yiqun. Determination of Chloramphenicol and Crystal Violet with Surface Enhanced Raman Spectroscopy. *Sens. Instrum. Food Qual. Saf.* **5**, 19–24 (2011).

176. Harraz, F. A., Ismail, A. A., Bouzid, H., Al-Sayari, S. A., Al-Hajry, A. & Al-Assiri, M. S. Surface-Enhanced Raman Scattering (SERS)-Active Substrates from Silver Plated-Porous Silicon for Detection of Crystal Violet. *Appl. Surf. Sci.* **331**, 241–247 (2015).

177. Trügler, Andreas, Tinguely, Jean Claude, Jakopic, Georg, Hohenester, Ulrich, Krenn, Joachim R. & Hohenau, Andreas. Near-Field and SERS Enhancement from Rough Plasmonic Nanoparticles. *Phys. Rev. B - Condens. Matter Mater. Phys.* **89**, 165409-1-165409–6 (2014).

178. Fang, Sheng Uei, Hsu, Ching Ling, Hsu, Ting Chu, Juang, Ming Yu & Liu, Yu Chuan. Surface Roughness-Correlated SERS Effect on Au Island-Deposited Substrate. *J. Electroanal. Chem.* **741**, 127–133 (2015).

179. Dridi, H., Haji, L. & Moadhen, A. Rough SERS Substrate Based on Gold Coated Porous Silicon Layer Prepared on the Silicon Backside Surface. *Superlattices Microstruct.* **104**, 266–270 (2017).

180. Dizajghorbani-Aghdam, Hossein, Miller, Thomas S., Malekfar, Rasoul & McMillan, Paul F. SERS-Active Cu Nanoparticles on Carbon Nitride Support Fabricated Using Pulsed Laser Ablation. *Nanomaterials* **9**, (2019).

181. Olson, L. G., Lo, Y. S., Beebe, T. P. & Harris, J. M. Characterization of Silane-Modified Immobilized Gold Colloids as a Substrate for Surface-Enhanced Raman Spectroscopy. *Anal. Chem.* **73**, 4268–4276 (2001).

182. Zhang, L., Wang, C. & Y., Zhang. A Facile Strategy to Synthesize Bimetallic Au/Ag Nanocomposite Film by Layer-by-Layer Assembly Technique. *Appl. Surf. Sci.* **258**, 5312–5318 (2012).

183. Liu, D., Tang, H., Yuan, Y. & Zhu, C. Seed-Assisted Electrodeposition of Multilayer Au Nanoparticles-Assembled Films for Sensitive Surface-Enhanced Raman Scattering Detection. *Microchem. J.* **191**, 1–8 (2023).

184. Zhang, Lingling, Li, Xiaodie, Liu, Weihua, Hao, Rui, Jia, Hongrui, Dai, Yanzhu, Usman Amin, Muhammad, You, Hongjun, Li, Tao & Fang, Jixiang. Highly Active Au NP Microarray Films for Direct SERS Detection. *J. Mater. Chem. C* **7**, 15259–15268 (2019).

185. Bali, Krisztina, Bak, Mónika, Szarka, Katarina, Juhász, György, Sáfrán, György, Pécz, Béla, Mihály, Judith & Mészáros, Róbert. Controlling the Morphology of Poly(Ethyleneimine)/Gold Nanoassemblies through the Variation of PH and Electrolyte Additives. *J. Mol. Liq.* **322**, 114559 (2021).

186. Gupta, Nitin, Rai, Divya Bharti, Jangid, Ashok Kumar & Kulhari, Hitesh. Use of Nanotechnology in Antimicrobial Therapy. *Methods Microbiol.* **46**, 143–172 (2019).

187. Kim, In Hyun, Kim, Ji Hoon, Choi, Jeong Yong, Shin, Chae Ho, Kim, Jung Hwan, Bae, Gyun Tack & Shin, Kuan Soo. Tuning the Interparticle Distances in Self-Assembled Gold Nanoparticle Films with Their Plasmonic Responses. *Chem. Phys. Lett.* **715**, 91–99 (2019).

188. Cho, Tae Joon, Gorham, Justin M., Pettibone, John M., Liu, Jingyu, Tan, Jiaojie & Hackley, Vincent A. Parallel Multi-Parameter Study of PEI-Functionalized Gold Nanoparticle Synthesis for Bio-Medical Applications: Part 1—a Critical Assessment of Methodology, Properties, and Stability. *J. Nanoparticle Res.* **21**, 1–14 (2019).

189. Sun, Xuping, Dong, Shaojun & Wang, Erkang. One-Step Preparation of Highly Concentrated Well-Stable Gold Colloids by Direct Mix of Polyelectrolyte and HAuCl4 Aqueous Solutions at Room Temperature. *J. Colloid Interface Sci.* **288**, 301–303 (2005).

190. Polte, Jörg, Herder, Martin, Erler, Robert, Rolf, Simone, Fischer, Anna, Würth, Christian, Thünemann, Andreas F., Kraehnert, Ralph & Emmerling, Franziska. Mechanistic Insights into Seeded Growth Processes of Gold Nanoparticles. *Nanoscale* **2**, 2463–2469 (2010).

191. Carotenuto, G. & Nicolais, L. Synthesis and Characterization of Gold-Based Nanoscopic Additives for Polymers. *Compos. Part B Eng.* **35**, 385–391 (2004).

192. Mohammed, Fiaz S., Cole, Scott R. & Kitchens, Christopher L. Synthesis and Enhanced Colloidal Stability of Cationic Gold Nanoparticles Using

Polyethyleneimine and Carbon Dioxide. *ACS Sustain. Chem. Eng.* **1**, 826–832 (2013).

193. Lin, Hai Xin, Li, Jie Ming, Liu, Bi Ju, Liu, De Yu, Liu, Jinxuan, Terfort, Andreas, Xie, Zhao Xiong, Tian, Zhong Qun & Ren, Bin. Uniform Gold Spherical Particles for Single-Particle Surface-Enhanced Raman Spectroscopy. *Phys. Chem. Chem. Phys.* **15**, 4130–4135 (2013).

194. Lin, Hai Xin, Li, Jie Ming, Liu, Bi Ju, Liu, De Yu, Liu, Jinxuan, Terfort, Andreas, Xie, Zhao Xiong, Tian, Zhong Qun & Ren, Bin. Uniform Gold Spherical Particles for Single-Particle Surface-Enhanced Raman Spectroscopy. *Phys. Chem. Chem. Phys.* **15**, 4130–4135 (2013).

195. Fuller, Melanie & Köper, Ingo. Polyelectrolyte-Coated Gold Nanoparticles: The Effect of Salt and Polyelectrolyte Concentration on Colloidal Stability. *Polymers (Basel).* **10**, (2018).

196. Huang, Haohao & Ruckenstein, Eli. The Bridging Force between Colloidal Particles in a Polyelectrolyte Solution. *Langmuir* **28**, 16300–16305 (2012).

197. Mengarelli, V., Auvray, L., Pastré, D. & Zeghal, M. Charge Inversion, Condensation and Decondensation of DNA and Polystyrene Sulfonate by Polyethylenimine. *Eur. Phys. J. E. Soft Matter* **34**, (2011).

198. Zhu, Jin, Li, Wenbin, Zhu, Mao, Zhang, Wei, Niu, Wencheng & Liu, Guohua. Influence of the PH Value of a Colloidal Gold Solution on the Absorption Spectra of an LSPR-Assisted Sensor. *AIP Adv.* **4**, 31338 (2014).

199. Kelly, K. Lance, Coronado, Eduardo, Zhao, Lin Lin & Schatz, George C. The Optical Properties of Metal Nanoparticles: The Influence of Size, Shape, and Dielectric Environment. *J. Phys. Chem. B* **107**, 668–677 (2003).

200. Andrade, Gustavo F. S., Fan, Mei Kun & Brolo, Alexandre G. Multilayer Silver Nanoparticles-Modified Optical Fiber Tip for High Performance SERS Remote Sensing. *Biosens. Bioelectron.* **25**, 2270–2275 (2010).

201. Fuller, Melanie & Köper, Ingo. Polyelectrolyte-Coated Gold Nanoparticles: The Effect of Salt and Polyelectrolyte Concentration on Colloidal Stability. *Polymers (Basel).* **10**, 1–9 (2018).

202. Hao, Encai, Schatz, George C. & Hupp, Joseph T. Synthesis and Optical Properties of Anisotropic Metal Nanoparticles. *Journal of Fluorescence* 331–341 at https://doi.org/10.1023/B:JOFL.0000031815.71450.74 (2004).

203. Kahraman, Mehmet, Daggumati, Pallavi, Kurtulus, Ozge, Seker, Erkin & Wachsmann-Hogiu, Sebastian. Fabrication and Characterization of Flexible and Tunable Plasmonic Nanostructures. *Sci. Rep.* **3**, (2013).

204. Khlebtsov, Boris N., Khanadeev, Vitaly A., Panfilova, Elizaveta V., Bratashov, Daniil N. & Khlebtsov, Nikolai G. Gold Nanoisland Films as Reproducible SERS Substrates for Highly Sensitive Detection of Fungicides. *ACS Appl. Mater. Interfaces* **7**, 6518–6529 (2015).

205. Rahim, Md Arifur, Ejima, Hirotaka, Cho, Kwun Lun, Kempe, Kristian, Müllner, Markus, Best, James P. & Caruso, Frank. Coordination-Driven Multistep Assembly of Metal-Polyphenol Films and Capsules. *Chem. Mater.* **26**, 1645–1653 (2014).

206. Erel-Unal, Irem & Sukhishvili, Svetlana A. Hydrogen-Bonded Multilayers of a Neutral Polymer and a Polyphenol. *Macromolecules* **41**, 3962–3970 (2008).

207. Liu, Fei, Kozlovskaya, Veronika, Zavgorodnya, Oleksandra, Martinez-Lopez, Claudia, Catledge, Shane & Kharlampieva, Eugenia. Encapsulation of Anticancer Drug by Hydrogen-Bonded Multilayers of Tannic Acid. *Soft Matter* **10**, 9237–9247 (2014).

208. Simon, S. A., Disalvo, E. A., Gawrisch, K., Borovyagin, V., Toone, E., Schiffman, S. S., Needham, D. & McIntosh, T. J. Increased Adhesion between Neutral Lipid Bilayers: Interbilayer Bridges Formed by Tannic Acid. *Biophys. J.* **66**, 1943–1958 (1994).

209. Lin, Daohui, Liu, Ni, Yang, Kun, Zhu, Lizhong, Xu, Yong & Xing, Baoshan. The Effect of Ionic Strength and PH on the Stability of Tannic Acid-Facilitated Carbon Nanotube Suspensions. *Carbon N. Y.* **47**, 2875–2882 (2009).

210. Costadinnova, L., Hristova, M., Kolusheva, T. & Stoilova, N. Conductometric Study of the Acidity Properties of Tannic Acid (Chinese Tannin). *J. Univ. Chem. Technol. Metall.* **47**, 289–296 (2012).

211. Oćwieja, M., Adamczyk, Z. & Morga, M. Adsorption of Tannic Acid on Polyelectrolyte Monolayers Determined in Situ by Streaming Potential Measurements. *J. Colloid Interface Sci.* **438**, 249–258 (2015).

212. Bensalah, Nasr, Chair, Khaoula & Bedoui, Ahmed. Efficient Degradation of Tannic Acid in Water by UV/H2O2 Process. *Sustain. Environ. Res.* **28**, 1–11 (2018).

213. Haslam, Edwin. Natural Polyphenols (Vegetable Tannins) as Drugs: Possible Modes of Action. *J. Nat. Prod.* **59**, 205–215 (1996).

214. Song, Chunyuan, Wei, Yuhan, Da, Bingtao, Zhang, Haiting, Cong, Xing, Yang, Boyue, Yang, Yanjun & Wang, Lianhui. In Situ Growth of Monolayer Porous Gold Nanoparticles Film as High-Performance SERS Substrates. *Mater. Res. Express* **3**, (2016).

215. Huang, Jian, Chen, Feng, Zhang, Qing, Zhan, Yonghua, Ma, Dayan, Xu, Kewei & Zhao, Yongxi. 3D Silver Nanoparticles Decorated Zinc Oxide/Silicon Heterostructured Nanomace Arrays as High-Performance Surface-Enhanced Raman Scattering Substrates. *ACS Appl. Mater. Interfaces* **7**, 5725–5735 (2015).

216. Celik, F. A., Kazanc, S., Yildiz, A. K. & Ozgen, S. Pressure Effect on the Structural Properties of Amorphous Ag during Isothermal Annealing. *Intermetallics* **16**, 793–800 (2008).

217. Sapkota, Kanti & Han, Sung Soo. A Novel Environmentally Sustainable Synthesis of Au-Ag@AgCl Nanocomposites and Their Application as an Efficient

and Recyclable Catalyst for Quinoline Synthesis. *New J. Chem.* **41**, 5395–5402 (2017).

218. Zhang, Xin, Zhang, Guangyu, Zhang, Bodong & Su, Zhaohui. Synthesis of Hollow Ag-Au Bimetallic Nanoparticles in Polyelectrolyte Multilayers. *Langmuir* **29**, 6722–6727 (2013).

219. Zhang, Xin & Su, Zhaohui. Polyelectrolyte-Multilayer-Supported Au@Ag Core-Shell Nanoparticles with High Catalytic Activity. *Adv. Mater.* **24**, 4574–4577 (2012).

220. Shang, Li, Jin, Lihua, Guo, Shaojun, Zhai, Junfeng & Dong, Shaojun. A Facile and Controllable Strategy to Synthesize Au-Ag Alloy Nanoparticles within Polyelectrolyte Multilayer Nanoreactors upon Thermal Reduction. *Langmuir* **26**, 6713–6719 (2010).

221. Rahim, Md Arifur, Nam, Bora, San Choi, Won, Lee, Ha Jin & Jeon, Il Cheol. Polyelectrolyte Complex Particle-Based Multifunctional Freestanding Films Containing Highly Loaded Bimetallic Particles. *J. Mater. Chem.* **21**, 11831–11837 (2011).

222. Li, Shi-Kuo, Zhang, Li, Huang, Fang-Zhi, Yu, Xue-Rong, Xie, An-Jian, Shen, Yu-Hua & Wang, Yang. AuCl4− Ions-Assisted Fabrication of Bimetallic {Poly(Ethylenimine)-Ag/Au} Multilayer Polyelectrolyte Film and Application in Electrocatalysis. *Thin Solid Films* **519**, 5609–5615 (2011).

223. Khan, Merajuddin, Al-Hamoud, Khaleel, Liaqat, Zainab, Shaik, Mohammed Rafi, Farooq Adil, Syed, Kuniyil, Mufsir, Alkhathlan, Hamad Z., Al-Warthan, Abdulrahman, Rafiq, Mohammed, Siddiqui, H., Mondeshki, Mihail, Tremel, Wolfgang, Khan, Mujeeb & Tahir, Muhammad Nawaz. Synthesis of Au, Ag, and Au-Ag Bimetallic Nanoparticles Using Pulicaria Undulata Extract and Their Catalytic Activity for the Reduction of 4-Nitrophenol. *Nanomaterials* **10**, 1–14 (2020).

224. Chuntonov, Lev, Bar-Sadan, Maya, Houben, Lothar & Haran, Gilad. Correlating Electron Tomography and Plasmon Spectroscopy of Single Noble Metal Core-Shell Nanoparticles. *Nano Lett.* **12**, 145–150 (2012).

225. Mallin, Michael P. & Murphy, Catherine J. Solution-Phase Synthesis of Sub-10 Nm Au−Ag Alloy Nanoparticles. *Nano Lett.* **2**, 1235–1237 (2002).

226. Han, Qingyan, Zhang, Chengyun, Gao, Wei, Han, Zhihang, Liu, Tingzhuo, Li, Caixia, Wang, Zhaojin, He, Enjie & Zheng, Hairong. Ag-Au Alloy Nanoparticles: Synthesis and in Situ Monitoring SERS of Plasmonic Catalysis. *Sensors Actuators, B Chem.* **231**, 609–614 (2016).

227. Jiang, Chaoyang, Markutsya, Sergiy & Tsukruk, Vladimir V. Collective and Individual Plasmon Resonances in Nanoparticle Films Obtained by Spin-Assisted Layer-by-Layer Assembly. *Langmuir* **20**, 882–890 (2004).

228. Rodríguez, Rusbel Coneo, Troiani, Horacio, Moya, Sergio E., Bruno, Mariano M. & Angelomé, Paula C. Bimetallic Ag-Au Nanoparticles Inside Mesoporous Titania Thin Films: Synthesis by Photoreduction and Galvanic Replacement, and Catalytic Activity. *Eur. J. Inorg. Chem.* **2020**, 568–574 (2020).

229. Kislenko, V. N. & Oliynyk, L. P. Complex Formation of Polyethyleneimine with Copper(II), Nickel(II), and Cobalt(II) Ions. *J. Polym. Sci. Part A Polym. Chem.* **40**, 914–922 (2002).

230. Chaffin, Elise, O'Connor, Ryan T., Barr, James, Huang, Xiaohua & Wang, Yongmei. Dependence of SERS Enhancement on the Chemical Composition and Structure of Ag/Au Hybrid Nanoparticles. *J. Chem. Phys.* **145**, 054706-1-054706–8 (2016).

APPENDICES

A. The Intensity and Volume Particle Size Distribution of BPEI-capped Au NPs Solution at pH 5.0

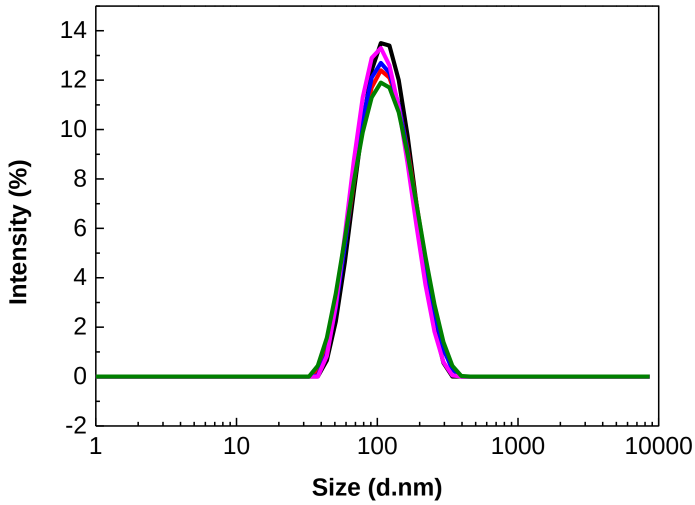

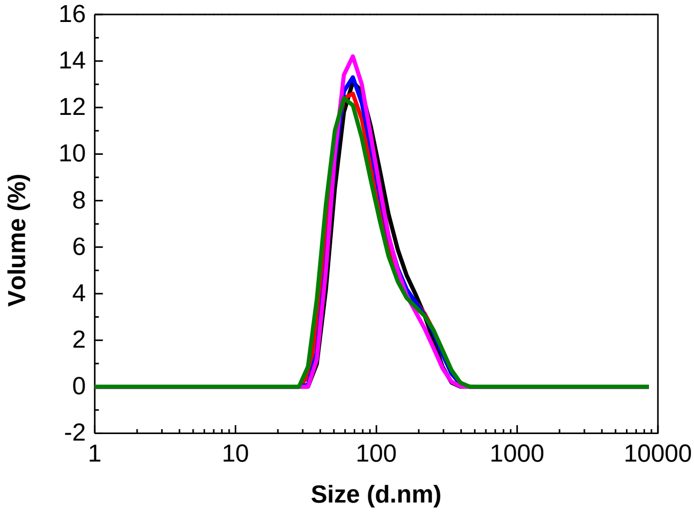

B. The Change of Particle Size Distribution with Increasing pH of BPEI-capped Au NPs solution

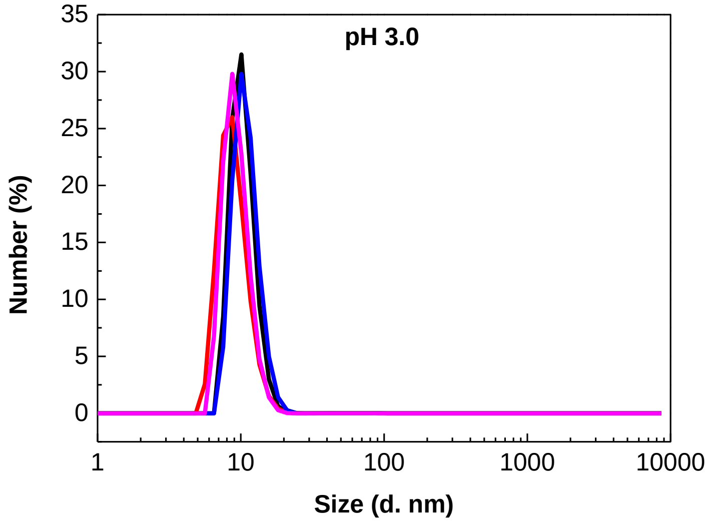

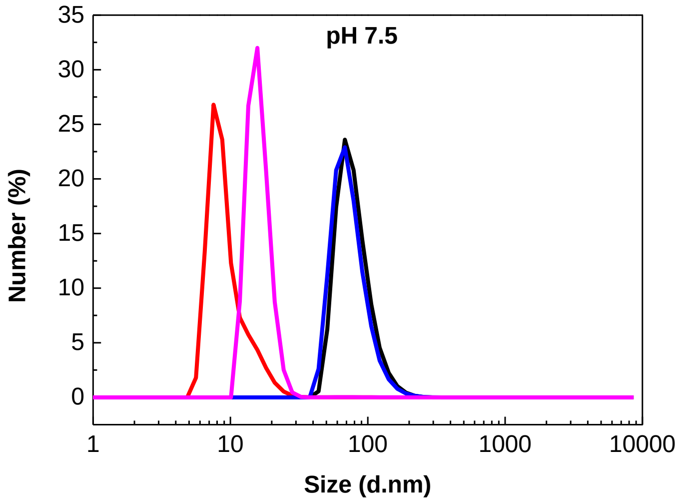

CURRICULUM VITAE

Surname, Name: Özdemir, Sezin

EDUCATION

Degree	Institution	Year of Graduation
MS	METU Chemistry	2016
BS	METU Chemistry	2013
High School	Mehmet Emin Resulzade Anatolian High School, Ankara	2008

FOREIGN LANGUAGES

Advanced English, Beginner German

INTERNATIONAL SYMPOSIUMS

- S.Özdemir, İ. Erel Göktepe, G. Ertaş, "Use of Layer by Layer Assembly of Polyelectrolytes and Gold Nanoparticle for SERS Substrate", Euroanalysis 2019, 1-5 September, 2019, İstanbul University- İstanbul, Turkey.
- S.Özdemir, E.Özdemir, G.Ertaş, "Synergic and Antagonistic Effects between Boron and Arsenic in Yeast (Saccharomyces cerevisiae) Cells", 10. Aegean Analytical Chemistry Days, 29 September- 2 October, 2016, Çanakkale Onsekiz Mart University-Çanakkale, Turkey.
- P.Mercan., S.Atıcı., O.Y.Ataman, "Inorganic Tellurium Speciation Using Tungsten-coil Atom Trap and Hydride Generation Atomic Absorption Spectrometry", 6th Black Sea Basin Conference on Analytical Chemistry, 10-14 September 2013, Trabzon, Turkey.

NATIONAL SYMPOSIUMS

- S.Özdemir, G. Ertaş, "Maya Hücrelerinde Bor ve Arseniğin DNA'ya Etkisi", 29th National Chemistry Congress, 10-14 September 2017, METU, Ankara, Turkey.
- E.Özdemir, S.Atıcı, E.Büber, G.Ertaş, O.Y.Ataman, "Fotokimyasal Buhar Oluşturma ve Atomik Absorpsiyon Spektrometre ile Selenyum Tayini", 7th National Analytical Chemistry Congress, 1-5 September 2014, Kahramanmaraş, Turkey.

PUBLICATION DRAFT

S. Özdemir, İ.Erel Göktepe, G.Ertaş, (in preparation) "Multilayer Structure and Signal Relationship in SERS Substrates Based on Layer-by-Layer Films".

CERTIFICATES AND EDUCATIONS

- *2 May 2023-continued,* mtRS Management Trainee Program
- *7 April 2023,* Application of Decision Rule and Education of Calibration Certificate Evaluations
- *6 April 2023,* Education of Statistical Process Control and Shewart Control Cards
- *22-23 March 2023,* Measurement Traceability and Uncertainty Education-TÜRKAK
- *13-15 March 2023,* TS EN ISO/IEC 17025:2017 Standard Education-TÜRKAK
- *2 March 2023,* Education of Laboratory Statistics

WORK EXPERIENCE

August 2022-continued- Leader Engineer at Roketsan Missile Inc., The Team Leader of Chemical Test Laboratory Unit

- Wet chemistry (titrimety and gravimetry) and instrumental analysis

    - Used instruments: Inductively-coupled plasma optical emission spectrometry (ICP-OES), Ultraviolet-visible spectrometry (UV-vis), Fourier-transform infrared spectrometry (FTIR), near-IR spectrometry (NIR), gas chromatography (GC), high-performance liquid chromatography (HPLC), simultaneous thermal analysis (STA), differential scanning calorimetry (DSC), gas pycnometry, Soxhlet extraction apparatus, laser diffraction analyzer (LDA) and surface area analysis (BET).
- Installation of laboratory substructure
- Preparation and evaluation of technical specifications

January 2015-July 2022- Research and Teaching Assistant at METU, Department of Chemistry

- Analytical chemistry laboratory, instrumental analysis laboratory and general chemistry laboratory

INTERNSHIP

July 2012-September 2012- Novartis, Product Control Laboratory, Effervescent Unit

PROJECT

January 2021-January 2022- "Gümüş Nanoparçacıkların Fotokimyasal Yöntemle Çok Katmanlı Polielektrolit Filmler İçinde Hazırlanarak SERS Alttaşı Olarak Kullanılması", METU BAP, Researcher.

January 2020-January 2021- "Polielektrolit ve Altın Nanoparçacık İçeren Çok Katmanlı Filmlerin Yüzeyde Güçlendirilmiş Raman Spektroskopisi (YGRS) Alttaşı Olarak Kullanılması", METU BAP, Researcher.

February 2013- September 2013- "Inorganic Tellurium Speciation Using Tungsten-coil Atom Trap and Hydride Generation Atomic Absorption Spectrometry", CHEM499 Course, Supervisor: Prof. Dr. O. Yavuz Ataman.